EARTH RADIATION BUDGET MEASUREMENT FROM
A SPINNING SATELLITE: CONCEPTUAL
DESIGN OF DETECTORS

by

L. A. Sromovsky
H. E. Revercomb
V. E. Suomi

V. E. Suomi, Principal Investigator
L. A. Sromovsky, Co-Investigator

TABLE OF CONTENTS

I. INTRODUCTION

This final report to the NASA Langley Research Center describes the
results of work performed under NASA Contract NAS-1-13204 initiated on
6 June 1974 and terminating on 20 April 1975. The objective of this work
as stated in the Statement of Work is

> "to determine the conceptual design, sensor characteristics,
> sensor performance and accuracy, and spacecraft and orbital
> requirements for a Spinning Wide-Field-of-View Earth Energy
> Budget Detector."

The guidelines implied by this objective are the scientific requirements
for measurement of the radiative energy budget of the earth. These
requirements (stated in Section II) appear to us to demand an observing
system of at least 6 to 8 satellites in order to obtain adequate space
time sampling. The economics of multiple satellite systems indicated
that design simplicity and reliability should also be guiding factors
in this work. In fact, the idea of using a spinning satellite platform
for these measurements arose at Wisconsin for these very reasons. This
system concept, which is described in Section II, was well developed
prior to the work conducted under this contract and is restated here
to provide the context within which the present studies were conducted.
The results of the present study support the original concept, indicating
that spinning wide field-of-view sensors can meet scientific requirements
and, in fact, have many advantages over earth oriented sensors.

II. SCIENTIFIC REQUIREMENTS

The purpose of this section is to define the radiation parameters which are to be measured, to state the corresponding accuracy requirements for measurement, and to examine the known variabilities of these parameters to establish approximate sampling and instrumental requirements.

1. Definition of Planetary Radiation Parameters

Figure II.1 depicts a spherical shell centered over the earth at satellite altitude (the exact altitude is not important for the immediate discussion). The coordinate system shown is relative to the earth sun line and the earth's orbital plane. Since the $\hat{x}$ axis points in the direction of the earth's orbital motion and the $\hat{y}$ axis towards the sun, the Θ and ϕ coordinates do not correspond to earth coordinates of latitude and longitude. Useful quantities which can be rigorously measured at the surface of the shell are:

$H(t)$ = Solar flux incident on the earth at time t

$F_R(r_s,\Theta,\phi,t)$ = Plane flux of reflected solar radiation at radius r_s, coordinates Θ, ϕ, and time t

$F_E(r_s,\Theta,\phi,t)$ = Plane flux of earth emitted (long wave) radiation at radius r_s, coordinates Θ, ϕ, and time t.

At a single instant in time the total reflected solar power is precisely equal to the integral of the reflected plane flux $F_R(r_s,\Theta,\phi,t)$ integrated over the entire surface of the shell of the long wave plane flux $F_E(r_s,\Theta,\phi,t)$. Note that conservation of energy implies that these integrated values do not depend on the shell radius r_s. In order to determine the total solar power incident on the earth at time t it is necessary to define the cross sectional

Normal to Earth's
Orbital Plane

$dS = r_s^2 \sin\theta\, d\theta\, d\phi$

θ

r_s

α

Orbital
Motion

ϕ

To Sun

Incident
solar radiation

Earth reference
level surface

Spherical Shell at
satellite altitude
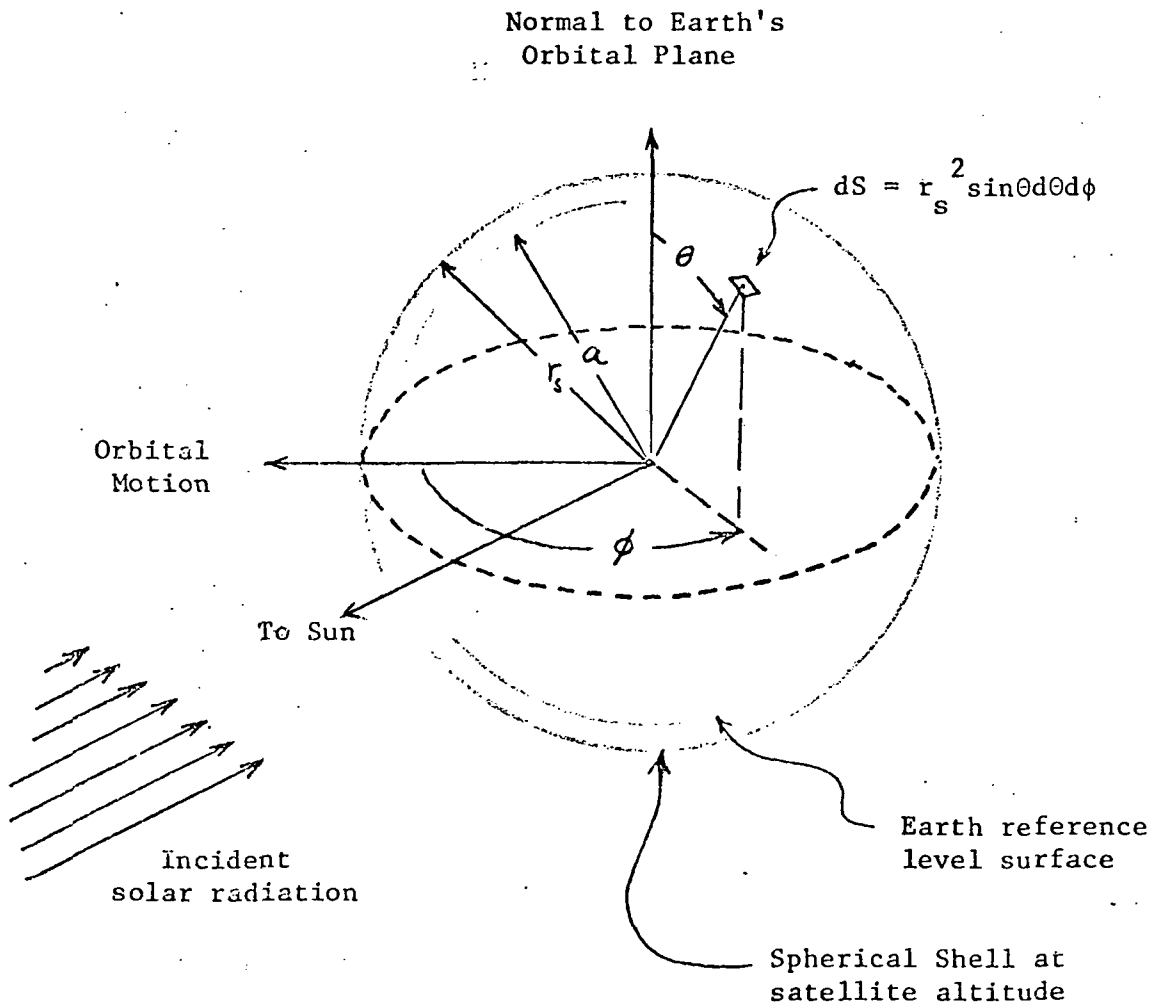
Figure II.1 Geometry for defining planetary radiation parameters. Reflected
radiation passing through an element dS of the spherical shell at satellite
altitude is $F_r(\theta,\phi)dS$. The long wave emitted radiation passing through dS
is $F_e(\theta,\phi)dS$.

area of the earth normal to the earth - sun line. This is done in terms

of a reference radius r_a corresponding to an altitude 30 km above the

earth's surface. The expressions for the total radiative power components

at time t are thus

$$\pi r_a^2 H(t) = \text{Total incident solar power}$$

$$\oint_s F_R(r_s,\Theta,\phi,t)ds = \text{Total reflected solar power}$$

$$\oint_s F_E(r_s',\Theta,\phi,t)ds = \text{Total earth emitted power}$$

From these quantities we can define the more common parameters: the

planetary albedo $A_p(t)$; the average flux of incident solar radiation

$<F_s(t)>$; the average flux of reflected solar radiation $<F_R(t)>$; the

average flux of emitted radiation $<F_E(t)>$; and the average net flux

of radiation $<F_{NET}(t)>$.

$$A_p(t) = \oint_s F_R ds/(\pi r_a^2 H(t)) = <F_R(t)>/<F_s(t)> \tag{1}$$

$$<F_s(t)> = \pi r_a^2 H(t)/(4\pi r_a^2) = \frac{1}{4}H(t) \tag{2}$$

$$<F_R(t)> = \oint_s F_R ds/(4\pi r_a^2) \tag{3}$$

$$<F_E(t)> = \oint_s F_E ds/(4\pi r_a^2) \tag{4}$$

$$<F_{NET}(t)> = <F_E(t)> + <F_R(t)> - <F_s(t)>$$
$$= <F_E(t)> - \frac{1}{4} (1-A_p(t))H(t) \tag{5}$$

Note that the flux values are defined at the reference radius r_a.

The replacement of the integrals in equations (1), (3), (4), and (5) by

sums over discrete measurement points is justifiable provided that the

variations of the plane flux in Θ and ϕ are adequately sampled by the

measurement system. At any instant in time Θ and ϕ variations due to

weather systems on earth would lead to sampling requirements far beyond

the capabilities of any conceivable measurement system. However, the

time averaged parameters for a period of the order of a month contain

much less variability mainly due to the rotation of the earth in the

Θ, ϕ coordinate system. The time averaged parameters are defined as

follows:

$$\langle F_s(t) \rangle^T = \frac{1}{T} \int_{t-\frac{T}{2}}^{t+\frac{T}{2}} [\frac{1}{4}H(t)]dt \tag{6}$$

$$\langle F_R(t) \rangle^T = \oint_S F_R{}^T \, ds/(4\pi r_a{}^2) \tag{7}$$

$$\langle F_E(t) \rangle^T = \oint_S F_E{}^T \, ds/(4\pi r_a{}^2) \tag{8}$$

$$\langle F_{NET}(t) \rangle^T = \langle F_E(t) \rangle^T + \langle F_R(t) \rangle^T - \langle F_s(t) \rangle^T \tag{9}$$

$$A_p(t)^T = \langle F_R(t) \rangle^T / \langle F_s(t) \rangle^T \tag{10}$$

where, if x denotes either E or R,

$$F_x{}^T = \frac{1}{T} \int_{t-\frac{T}{2}}^{t+\frac{T}{2}} F_x(r_s,\Theta,\phi,t)dt. \tag{11}$$

Note that $A_p(t)^T$ is not equal to the time average of $A_p(t)$.

2. <u>Definition of Geographical Radiation Parameters</u>

The previous section dealt with radiation parameters for the planet as

a whole. Perhaps more significant is the way in which radiative interchange

is distributed over the earth. The basic character of the general circulation

of the atmosphere is a result of excess solar energy absorption in the tropics.

The equator to pole gradient of net flux is the driving force for oceanic as

well as atmospheric circulation.

The desired geographical distribution measurements are measurements of local radiation parameters at the reference surface radius r_a. The definition of local parameters is aided by Figure II.2 which depicts a flat surface element receiving an incident radiative flux $H\cos\Theta$ from the sun. The surface element scatters radiation in all directions in general and with highly variable intensity. The integral of all this scattered solar radiation is the outgoing reflected flux F_r at the surface. A similar integral of the emitted long wave radiation is the outgoing emitted flux F_e at the surface. The albedo of the surface element is then defined by the relation

$$A = \frac{F_r}{H\cos\Theta} \tag{12}$$

and the net radiative loss to space F_{NET} is given by

$$F_{NET} = F_e + F_r - H\cos\Theta = F_e - (1-A)H\cos\Theta. \tag{13}$$

These definitions are applicable regardless of the nonuniformity of the surface characteristics and non-Lambertian nature of the scattering. However, since both surface character and sun angle can vary with time, accurate measurement of these quantities requires instantaneous measurement of emitted and reflected radiation in all directions. This would require so many satellites that they would darken the sky.

If the surface is uniform (or if it is uniform in a time average sense) then it is possible to make an integrated measurement of all emitted (or reflected) radiation at all directions by measuring the plane flux at (or very close to) the surface in question. This measurement is a sampling of the surface and is equal to the outgoing flux averaged over the area of the surface. Even if the surface properties are highly anisotropic with respect to scattering direction, this measurement yields
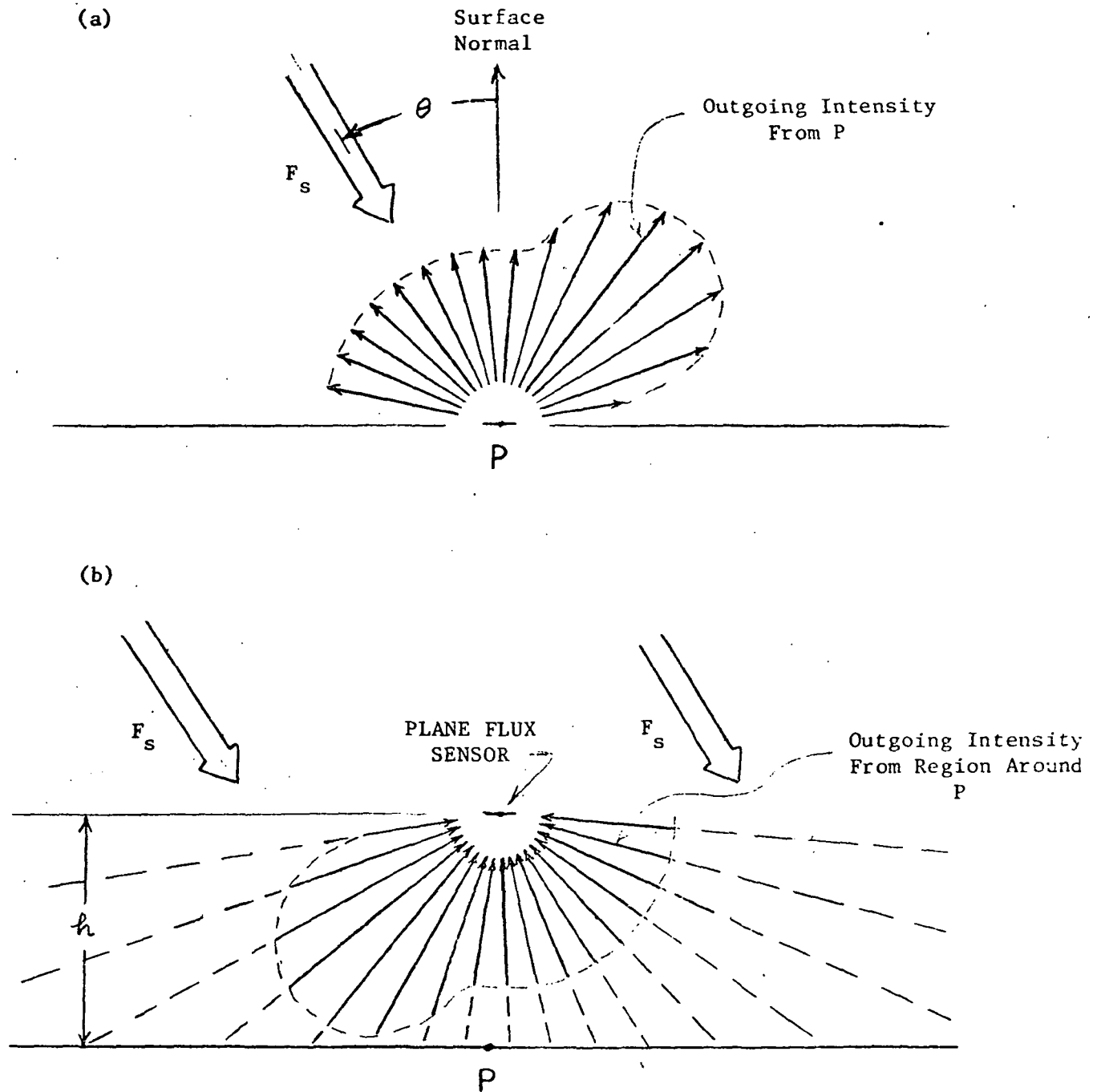
Figure II.2. Geometry for defining local albedo and local outgoing flux (a), and
their relationship to plane flux measured at h. The local outgoing flux at
P is the integral of the intensity at P over all angles (a). The plane flux
measured at h integrates over intensities and simultaneously averages over
space (b). If the region surrounding P has the same scattering (or emitting)
properties as P then the results are equivalent.

rigorously correct values for A and F_{NET} provided that the assumption of uniformity is valid. Measurements of non-planar fluxes do not have this property.

It must be noted that flux measurements at satellite altitude, although they provide for rigorous determination of global albedo and energy balance, are equivalent neither to the reference level plane fluxes at the subsatellite point nor to the average reference level plane fluxes over the sensor field of view unless the satellite orbits at the reference level. At altitudes required for 5 to 10 year lifetimes the curvature of the earth can become significant. As a result, the sensor field of view, which weights incoming intensity as the cosine of the incident angle, does not weight the intensity as the cosine of the emitted (or reflected) angle. Although inference of local reference level parameters will be more accurate for plane flux sensors than would be the case for spherical sensors, errors will be present. Errors in this inference are likely to be consistent on the average and affect the relative change in reference level radiative parameter estimates far less than the absolute values.

In view of the inability to derive rigorous values of reference level fluxes it is better to express the geographical variation of radiative fluxes in terms of direct measurements at satellite altitude, i.e., in terms of average fluxes at satellite altitude as a function of earth coordinates of latitude and longitude. The latter description provides an essential boundary condition for climatic modelling and atmospheric and oceanic energy transport estimates. This description could also be used to derive approximate reference level parameters assuming, for example, that the reference level surface is Lambertian.

3. Required Measurements and Accuracy

At present weather and climate models are insufficiently developed to provide definite predictive information regarding the effects of changes in the earth's radiative boundary conditions. It is in fact a major object of earth energy budget measurement programs to provide the long term observations to aid in the development and testing of such models. In the absence of definitive requirements we must rely on estimates.

In recent years a number of study groups have dealt with the problem of establishing meaningful requirements for earth energy budget measurements. Reports from these groups (SCEP, 1970; SMIC, 1971; RMOP, 1971) indicate an agreement that radiation budget components must be measured to an accuracy of at least 1% and perhaps much better. For example, in the MIT "Report of the Study of Man's Impact on Climate" (SMIC, 1971), it was stated:

"We recommend

1. Monitoring the temporal and geographical distribution of the Earth-atmosphere albedo and outgoing flux over the entire globe, with an accuracy of at least 1%...

4. Determining the absolute value of the solar constant to better than ± 0.5%...

More detailed requirements were outlined very recently in the "Report of the GARP Study Conference on the Physical Basis of Climate and Climate Modeling" (1975). The requirements listed in Table II.1 make use of this later document, as well as previous reports. An attempt was made to improve the self consistency of the parameter requirements and to make the requirements more specific by stating them in terms of flux errors on each component rather than in terms of percentages. It should be noted that requirements dealing with local radiation budget measurements

TABLE II.1. ESTIMATED REQUIREMENTS FOR LONG TERM EARTH ENERGY BUDGET MEASUREMENTS
(Time Resolution for all Parameters is one Month).

DIRECT PARAMETERS	SPATIAL RESOLUTION	EXPECTED MEAN VALUE	MEASUREMENT REQUIREMENTS*		ABSOLUTE**** ACCURACY TARGET
			ABSOLUTE ACCURACY	REPRODUCIBILITY	
Direct Solar Irradiance (Solar Constant)	-	$1350\ WM^{-2}$	$5\ WM^{-2}-13WM^{-2}$	$1\ WM^{-2}-5WM^{-2}$	$2\ WM^{-2}$
Reflected Solar Flux	GLOBAL	$105\ WM^{-2}$	$1\ WM^{-2}-4\ WM^{-2}$	$0.3\ WM^{-2}-1WM^{-2}$	$0.5\ WM^{-2}$
	$(10°GCA)^2$**	$105\ WM^{-2}$	$3\ WM^{-2}-15WM^{-2}$	$3\ WM^{-2}-5WM^{-2}$	$2\ WM^{-2}$
Long Wave Emitted Flux	GLOBAL	$230\ WM^{-2}$	$1\ WM^{-2}-4\ WM^{-2}$	$0.5\ WM^{-2}-1WM^{-2}$	$0.5\ WM^{-2}$
	$(10°GCA)^2$	$230\ WM^{-2}$	$5\ WM^{-2}-15WM^{-2}$	$3\ WM^{-2}-5WM^{-2}$	$3\ WM^{-2}$
DERIVED PARAMETERS***					
Planetary Albedo	GLOBAL	0.30	0.004 – 0.014	0.001 – 0.004	0.002
Planetary Net Radiation	GLOBAL	$14\ WM^{-2}$	$3\ WM^{-2}-11WM^{-2}$	$1\ WM^{-2}-3WM^{-2}$	$1.3\ WM^{-2}$
Zonal Net Radiation (Equator to Pole Difference)	$(10°GCA)^2$	$140\ WM^{-2}$	$9\ WM^{-2}-33WM^{-2}$	$6\ WM^{-2}-11WM^{-2}$	$5.5\ WM^{-2}$

*   Smaller values are desired; larger values are useful.

**   GCA denotes great circle arc.

*** Error values listed for selected derived parameters are deduced from error requirements stated for direct parameters.

**** The absolute accuracy target values are those chosen for the sensor system described in this document. They also insure satisfaction of reproducibility requirements.

have not been included because the spatial resolution required (100 km to 200 km) is not attainable with plane flux sensors at orbital altitudes.

4. Sampling Problems and Requirements

Desired radiation budget parameters are spatial and time averages of direct measurements of variable radiation fluxes. Even a perfect radio- meter will not yield accurate results unless the variabilities are adequately sampled. In order to estimate the variabilities of F_R^T and F_E^T we shall make use of previous earth energy budget measurements (Vonder Haar, 1968).

Figure II.3 is a series of meridional plots of outgoing short wave and long wave radiation from the earth for three month time averages of non- optimally sampled data. Although earth latitude does not accurately correspond to Θ in Figure II.1, the variations shown in Figure II.3 are expected to be comparable in percentages to the variations of F_T with Θ. The smooth variations shown in Figure II.3 indicate that polar or near polar satellites should provide Θ resolution far in excess of the minimum require- ment for seasonal averages; it is expected that monthly and perhaps even weekly averages will be adequately sampled as well.

The variations of F_T with ϕ are expected to be comparable to the diurnal variations derived by Vonder Haar (shown in Figure II.4). In this case, although the variation is quite smooth, the difficulty in obtaining adequate sampling is much greater than it is for Θ variations if we do not want to mix ϕ variations with monthly or seasonal variations. Figure II.5 displays estimated outgoing flux errors as a function of diurnal sampling intervals based on the data presented in Figure II.4.

MERIDIONAL VARIATIONS
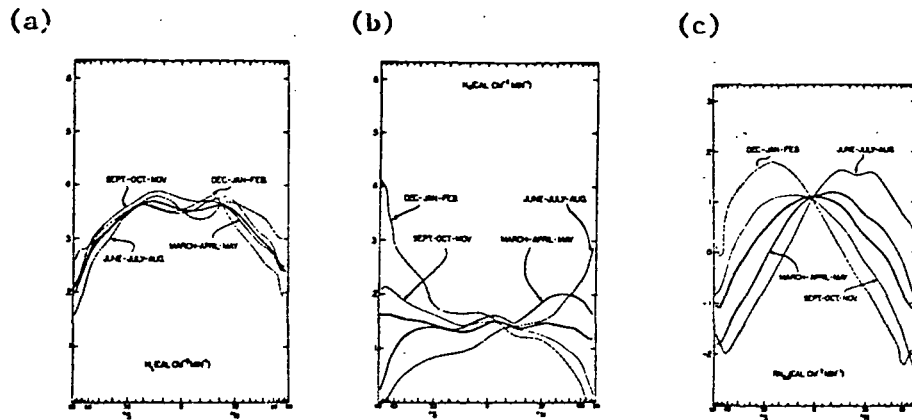
Figure II.3. Mean meridional profiles of long wave fluxes (a), reflected solar fluxes (b), and net fluxes (c) for each season. The solid line in each case indicates the annual mean (Vonder Haar, 1968).

DIURNAL VARIATIONS
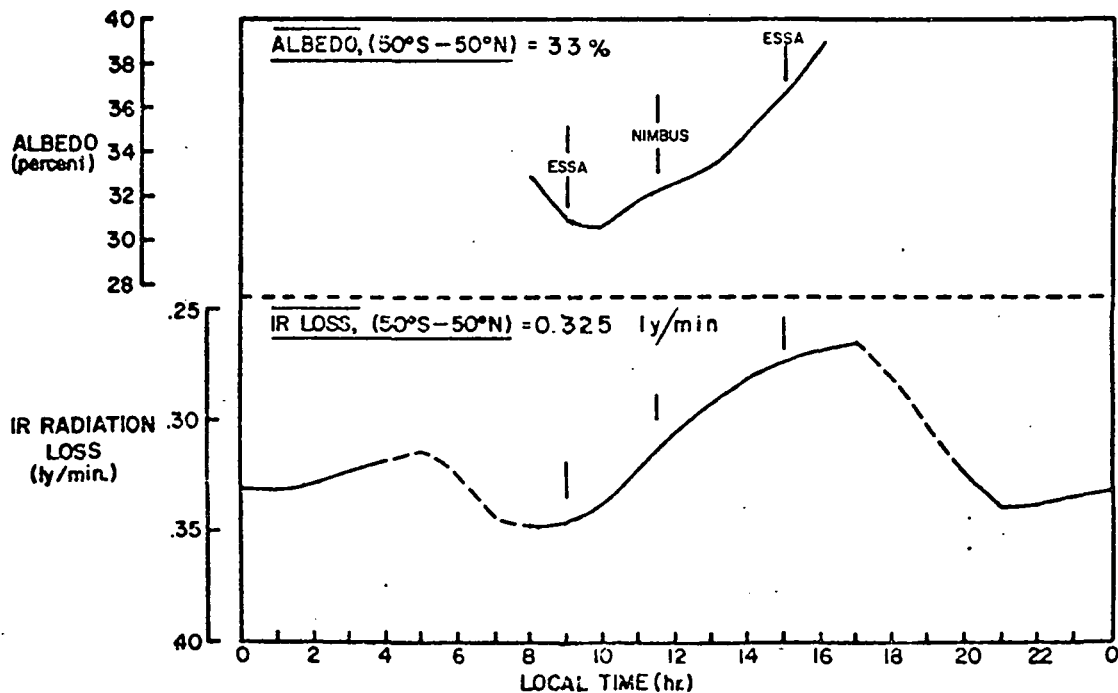
Figure II.4. Diurnal variation of planetary albedo and outgoing long wave flux based on TIROS IV measurements (Vonder Haar, 1968).

Since the diurnal modulation of the long wave flux is only $\pm$ 10% about
the mean value, a modest diurnal time interval of 2 to 4 hours appears to be
adequate if errors are required to stay below 0.2%. This time interval
range roughly corresponds to ϕ intervals of 30° to 60° (see Figure II.1),
which could be obtained with 3 to 6 polar satellites.

The 100% diurnal modulation of the reflected solar flux produces much
more severe sampling constraints based on the estimates shown in Figure II.5(a).
It appears, in this case, that even one hour sampling intervals may be
inadequate. At this point it should be noted that the estimated errors are
those that would occur if outgoing fluxes were directly averaged over the
satellite orbit shell without using any external information about the form
of the diurnal variation. By using such external auxilliary information, or
by using satellite orbital procession to provide continuous diurnal sampling,
the actual errors can be reduced substantially below the estimates in Figure II.
5. If we use N near polar satellites providing 2N diurnal samples per day,
their precessional rates must be large enough to cover the 2N diurnal time
gaps before seasonal variations become significant. A precession rate of
360°/2N per month would provide complete diurnal sampling every month and
probably insure minimal errors due to seasonal effects.

5. Deficiencies in Previous Energy Budget Measurements

The best measurements to date of the radiative energy budget of the
earth are those of Vonder Haar and Suomi (Vonder Haar and Suomi, 1969,
and Vonder Haar, 1969). Their results (probably accurate to $\pm$ 2%) are
based on measurements from several satellites, with varying instrumental
and orbital characteristics. A summary of the instrumental characteristics

(a) Estimated error in average reflected solar flux

DIURNAL SAMPLING TIME INTERVAL
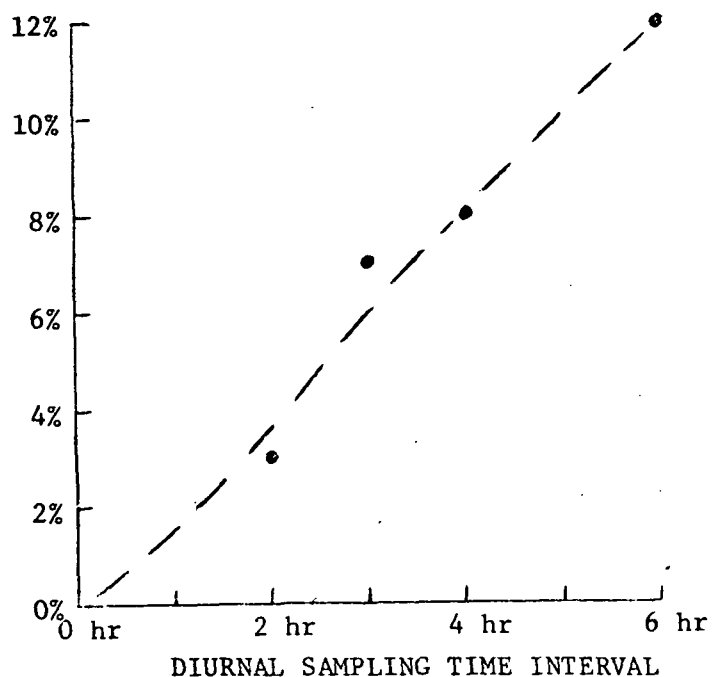
(b) Estimated error in average long wave flux

DIURNAL SAMPLING TIME INTERVAL
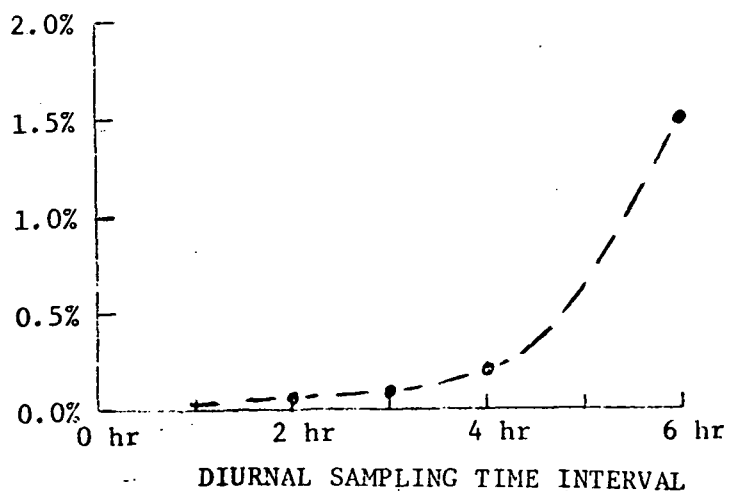
Figure II.5. Estimated errors in averages of reflected solar flux (a) and long wave flux (b) as a function of diurnal sampling frequency. These estimates are for direct averages of discrete samples at fixed local times and do not allow for the sampling improvements obtained from orbital precession

and sampling characteristics of these satellites can be found in a paper

by Vonder Haar (1969). Significant shortcomings of these observations

can be summarized as follows:

(a) Low resolution spherical sensors (those on Explorer VII,

TIROS IV, and TIROS VII) suffered from several problems:

Orbital precession rates required between 65 and 75
days to obtain maximum diurnal sampling.

Spherical sensor characteristics produced 3.5 hour
diurnal gaps.

Sensors had a crude wavelength descrimination
capability, all three radiation currents affecting
each sensor.

Modeling was required to derive fluxes.

(b) Medium resolution sensors (MRIR) suffered from very restricted

angular sampling, incomplete spectral coverage, and post launch

deterioration, requiring estimate of correction factors and an

angular distribution model to utilize the data.

(c) The only plane flux sensors (DISC LRIR's) were in sun-synchronous

orbits and provided inadequate sampling.

(d) Latitude coverage was limited in the worst case to $\pm$ 50° and in

the best case to $\pm$ 85°. On the average, sampling of the polar

regions was inadequate.

(e) No measurements of the solar output were made thus preventing

accurate determination of the net radiative interchange. (It

should be noted that the uncertainty in the solar output was

not a major error source in this case because of the relatively

large magnitude of other errors).

6. Basic Requirements for Earth Energy Budget Observing Systems

From the theoretical discussion presented earlier, the work of Bartman (1967), Bignell (1961), and others it is possible to list general requirements for measurement systems for determining the radiative energy budget of the earth. These should include the following features:

(a) Measurement of plane flux of radiation from the earth.

(b) Accurate spectral separation of reflected short wave radiation and emitted long wave radiation as well as flat spectral response within each range.

(c) Absolute in-flight calibration capability.

(d) Monitoring of the absolute radiative flux incident from the sun. (This flux normalized to the earth's mean orbital radius is termed the solar "constant").

(e) Multiple satellites to provide complete spatial sampling and rapid diurnal sampling.

(f) The combined effects of sampling and radiometric errors should approach levels indicated in Table II.1.

III. OBSERVING SYSTEM CONCEPT

The design of detectors for measuring the radiative energy budget of the earth is determined not only by radiometric requirements but also by the observing system in which they are to be used. The purpose of this section is to describe the basic features of the observing system for which the spinning wide field of view detectors are designed. These features are summarized below:

(1) Measurement of plane fluxes of reflected solar radiation and long wave emitted radiation at satellite altitude using short time constant sensors on board a spinning satellite.

(2) Periodic measurement of incident solar flux using active cavity radiometers on board each satellite.

(3) In-flight calibration based either directly on absolute radiometers or indirectly with intermediate comparison against the sun.

(4) Complete spatial and rapid diurnal sampling using 6-8 satellites in different orbits launched two at a time.

(5) Use of simple satellites with 10 year design life which contain no moving parts and use spin stabilization and magnetic torquing for attitude control.

(6) Use of a single simple ground station for data readout from all satellites and data reduction and archive.

The observing system concept as outlined above is dictated by the general requirements listed in Section II, and by the additional objectives of making the system long lived, reliable, and economical both in fabrication and operation. These objectives and requirements present a convincing case for choosing a simple spin stabilized spacecraft. A spinning spacecraft which

permits sensors to view the earth, the sun, and space on each revolution

provides the capability for accurate in-flight calibration with no moving

parts. Therefore, the probability for a long lifetime is larger than for

an earth oriented spacecraft. Also a spinning spacecraft is simpler to

build than an earth oriented spacecraft making it economically compatible

with the requirement for a fleet of satellites to properly sample diurnal

variations. A more detailed system discussion, mainly with respect to

sensors and sensor operation, is presented in the following subsections.

1. Plane Flux Measurements

Measurements of plane flux at satellite altitude will be made in two

spectral intervals: (1) from 0.2 µm to 4 µm containing approximately 99%

of the reflected solar radiation; and (2) the complete solar and long wave

spectrum from less than 0.2 µm to greater than 100 µm. The latter range is

obtained from a black sensor referred to as the TRS (Total Radiation Sensor)

and the former using a black sensor, termed the SWS (Short Wave Sensor), with

a window probably of fused, water-free, quartz (Suprasil W). The reflected

solar flux is determined directly from the TRS and the long wave emitted

flux from the difference between TRS and SWS outputs.

Since these sensors are on the rim of a satellite spinning at a rate

near 6 RPM, they must have moderately short time constants. In order to

insure response within 0.1% of equilibrium values at sample positions the

time constant must be ~50 milliseconds. The fact that the sensors are

spinning provides for views of space and incident solar flux which, together

with absolute solar flux measurements, provide information required for

in-flight calibration.

The sensor field of view, although planar in angular response, will be restricted to cover an angular region slightly larger than the angular size of the earth at satellite altitude in order to minimize twilight gaps in diurnal coverage which result when outgoing fluxes and incident solar fluxes both fall within the detector field of view. An illustration of the sensor viewing geometry can be found in Figure III.1. The angular size of the earth depends on altitude, taking the specific value of 128° for a 380 nm orbit altitude. The spatial weighting of the plane flux sensors are indicated in Figure III.2 for 700 km and 400 km orbits.

2. Measurement of Incident Solar Radiative Flux

An ACR (Active Cavity Radiometer) is used to measure the absolute value of the incident solar flux with an estimated error of approximately $\pm$ 0.1% absolute. This instrument is a primary standard and does not require calibration by comparison with any other total radiation instrument. The ACR is mounted in the hub of the spinning satellite and is used only when the normal to the orbital plane reaches a minimum angular distance from the earth-sun line. For a two degree/day orbital precession rate relative to the sun the solar flux measurement opportunities occur four times per year per satellite. For a six satellite system, this would provide solar flux measurements 24 times per year. During each measurement the satellite must undergo an attitude change to point the spin axis within 0.5° of the sun.

3. In-Flight Calibration

Earth viewing sensors are calibrated by two measurements made of known incident flux levels: the zero level is provided by space, and the incident
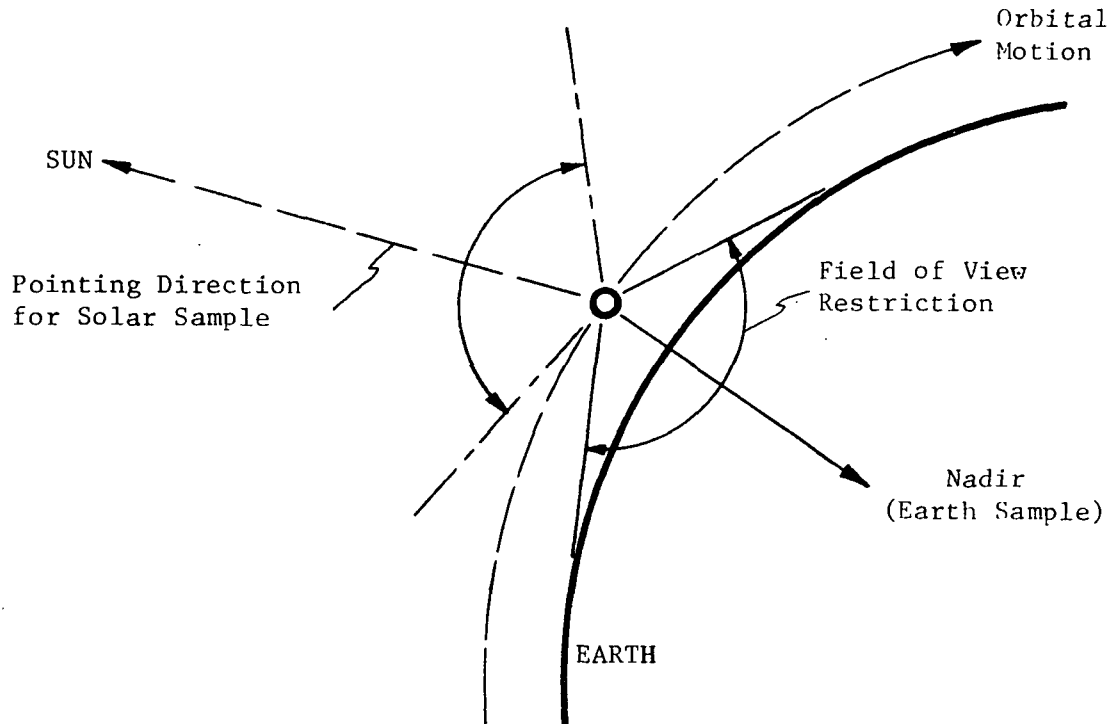
Figure III.1. Viewing geometry for earth-viewing plane flux sensors. Only Earth and Sun sample directions are indicated.

SATELLITE ALTITUDE = 400 KM   SATELLITE ALTITUDE = 700 KM
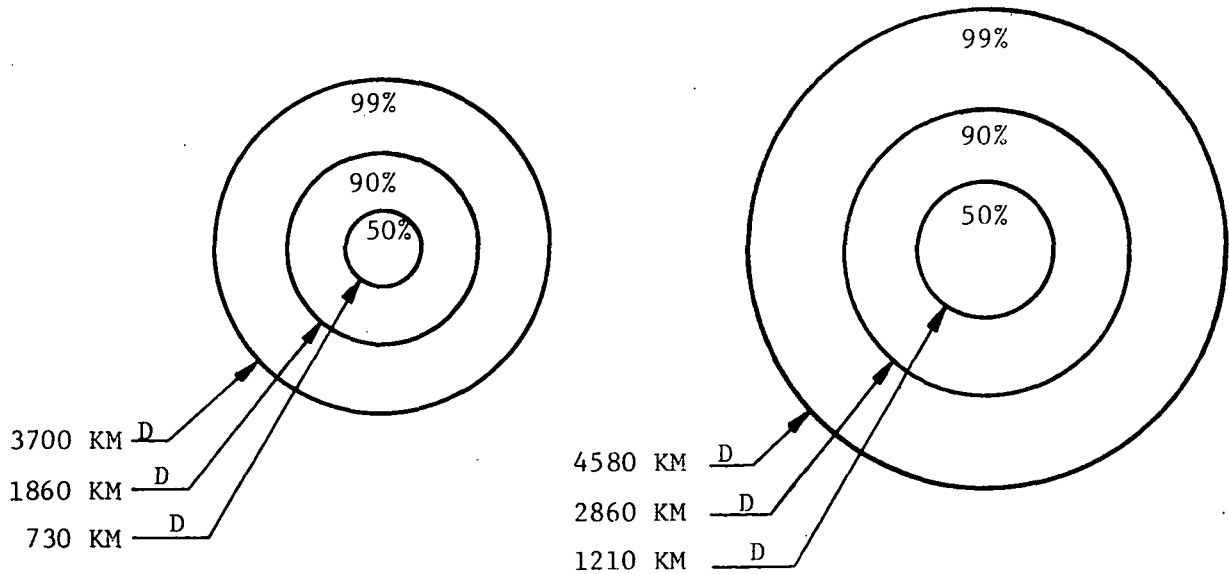
Figure III.2. Spatial weighting of plane flux sensors (TRS and SWS) for two possible satellite altitudes. Percentage levels describe the fraction of received energy coming from within a circle of the indicated diameter.

solar flux level provides the second point. The value of the solar flux level is determined from the solar constant ACR measurement.

The ACR calibration is based on electrical power measurement standards, aperture area measurement, and surface coating emissivity measurement and predicted degradation. Since the ACR has a cavity receiver the uncertainty in surface emissivity has a greatly reduced effect on the uncertainty of the ACR calibration (a reduction by more than a factor of fifty is achieved with the proposed design).

4. Sampling Characteristics

The spatial and temporal sampling capabilities of the observing system are largely determined by the number of satellites and the configuration of their orbits. A fleet of six to eight satellites (shown in Figure III.3 in equally spaced (in longitude), near polar orbits would provide excellent spatial sampling, and with 2°/day orbital precession would provide for rapid diurnal sampling (complete diurnal coverage in one month). However, practical limitations imposed by booster guidance dispersion and the cost and weight required for an orbit plane adjust capability, lead us to believe that a set of six to eight satellites in orbit having different inclinations from 20° to polar is more practical than a plan based on precise orbit to orbit spacing. Preliminary studies indicate that satisfactory coverage may be achieved by eight satellites having four different orbit inclinations. These studies lead us to believe that system accuracy will not suffer unacceptably with six satellites in orbits of different inclinations if the orbits are optimized.

Earth Rotates beneath
Satellites (once per day)

Satellite orbits
precess slowly

Region of Incident
Solar flux measurement

Terminator

1

5

North Pole

2

30°

4

3

Satellite
Rotates 180°

Spin Axis

Spacecraft

TO SUN
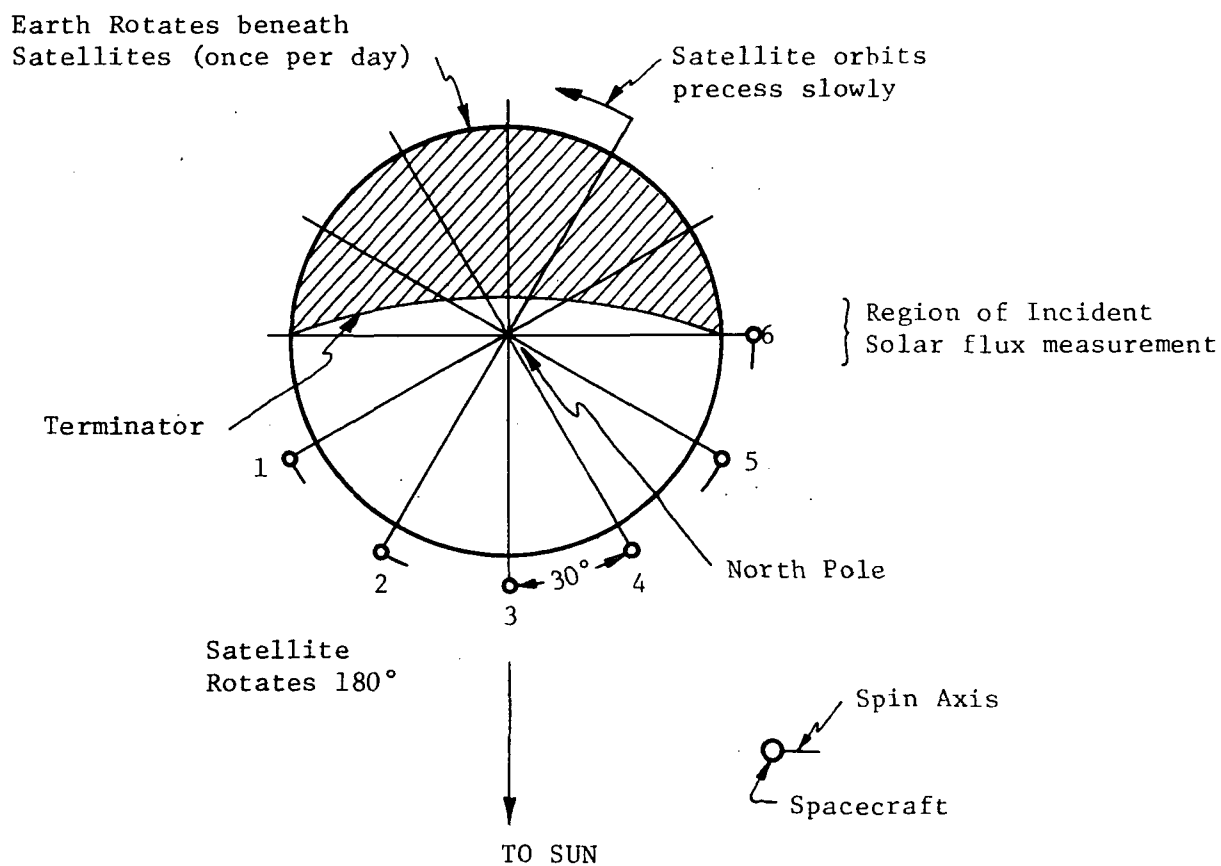
Figure III.3.   Earth-spacecraft configuration for a six-satellite
implementation of the radiative energy budget
observing system.

5. The Satellite Concept

A baseline satellite configuration is shown in Figure III.4. Many small satellites have been designed for, and operated under orbital and other constraints similar to those required for the albedo measuring system. As a result, existing designs and proven technology can be taken advantage of. In fact, there are no parts of the satellite system which require major development; only adaptions of existing designs to fit together and utilization of modern components would be required.

Because the satellite must operate in all possible positions relative to the sun and earth, a shape approaching a sphere is optimum. This same shape has, for the same reasons, been used on many satellite programs. The size of the satellite is determined principally by the surface area required for solar cells.

The most efficient, most reliable, and longest lived attitude control system which will meet program requirements is the spin stabilized magnetic torque and magnetic spin control system thoroughly proven in the TIROS and military satellite systems.

The satellites proposed for the albedo and radiative energy balance measurements consist of the following basic subsystems:

(1) Radiometer Subsystem – This consists of earth viewing plane flux sensors (TRS and SWS), the incident solar flux radiometer (solar constant ACR) and associated electronics.

(2) Attitude and Spin Control Subsystem – This consists of magnetic coils to adjust spin rate and spin axis by magnetic torquing against the earth's field, horizon sensors to provide spin rate and attitude error signals, and control logic for adjusting torques to match error inputs.
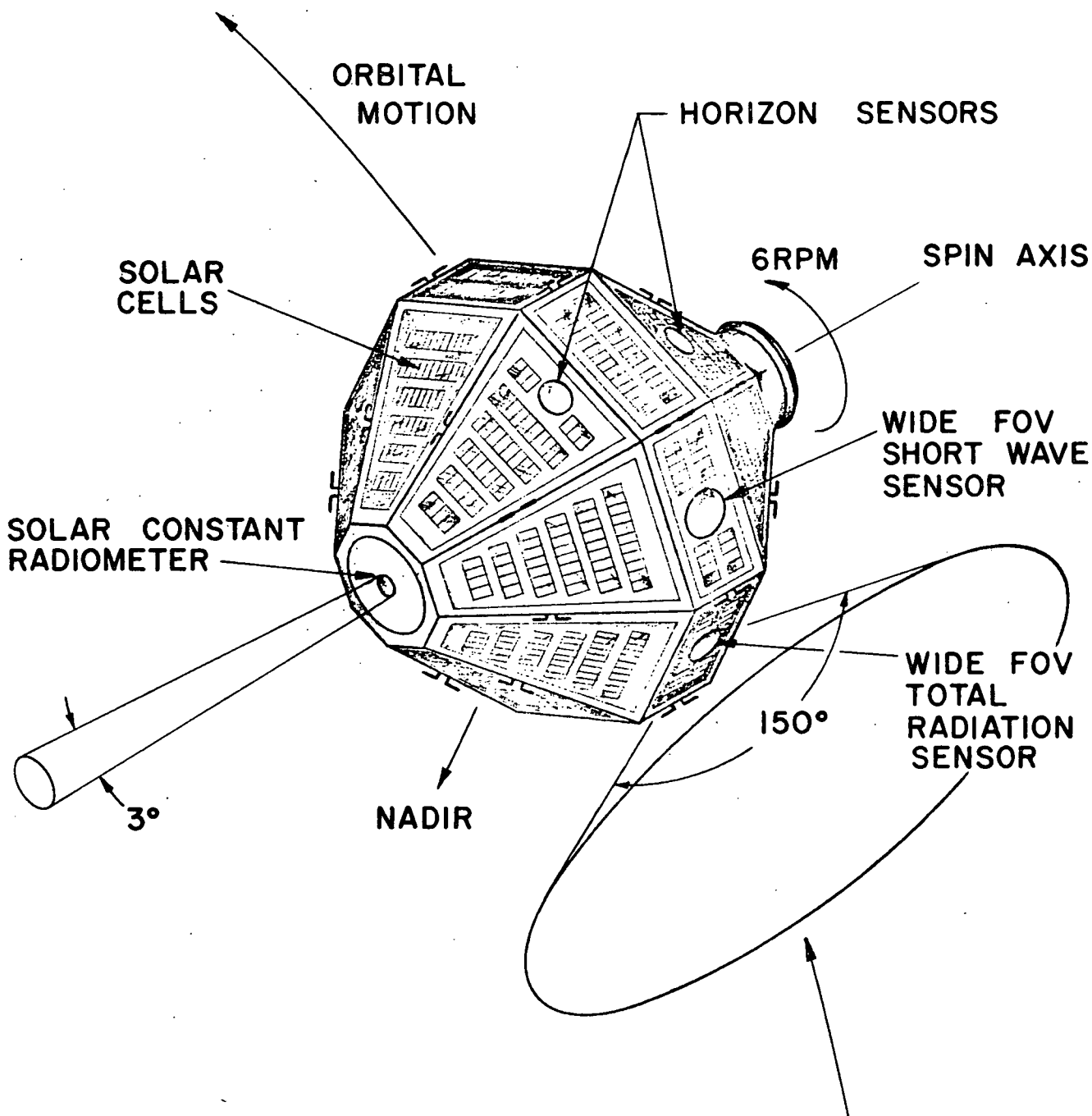
Figure III.4.   Baseline Satellite Configuration

(3) Data Collection Subsystem - This provides sample timing, analog to digital conversion, data averaging and storage.

(4) Telemetry and Command Subsystem - This provides for downlink transmission of radiometer data and housekeeping information, and reception, storage, and processing of commands from the ground station.

(5) Power Subsystem - This consists of solar cells as primary power source and batteries to provide continuous operation day and night.

(6) Mechanical Subsystem - Provides support and thermal control for the other subsystems.

A block diagram of the system is shown in Figure III.5.

6. Sensors in Operation

The plane flux sensor operation to measure albedo and earth emission is shown in Figure III.6. The trace labeled "a" shows what is seen by the total radiation sensor and the short wave sensor when not seeing the sun. When the horizon sensors indicate that these sensors are pointing to the nadir, a sample is taken. Shortly thereafter, the sensors are looking at empty space and another sample is taken.

On the sunlit side of the earth, the sensors will also see the sun at times when looking away from the earth. The sun pulse is detected and sampled at its peak with a photo cell slit trigger system to insure proper sampling time. Depending on the position of the sun with respect to the earth and the spacecraft, three qualitatively different types of signal traces are possible, as shown in Figure III.6 b-d. Trace "b" illustrates the situation where both an uncontaminated earth and sun sample are obtained. If the sun is closer to the horizon than shown in
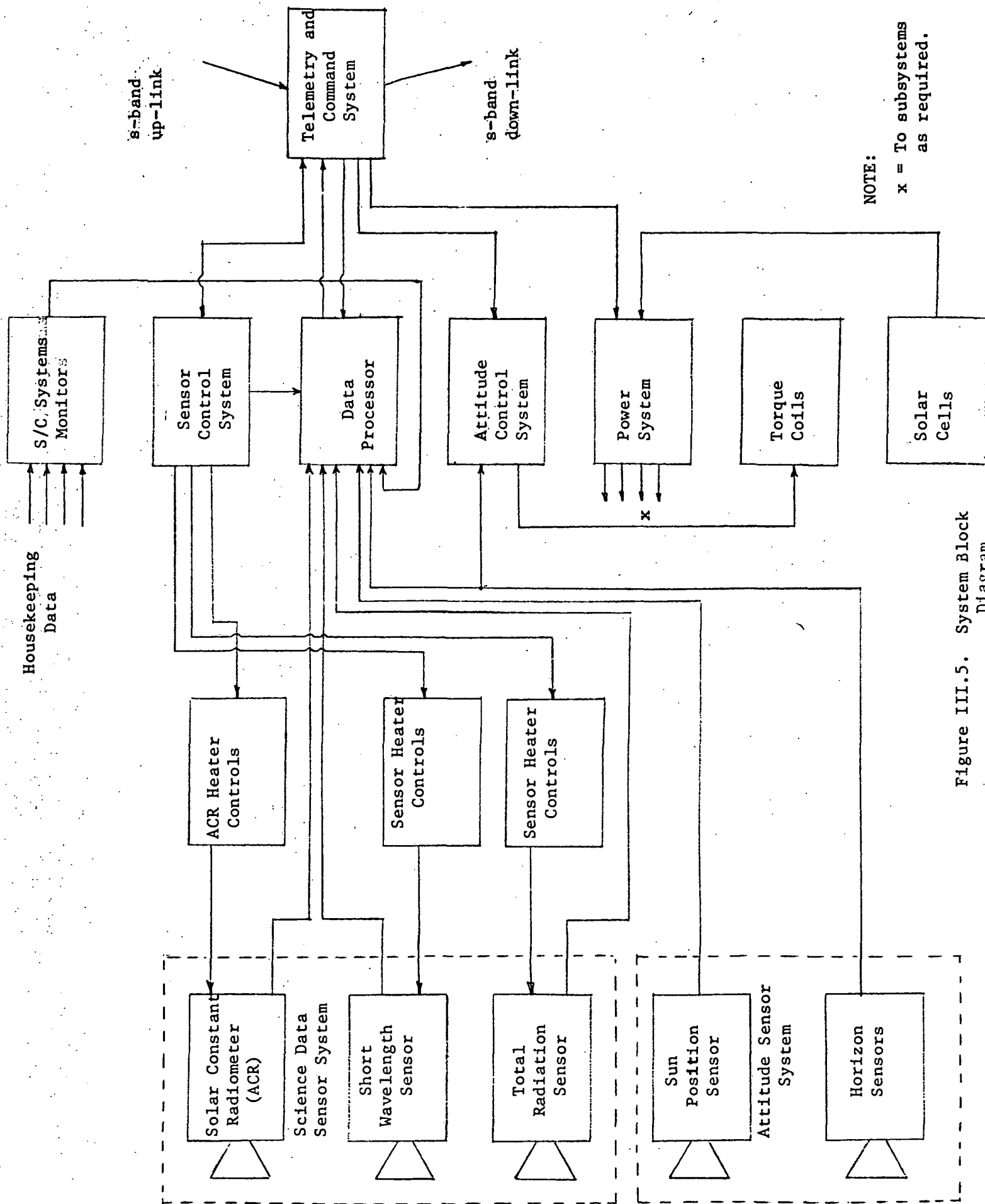
Figure III.5. System Block Diagram

Sensor Signal

(a)

Space Sample

Angle between nadir
and the sensor
pointing axis

270°   0°   90°   180°

Earth Sample
(nadir)

(b)

Earth Sample   Sun Sample

(c)

Earth Sample   Sun Sample   Space Sample
                (contaminated)

(d)

Earth Sample   Sun Sample
(contaminated) (contaminated)
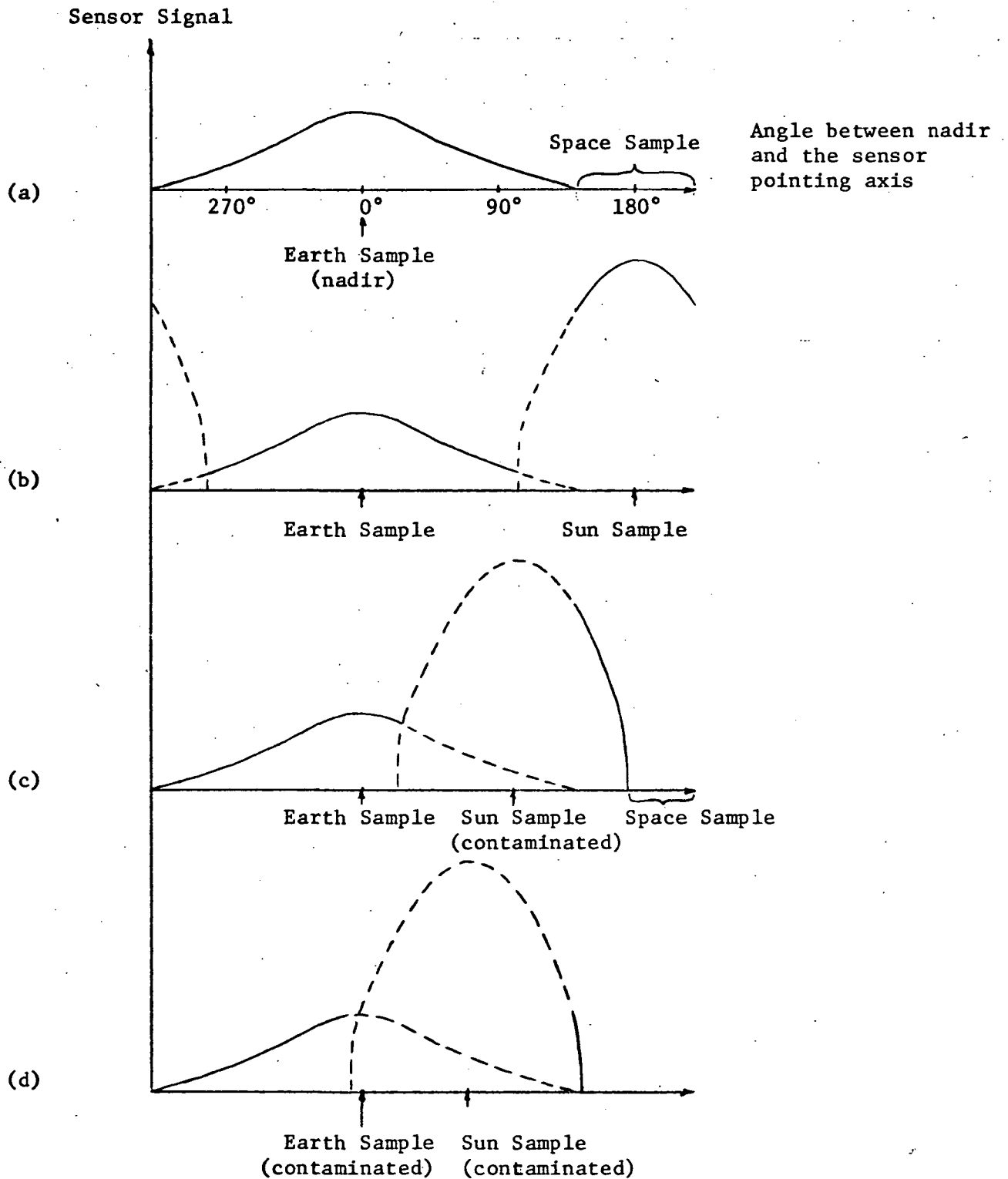
Figure III.6.   Sensor Operation Diagram for Plane Flux Sensors.   In (a) the
      sensor does not see the sun at all during a complete rotation.   Traces
      (b), (c) and (d) show the sun in three different positions to illustrate
      qualitatively different sampling possibilities.   A sensor field of view
      restriction of 150° was assumed.   Where the signal has contributions
      from both the sun and the earth the individual contributions are shown
      as dashed lines.

"b", it is possible for the solar sample to be contaminated by earth

radiation as shown in "c". Such solar data is discarded on the ground

without loss of the earth sample. Finally, when the sun is very close

to the horizon it is possible for both the sun and the earth samples

to be contaminated (see trace "d"). The sampling void caused by such

cases depends on the sensor field of view restriction.

It is desirable, and probably necessary, to separate the earth measure-

ment positively from the sun measurement. To do so, the field of view of

the flux radiometers will be restricted to about 150° so that the sensor

sees only slightly more than the earth when the sample is taken. With

a 150° FOV it will not be possible to obtain isolated "pure" measurements

of the sun and of space on every satellite spin. However, it is not

necessary to have such measurements on every spin; it is only necessary

to collect them frequently enough to prevent data contamination by sensor

drift or change in solar output, both of which are slow processes.

With two flux sensors, up to six samples (earth, space, sun) will be

taken each satellite spin and will be accumulated in six separate registers.

Every six spins these registers will be averaged and stored in the space-

craft solid-state memory. This system will provide samples about 216 n. mi.

apart along the orbit track. Between track spacing with six satellites would

average about 1800 n miles at the equator and be much closer at higher latitudes.

If data words are 10 bits long, only about 40,000 bits need be stored if

the satellite is read out twice daily. A single unmanned station located at

about 45° latitude is sufficient to handle the system even if eight satellites

are included in randomly drifting orbits since readout can be accomplished

easily during a small portion of the satellite's pass over the station.

As the satellite's orbit plane precesses relative to the sun, the sun

will be seen within a short period of time at all possible angles within

the FOV of the plane flux sensors. Thus, even if only one sample is taken every six satellite spins, the complete angular response of the sensor will be mapped by the sun each six months with very fine resolution. The shape of the plane flux sensor sun pulse will yield information on aging characteristics. It should be noted that since the incident solar flux radiometer views at 90° to the flux sensors, the observation of the sun from one satellite will be used to calibrate the flux sensors in all the other satellites--not the flux sensors on board the same satellite. This characteristic provides a significant system advantage. With six satellites, each reaching calibration position four times each year, each satellite's plane flux sensors will be calibrated 20 times each year by five different solar reference measurements.

IV. SOLAR CONSTANT RADIOMETER DESIGN

The function of the solar constant radiometer is measurement of the incident solar flux with an accuracy approaching .1%. The measurements are used to calibrate the solar views of the TR and SW sensors, thereby providing accurate measurements of the solar incident flux at daily intervals. A series of absolute radiometers known as Active Cavity Radiometers (ACR's) has been developed at JPL in recent years. A minor modification of one of these designs is especially well suited to this task.

1. Principle of ACR Operation

The active cavity radiometer consists of a cavity which can be heated electrically, a heat sink which surrounds the cavity exterior except for the aperture region, and an electronic servo system which controls the cavity temperature. The degree of thermal coupling between the cavity and the heat sink varies with the specific design. However, all of the designs operate using electrical substitution. That is, the power absorbed by the cavity from an unknown radiation source is determined by measuring the additional electrical power necessary to maintain the cavity temperature when the radiation source is removed. The thermal environment of the cavity is controlled by the heat sink so that any power losses from the cavity (e.g. conduction through the electrical leads, radiative exchange with the heat sink, etc.) which occur when the source is present are nearly identical to those which occur when it is removed. Therefore, the difference of the electrical heating required to maintain the cavity temperature with and

without the source present is essentially independent of cavity power losses; measurement of the incident source flux depends only on the electrical power measurements, the cavity aperture area and the apparent cavity absorptance. Since absorptances are notoriously difficult to measure precisely, the ACR operation depends heavily on the cavity design which enhances the apparent absorptance. The cavity dimensions are chosen such that the apparent absorptance is so close to unity that errors in the apparent absorptance calculated from the measured surface coating absorptance are much smaller than the errors of the measurement.

2. Demonstrated Accuracies of Active Cavity Radiometers

A large number of ACR's have been built and operated by JPL since about 1967. These radiometers fall into two major classes: those in which the cavity and the heat sink are thermally isolated (generally referred to as standard active cavity radiometers or SACRAD's), and those in which the cavity and heat sink are conductively coupled (the first radiometers of this type are referred to as primary active cavity radiometers or PACRAD's and the later models simply as ACR's). Since the ACR is at present the best radiation detector available, it is not possible to measure its absolute accuracy directly. However, an important experiment was performed by J. M. Kendall, Sr. (1970) which, in conjunction with comparisons of measurements made by different types of ACR's, shows that the actual performance of the radiometers is consistent with theoretical predictions of their measurement uncertainties.

Kendall used a SACRAD to measure the Stefan-Boltzmann constant which can be determined independently to better than .02% using a well established relationship involving fundamental constants. The results of measurements at four different cavity temperatures show a mean deviation from the theoretical value of 0.3%. The theoretical analysis of the SACRAD yields a measurement uncertainty of 0.37%.

A large number of radiometric intercomparisons have been made during solar constant measurements from mountain top and balloon. The results are summarized below along with the predicted instrument uncertainties.

	THEORETICAL UNCERTAINTY	
SACRAD (In Vacuum)	0.40%	(Willson, 1969)
PACRAD	0.22%	(Kendall, et. al. 1970)
ACR	0.22%	(Willson, 1973)

TYPE OF RADIOMETERS COMPARED	MEASUREMENT DIFFERENCES
SACRAD-PACRAD	<0.5%
PACRAD-PACRAD (8 Radiometers)	<0.15%
ACR-PACRAD	<0.3%

The SACRAD-PACRAD comparison was the most difficult to perform accurately because the SACRAD had to be operated in vacuum. The results indicate that the theoretical calculations of radiometer uncertainties are probably a good estimate of the absolute ACR accuracies.

To further emphasize the capabilities of the ACR it should be noted that comparisons have also been made between ACR's and the Angström pyrheliometer which in conjunction with the Abbott water-flow calorimeter has established the International Pyrheliometric Scale (IPS). The theoretical uncertainty of the Angström pyrheliometer has been calculated to be 2.6% (Willson, 1969). The ACR measurements indicate a -2.2% (Willson, 1972) error in the IPS as reproduced by Angström pyrheliometers.

3. Design for Present Application

One of the latest ACR designs, the ACR III, will be used with minor modifications for the solar flux measurement. The basic construction of the ACR III is shown in Figure IV.1. The detector cavity is connected to a heat sink by a cylindrical thermal impedance. Platinum resistance sensors placed at either end of the thermal impedance are used to detect the cavity-heat sink temperature difference. A bridge circuit, using the platinum resistance sensors as two elements, senses the temperature difference and directs power to the cavity heater until the difference is driven to a fixed value. Changes in the incident irradiance are thus balanced by changes in electrical power. As mentioned earlier, operation of the ACR requires two electrical power measurements, one for the unknown source and one for a reference source. The cavity thermal environment is maintained constant for the two measurements so that the unknown irradiance is proportional to
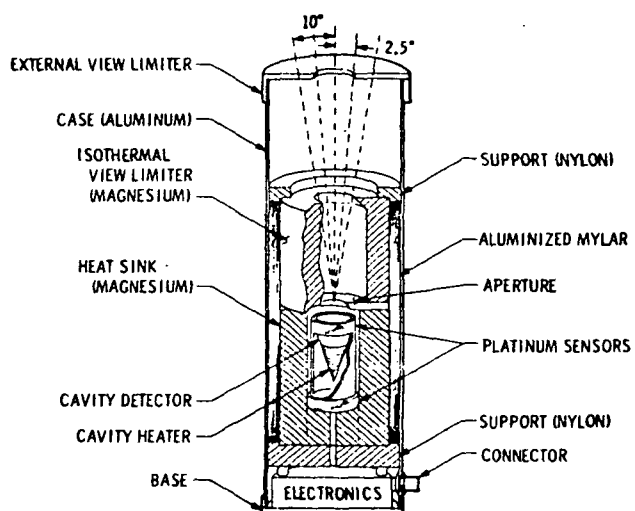
Figure IV.1.   JPL Active Cavity Radiometer (ACR III) Mechanical Configuration
(from Willson 1971).

the difference of the power measurements.

The ACR III was designed to operate using a shutter for the reference source. In this mode of operation the cavity thermal environment is maintained by the heat capacity of the heat sink; that is, the heat sink temperature is not actively controlled, but is allowed to drift. To avoid the need for a shutter and to control the heating of the heat sink by the source irradiance, a modification will be made to temperature control the heat sink to about 10° above the highest spacecraft ambient temperature. Platinum heater and sensor wires placed on the heat sink will allow electrical servo control of the heat sink temperature with a reproducibility of $\pm 10^{-3}$°K. With this modification, space can be used as the reference source because it is not necessary for the solar view and the reference view to be closely spaced in time.

The specific ACR design chosen is illustrated schematically in Figure IV.2. The cavity shape has been altered from that of the ACR III to enhance its emittance. A technique for calculating a lower bound to the cavity apparent emittance is developed in Appendix A. The results for several surface coating emittances are:

ε SURFACE	LOWER BOUND TO APPARENT EMITTANCE
0.88	.9981
0.90	.9986
0.95	.9995

With a 5% uncertainty or degradation of the surface emittance the apparent cavity emittance uncertainty is less than 0.1%.

The aperture dimensions have also been altered for this application. The view limiting aperture has been chosen to block all radiation with an incident angle greater than 24°. To restrict the view much further would either permit

IV-7

1.5°

0.634

24°

2.692

Heat Sink

0.564

30°

Platinum wire
Heat Sink
Sensor-heater

0.800

1.128

Platinum wire
temperature
difference
sensors

Cavity

15°

Platinum wire
Cavity Heater

Thermal Resistor

1.500
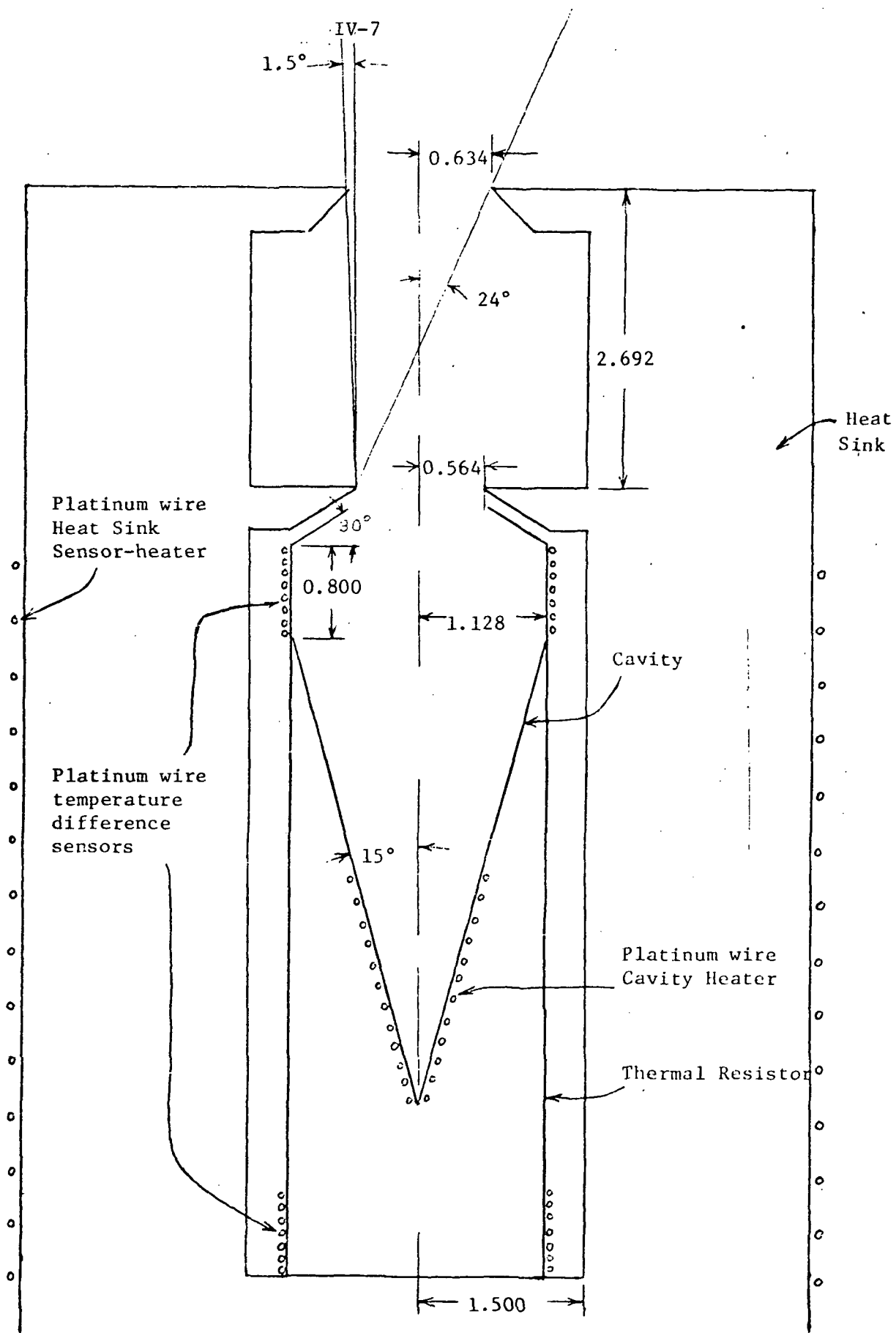
Figure IV.2.   Specific Solar Constant ACR Design Configuration.   Dimensions are in
               Centimeters.

more solar radiation to be reflected into the cavity causing error, or would place more stringent requirements on the pointing accuracy necessary to avoid missing part of the sun. For a 380 nm inclined orbit, the 24° aperture permits the sun to be viewed without earth radiance contamination for at least half of each orbit used for solar flux determinations. The pointing accuracy required for this ACR design is about ±0.5°. Pointing is necessary to provide nearly equivalent electrical and radiative heating of the detector cavity and to allow determination of the cavity aperture area to ±0.05%.

4. Servo System Description

The ACR requires very precise control of both the cavity base temperature and the temperature difference across the thermal resistance. An electronics design study shows that these requirements can be met using state of the art technology. (See Appendix B). The control requirements are as follows:

Base temperature servo:

Base temperature setting	$300°K \pm 0.1°K$
Base temperature variation between sun and space looks	$\leq 10^{-3}°K$
Base temperature stability during 100 second observation	$\leq 10^{-3}°K/100$ Sec

Difference temperature servo:

Difference temperature (ΔT) setting	$0.3°K \pm 0.1°K$
Variation in ΔT between sun and space looks	$\leq 2.5 \times 10^{-4}°K$
Stability over 100 seconds	$\leq 1.0 \times 10^{-4}°K$

The difference temperature servo design is shown in Figure IV.3. The important aspects of this design are:

(1) The electronics modules which control sensor temperature drift are temperature regulated within $\pm 0.1°C$ using an auxiliary servo.

(2) The base temperature control servo uses the heater winding as a temperature sensor. This avoids oscillation problems that would arise from heater-sensor time delay.

(3) The difference temperature control servo uses two platinum wire sensors in a bridge circuit. Bridge output (i.e., error voltage) is amplified and sign detected.

Depending on the sign of the bridge output, count in a 16 bit up/down counter is updated every time the slow clock pulse occurs. The counter output drives a high resolution (16 bit) digital to analog (D/A) converter whose output voltage is proportional to the binary value of the 16 bit count. D/A output drives a stable constantan wire heater via a unity gain power amplifier. Thus, at the end of every slow clock pulse the heater power is varied (adjusted) to control the difference temperature without an overshoot or oscillation. Moreover, the high resolution 16 bit output from the counter provides an accurate high resolution measure of heater voltage and hence heater power.

5. Error Analysis Summary

An error analysis of the ACR design shown in Figure IV.2 is given in Appendix C. The basic operating equation of the ACR used there is as follows:

$$H = \frac{P_e' - P_e}{A_c(\alpha_c + \rho\rho_c)}$$
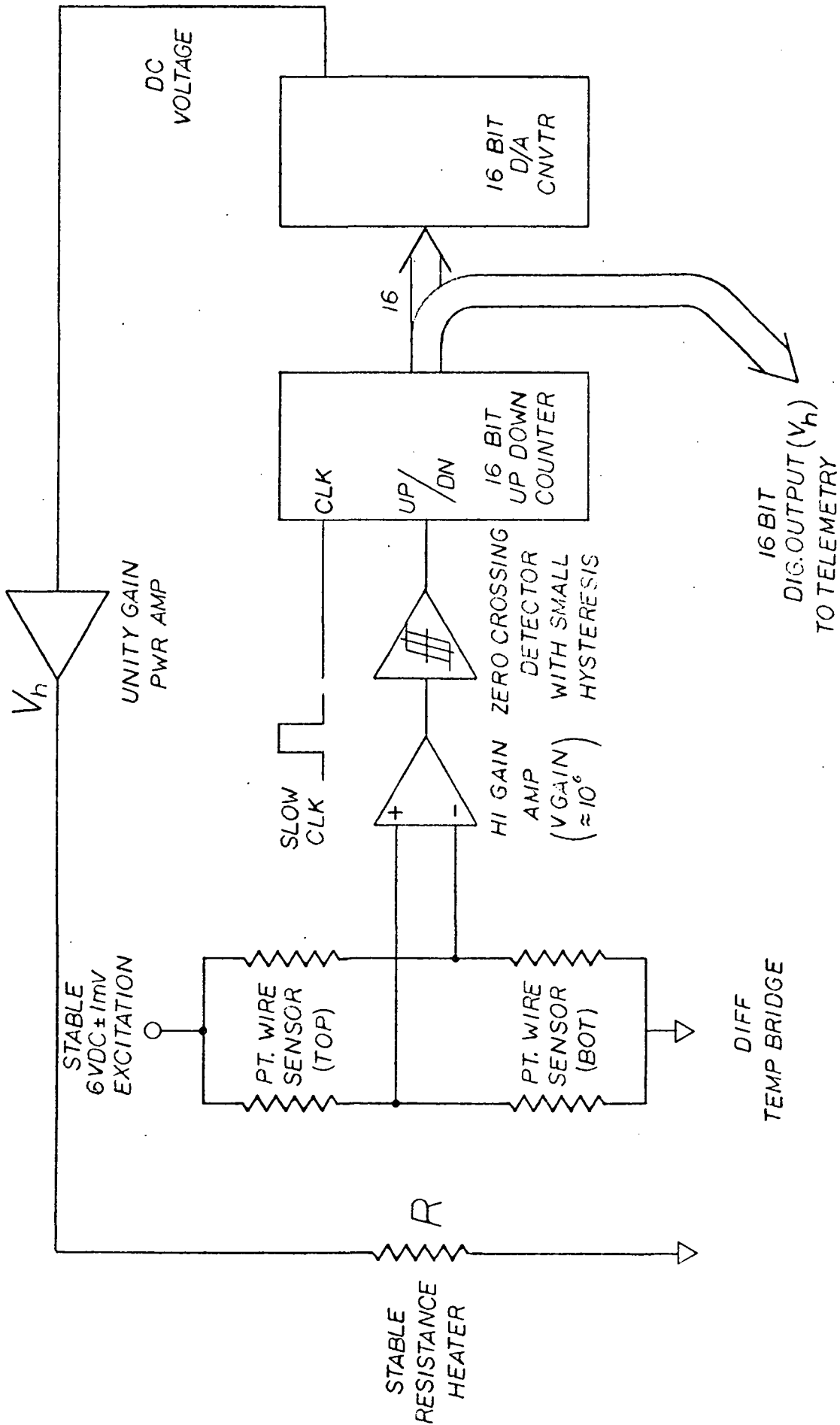
Figure IV.3. ACR Difference Temperature Control Servo

where

H = Solar incident flux

P_e = Electrical power input to the cavity while viewing the sun

P_e' = Electrical power input to the cavity while viewing space.

A_c = Cavity aperture area.

α_c = Cavity apparent absorptance.

ρ = Reflectance of the upper heat sink cavity.

ρ_c = Reflectance of the cavity and cavity aperture.

The analysis shows that a small correction to this equation is necessary to account for the cavity heat sink temperature difference increase of $2.5 \times 10^{-4}\,°K$ which occurs when the sun is viewed. The correction is 0.13 mW or 0.1% for this design. The corrections due to the difference in radiative sink-cavity exchange between sun and space views are negligibly small.

The solar constant measurement uncertainty was calculated by summing the standard deviations of the independent cavity parameters ξ_i (including the temperature uncertainties) according to the equation:

$$\sigma(H) = [\sum_i (\frac{\partial H}{\partial \xi_i})^2 \sigma^2(\xi_i)]^{1/2}$$

where $\sigma(\xi_i)$ is the standard deviation of parameter ξ_i. The largest source of error is the cavity absorptance which was assumed known to $\pm0.1\%$. The result for the standard deviation of the solar constant measurement, which can probably be slightly improved by optimization of the design, is 0.17 mW/cm^2 or 0.13%.

V. PLANE FLUX WIDE FOV SENSOR DESIGN

Two wide field of view (FOV) sensors are required for the earth energy budget observations: a short wavelength sensor (SWS) and total radiation sensor (TRS). Their angular and spectral ranges are listed in Table V.1.

Table V.1. Wide FOV Sensor Identification

SENSOR DESIGNATION	ANGULAR FOV	SPECTRAL FILTER	SPECTRAL RANGE
SWS	150°	Suprasil W	$0.2\mu-5\mu$
TRS	150°	None	$<0.2\mu->50\mu$

The major requirements of these sensors, in addition to spectral response are as follows:

(1) Short time constant ($\leqslant 50$ ms)

(2) Flat spectral response within spectral range

(3) Lambertian angular response within angular range

(4) Linearity of the order of 0.1% or better

(5) In-flight or absolute calibration capability.

Two approaches are being considered for these sensors. The first uses a short time constant active cavity radiometer and the second is based on thermopile detectors. The fast ACR appears most attractive at the present. This section will discuss design considerations common to both detector options. Specific detector characteristics and a comparison will be made in the following sections.

1. Basic Construction Geometry

Common features of the wide FOV sensors are indicated in Figure V.1. These consist of
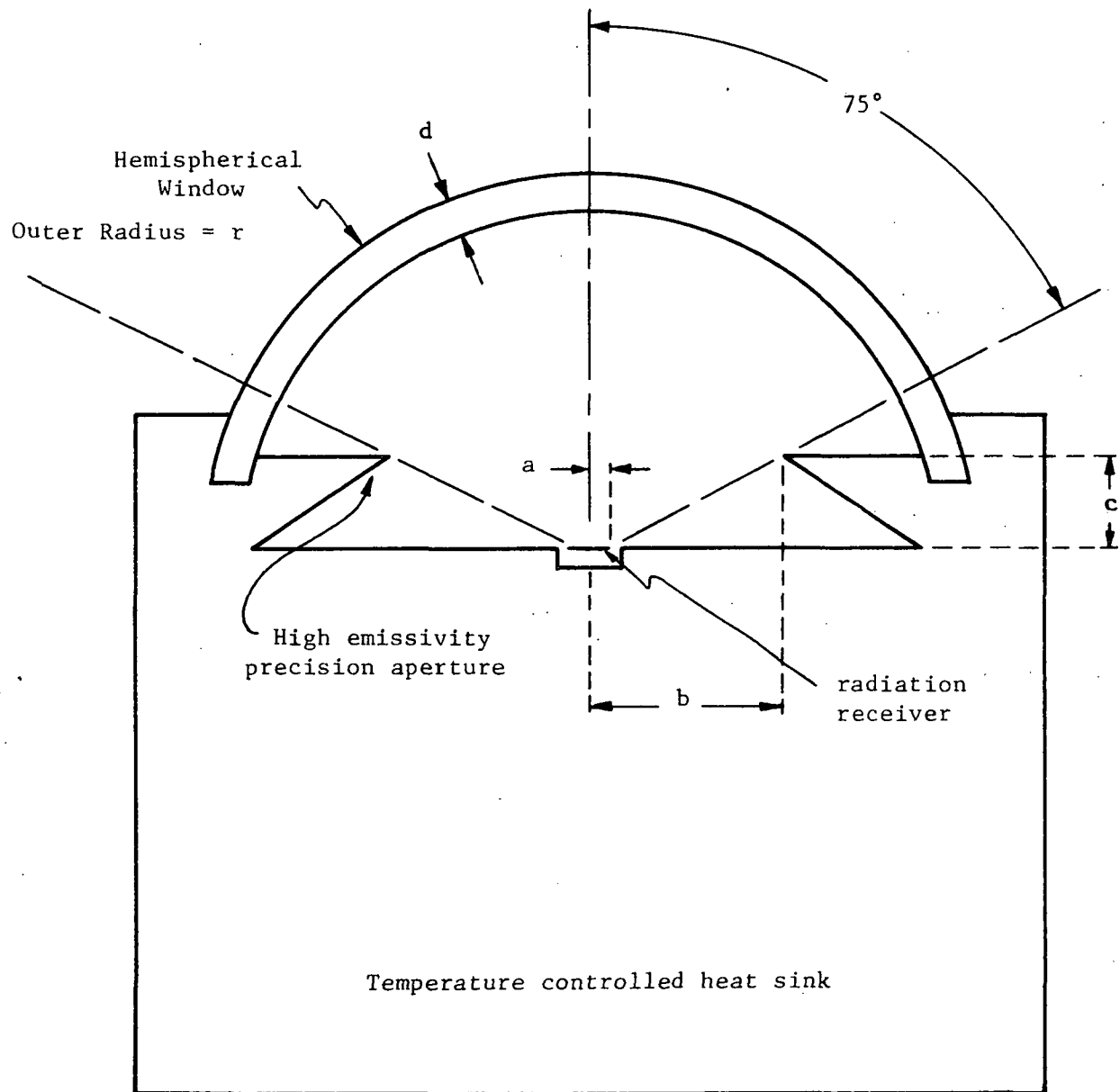
Figure V.1. Configuration of wide FOV sensors (the hemispherical window is used only on the short wave sensor).

(1) a temperature controlled heat sink,

(2) a radiation receiver (a defined area within which the detector responds to incident radiation),

(3) an external aperture defining the angular FOV, and

(4) a hemispherical window (SWS only).

Geometrical parameters identified in Figure V.1 are defined below:

a = radius of an assumed circular radiation receiver

b = radius of the external aperture

c = altitude of the external aperture above the plane of the radiation receiver

r = outer radius of the hemispherical window centered at the receiver center

d = thickness of the window.

The finite detector size has two effects on angular response characteristics: (1) the angular FOV is not precisely determined by the aperture but has a transition region between zero and full detector irradiation; (2) the angular response of the SW sensor is non-Lambertian within the region of full detector irradiation because not all parts of the radiation receiver are at the center of curvature of the window.

The first effect can be simply described by the angular size of the transition region $\Delta\theta$ where $\Delta\theta$ is given by

$$\Delta\theta = \tan^{-1}[c/(b-a)] - \tan^{-1}[c/(b+a)]. \tag{1}$$

Note that $\Delta\theta$ is the difference between the half angle corresponding to full receiver irradiation θ_1 and the half angle corresponding to zero irradiation θ_2, where

$$\theta_1 = \pi/2 - \tan^{-1}[c/(b-a)] \tag{2}$$

$$\theta_2 = \pi/2 - \tan^{-1}[c/(b+a)] \tag{3}$$

In order to insure full response to the earth, the half angle Θ_1 must be at least as large as the sum of the half angle subtended by the earth Θ_E and the attitude angular tolerance $\delta\Theta$. At an altitude of 380 nm we find the $\Theta_E = 64.22°$. Allowing for an attitude uncertainty $\delta\Theta = 0.75°$, and an angular margin Θ_t for assuring full view of the earth for 7 detector time constants, a reasonable choice for Θ_1 is 75°. This leads to the condition

$$c = (b-a) \tan 15°. \qquad (4)$$

Given a receiver radius a, we can thus determine c and $\Delta\Theta$ as a function of b. Results for a = 0.1 cm (typical of thermopile detectors) and for a = 0.5 cm (typical of the fast active cavity detector) are given in Tables V.2 and V.3.

Table V.2. Aperture Design Parameters for a = 0.1 cm (TP Detectors)

APERTURE RADIUS b	APERTURE ALTITUDE c	$\Delta\Theta$	DIURNAL SAMPLING GAP $(\delta\Theta + \Delta\Theta + \Theta_t)$
0.3 cm	0.054 cm	7.4°	1.21 hr
0.5 cm	0.107 cm	4.9°	1.04 hr
1.0 cm	0.241 cm	2.6°	0.89 hr
1.5 cm	0.375 cm	1.8°	0.84 hr

Table V.3. Aperture Design Parameters for a = 0.5 cm (Fast Active Cavity Detectors)

APERTURE RADIUS b	APERTURE ALTITUDE c	$\Delta\Theta$	DIURNAL SAMPLING GAP $(\delta\Theta + \Delta\Theta)$
1.0 cm	0.134 cm	9.9°	1.38 hr
2.0 cm	0.402 cm	5.9°	1.11 hr
3.0 cm	0.670 cm	4.2°	1.00 hr
4.0 cm	0.938 cm	3.2°	0.93 hr
5.0 cm	1.206 cm	2.6°	0.89 hr

The diurnal sampling gaps tabulated are local time intervals (near sunrise and sunset) during which measurements cannot be used because direct solar radiation can enter the detector FOV. From the tabulated results an aperture radius of 1 cm for TP detectors and 3 cm for cavity detectors appears reasonable.

An important constraint on window size is its effects on angular response. The result of detailed calculations presented in Appendix D can be expressed as

$$R(\Theta) = \cos\Theta \, [1-E(\Theta)] \tag{5}$$

where $R(\Theta)$ is the relative power incident on the receiver from an infinitely distant point source at angle Θ away from the receiver normal. The $\cos\Theta$ factor is the ideal response of a plane receiver, and $E(\Theta)$ is the deviation produced by the window as a function of angle. $R(\Theta)$ is normalized so that

$$R(0) = 1. \tag{6}$$

The approximate expression for $E(\Theta)$ is

$$E(\Theta) = \sin^2\Theta \; a^2 d(n^2-1)/(2n^3 r^3) \tag{7}$$

where n is the index of refraction of the window. Equation (7) is strictly valid only for

$$\frac{a}{r-d} \ll 1, \quad \frac{d}{r} \ll \frac{n}{n-1}. \tag{8}$$

Requiring the maximum value of $E(\Theta)$ to be less than 10^{-3}, which insures a negligible response deviation, yields the condition

$$d \leq 10^{-3} \frac{2n^3 r^3}{a^2(n^2-1)} \tag{9}$$

where, for fused quartz, $n \approx 1.46$. For the two a values of interest we have the conditions

$$d \leq .55 \ cm^{-2} r^3, \ a = 0.1 \ cm \tag{10}$$

$$d \leq .022 \ cm^{-2} r^3, \ a = 0.5 \ cm. \tag{11}$$

Choosing $r = 1$ cm for $a = 0.1$ cm and $r = 3$ cm for $a = 0.5$ cm yields

$$d \leq 0.55 \ cm; \ a = 0.1 \ cm, \ r = 1 \ cm \tag{12}$$

$$d \leq 0.59 \ cm; \ a = 0.5 \ cm, \ r = 3 \ cm \tag{13}$$

These conditions leave considerable leeway in choosing window size, although the conditions are not exact because the upper bounds, especially for (12), do not satisfy (8) very well.

2. Window Heating Effects

During its rotation about the S/C spin axis the sensor will be exposed to a time varying long wave flux from the earth. The SW sensor window will absorb this flux and thus experience radiative heating. Window temperature excursion caused by this heating will produce background flux variations within the detector FOV. Errors in the SWS flux readings caused by this effect can be reduced to negligible levels by invoking appropriate constraints on window design.

The results of the detailed analysis presented in Appendix E can be summarized fairly simply. If the time dependent part of the incident long wave flux is given by

$$F(t) = F_o \cos \omega t, \tag{14}$$

then the induced background flux variation is given by

$$F_B(t) = 4\sigma T_w^3 \sqrt{2} \ (\omega c \rho d)^{-1} F_o \cos(\omega t + \phi) \tag{15}$$

where the parameters employed are defined as follows:

ω = angular rotation frequency of the S/C

c = specific heat of the window material

ρ = density of the window material

d = window thickness

F_o = half the flux difference between earth and space views

T_w = mean window temperature

ϕ = a phase shift approximately equal to $\pi/2$ (exactly defined in Appendix E).

For a fused quartz window and a 6 RPM spin rate we have the following specific parameter values:

ω = 0.628 sec^{-1}

c = 0.753 W-sec/gm-°C

ρ = 2.203 gm/cm^3.

Choosing $F_o = 150 \text{ W-M}^{-2}$ and $T_s = 300°K$ we can rewrite (15) in the specific form

$$F_B(t) = 0.125 \, \frac{W}{M^2} \, \frac{cm}{d} \cos(\omega t + \phi) \tag{16}$$

where, for $a \geqslant 1$ cm, $|\phi - \pi/2| \leqslant .004$ (see Appendix E). At the Nadir position (earth sample) $F_B(t) = 0$ since $t = 0$. The background value for the space sample or solar sample depends on the sampling time. If either is taken at anti-nadir position no measurable error is present. For other positions the error can be estimated in terms of the angular distance between the sample position and the anti-nadir position. If the angular deviation is Θ_s then the background flux is given by

$$F_B = 0.125 \, \frac{W}{M^2} \frac{cm}{d} \sin\Theta_s. \tag{17}$$

The worst case value of Θ_s is determined by the sensor FOV and has the value $\Theta_s \approx 40°$. For this case we have

$$F_B = .08 \text{ W-M}^{-2} \text{ cm/d}. \qquad (18)$$

In order to meet the absolute accuracy target expressed in Table II.1 (Section II) for this worst case condition, without correction, the window thickness should satisfy

$$d \gtrsim 0.16 \text{ cm}. \qquad (19)$$

A thinner window could be used if window heating effects (which are fairly predictable) were corrected for in data analysis, or if samples of space or sun were restricted to a smaller angular deviation about the anti-nadir point. None of these comments apply to the TR sensor since it has no window which can produce such effects.

3. Spectral Response

The objective for both the TRS and the SWS is to obtain flat spectral response within the spectral passband. In both cases the spectral response uniformity is limited by the characteristics of the radiation receiver, which in turn is limited more or less by the characteristics of a black painted surface. In the case of the fast cavity radiometer this limitation is considerably reduced.

Appendix F contains an analysis of long wave flux errors produced by spectral variations in receiver emissivity. These errors can be described in terms of the variation of average emissivity with variations in the spectral distribution of incident flux. Defining

$\varepsilon(\nu)$ = emissivity at wavenumber ν

$F(\nu)$ = incident flux at wavenumber ν

the average effective emissivity for the given incident spectral flux is given by

$$\bar{\varepsilon}_F = \int_0^\infty \varepsilon(\nu)F(\nu) \ d\nu \bigg/ \int_0^\infty F(\nu) \ d\nu \tag{20}$$

Average emissivities for spectral fluxes typical of earth emissions are compared with the average emissivity for blackbody radiation at 270°K in Table V.4. The spectral emissivity values $\varepsilon(\nu)$ are for flat painted surfaces using Parson's Black in one case, and 3M Black in the other (See Appendix F). The value of emissivity that would be obtained during calibration (at 270°K) differs from the average of the ε_F for earth fluxes. This would result in a bias error as well as a variable deviation about the mean error. Both errors are listed in Table V.5. These values are close to exceeding the absolute accuracy target listed in Table II.1. Allowing for degradation effects these may be marginally acceptable. The situation is much better for the fast cavity radiometer because of the emissivity enhancement of the cavity receiver. For this case errors are estimated to be a factor of ten lower than those listed in Table V.5.

The short wavelength sensor is affected not only by the spectral variations in the receiver emissivity but also by the spectral variation in window transmission. The spectral variation of transmission for Suprasil-W (a water-free fused silica material produced by Amersil, Inc.) is displayed in Figure V.2. For most of the solar spectral range the transmission is exceptionally flat. The wavelength region which does show significant variations is near the long wavelength cutoff ($\sim 4\mu$). Since window thickness is a major factor in determining SWS cutoff it must be chosen to minimize the error involved in spectral separation of reflected and long wave radiation components. The results of an analysis

Table V.4. Average Emissivities as a Function of Spectral Flux
            Distribution for Two Black Surfaces

SPECTRAL FLUX CLASSIFICATION	$\bar{\varepsilon}$ FOR PARSON'S BLACK	$\bar{\varepsilon}$ FOR 3M BLACK @373°K
Blackbody @270°K	0.917	0.933
Winter Arctic Atm.	0.918	0.933
Western US Summer (Clear)	0.922	0.926
Cloudy Tropical Atm.	0.919	0.929

Table V.5. Flux Errors Produced by Nonuniform Emissivities

	PARSON'S BLACK	3M BLACK @373°K
Bias error using 270°K Calibration	-0.3%	+0.4%
Standard Deviation about Mean Error	0.2%	0.3%

TRANSMISSION OF SUPRASIL W
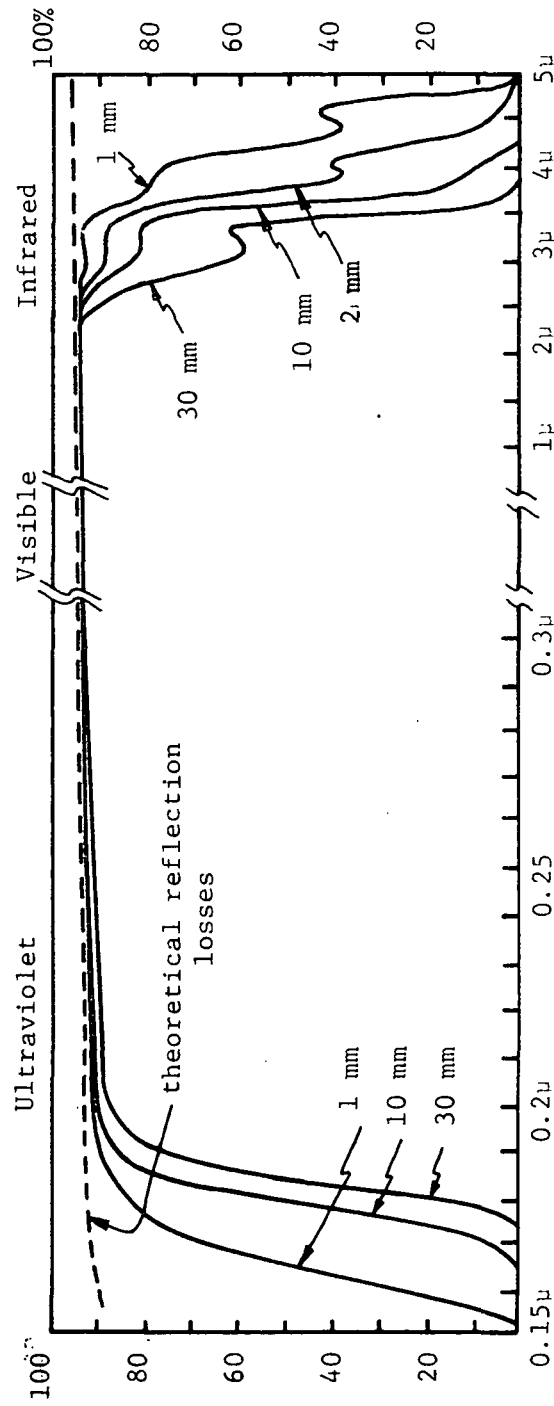
Figure V.2. Window transmission as a function of wavelength and thickness.

of this problem (Appendix G), which are by no means conclusive, indicate

an optimum thickness between 1mm and 2mm. This is not in serious conflict

with other const.aints on window thickness.

We do not have accurate information on SWS flux errors resulting from

receiver emissivity variations. An analysis of this problem is made

especially difficult by lack of an adequate means for parameterizing spectral

variations of reflected flux. At present this is an uncertain area for

thermopile detectors, and probably very safe for the fast cavity radiometer

because of the cavity emissivity enhancement (and the resulting factor of

twelve decrease in sensitivity to emissivity variations).

4. Angular Response

For both SW sensor and the TRS sensor angular response is determined by

the angular response of the radiation receiver (we have already seen that

the focusing effects of the SWS window can easily be made negligible).

The plane flux errors resulting from non-Lambertian angular response

are treated in Appendix H for an angular response model of the form

$$R(\Theta) = (1-\alpha)\cos\Theta + \alpha\cos^2\Theta, \tag{21}$$

where Θ is the angular distance from the receiver normal and α is an error

parameter. Equation (21) is equivalent to an angular emissivity variation

of the form

$$\epsilon(\Theta) = \epsilon_o [1-\alpha(1-\cos\Theta)]. \tag{22}$$

The flux errors resulting from such a variation depend on the angular

distribution of incident fluxes as well as α. Table V.6 summarizes errors

for limb darkening and brightening (100% modulation from nadir to limb).

Table V.6. Percentage Flux Errors Resulting as a Function of the Angular Nonuniformity Parameter α.

α	LIMB DARKENING	LIMB BRIGHTENING
.01	+0.2%	-0.2%
.02	+0.4%	-0.3%
.05	+1.1%	-0.8%
.10	+2.1%	-1.7%

Measured data for 3M Black (401-C10) are presented in Figure V.3. Although they do not fit the model (Equation 22) very well, an α value of 0.04 seems to be the best characterization. According to Table V.6 the measured response could lead to errors of ±1% in the visible flux (where large nadir to limb modulations are frequent) and probably much less than this in the IR where only (relatively small) modulations are typical. However, if the SW and TRS sensors have different angular variations in emissivity, then both reflected solar and long wave fluxes could be significantly in error.

Present information suggests that thermopile detectors may not be able to obtain adequate angular response unless surface coatings better than 3M (401-C10) can be employed. This is not the case for the fast cavity radiometer which again benefits from the cavity receiver. For this detector angular response errors can be reduced below 0.2% even using 3M(401-C10) for the interior coating of the cavity.

5. Required Time Constant

Earth viewing sensors rotate at 6 RPM (nominal) about an axis normal to the orbit plane. During each rotation three samples of detector output are
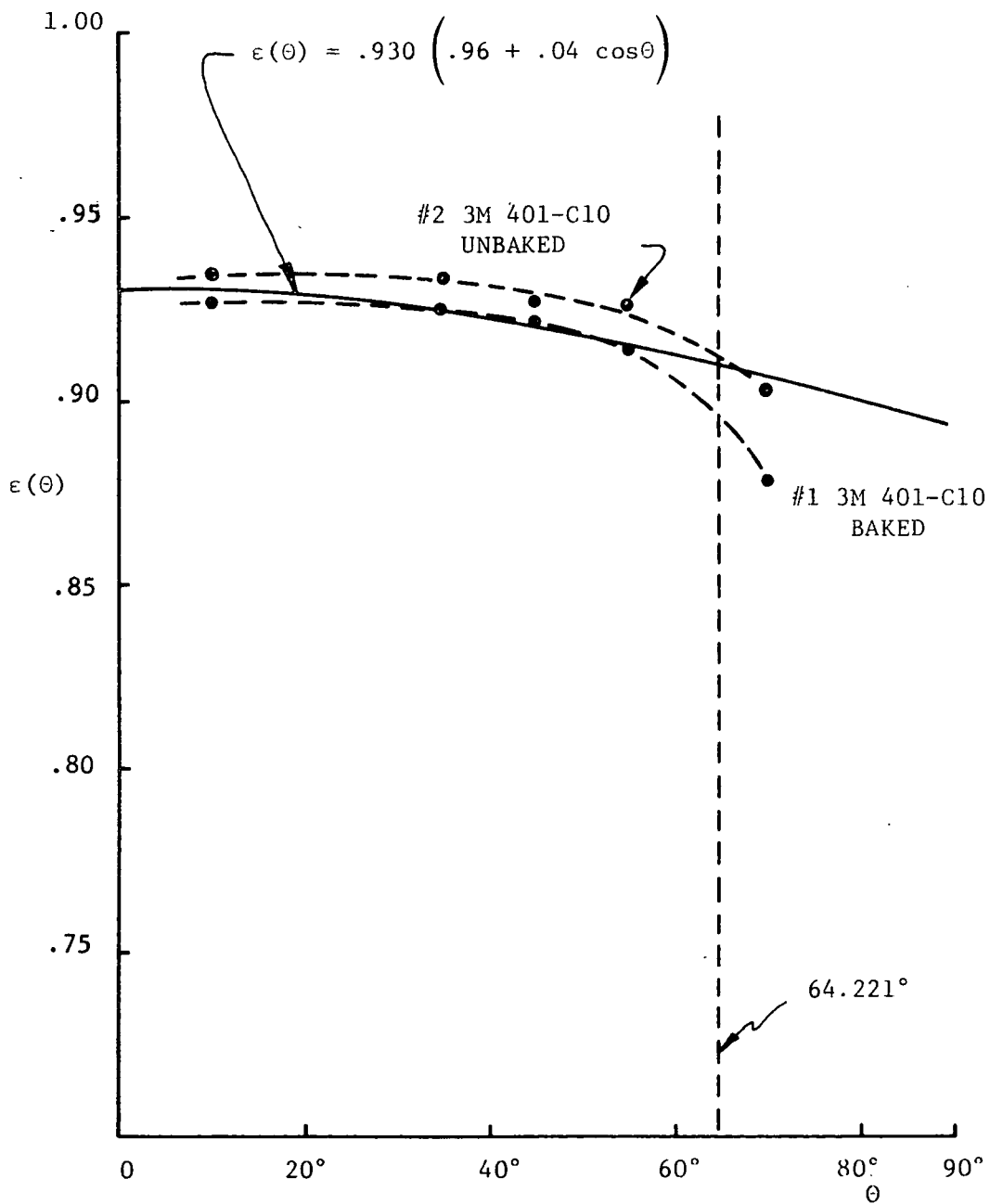
FIGURE V.3. Angular emissivity variation of 3M 401-C10.

recorded (if viewing requirements are satisfied). These samples are listed below:

(1) Earth-only (taken at nadir)

(2) Sun-only (taken at the rotation angle corresponding to the minimum angular distance between the sun and the sensor normal)

(3) Space-only (sampling angle not critical except for the constraint that the edges of the detector FOV be at least 5° away from both sun and earth nearest points).

It can be shown that near nadir and solar sample angles the sensor radiation input is approximately proportional to the cosine of the angular deviation of the sensor normal to the nominal sample angle. For the purpose of estimating the required time constant we shall assume that the sensor signal varies as the cosine of the rotation angle for large angular deviations as well as small ones.

If the sensor time constant is τ then the sensor output at time t in response to a step function radiation input ΔF at time t' is given by the following expression

$$F_m(t) = \Delta F \, [1 - e^{-(t-t')/\tau}]. \tag{23}$$

The response to a time dependent function F(t) is just the integral of the responses to the differential step changes in F(t), i.e

$$F_m(t) = \int_0^t \frac{dF(t')}{dt'} \, [1 - e^{-(t-t')/\tau}] dt' \tag{24}$$

where we assume $F(t') = 0$ for $t' \le 0$. Since F(t') has been assumed to have the form

$$F(t') = F_0 \sin(\omega t'), \tag{25}$$

where ω is the spacecraft angular rotation frequency, the sensor response is found to be

$$F_m(t) = \omega F_o \int_0^{\pi/2\omega} \cos(\omega t') [1 - e^{-(t-t')/\tau}] dt'. \tag{26}$$

Integrating (26) and writing the solution in terms of the fractional deviation from full response yields

$$\frac{F_o - F_m(T)}{F_o} \approx (1 + (\omega\tau)^{-2})^{-1}. \tag{27}$$

In order to keep the response within 0.1% of F_o, τ must satisfy the condition

$$\tau \lesssim 0.03\omega^{-1} \tag{28}$$

For $\omega = 0.628 \ \text{sec}^{-1}$ (corresponding to 6 RPM) we find the requirement

$$\tau \lesssim 48 \ \text{ms}. \tag{29}$$

It should be noted, however, that (29) is an accurate condition only for a plane sensor with a hemispheric field of view (in fact, for this case, it is a conservative condition). For a plane sensor with an aperture limited FOV the assumed cosine behavior only applies over an angular region equal to the difference between the angle subtended by the earth and the angle subtended by the aperture. In order for the cosine assumption to be valid starting seven time constants prior to the nadir position, the aperture clearance should be approximately 12° in half angle. This would lead to a twilight diurnal sampling gap of approximately one hour in local time. This should not result in significant diurnal sampling errors because the level of reflected fluxes during twilight is relatively low.

VI. FAST ACTIVE CAVITY THEORY

The advantages of cavity radiometers have been referred to several
times in Section IV and in Section V in reference to the solar constant
radiometer. Among these advantages the following should be emphasized.

(1) Flat spectral response

(2) Lambertian angular response

(3) Absolute calibration

For the wide FOV earth viewing sensors we must also obtain a relatively
small time constant in the range from 40 to 60 milliseconds. The purpose
of this section is to present the theoretical basis for design of a fast active
cavity radiometer (FACR) without sacrificing any of the major ACR advantages.
Laboratory measurements verifying the theoretical predictions have been made
with a FACR test model described in Appendix M.

1. Basic Operating Principles of the Fast ACR

The basic design features of the fast ACR cavity and viewing aperture
are illustrated in Figure VI.1. (The specific design details are discussed
in the following section). The nearly spherical cavity is a thin shell formed
of a thermally sensitive resistance wire coated with a high emissivity paint.
The resistance wire acts both as the cavity heater and as the cavity temperature
sensor. The cavity is conductively insulated from its heat sink such that
the primary coupling between the cavity and the heat sink is radiative. The
operating principle of this ACR is fundamentally the same as that for the
ACR discussed for the solar constant measurement. Electrical power supplied
to the cavity heater is servo controlled to maintain a fixed temperature
difference between the cavity and the heat sink. Two measurements of the
electrical power supplied to the cavity are again required, one obtained

Secondary view
limiting aperture

FOV

Primary view limiting aperture

Coated thermal
resistance
wire cavity

Clearance between
cavity and heat sink.

Heat Sink
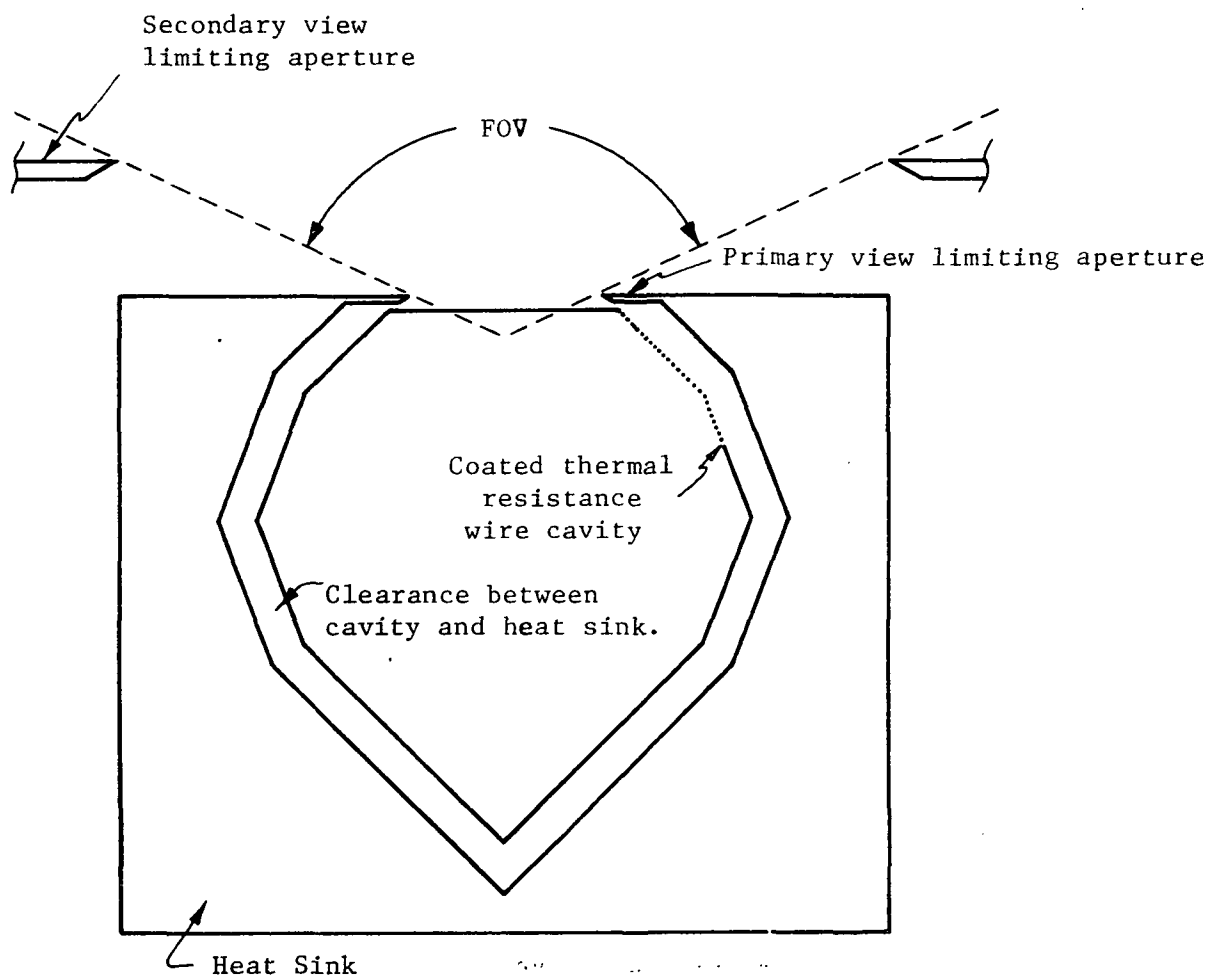
FIGURE VI.1   Basic design concept for a "high speed" ACR.
The wire wound cavity provides heating and
sensing functions.

while viewing the unknown source and one obtained while viewing space. The difference of these measurements is proportional to the unknown irradiance with a proportionality factor depending on the cavity area and absorptance.

Two different operating modes have been considered for the fast ACR during its development. For one, the cavity and the heat sink are operated at the same elevated temperature somewhere near 400°K. This forces the net radiation from the cavity to always be outward such that a constant temperature can be maintained by electrical control. For this mode of operation the radiation coupling between the cavity and the heat sink should be minimized to minimize errors. The second mode relies on a large radiative coupling between the cavity and the heat sink to transfer the power input to the cavity to the heat sink. Since the radiation resistance is necessarily large, a temperature difference of about 20° between the cavity and the heat sink is required. The second mode was chosen for two reasons: (1) cavity operating temperatures could be reduced and thus the thermal requirements on high emissivity coatings could also be reduced; (2) the presence of an IR blocking window did not allow the first method to be used for the short wavelength sensor.

The ACR considered for earth viewing is different from the solar flux ACR in two major aspects. First, because the earth viewing sensors view the earth, the sun, and space for each revolution of the spacecraft, the time constant of the ACR must be about 50 ms while the time constant for the solar output ACR is essentially unconstrained. (The time constant of the fast ACR is such an important aspect of its operation that it will be discussed in considerable detail in the following subsections). Second, while the solar constant ACR is always measuring normally incident radiation this

is not true for the earth viewing radiometer; thus its design must insure that the response is independent of the portion of the cavity heated by the incident flux. This cannot be achieved by coupling the cavity to the heat sink conductively unless the conducted power is uniformly distributed over the cavity surface. However, using radiative coupling to the sink and a nearly spherical cavity shape will essentially guarantee that the response will be the same for all angles of incidence because all portions of the cavity have nearly identical views out the aperture and towards the heat sink. The importance of the geometry for radiation exchange between the cavity and the sink in obtaining uniformity in angular response is discussed in a separate subsection.

The short cavity time constant is obtained using a high gain servo system to enhance the natural time constant. The natural time constant for the establishment of a steady state following a discontinuous jump in the input power to a cavity connected by a thermal resistance R to a heat sink is given by $\tau = RC$, where C is the cavity heat capacity. Without servo control the cavity temperature changes exponentially until a temperature change equal to the product of the thermal resistance and the input power change has been attained. For the earth viewing ACR the resistance R is a radiative resistance which is given by

$$R = (T_c - T_s)/\varepsilon A\sigma(T_c^4 - T_s^4) = [\varepsilon A\sigma(T_c^2 + T_s^2)(T_c + T_s)]^{-1}, \qquad (1)$$

where ε is the effective emittance for radiative transfer between the cavity and the heat sink, σ is the Stefan Boltzmann constant, T_c and T_s are the cavity and sink temperatures respectively, and A is the exterior cavity area. For the cavities under consideration this time constant is on the order of 30 sec. The desired time constant of 40 to 60 ms represents

an enhancement factor of approximately 600. With sufficient gain the
servo system can detect very small changes in cavity temperatures and
rapidly change the electrical power to the cavity. When the net power
to the cavity reaches equilibrium no further temperature change can occur.
Although the initial change in cavity temperature as a result of the change
in irradiance proceeds at a rate determined by the natural time constant,
the servo can produce power equilibrium long before the full temperature
excursion can occur. If Γ is the servo gain in units of electrical power
input to the cavity per degree change in cavity temperature, the radiometer
time constant can be expressed as

$$\tau = \frac{RC}{1+\Gamma R} \, .$$
(2)

Since ΓR is much greater than 1, we see that the radiative resistance R
becomes unimportant and the time constant is given by C/Γ. Detailed
analysis of the fast active cavity transient response can be found in
the following sections.

2. Cavity Emissivity Calculation

The variations of the apparent emittance of a cavity with wavelength and
angle can be made much smaller than those for a flat plate. This point was
mentioned in regards to the solar constant radiometer, but is discussed in
additional detail here because of its relevance to the angular response of
the earth viewing sensors.

The angular response of a cavity of course depends on its shape. We
will restrict attention to spherical or nearly spherical cavities because
isotropic emission and absorption is desired. An isothermal spherical
cavity with a diffusely emitting and reflecting surface coating displays

an isotropic angular response because all portions of the cavity have identical view factors to the aperture. Although a flat plate has this response by definition for a diffusely reflecting and emitting surface coating, deviations of the coating from this ideal are suppressed by a cavity design. The apparent hemispherical emittance of an isothermal spherical cavity with a diffusely emitting and reflecting surface coating is given by

$$\varepsilon_a = \frac{\varepsilon}{\varepsilon + (1-\varepsilon)(1-A_c/A_s)} \qquad (3)$$

where A_c is the cavity area and A_s is the area of the whole sphere. The derivation of this result is presented in Appendix A. The apparent hemispherical emittance ε_a for two values of the surface emittance ε are given in the Table VI.1 as a function of the ratio of the aperture radius to the cavity radius $(\frac{r}{R})$. The third column labeled $\Delta\varepsilon_a/\Delta\varepsilon$ is the ratio of the apparent cavity emissivity change to the change in surface emittance. The advantages of the cavity radiation receiver are apparent from the Table. If the surface emittance varies with angle, wavelength, or as a result of degradation, the apparent emissivity of the cavity varies a great deal less. For example, for a radii ratio of 0.5 the cavity emissivity changes by only 0.4% if the surface emissivity changes by 5%. This same radii ratio with the 3M Black (401-C10) coating discussed in Section V would insure that flux errors due to angular response variations would stay well below ±0.2%. Flux errors due to spectral variations of emissivity would be even smaller (probably below ±0.05%).

Table VI.1. Hemispherical Emittance of an Isothermal
Spherical Cavity with a Diffusely Emitting
and Reflecting Interior.

r/R	$\varepsilon_a(\varepsilon = 0.9)$	$\varepsilon_a(\varepsilon = 0.95)$	$\Delta\varepsilon_a/\Delta\varepsilon$
.2	.9989	.9995	0.012
.3	.9975	.9988	0.026
.4	.9954	.9978	0.048
.5	.9926	.9965	0.078
.6	.9890	.9948	0.116
.7	.9844	.9925	0.162

3. Analysis of Transient Response

The transient behavior of the fast cavity radiometer depends on both the servo characteristics and the thermal properties of the cavity receiver. The latter properties require the following parameters for description:

$T_c(t)$ = Cavity temperature at time t

T_o = Equilibrium cavity temperature with zero incident flux

T_s = Sink temperature

A_a = Cavity aperture area

A_s = Cavity exterior surface area

ε_a = Effective cavity emissivity within its aperture

ε_s = Cavity effective emissivity for radiative exchange with the sink

K_1 = Conductance between cavity and sink via leads, supports, etc.

$P_e(t)$ = Electrical power dissipated in the cavity at time t

$P_r(t)$ = Incident radiative power absorbed by the cavity at time t

C = Cavity heat capacity

The rate of change of cavity temperature depends on the difference between incoming and outgoing powers. If we define the incoming power at time t by

$$P_{in}(t) = P_r(t) + P_e(t),$$ (4)

then the power leaving the cavity at time t is given by

$$P_{out}(t) = \varepsilon_a A_a \sigma T_c(t)^4 + \varepsilon_s A_s \sigma [T_c(t)^4 - T_s^4] + K_1(T_c(t) - T_s).$$ (5)

Since the cavity temperature will never differ from T_o by more than a small fraction of a degree, a linearization of equation (5) introduces completely insignificant error. The result of the linearization is

$$P_{out}(t) = P_{out}^o + K(T_c(t) - T_o)$$ (6)

where we have defined

$$P_{out}^o = \sigma T_o^4 [\varepsilon_a A_a + \varepsilon_s A_s] - \varepsilon_s A_s \sigma T_s^4 + K_1(T_o - T_s),$$ (7)

$$K = 4\sigma T_o^3 [\varepsilon_a A_a + \varepsilon_s A_s] + K_1.$$ (8)

Conservation of energy requires that the rate of energy stored in the cavity satisfy

$$C\frac{dT_c(t)}{dt} = P_{in}(t) - P_{out}(t)$$ (9)

which can be rewritten, using equations (4) and (6), as

$$C\frac{dT_c(t)}{dt} = P_r(t) + P_e(t) - P_{out}^o - K(T_c(t) - T_o).$$ (10)

Proceeding any further in the analysis requires characterization of the servo, i.e. a defined relationship between $P_e(t)$ and $T_c(t)$. The desired relationship is given by

$$P_e(t) = P_e^o - \Gamma [T_c(t) - T_o]$$ (11)

where P_e^o is the electrical power required to keep the cavity at T_o while viewing space. The parameter Γ characterizes the servo gain in units of

power per unit temperature change. The ideal nature of the stated relation-ship will become clear when the final solution for $P_e(t)$ is obtained. The electronics required to obtain the relationship defined by equation (11) are described in the following subsection.

Defining $T(t) = T_c(t) - T_o$, and substituting (11) in equation (10) yields the following differential equation for $T(t)$, i.e.

$$C \frac{dT(t)}{dt} + (K + \Gamma) T(t) = P_r(t) + P_e^\circ - P_{out}^\circ. \tag{12}$$

Since T, dT/dt, and $P_r(t)$ are all zero when the radiometer response to space has reached equilibrium, we conclude that

$$P_e^\circ = P_{out}^\circ. \tag{13}$$

As a result, equation (12) takes on the simpler form

$$C \frac{dT(t)}{dt} + (K + \Gamma) T(t) = P_r(t). \tag{14}$$

The general solution to the equation (14) is given by the following expression

$$T(t) = T(o) + \tau \dot{T}(o)(1-e^{-t/\tau}) + \frac{\tau}{c} \int_o^t \frac{dP_r(t')}{dt'} [1 - e^{-(t-t')/\tau}]dt' \tag{15}$$

where the time constant τ is defined by

$$\tau = \frac{C}{K+\Gamma}. \tag{16}$$

The first term of equation (15) represents the initial condition, the second term the decay from the initial rate of change at $\dot{T}$ at t = 0, and the third term the response to the time dependent radiative power incident from 0 to t.

For the special case of a step function change in $P_r(t)$ at t = 0 from $P_r^{(1)}$ to $P_r^{(2)}$ the temperature response is given by

$$T(t) = T(o) + \frac{P_r^{(2)}-P_r^{(1)}}{K+\Gamma} [1 - e^{-t/\tau}]. \tag{17}$$

The corresponding time dependence of the electrical power is just

$$P_e(t) = P_e^{(1)} - \frac{\Gamma}{K+\Gamma} [P_r^{(2)} - P_r^{(1)}] [1-e^{-t/\tau}].$$ (18)

At equilibrium we find that

$$P_e^{(2)} - P_e^{(1)} \backsim - [P_r^{(2)} - P_r^{(1)}] [1 - \frac{K}{\Gamma}].$$ (19)

For $K/\Gamma \ll 1$ the change in electrical power is equal and opposite to the change in absorbed radiative power. Since typical values of K/Γ are of the order of 10^{-3} (see next section), the electrical power difference is only about 0.1% less than the radiative power difference. Since this is a correctable effect, the actual error introduced is very much less than 0.1%.

Thus we see that the transient response of the radiometer can be simply characterized by a single time constant τ. This is an important feature resulting from the servo relationship stated in equation (11). Servo systems producing power changes which are not linear in the cavity temperature difference would lead to non-linear differential equations, the solutions of which would in general contain a mixture of short and long time constant effects and, in some cases, resonances. The servo system design concept which satisfies equation (11) is described in the following subsection.

4. Linear Servo Analysis

The electronic servo system which produces the desired linear relationship between electric power and cavity temperature, as stated in equation (11), is based on a standard Wheatstone bridge circuit. A block diagram of the electronics is presented in Figure VI.2. The operation of the servo
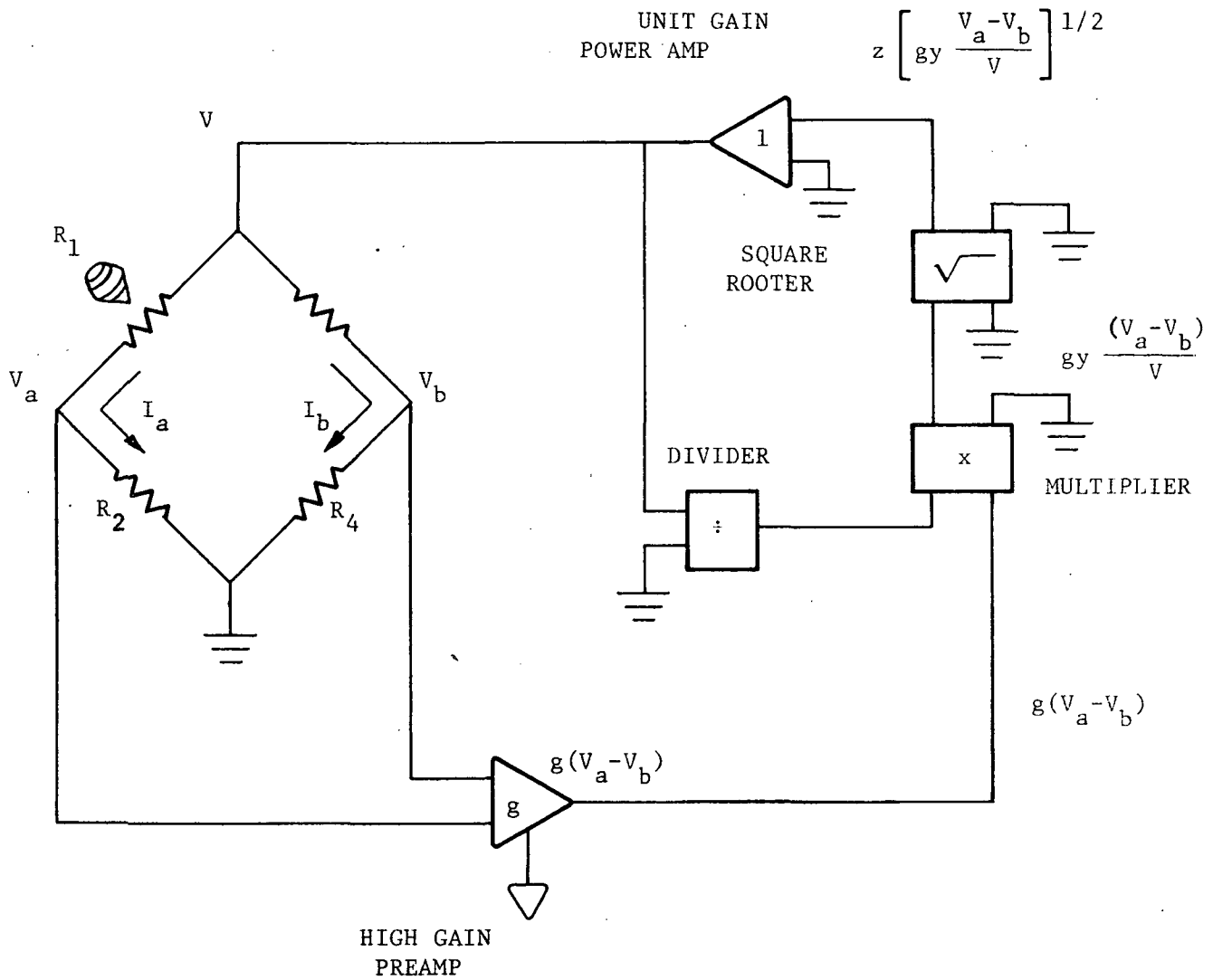
FIGURE VI.2 Linear Servo Electronics
Block Diagram

can be roughly explained by considering the response of the system to a decrease in irradiance of the cavity. The sequence of events which follow are listed below:

(1) The cavity begins to cool, lowering its resistance R_1.

(2) V_a increases due to the R_1 decrease, thus increasing the imbalance voltage $V_a - V_b$.

(3) The high gain preamp amplifies the imbalance voltage to the level $g(V_a - V_b)$.

(4) The amplified imbalance voltage undergoes several analog operations which ultimately result in an increase in the bridge supply voltage to the level $V = z[gy \ (V_a - V_b)/V]^{1/2}$.

(5) The increased supply voltage causes increased electrical dissipation in the cavity.

(6) The cavity begins to heat as a result of the increased power dissipation, thus tending to increase the cavity resistance toward its initial value.

(7) As the cavity resistance increases the voltage imbalance decreases eventually stabilizing the electrical power at its new equilibrium value.

The function of the divider-multiplier circuit is to prevent the positive feedback effect which results from the imbalance voltage being proportional to the bridge supply voltage. Without this circuit it is possible to have resonance or very strong negative feedback, depending on the size of the preamplifier input offset voltage. The square rooter circuit is required to make the power linearly related to the cavity temperature.

It is easy to mathematically verify that the servo satisfies equation (11) and thus behaves as described above. Since the bridge imbalance voltage

is given by

$$V_{ab}(t) \equiv V_a(t) - V_b(t) = V(t) \ [\frac{R_2}{R_1(t)+R_2} - \frac{R_4}{R_3+R_4}], \tag{20}$$

and since the bridge supply voltage satisfies

$$V(t) = z[gy \ V_{ab}(t)/V(t)]^{1/2}, \tag{21}$$

the supply voltage is directly related to the resistance imbalance, i.e.

$$V(t) = z[gy]^{1/2} \ [\frac{R_2}{R_1(t)+R_2} - \frac{R_4}{R_3+R_4}]^{1/2}. \tag{22}$$

Note that R_2, R_3, and R_4 have been assumed constant, a result insured by using resistors with low temperature coefficients and proper coupling to a temperature controlled sink.

In order to proceed further it is necessary to linearize the resistance imbalance relationship. Defining the cavity temperature coefficient of resistance α by the relationship

$$R_1(t) = R_1^\circ[1 + \alpha T(t)] \tag{23}$$

we can make the extremely accurate approximation

$$\frac{R_2}{R_1(t)+R_2} \doteq \frac{R_2}{R_1^\circ + R_2} \ [1 - \frac{\alpha R_1 T(t)}{R_1^\circ + R_2}]. \tag{24}$$

Since the product $\alpha T(t)$ is typically smaller than 0.0001 errors in the linearization are completely negligible.

Inserting (24) into equation (22) and squaring yields

$$V^2(t) = z^2 y \ [\frac{(R_2 R_3 - R_1^\circ R_4)g}{(R_1^\circ + R_2)(R_3+R_4)} - G \ T(t)] \tag{25}$$

where we define

$$G \equiv \alpha g \ R_1^\circ R_2 (R_1^\circ + R_2)^{-2}. \tag{26}$$

Since the electrical power dissipation in the cavity is given by

$$P_e(t) = [I_a(t)]^2 R_1(t) \doteq V^2(t) R_1^\circ (R_1^\circ + R_2)^{-2}, \tag{27}$$

where the approximation error is again negligible, we can obtain the desired result from equation (25), i.e.

$$P_e(t) = P_e^\circ - \Gamma \, T(t), \tag{28}$$

where we have used the notation

$$P_e^\circ = g z^2 y \frac{(R_2 R_3 - R_1^\circ R_4)}{(R_3 + R_4)} R_1^\circ (R_1^\circ + R_2)^{-3} \tag{29}$$

$$\Gamma = G \, z^2 y \, R_1^\circ (R_1^\circ + R_2)^{-2} \tag{30}$$

Note that equation (28) is identical to equation (11).

In addition to the basic power temperature equation several of the servo relationships derived above, as well as several additional corollary relationships, are significant in optimizing the servo design. These are summarized in Table VI.2.

5. Angular Response Variations Due to Cavity Non-Isothermalities

Angular response deviations for a nearly spherical isothermal cavity have already been treated in Section VI.2 and shown to be well within required limits for typical design parameters. However, the radiometer cavity is not strictly isothermal as a result of three distinct effects:

(1) Variation in the angular distribution of incident flux;

(2) Variation over the cavity surface of radiative transfer between the cavity and the heat sink; and

Table VI.2. Summary of Servo Relationships

(1) $\beta \equiv R_1^{\circ}/R_2$

(2) $\Gamma \equiv \dfrac{\beta^3}{(1+\beta)^4}\ [\dfrac{\alpha g\ z^2 y}{R_1^{\circ}}]$

(3) $V_{ab}(t) = (R_1^{\circ}P_e(t))^{3/2}(1 + \dfrac{1}{\beta})^3 (gz^2 y)^{-1}$

(4) $P_e^{\circ} = gz^2 y\ (R_3 - \beta R_4)(1+\beta)^{-3}(R_3+R_4)^{-1}(R_1^{\circ})^{-1}\beta^2$

(5) $P_T(t) = $ Total electrical power dissipated in cavity leg of the bridge

(6) $P_T(t) = (1 + \dfrac{1}{\beta})P_e(t)$

(7) $V(t) = (gz^2 y V_{ab}(t))^{1/3} = (1 + \dfrac{1}{\beta})\ (R_1^{\circ}P_e(t))^{1/2}$

(3) Non-uniform heat conduction resulting from support and lead

wire contact with the cavity.

If (1) were not true, the effects of (2) and (3) would be insignificant,

as it is in the case of the ACR used for measuring the solar constant.

The way in which (1), which does apply to the wide FOV ACR, can make (2)

and (3) significant is best illustrated by an extreme example. Suppose

the cavity is in contact with the heat sink at one point and thus has a

fixed temperature there. Radiation striking the cavity a large distance

away will result in a temperature gradient between the point of incidence

and the contact point, thus raising the mean cavity temperature and causing

the servo to reduce the electrical power input. However, if the same

radiative power input occurs at the contact point, the mean cavity

temperature will not be raised and the servo power will not change. Since

different electrical power levels are produced for the same irradiance

level, the measured powers are in error.

In order to treat these effects numerically it is necessary to simplify

the geometry of the cavity. Effects of wire conduction will be treated

using a disc shaped "cavity", and non-uniform radiative transfer effects

will be treated using a one dimensional "cavity". Although the results

obtained with these simplified models are not exact, they do establish

parameterizations which show what factors influence the error and also

yield order of magnitude estimates for the size of the errors. The only

significant uncertainty in using these model results is in transforming

a geometrical coefficient to the case of the spherical cavity. (Accurate

values for the coefficients can be obtained by measurement).

The effects of non-uniform radiative transfer between the cavity and the sink are parameterized in Appendix I. The resulting errors can be kept well under control by appropriate cavity design. The effects are significant enough, however, to result in an important design constraint. How this constraint is used in the cavity design is discussed in Section VII.

The parameterization of errors produced by wire and support conduction is developed in Appendix J. To first order these effects produce errors which are small and independent of cavity size and do not seriously constrain the cavity design.

VII-1

VII. FAST ACTIVE CAVITY DESIGN AND ERROR ANALYSIS

1. The Design Approach

The specification of the FACR design requires the following cavity physical properties, electronics parameters, and operating conditions:

(a.) Properties of the wire wound cavity shown in Figure VI.1.

    i. Wire material

        ρ_R - resistivity

        α - temperature coefficient of resistivity

        ρ - density

        k - thermal conductivity

        c - specific heat

    ii. Wire size

        w - wire diameter

    iii. Wire wound cavity size parameters

        r - cavity maximum external radius

        A_1 - cavity exterior area for unit cavity maximum radius

        r_a/r - ratio of the cavity aperture radius to the cavity maximum radius

    iv. Radiative coupling to the sink

        ε_s - effective emittance for radiative exchange

(b.) Servo parameters

        β - bridge resistance ratio as defined in Table VI.2

        gz^2y - servo gain, square rooter, and divider parameter product as defined in Section VI.4.

(c.) Operating conditions

        T_c - cavity temperature

        T_s - heat sink temperature

        P_e° - electrical power supplied to the cavity when viewing space (a super $^\circ$ will be used throughout this section to denote the space view).

The design approach was to first select a wire material and size for the basic cavity geometry shown in Figure VI.1, to then apply a series of constraints imposed by the theory of the FACR operation and by the system measurement concept, and finally to select the design which was the most practical with respect to servo construction and power consumption. The wire material and size selected was 3 mil nickel. This choice was based on the desire to make the bridge signal voltage large without making the time constant too large. To do this a material with a large resistivity and temperature coefficient of resistivity was chosen since the bridge signal voltage is proportional to the cavity resistance to the 3/2 power and the time constant is inversely proportional to the temperature co-efficient of resistivity (See Table VI.2). The values of the pertinent properties of nickel which were used for design considerations are the following:

$$\rho_R = 6.55 \times 10^{-6} \Omega\text{-cm at } 0°C$$

$$\alpha = .0064 \text{ at } 0°C$$

$$\rho = 8.9 \text{ g/cm}^3$$

$$k = .578 \text{ W/cm-}°K$$

$$c = .481 \text{ J/g-}°K$$

2. Design Constraints

Constraints on the values of the FACR parameters listed in subsection 1 are imposed by the theoretical expressions for the time constant, the bridge signal voltage, the radiative power loss of the cavity, the non-uniformity of the angular response, and also by the desired cavity emittance enhancement. Using the same notation as Section VI, they are as follows:

(a) The FACR time constant $\tau = C/\Gamma$ can be expressed in terms of the parameters listed in subsection 1. The required time constant was found to be 48 ms in Section V.

(b) A bridge signal voltage ΔV_{ab} which is much larger than the amplifier noise is required. The signal voltage is defined by $V_{ab} = V_{ab} - V_{ab}^{\circ}$, where V_{ab}° is the total imbalance voltage for the space view and V_{ab} is the imbalance voltage for the source view. A signal voltage ΔV_{ab} of 250 μV was selected for an irradiance at the cavity aperture corresponding to 1 solar constant. The resulting signal to noise ratio will be discussed later in this section.

(c) The electrical power supplied to the cavity P_e is related to the cavity and heat sink temperatures by the expression for the radiative losses of the cavity to the heat sink and to space. This relationship is given by

$$P_e = A_s \varepsilon_s \sigma (T_c^{\,4} - T_s^{\,4}) + A_a \varepsilon_a \sigma T_c^{\,4}. \tag{1}$$

The first term represents cavity-heat sink exchange of radiation and the second the radiation to space. The conductive transfer of power to the sink was assumed to be negligible.

(d) The non-uniformity of the angular response due to the variation over the cavity surface of the effective emittance for cavity-sink radiative exchange ε_s should not limit the accuracy of the measurements. The fractional error f in the measurement of the source power absorbed by the cavity caused by an emittance variation of $\Delta \varepsilon_s$ can be approximated using the results of Appendix I to yield,

$$f = \frac{A_s \Delta\epsilon_s \sigma T_c^3}{6kw} \qquad (2)$$

where A_s is the cavity exterior area ($A_s = A_1 r^2$). This fraction f was chosen to be 5×10^{-3} which according to Appendix H corresponds to a .1% error for a scene with extreme limb darkening or limb brightening.

The variation of ϵ_s over the surface of the cavity occurs because of the variation of the relative cavity-heat sink geometry. A detailed analysis of the variation of ϵ_s over the cavity has not been performed. However, because of the nearly spherical shape of the cavity and heat sink a reasonable estimate of ϵ_s and its variations can be obtained from a simple result for concentric spheres. The effective emittance for radiative exchange between concentric spheres with diffusely reflecting and emitting surface coatings is given by

$$\epsilon_{eff} = \frac{\epsilon_1 \epsilon_2}{\epsilon_2 + \epsilon_1(1-\epsilon_2)a_1/a_2} \qquad (3)$$

where $\epsilon_1(\epsilon_2)$ and $a_1(a_2)$ are the surface emittance of the inner (outer) sphere and the area of the inner (outer) sphere respectively. For $\epsilon_1 = \epsilon_2 = .93$ and an area ratio of .70, which is reasonable for the FACR, the effective emittance is 0.89. The major deviation of ϵ_s from this result will occur at the apex of the FACR cavity where an area element on the sink has less of its field of view filled by the cavity. As a result the effective emittance is larger there because less of the cavity radiation can be returned by diffuse reflection. Equation (3) shows that ϵ_{eff} is always less than ϵ_1 for any finite area ratio so a reasonable estimate of the variation of ϵ_s is less than 0.04. For design purposes we have used a $\Delta\epsilon$ of 0.03 which is considered a conservative value because the area of the cavity

where ε_s is large is small compared to the area irradiated by radiation from a given direction. A value of 0.90 was assumed for ε_s.

(e) The ratio of the cavity aperture radius to the maximum radius, r_a/r should be sufficiently small to allow accurate determination of the apparent cavity emittance from measurements of its surface coating emittance and also to make the cavity emittance insensitive to variations of the coating emittance due to its spectral response characteristics or degradation. A ratio of 0.5 was selected based on the results shown in Table VI.1 which show that for this choice the apparent emittance uncertainty is a factor of 12 smaller than the uncertainty in the coating emittance.

3. The Design

The final design was determined from the theory of the FACR operation by applying the constraints discussed in the last subsection for a cavity constructed from 3 mil nickel wire. The geometrical design of the cavity as shown in Figure VI.1 was represented by choosing the cavity exterior area A_1 for unit maximum radius to be 10.97, the effective emittance ε_s for radiative exchange between the cavity and sink to be 0.90, and the ratio of the viewing aperture radius to the cavity aperture radius to be 0.80. The resulting FACR design parameters were determined for a number of different cavity and sink operating temperatures.

It was found that the power required to operate the cavity decreases as the sink temperature T_s decreases and also as the cavity-sink temperature

difference $T_c - T_s$ decreases. However, there are reasons for not making

T_s and $T_c - T_s$ too small. First the power required by the sink temperature

control servo increases as T_s approaches the maximum spacecraft temperature.

Second, it is clear that the operation of the cavity control servo depends

on $T_c - T_s$ being large enough that the electrical power supplied to the cavity

to maintain the cavity-sink temperature difference while viewing space is

larger than the power absorbed by the cavity for any source irradiance.

The choice of T_c and T_s was not optimized, but values of $T_c = 345°K$ and

$T_s = 320°K$ were selected as reasonable with respect to the resulting power

requirements and the above considerations. The resulting FACR design

parameter values are shown in Table VII.1. The corresponding operating

characteristics are summarized in Table VII.2.

The noise characteristics of the FACR were analyzed assuming use of

the AC sense - DC heat servo discussed in Appendix N. The major advantage

of this servo design is the noise reduction obtained by placing a trans-

former between the bridge output and the preamplifier. In the DC servo

case the dominant source of noise is the preamplifier. However, through

the use of a transformer in the AC sense case, both the signal and the

noise are amplified before reaching the preamplifier and the Johnson

noise of the bridge dominates. The RMS noise voltage V_n at the bridge

is about 20 nV (see Appendix N).

The equations for the AC sense - DC heat servo corresponding to those

summarized in Table VI.2 for the DC servo are given in Table VII.3. Except

for equations (3) and (7) these relationships are the same as those for the

DC servo with gz^2y replaced by $z^2A_p^2nmA_cV_{AC}$. The signal to noise ratio was

calculated as follows using the DC servo design value of 3.4×10^7 for

Table VII.1. Fast ACR Design Parameter Values

Cavity Maximum Radius (r)	1.31 cm
Viewing Aperture Area ($\pi(.8r)^2/4$)	0.865 cm^2
Cavity Aperture Area ($\pi r^2/4$)	1.352 cm^2
Cavity Exterior Area ($A_1 r^2$)	18.88 cm^2
Cavity Apparent Emittance (assumed surface coating emittance of .90)	0.993

Cavity Heat Capacity
  3 mil Ni wire 0.48 w-s/°K
  paint   0.48 w-s/°K
	0.96 W-s/°K

Cavity Resistance at Operating Temperature	520
Cavity Temperature	345°K
Sink Temperature	320°K
Ratio of Cavity Space View Resistance to the other resistance in the cavity leg of the bridge (β)	1.131
Servo Power Gain Parameter (Γ)	20.2 W/°K
Servo Parameter z^2gy (See Section VI)	3.41×10^7

Table VII.2.   Fast ACR Operating Characteristics

Time Constant	48 ms
Total Bridge Power for the Space View (P_T°)	0.80 W
Electrical Power to the Cavity for the Space View (P_e°)	0.42 W
Minimum Electrical Power to the Cavity (Normal Incident Solar View)	0.31 W
Per Cent Variation in Angular Response due to Variations of the Effective Emittance for Radiative Exchange between the Cavity and the Sink	0.5%
Bridge Signal Voltage ΔV_{ab} for 1 Solar Constant Incident Flux using the DC Servo	250 μV

Table VII.3. <u>Summary of AC Sense - DC Heat Servo Relationships</u>

(1) $\beta = R_1^\circ / R_2$

(2) $\Gamma = \dfrac{\beta^3}{(1+\beta)^4} \dfrac{\alpha [z^2 A_p^2 nm\, A_c V_{AC}]}{R_1^\circ}$

where,

V_{AC} = AC sense voltage applied to the bridge (constant)

n = Transformer turns ratio

m = Demodulator Gain

A_c = Preamplifier voltage gain

A_p = Power amplifier voltage gain

z = Gain of analog square rooter

(3) $V_{ab}^{AC}(t) = \dfrac{(1+1/\beta)^2 R_1^\circ P_e^{DC}(t)\, V_{AC}}{[z^2 A_p^2 nm\, A_c V_{AC}]}$

(4) $P_e^{\circ DC} = [z^2 A_p^2 nm\, A_c V_{AC}]\, (R_3 - \beta R_4)(R_3 + R_4)^{-1} R_1^{\circ -1} (1+\beta)^{-3} \beta^2$

(5) $P_T^{DC}(t)$ = Total DC electrical power dissipated in cavity leg of the bridge

(6) $P_T^{DC}(t) = (1+1/\beta)\, P_e^{DC}(t)$

(7) $V^{DC}(t) = \left[\dfrac{[z^2 A_p^2 nm\, A_c V_{AC}] V_{ab}^{AC}}{V_{AC}}\right]^{1/2} = (1+1/\beta)[R_1^\circ P_e^{DC}(t)]^{1/2}$

$z^2 A_p^2 nmA_c V_{AC}$ and an AC sense voltage V_{AC} of 6V.

$$\text{Signal to noise} = \frac{\Delta V_{ab}^{AC}}{V_n}$$

where ΔV_{ab}^{AC} is the bridge signal voltage defined as the change of the

bridge AC imbalance voltage for a given irradiance input to the cavity.

INCIDENCE IRRADIANCE mW/cm^2	V_{ab}^{AC}	SIGNAL TO NOISE RATIO
137 (1 solar constant)	38.4 μV	1920
35 (typical irradiance for the total radiation sensor)	10.2 μV	510
21 (typical irradiance for the short wave sensor)	6.0 μV	300

The noise equivalent flux NEF is probably a more useful quantity than

the signal to noise ratio because it is essentially independent of the

input irradiance value. It can be calculated from the equation.

$$NEF = \frac{[(\delta P_e^{DC})^2 + (\delta P_e^\circ)^2]^{1/2}}{A_a \epsilon_a} \tag{4}$$

where the cavity heating power variation P_e^{DC} caused by a noise voltage

V_n on the bridge imbalance voltage is given by:

$$\delta P_e^{DC} = \left(\frac{\partial P_e^{DC}}{\partial V_{ab}^{AC}}\right) V_n = \frac{P_e^{DC}}{V_{ab}^{AC}} V_n. \tag{5}$$

Equation (3) of Table VII.3 was used to evaluate the partial derivative. The

noise equivalent flux for V_n = 20 nV is approximately .1 mW/cm^2. Although

this NEF is .5% of the typical short wave flux of 21 mW/cm^2, many

samples of the same region of the earth obtained by the 6 to 8 satellite

system will be averaged either before transmission to the ground or

during data processing. The averaging process, which is inherent to

this mission, will make the effects of noise unimportant.

4. Error Analysis

An error analysis of the FACR was performed using the same technique explained in Appendix C for the solar constant ACR. The basic operating equation for the FACR can be written as:

$$F = \frac{(P_e^\circ - P_e)\ [1 + K/\Gamma]}{A_a \varepsilon_a} \tag{6}$$

where A_a is the aperture area, ε_a is the apparent absorptance of the aperture and K is defined in Equation (8) of Section VI. The ratio K/Γ is very small (8.4×10^{-4}) and is known to better than 5% so the factor $[1 + K/\Gamma]$ introduces no significant error. The electrical power P_e supplied to the cavity is determined from two voltage measurements as follows:

$$P_e = \frac{(V-V_2)V_2}{R_2} \tag{7}$$

where V is the total voltage across the bridge circuit and V_2 is the voltage across the resistance R_2 in series with the cavity resistance in the current carrying leg of the bridge.

The measurement uncertainty of F was calculated for three different input fluxes by root sum squaring the weighted standard deviations of the parameters involved in equations (6) and (7). The standard deviations assumed for each parameter and their contribution to the total uncertainty are shown in Tables VII.4, 5 and 6. As was the case for the solar constant ACR, the uncertainty in the cavity absorptance is the largest source of error. Therefore, most of the uncertainty is an absolute not a random error. The effects of cavity temperature variations were found to be

negligible. The effects of sink temperature variations are also
negligible when a reference view of space is available on each rotation
of the spacecraft. However, for certain orbits a space view may not be
available for 10 minute periods where the sun is near the anti-nadir
position. For these cases sink temperature stability relies on the
sink control servo which allows temperature variations of $\pm$ 1 m°K (the
same sink control servo is used for the FACR as for the solar constant
radiometer). This temperature uncertainty translates into a flux
uncertainty of .02 mW/cm^2 which should be root sum squared with the
results of Tables VII.4, 5 and 6 to get the results when a space view is
not available for each spacecraft spin.

The measurement uncertainty calculations presented in Tables VII.4, 5
and 6 assume no use of the solar constant radiometer for calibration
of the FACR. Incorporating the solar constant radiometer measurements
into the calibration of both the TR and SW sensors will probably reduce
the measurement uncertainties from those presented here.

Table VII.4.   FACR Uncertainty with 1 Solar Constant Input

Parameter (ξ_i)	Nominal Value	Standard Deviation (σ_i)	$\left\lvert\frac{\partial F}{\partial \xi_i}\right\rvert \sigma_i$ (mW/cm^2)
ε_a	0.993	0.003	0.41
A_a	0.865 cm^2	0.0007 cm^2	0.11
R_2	460Ω	0.1Ω	0.03
V	23.8 V	1 mV	0.03
V°	28.0 V	1 mV	0.03
V_2	11.2 V	1 mV	0.01
V_2°	13.1 V	1 mV	0.01

$$\left[\sum_i \left(\frac{\partial F}{\partial \xi_i}\right)^2 \sigma i^2\right]^{1/2} \quad = \quad 0.43 \text{ mW/cm}^2$$

Percent Uncertainty   0.31%

Table VII.5.   FACR Uncertainty for Typical Total Wave Sensor Input (35 mW/cm^2)

Parameter (ξ_i)	Nominal Value	Standard Deviation (σ_i)	$\left\lvert\frac{\partial F}{\partial \xi_i}\right\rvert \sigma_i$ (mW/cm^2)
ε_a	0.993	0.003	0.106
A_a	0.865 cm^2	0.0007	0.028
R_2	460Ω	0.1Ω	0.008
V	27.0 V	1 mV	0.032
V°	28.0 V	1 mV	0.033
V_2	12.7 V	1 mV	0.004
V_2°	13.1 V	1 mV	0.004

$$\left[\sum_i \left(\frac{\partial F}{\partial \xi_i}\right)^2 \sigma i^2\right]^{1/2} \quad = \quad 0.11 \text{ mW/cm}^2$$

Percent Uncertainty   .32%

Table VII.6. <u>FACR Uncertainty for Typical Short Wave Sensor</u>
            <u>Input (21 mW/cm^2)</u>

Parameter (ξ_i)	Nominal Value	Standard Deviation (σ_i)	$\left\|\frac{\partial F}{\partial \xi_i}\right\| \sigma_i$ (mW/cm^2)
ϵ_a	0.993	0.003	0.063
A_a	0.865 cm^2	0.0007	0.017
R_2	460Ω	0.1Ω	0.008
V	27.4V	1 mV	0.033
$V°$	28.0V	1 mV	0.033
V_2	12.9V	1 mV	0.004
$V_2°$	13.1V	1 mV	0.004

$$\left[\sum_i \left(\frac{\partial F}{\partial \xi i}\right)^2 \sigma_i 2\right]^{1/2} = \quad 0.08 \text{ mW/cm}^2$$

Percent Uncertainty   .38%

VIII. THERMOPILE DETECTORS AS AN ALTERNATIVE

Except for apparent deficiencies in spectral response, angular response, and possibly time constant, thermopile detectors offer a number of advantages over the fast active cavity for use in the wide FOV sensors. Among these are:

(1) high signal to noise;

(2) relatively simple associated electronics;

(3) wide range of operating temperature; and

(4) small and rugged construction.

Since most of the limitations of thermopiles depend on absorbing characteristics of the black coating on its radiation receiver, they must be considered for possible application pending more complete analysis of the coating problem. The purpose of the present section is to describe the characteristics of thermopiles, their special requirements, and their overall capabilities compared to the fast active cavity.

1. Thermopile Characteristics

A wide variety of thermopile detectors are available commerically. Among these we are mainly concerned with thin-film devices because of the time constant constraints for the spinning sensors. (Most wire wound thermopiles have time constants measured in seconds instead of milliseconds).

Table VIII.1 summarizes the significant performance characteristics of devices which have been considered because of their relatively short time constants. Note that there are two time constants listed for each

Table VIII.1.   Thin-Film Thermopile Characteristics (SI = Sensors Inc.;
                BEC = Barnes Engineering Corporation)

	SI C1	BEC 2-214	BEC 2-215
Target Size	1 mm diam	1 m x 8 mm	4.7 x 5.6 mm
No. of Junctions	12	120	308
Operating Temp.	$-65°C - 125°C$	$-60°C - 125°C$	$-60°C - 125°C$
D* (500°K, DC) (cm Hz 1/2/W)	5×10^8	0.5×10^8	0.5×10^8
Responsivity (500°K, DC)	15 Volts/W	1 Volt/W	1.1 Volt/W
Time Constant* with vapor deposited coating	~20 ms	25 ms	30 ms
Time Constant with 3 M Black Coating**	~100 ms	~50 ms	—

*   All time constants are stated for vacuum conditions

** Time constant estimates for 3M-Black coatings are based on telephone
    conversation with manufacturer representatives

detector. The short time constant is obtained using a thin vapor deposited black coating. As indicated in Figures VIII.1 and VIII.2 the spectral response of the detectors using this thin coating is rather poor compared to 3M-Black or Parson's black which are themselves marginal for accurate integrated flux measurements. The second set of time constants in Table VIII.1 are obtained for the same sensor using a coating of 3M-Black instead of the thin film coating. The penalty for the improved spectral flatness is seen to be an increased time constant. The added heat capacity produced by the more massive 3M coating can probably be compensated for by reducing the thermal resistance between the radiation receiver and the heat sink (See Appendix K). The only penalty in this case would be a drop in D* and responsivity, both of which are well beyond requirements anyway. Thus we expect that thermopile detectors with short time constants (~20 to 40 ms) and relatively flat spectral response can be obtained, although we have not yet seen any as standard products.

The output characteristics of thermopile detectors when mounted in the wide FOV sensors is derived in Appendix K. The basic equations for the SW sensor and the TR sensor are somewhat different due to the emission from the window used for the SW sensor. Using the parameters

τ_λ = window transmission at wavelength λ

$F_{SW,\lambda}$ = incident short wave flux at wavelength λ

F_A = long wave flux emitted by the aperture

F_W = long wave flux received from window emission and reflection

the voltage output of the detector used in the SW sensor can be written as

$$V_{SW} = k_2 [\epsilon_{SW} \tau F_{SW} + \epsilon_{LW}(F_A + F_W - \sigma T_s^4)] \tag{1}$$
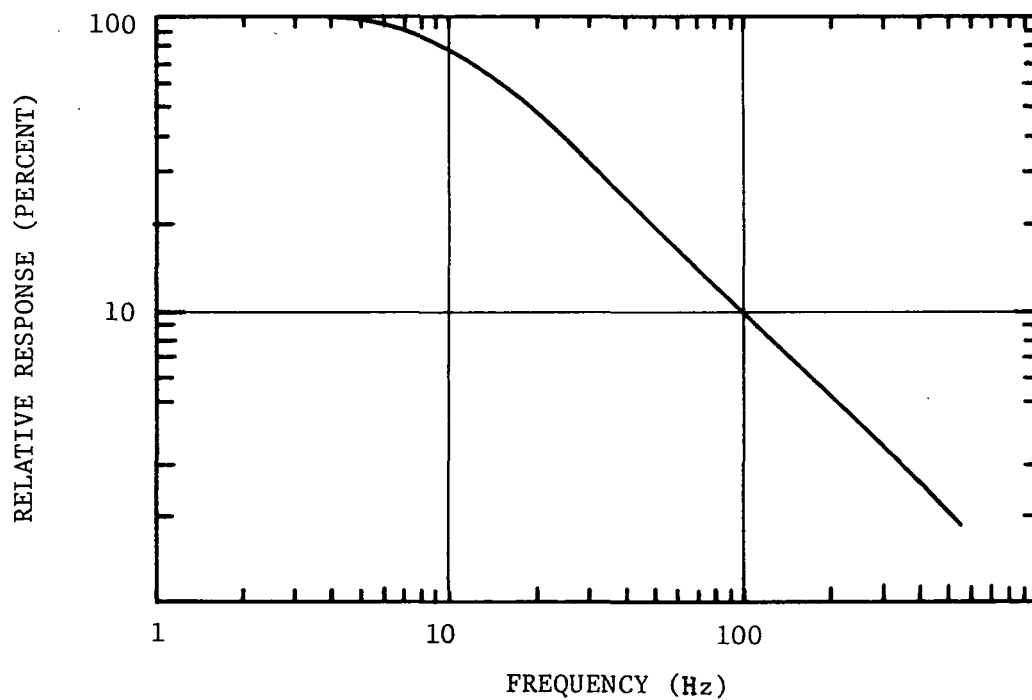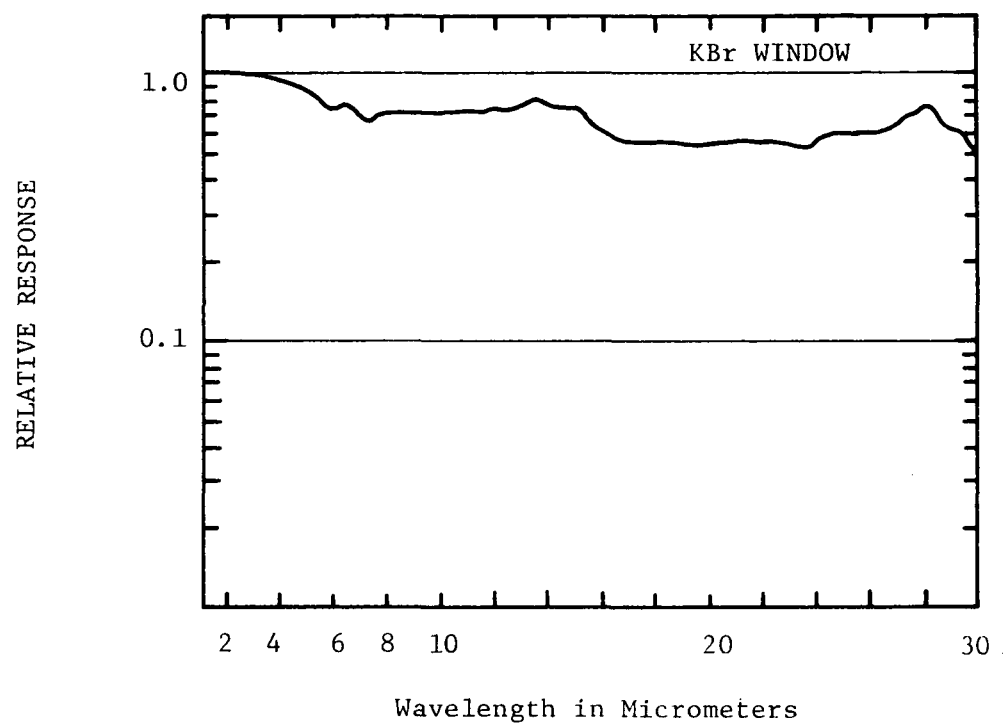
FIGURE VIII.1.   Performance Characteristics of Sensors
                 Incorporated series Cl Thermopile detectors
                 (Technical Bulletin 10, Sensors Inc.)
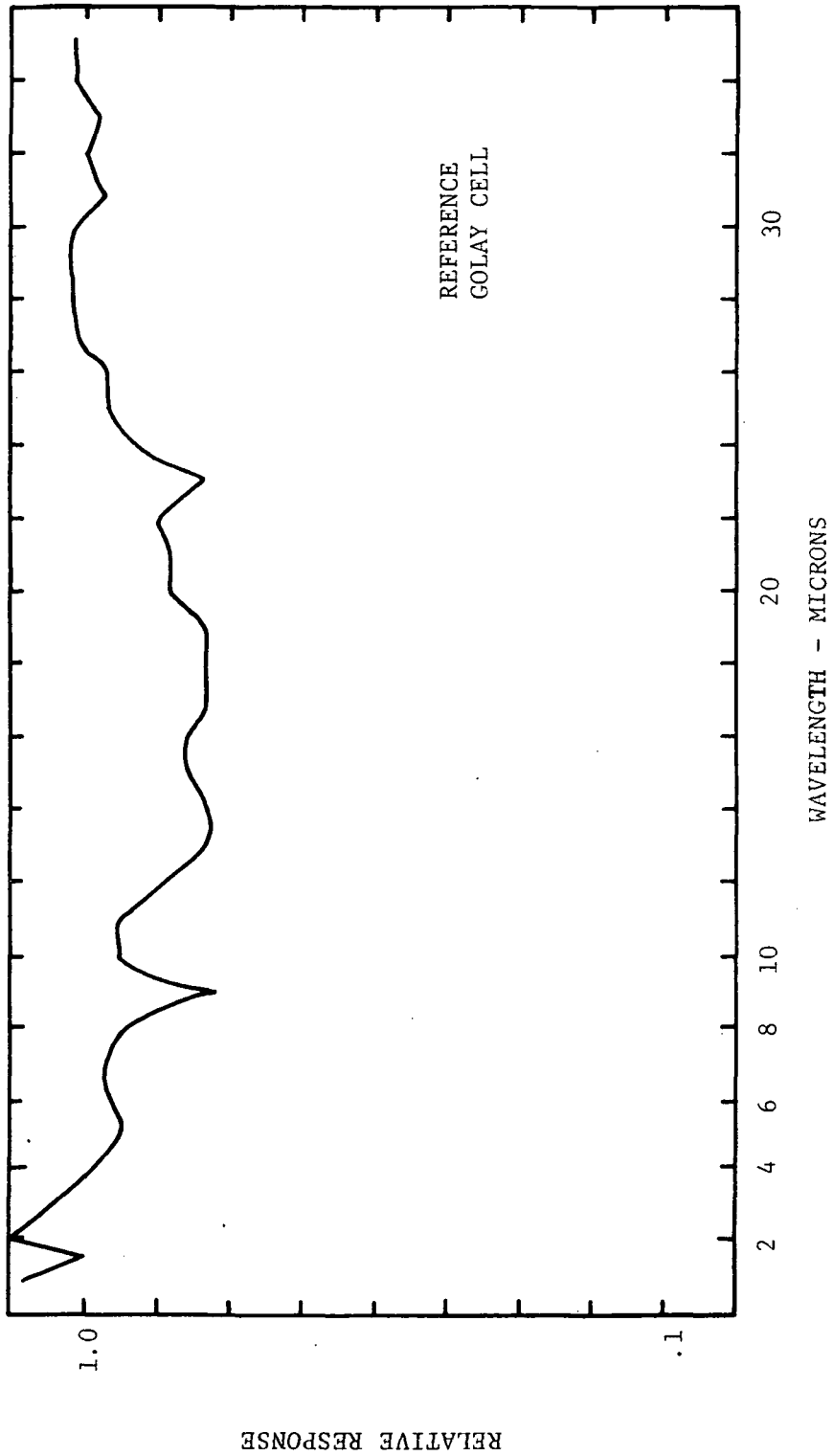
FIGURE VIII.2. Relative Spectral Response of Barnes Thin - Film Thermopile Detectors (Bulletin 2-212, Barnes Engineering Corporation)

where ϵ_{LW} is the average long wave emissivity defined in Appendix K and where

$$\tau = \int_0^\infty \tau_\lambda F_{SW,\lambda} d\lambda / F_{SW} \qquad (2)$$

$$\epsilon_{SW} = \int_0^\infty \epsilon_\lambda \tau_\lambda F_{SW,\lambda} d\lambda / \tau F_{SW} \qquad (3)$$

$$F_{SW} = \int_0^\infty F_{SW,\lambda} d\lambda. \qquad (4)$$

Since both the aperture and the window which are in contact with the heat sink will be at very nearly the same temperature as the sink, the term in (1) involving ϵ_{LW} will be very small. However, in view of the possibility of slight deviations of the window temperature from T_s we will retain this term in the analysis.

The voltage output of the total radiation sensor is given by the simpler expression

$$V_{TR} = k_2 [\epsilon_{SW} F_{SW} + \epsilon_{LW} [F_{LW} + F_A - \sigma T_s^4]] \qquad (5)$$

where k_2, ϵ_{LW} and ϵ_{SW} are not identical to the same parameters in equation (1), because slight variations in construction result in differences in k_2, and ϵ from one sensor to the other.

Figure VIII.3 displays the general character of the output as a function of incident flux for both SW and TR sensors. For illustrative purposes we consider two cases for the TR sensor: (1) incident flux is all short wave; and (2) incident flux is all long wave.

2. In-Flight Calibration of the SWS

In condensed form, we can write the equation relating the SWS thermopile voltage output to sensor input as follows:
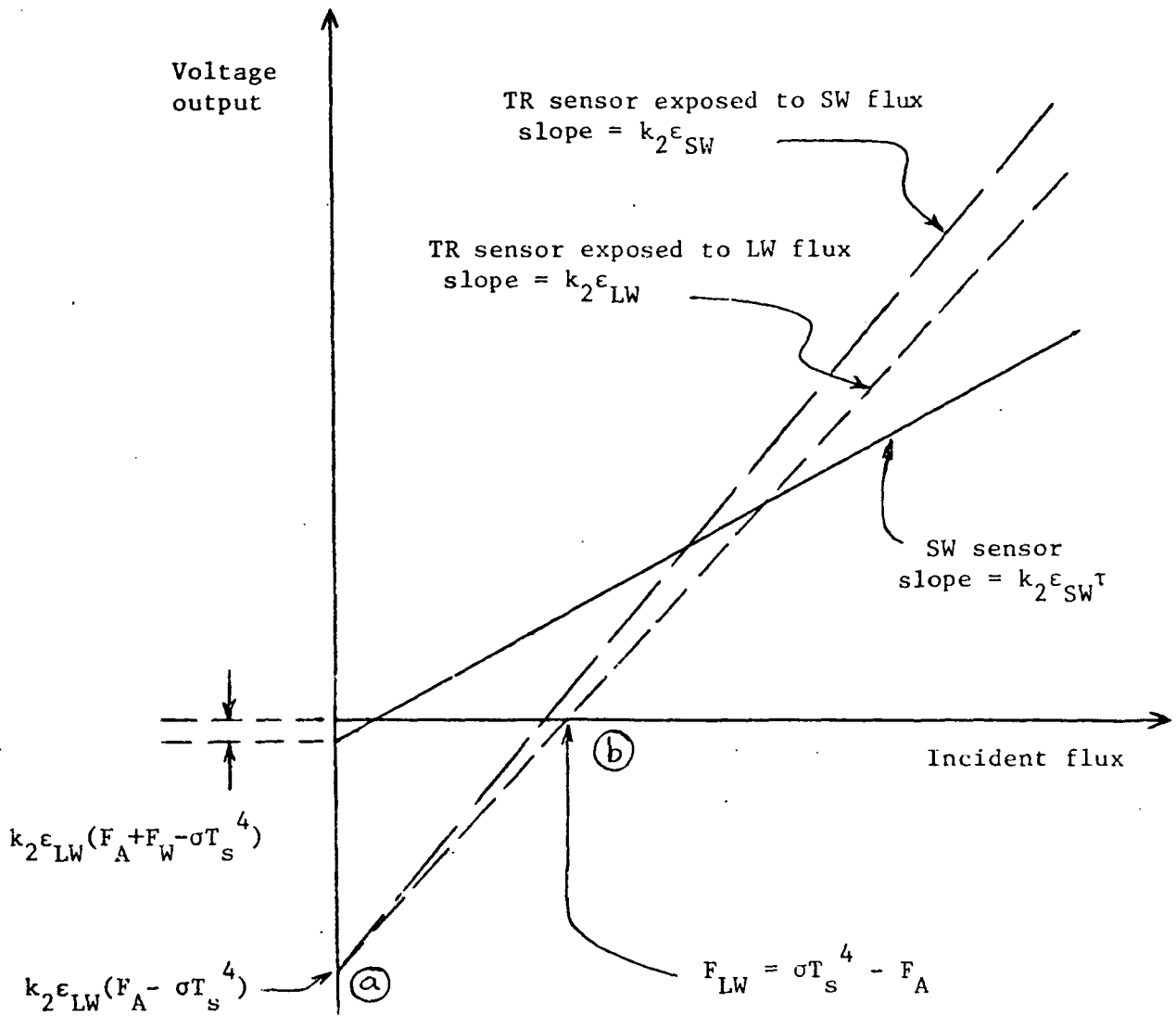
Figure VIII.3. Voltage output characteristics for SW and TRS sensors. The voltage intercept of the SW sensor could be positive or negative, depending on the relative temperature difference between the window and the heat sink.

$$V_{SW} = R\,F_{SW} + V_{o,SW} \qquad\qquad (6)$$

where the calculated value of the responsivity R and the voltage intercepts $V_{o,SW}$ can be found by comparing (6) with (1). It is the object of in-flight calibration to determine these parameters on a regular basis so that deviations from ground measurements and theoretical calculations can be tracked and accounted for as the sensor changes its characteristics in orbit.

To determine R and $V_{o,SW}$ we propose to use voltage outputs measured when the sensor views space and when it views the sun. Assuming that the flux input from space is zero (a good assumption) and that the solar flux is known (it will be periodically measured by on-board absolute radiometers to an estimated accuracy of better than 0.2%) we obtain the following system of equations for the desired parameters:

$$V_{SW}(SUN) = R\,F(SUN) + V_{o,SW} \qquad\qquad (7)$$

$$V_{SW}(SPACE) = V_{o,SW} \qquad\qquad (8)$$

Subtracting (8) from (7) we obtain the responsivity value

$$R = [V_{SW}(SUN) - V_{SW}(SPACE)]\,\frac{1}{F(SUN)} . \qquad\qquad (8)$$

The same technique would be used for the fast active cavity to account for changes in window transmission.

3. In-Flight Calibration of the TRS

The total radiation sensor output as indicated in equation (5) depends on both F_{SW} and F_{LW}. The condensed expression for its voltage output

$$V_{TR} = R_{SW}F_{SW} + R_{LW}F_{LW} + V_{o,TR} \qquad\qquad (9)$$

shows three constants to be determined by calibration: the two responsivities R_{SW}, R_{LW}; and the offset $V_{o,TR}$. It should be noted that for detector coatings

with perfectly flat spectral response, which is not the case here, $R_{SW} = R_{LW}$. The short wave responsivity R_{SW} and the offset $V_{o,TR}$ can be determined from space and sun measurements the same way R and $V_{o,SW}$ were determined.

At first sight it would appear that determining R_{LW} requires an on-board blackbody reference to provide the second point in a two point calibration process. The usual way to implement this second calibration point is to rotate the sensor so that it views an on-board blackbody cavity instead of the earth. Since this involves the complexities of moving parts, changes in thermal gradients, and changes in frequency content of the flux input, it conflicts with the system objectives of simplicity, reliability, and long life. An alternative method, which uses a temperature variable aperture and no moving parts, appears to be feasible.

Rewriting the TRS voltage output response to a long wave input flux F as

$$V = R_{LW}F - B, \tag{10}$$

the specific form of the background B is given by

$$B = R_{LW} \, \sigma T_s^{\,4} - R_A \, \sigma T_A^{\,4}, \tag{11}$$

where T_s = sensor temperature and T_A = aperture temperature. The responsivity factor R_{LW} is dependent on the long wave emissivity, the number of thermopile junctions, dV/dT per junction, and the conductivity of the thermal resistor (See Appendix K). The responsivity factor R_A differs from R_{LW} by a geometrical factor accounting for the cosine-weighted solid angle of the aperture and an emissivity connection factor accounting for the fall-off near grazing incidence.

Two space views at two different aperture temperatures are used to determine R_{LW} and R_A. Voltage outputs for the two space views are given by

$$V_1 = R_A \sigma T_{A,1}^4 - R_{LW} \sigma T_s^4 \tag{12}$$

$$V_2 = R_A \sigma T_{A,2}^4 - R_{LW} \sigma T_s^4. \tag{13}$$

It has been assumed that an accurate temperature control servo keeps T_s constant for both views. The solution for R_A and R_{LW} in terms of the measured voltages and temperatures are given by

$$R_A = (V_2 - V_1) \, [\sigma(T_{A,2}^4 - T_{A,1}^4)]^{-1}, \tag{14}$$

$$R_{LW} = (T_{A,1}^4 V_2 - T_{A,2}^4 V_1)[\sigma T_s^4(T_{A,2}^4 - T_{A,1}^4)]^{-1}. \tag{15}$$

In order to estimate the effects of measurement uncertainties in the calibration on the derived flux values we shall first invert equation (10) to express the incident long wave flux F in terms of the calibration parameters, i.e.

$$F = R_{LW}^{-1} \, [V + \sigma(R_{LW}T_s^4 - R_A T_A^4)], \tag{16}$$

where in this case T_A and T_s will be very nearly equal. The standard error in the flux (σ_F) is related to the errors in the measured parameters x_k, k = 1,7 by the equation

$$\sigma_F = \{\sum_{k=1}^{7} (\frac{\partial F}{\partial x_k})^2 \sigma_{x_k}^2\}^{1/2} \tag{17}$$

where $x_1, \ldots x_7 = V_1, V_2, T_{A,1}, T_{A,2}, T_s, T_A, V$. The derivatives are determined from equations (14), (15) and (16).

For the typical parameter values listed below, the value of σ_F can be estimated

$$R_{LW} = 15 \ \dot{V}/W\text{-}M^{-2}$$

$$R_A = 0.2 \ R_{LW}$$

$$T_s = T_A = T_{A,1} = 270°K$$

$$T_{A,2} = 320°K$$

$$\sigma T_s = 0.05°K$$

$$\sigma T_A = 0.10°K$$

$$\sigma_V = 1\mu V$$

Inserting these values into equation (17) yields a standard flux error of 0.3 W/M^2 which is within the required limits presented in Section II.

4. Deriving Long Wave and Short Wave Fluxes from Thermopile Sensor Outputs

For a single measurement the short wave flux from the earth is obtained by inverting equation (6), i.e.

$$F_{SW} = \frac{1}{R} \ (V_{SW} - V_{o,SW}). \tag{18}$$

The long wave flux emitted by the earth is determined by inverting equation (9) and inserting (18), i.e.

$$F_{LW} = \frac{1}{R_{LW}} \ (V_{TR} - V_{o,TR}) - \frac{R_{SW}}{R_{LW}} \ F_{SW}. \tag{19}$$

Similar equations would apply to the fast active cavity option, except that the short wave and long wave responsivities of the TRS will be known absolutely.

5. Radiometric Noise Estimates for Thermopile Sensors

The noise equivalent flux (NEF) can be determined from the following relationship

$$NEF = \gamma(\Delta f_N)^{1/2} \ (A_d^{1/2} D*)^{-1}, \ \text{where} \tag{20}$$

Δf_N = the system noise equivalent, bandwidth

A_d = the detector area,

$D*$ = the specific detectivity of the thermopile, and

γ = the amplifier noise factor.

In the case of thermopiles the noise power spectrum is flat; thus, assuming a similar noise spectrum for the electronics, the noise equivalent bandwidth is equal to the information bandwidth. In order to prevent reduction of the inherent time constant of the detector, we will assume an electronic band-pass of 0 - 500 Hz. Assuming a conservative amplifier noise factor of $\gamma = 2$, the NEF's for the three TP detectors described in Table VIII.1 are found to be

$$NEF = 0.005 \text{ W M}^{-2} \text{ (SI C1)}$$

$$NEF = 0.03 \text{ W M}^{-2} \quad \text{(BEC 2-214)}$$

$$NEF = 0.02 \text{ W M}^{-2} \quad \text{(BEC 2-215)}$$

all of which are well below the required limits (by at least an order of magnitude).

IX. PRE-FLIGHT AND IN-FLIGHT CALIBRATION PLANS

Although sensor calibration procedures have been discussed previously in Sections III, IV, VI and VIII, the importance of this topic warrants a separate and more detailed description. The system calibration discussed in the following subsections applies specifically to the preferred option which employs a slow ACR as the solar constant radiometer and two FACR's for the wide field of view sensors. The special calibration problems of the thermopile alternative are discussed in Section VIII.

1. Calibration Objectives

The basic objective of any instrument calibration is to define the relationship between instrument measurements and fundamental laboratory standards. Successfully meeting this objective requires thorough understanding of instrument behavior, carefully designed specific comparison measurements referenced to laboratory standards, and instrument stability between calibration and utilization. In the case of radiometers based on thermopile sensors, instrument behavior is not understood sufficiently to obviate the need for direct comparison with laboratory radiometric standards. Given a linear instrument, the comparison with laboratory radiometric standards is required to determine the constant of proportionality. The ERB calibration plan (Hickey, 1974) provides a complex mechanism for making this determination. The ERB long wave calibrations are based on blackbody cavity sources ultimately traceable to the IPTS 1968 temperature scale. The short wave calibrations are derived from comparison with reference radiometers using controlled radiation sources. The ERB flight

instruments are calibrated by comparison with a reference sensor model
which is itself calibrated by comparison with normal incidence pyrheli-
ometers which are in turn transfer standards referenced to a Kendall-
type Primary Active Cavity Radiometer (PACRAD) which serves as the
primary standard.

Since the sensor system proposed in this document contains an
absolute cavity radiometer standard (the solar constant ACR) as part
of the flight package, the calibration plan in this case does not
require laboratory comparisons with radiometric standards and, in
general, is much simpler and more direct than that required by ERB.
Both the Wisconsin Solar Constant ACR and the PACRAD referred to by
Hickey are absolute radiometers in the sense that they derive their
calibration mainly from absolute electrical standards and not from
other radiometric standards. The theory of these types of electrical
substitution cavity radiometers is well understood and experimentally
verified (See Section IV); and their stability is exceptionally good,
mainly limited by the stability of the power measurement electronics.

The wide FOV sensors proposed for the Wisconsin system (the Short
Wave FACR and the Total Radiation FACR) are also electrical substitution
absolute cavity radiometers and will be calibrated in much the same way
as the solar constant ACR. However, the cavity emissivity enhancement
factor for these instruments (~12) is not as large as it is for the
solar constant ACR (~50). Since this might lead to small changes in
calibration resulting from surface coating changes, the solar constant
ACR, which is four times less sensitive to this effect, will be used
in-flight as a reference radiometer for updating the wide FOV radiometer

calibration using the sun as a source.

2. Pre-Flight Calibration

The pre-flight calibration of the solar constant ACR is established by a combination of laboratory measurements and theory. The several factors involved in this process are indicated in the block diagram of Figure IX.1. Surface emittance measurements are used in conjunction with the theory of cavity emittance to establish the emittance of the cavity. Since the normal incidence emittance enhancement for this cavity is approximately 50, absolute surface emittance uncertainties of <5% are required. Aperture area measurement, power measurement electronics calibration, and small correction factors (see Section IV) complete the absolute calibration. The small correction factors are derived from the ACR theory and some auxiliary measurements (e.g. the approximate thermal resistance between the cavity and its associated heat sink). The two comparisons indicated in Figure IX.1 serve two distinct functions. The PACRAD comparison serves as a quality control test. The Solar Constant ACR and the PACRAD should agree to within predicted uncertainties provided both function properly. The comparison with Angstrom Normal Incidence Pyrheliometers embodying the 1956 International Pyrheliometric Scale is planned merely to establish the relative difference between that scale and the Solar Constant ACR.

The FACR's used for the wide FOV sensors will undergo pre-flight calibration which is structurally similar to that described for the Solar Constant ACR (Table IX.1). The major difference occurs in the case of the short wave sensor, which uses a Suprasil-W window. For
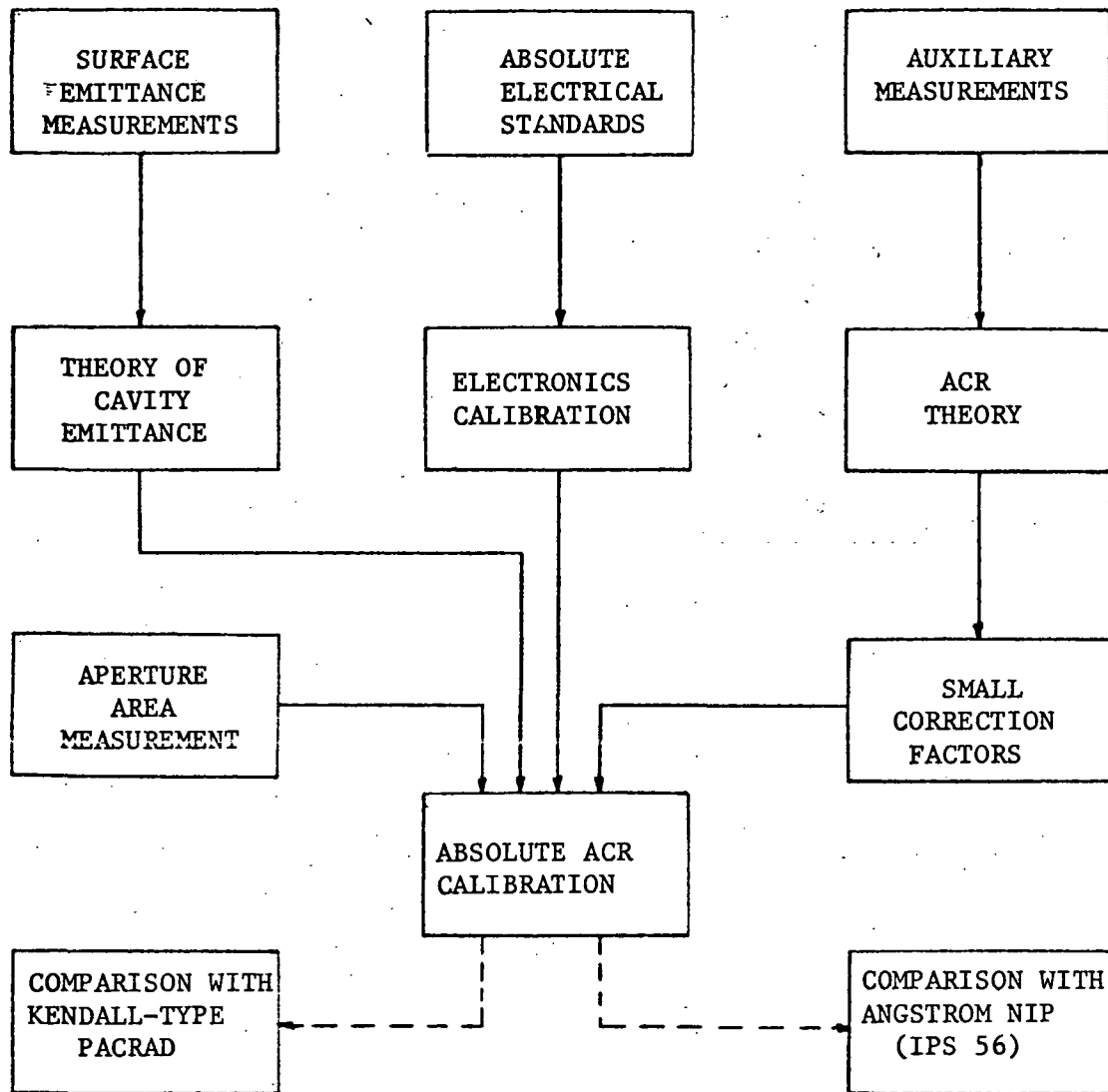
Figure IX.1. Absolute Calibration Chart for the Solar Constant
ACR. The comparisons are made for reference, not
as part of the calibration.

this sensor an additional step, i.e. determination of the window transmission, is required to establish pre-flight calibration. Since both wide FOV sensors are also calibrated in-flight using the solar constant ACR their pre-flight calibrations are, to a degree, redundant. Such redundancy is, however, a desirable feature which can aid in rapid identification of possible degradations resulting from launch.

3. In-Flight Calibration

As indicated previously, in-flight calibration of the wide FOV FACR's is accomplished using the sun as a source and the solar constant radiometers (ACR's) as reference radiometers. Because of the constraints of the spinning spacecraft assumed in this study it is not possible to perform these in-flight calibrations with a single spacecraft; both wide FOV sensors and the narrow FOV solar constant ACR on the same spacecraft cannot simultaneously view the sun. In the multiple spacecraft system proposed here the wide FOV sensors on S/C #1 use the reference ACR's on spacecrafts #2, #3, ..., n. This procedure is illustrated in Figure IX.2. Assuming 2°/day orbital precession relative to the earth-sun line, each S/C will be in favorable sun viewing position for calibration of wide FOV sensors at approximately 90 day intervals. At each such opportunity (which lasts for the order of a week or two) any of the Solar Constant ACR's on the other spacecrafts of the system can be used to measure the solar flux which, combined with the simultaneous wide FOV response to the same solar flux, establishes the in-flight calibration of the wide FOV sensors. Generally only one or possibly two other ACR's will be used at any given opportunity since only this number of the other S/C's in the system will have attitudes near optimum for pointing their spin
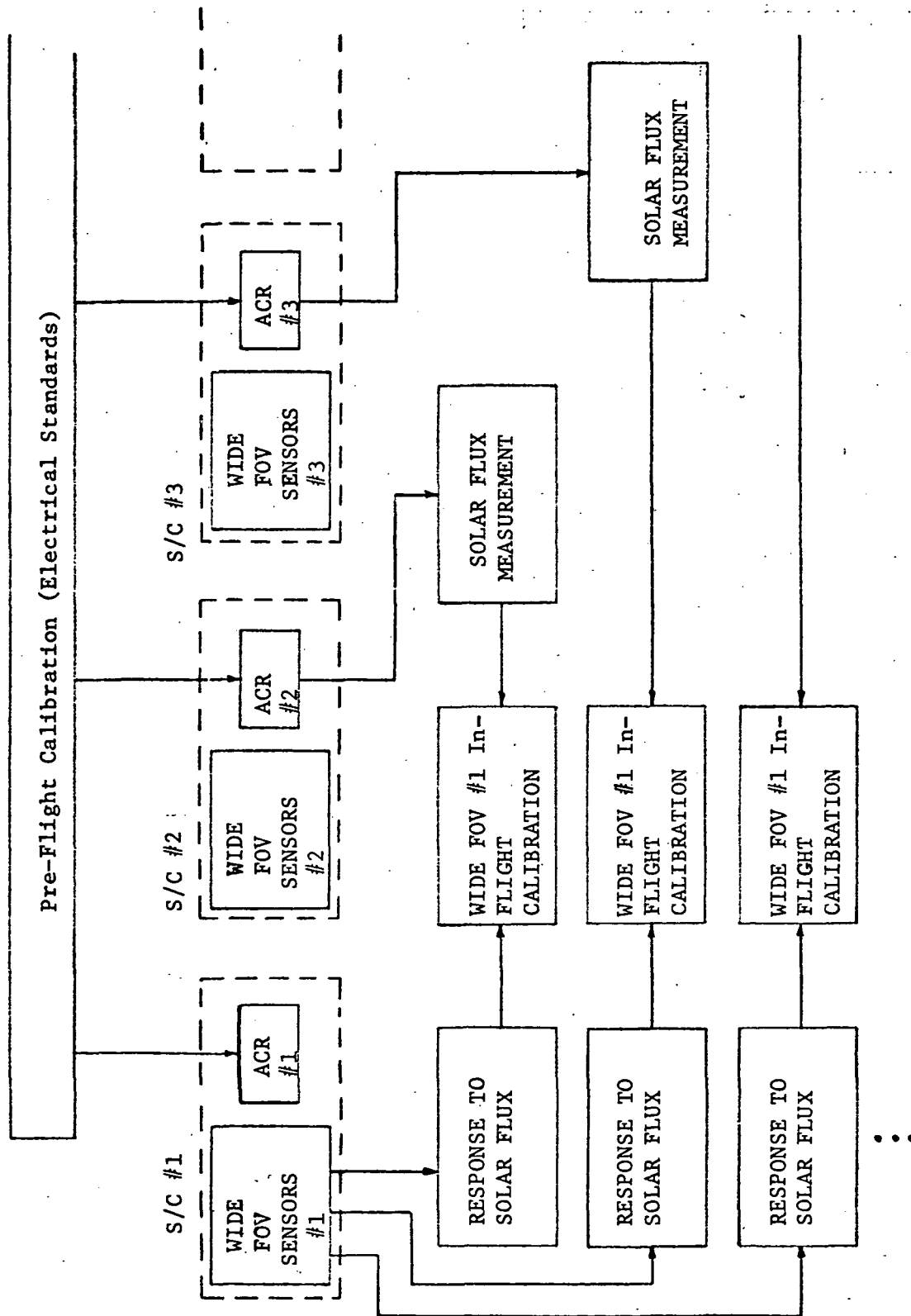
Figure IX.2. Wide FOV Sensor In-Flight Calibration using Solar Constant ACR's on Multiple Spacecrafts. In-flight Calibrations could occur every few months for each set of wide FOV Sensors. For simplicity only the calibration sequence for sensors on S/C #1 are shown in the diagram.

axis at the sun. Using all other Solar Constant ACR's is not only unnecessary but also inconvenient and inefficient since, at any given time, several of these S/C's would require large attitude changes before and after each calibration event.

Both the Solar Constant ACR and the wide FOV sensors actually do not measure absolute flux directly. Instead they measure absolute flux differences. Consequently, an external flux reference is required to establish the offset. In both cases a view of space provides this reference, i.e. zero incident flux. Figure IX.3 illustrates the role of the space reference in transferring calibration from ACR to FACR.

4. In-Flight Diagnostic Measurements

As already indicated, an important aspect of the process of calibration is thorough understanding of instrument behavior. The purpose of the in-flight diagnostic measurements is to monitor instrument characteristics so that changes from the theoretical and preflight behavior which can affect performance, yet not be observed easily in the transfer calibration methods, can be identified. Among these diagnostics the following list is selected for illustration of their significance and utilization:

(1) Space power offset variation with time - this measurement of FACR behavior uses the normal sampling mode, reveals out of specification electronics drifts.

(2) Intercomparison of wide FOV sensors (SWS and TRS FACR's) against the sun uses normal sampling mode, allows rapid discovery of sudden degradation of either of the wide FOV sensors.

Flux

Incident solar flux magnitude
determined from slope and power
difference between space and
sun views.

F_s

Solar Constant ACR
Slope determined by
Absolute Calibration.

0 ——————————————— Electrical power
provided to cavity

Solar View
Power
Measurement

Space View
Measurement

(a) SOLAR CONSTANT ACR

F_s

These two points determine FACR
slope providing in-flight calibration

0 ——————————————— Electrical Power
provided to Cavity

Space View
Power
Measurement

Space View
Measurement

(b) WIDE FOV FACR's

Figure IX.3.   Calibration transfer between Solar Constant ACR and
Wide FOV FACR's.

(3) Wide FOV sensor response to incident solar flux as a function of rotation angle - uses rapid sampling mode, establishes in-flight angular response characteristics, reveals non-uniform degradation of windows, degradation of black surfaces, and misalignments between cavity and aperture.

(4) Wide FOV sensor response to space (night measurement using SWS) - uses rapid sampling mode, yields a direct measure of window heating amplitude and phase, reveals changes in window thermal coupling to sink.

(5) Intercomparison of ACR measurements - verifies relative error predictions, identifies out-of-specification ACR's.

X. SYSTEM ERROR SUMMARY

A large number of system error sources are discussed both
in the body and in the appendices of this report. In order to put the
errors in a system perspective, representative values for the important
errors are shown in Table X.1. The errors are simply compiled for easy
reference: the table is not meant to represent a complete system error
analysis which cannot be performed at this time. Such an analysis would
require an optimized orbit set for prediction of the sampling errors
which are crucial to the system performance (see Section II). Also,
better data is required on black surface characteristics than is
generally available. The error totals shown in the table are worst
case estimates, since the errors were simply summed.

The single sample errors are divided into those which depend on the
scene viewed and those which do not. This was done to separate errors
having different impacts on the system. The scene independent errors
shown for the FACR are substantially larger than those for the TP sensor.
However, the FACR single sample noise and the measurement uncertainty are
errors which do not impair the system performance significantly. The
single sample noise will be reduced to a negligible level by the required
averaging of samples from designated earth areas, both on-board each
spacecraft, and for data processing. The FACR measurement uncertainty is
dominated by the small cavity absorptance uncertainty which is an absolute
percent error. Since data from FACR's on different spacecrafts can be
intercompared this error constitutes a constant system percent error. Also
the absolute error introduced by the cavity absorptance uncertainty can be
reduced by intercomparisons of solar irradiance measurements made by the

solar constant ACR and by the total radiation and short wavelength FACR's. The relative error portion of the FACR measurement uncertainty and calibration is comparable to the calibration error given for the thermopile sensors.

The scene dependent errors of the FACR indicates its substantial advantage over any instrument with a flat detecting surface. The errors introduced by non-uniformity of the detector response to angular and spectral variations of the scene irradiance are reduced from those of a flat plate by a factor 12.5 for the FACR design specified in this report. However, the expected thermopile errors indicate that a system of 8 satellites employing TP's would have capabilities adequate to meet the requirements of this mission as stated in Table X.1 and would be clearly superior to any past system used to measure the radiative energy budget of the earth. Which of the two wide FOV sensor options should be employed ultimately depends on surface coating emissivity characteristics and their in-orbit stability. Uncertainties in this area would heavily weight the balance in favor of the FACR option.

The solar constant radiometer accuracy is fully discussed in Section IV and Appendix C.

Table X.1. System Errors

	FACR		THERMOPILE		
ERROR SOURCE	TOTAL EARTH RADIATION	SHORT WAVE	TOTAL EARTH RADIATION	SHORT WAVE	LOCATION OF DISCUSSION IN THE REPORT
(1) Scene independent single Sample errors					
i. Noise	.08[a]	.14[a]	.01	.01	VII.3, VIII.5
ii. ACR measurement uncertainty[c]	.32	.38	-	-[b]	VII.4, C
iii. Calibration	.10[b]	.10[b]	.08	.24[b]	VIII.3, L, the SW case was not treated. An error of .3W/M^2 was assumed.
TOTAL of (1) excluding noise[a]	.32	.48	.08	.24	
(2) Scene dependent single sample errors					
i. Spectral Response					V.3, F, the SW case was not treated. Values assumed to be the same as the LW estimates.
- bias	.03	.03	.4	.4	
- random	.04	.04	.5	.5	
ii. Angular Response					
- ACR-non-uniform cavity sink exchange	.10	.10	-	-	VI.5, I, J
- Emittance variation	.01	.03	.1	.4	V.4, H
iii. Incomplete spectral coverage & separation	.10	.10	.10	.10	G
TOTAL OF (2)	.28	.30	1.1	1.4	

a By sample averaging the effect of noise will be reduced to a negligible level.

b Error of .1% included assuming the solar calibration necessary for SW calibration is performed with a sun-sensor axis angle of 10°. Smaller angles can be used. (See Appendix L).

c These values are the FACR measurement uncertainties from Section VII which are chiefly absolute errors. Use of the solar constant ACR on other satellite for calibration will reduce the uncertainties for both the TR and SW sensors.

d The scene independent single sample errors which were not given as % errors in the report assume a total radiation irradiance of 35 mW/cm^2 and a short wavelength irradiance of 21 mW/cm^2.

XI. INTERFACE REQUIREMENTS

The sensor design presented in this document has been developed for use in a fleet of spinning spacecrafts dedicated entirely to measurement of the earth's radiative energy budget. The mission objectives and corollary sensor requirements together determine spacecraft and orbital requirements. The purpose of this section is to describe the general requirements thus implied. Since the sensor system has not been designed as a bolt-on and plug-in package for riding on operational satellites, but is instead meant for integration in a dedicated spacecraft as the only observing instrument, specific configurations of subsystem components which would be determined mainly by dynamical considerations are not described.

1. Thermal Interface Considerations

All sensor subsystems are thermally controlled by servo systems and insulated from the S/C structure. However, there must be sufficient conductive coupling to maintain positive power flow from the sensor to the S/C under minimum temperature differences. If we define

$T_{S/C}^{(h)}, T_{S/C}^{(c)}$ = the hottest and coldest S/C temperatures experienced during a full year of precessional cycles,

T_s = the sensor sink temperature,

P_{min} = the minimum power which must be conducted from sink to S/C,

P_{max} = the maximum power conducted from sink to S/C, and

K = the thermal conductance of the insulation between sink and S/C

then the thermal conductance must satisfy

$$K \approx P_{min} (T_s - T_{S/C}^{(h)})^{-1},$$
(1)

and the resulting maximum power is thus found to be

$$P_{max} = K(T_s - T_{S/C}^{(c)}) = P_{min} (T_s - T_{S/C}^{(c)}) (T_s - T_{S/C}^{(h)})^{-1}.$$
(2)

For an integrated sensor S/C design T_s, $T_{S/C}^{(c)}$, $T_{S/C}^{(h)}$, would be system optimized as a group considering all constraints. From a bolt-on package point of view we will choose a fixed sink temperature $T_s = 320\,°K$ and require

$$T_s - T_{S/C}^{(h)} \geq 40\,°C$$
(3)

$$T_{S/C}^{(h)} - T_{S/C}^{(c)} \leq 20\,°C$$
(4)

in which we obtain

$$P_{max} \lesssim 1.50\ P_{min}$$
(5)

which will be used in estimating total power requirements.

2. Power

Lacking detailed electronics subsystem design, power estimates are only approximate. Values listed below are based on comparison with results for in-house spaceflight hardware of similar function and complexity.

Subsystem	Power (watts)	
	W/O CMOS	W/CMOS
Command & Control	0.8	0.4
Data Processor & Memory	1.0	0.5
Power Conversion (Converter Loss ~25%)	2.0	1.5
Attitude & Spin Control	0.65	0.65
Transmitter	0.07(4.0)	0.07(4.0)
Receiver	0.015 (1.0)	0.015(1.0)
Housekeeping	0.1	0.1
Sensor Servo Control Circuitry	1.0	1.0
FACR Sensor (2)	1.6	1.6
FACR Sink Control Power (2)	0.6 (0.8)	0.6 (0.8)
ACR Sensor	.003 (0.25)	.003 (0.25)
ACR Sink Control Power	0.004(0.4)	0.004 (0.4)
TOTALS	7.84	6.44

The maximum powers for those subsystems with variable loads are shown in parentheses. The transmitter and receiver powers assume a duty cycle of 2 and 5 minutes every 12 hours respectively. The solar constant ACR will only be used four times per year.

The power available from the solar panel array was estimated by R. Rassmussen of Electro Optical Systems to be 14.1 watts at the end of a 10 year mission. The following conditions were assumed:

1. Spherical spacecraft with 24" diameter.

2. Of the spacecraft surface, 90% is available for solar panels and 72% for solar cells.

3. Circular orbit with an altitude of 380 n.mi.

4. Worst case illumination of 54.6 min day light and 35.6 min night. The resulting power margin assuming a battery efficiency of 0.8 is 4.84 watts if CMOS are used and 3.44 watts otherwise. The satellite power profile is illustrated in Figure XI.1.

3. Weight

The weight estimate for a complete satellite is given below. The values are approximate but conservative and are based on comparisons with in-house spaceflight hardware of a similar function and complexity.

Subsystem	Estimated Maximum Weight (lbs)
Sensors	
FACR (2)	6.0
Solar Constant ACR	3.0
Sensor Electronics	2.0
Power	18.0
Communication	5.0
Cable Harness	4.0
Structure	15.5
Command and Control	5.0
Attitude Control	5.0
Data Processor	6.0
TOTAL	69.5 lbs ≈ 32 Kg.

Two satellites of this weight can easily be launched together on a single scout launch vehicle.
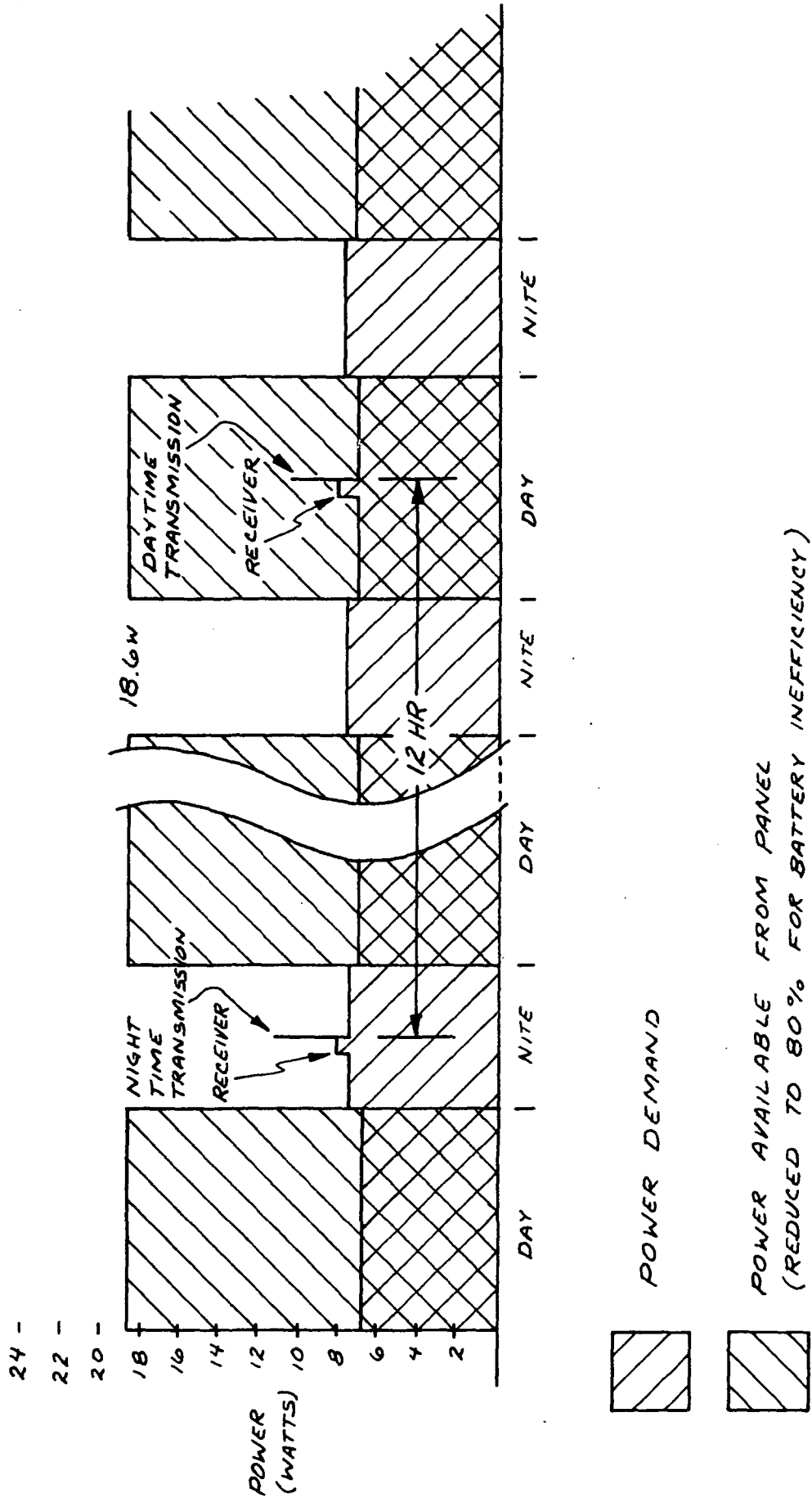
Figure XI.1. Satellite Power Profile

4. <u>Signal Interface Requirements</u>

The data processor subsystem (see block diagram Figure XI.2) requires the following timing signals:

    (1) Spin clock (frequency of S/C rotation x 1024)

    (2) SWS pointing at earth nadir

    (3) SWS pointing at min. relative sun angle

    (4) Read out clock frequency (to be determined)

    (5) Read envelope

Timing signal errors (for (1) through (3)) are assumed to be directly dependent on attitude errors. Requirements for the latter are outlined in a separate subsection. The read clock and read envelope are used to shift serial digital data from processor memory to the S/C communication system for transmission to the ground station. Data storage of approximately 40,000 bits requires ground read out twice per day. Additional commands required are

    (1) Read Command

    (2) Mode (normal, solar constant measurement, other)

    (3) Power on/off

Detailed signal characteristics (pulse widths, rise times, logic levels, etc) are to be determined. Housekeeping data for sensor systems are encoded digitally in the 40 K bit data block and do not require analog signal lines.

5. <u>Attitude Requirements</u>

In order to keep attitude errors from affecting accuracy of reflected solar and emitted fluxes we must have the nadir pointing accuracy better than $\pm$ 1.8°. The ACR used for measurement of the solar constant requires
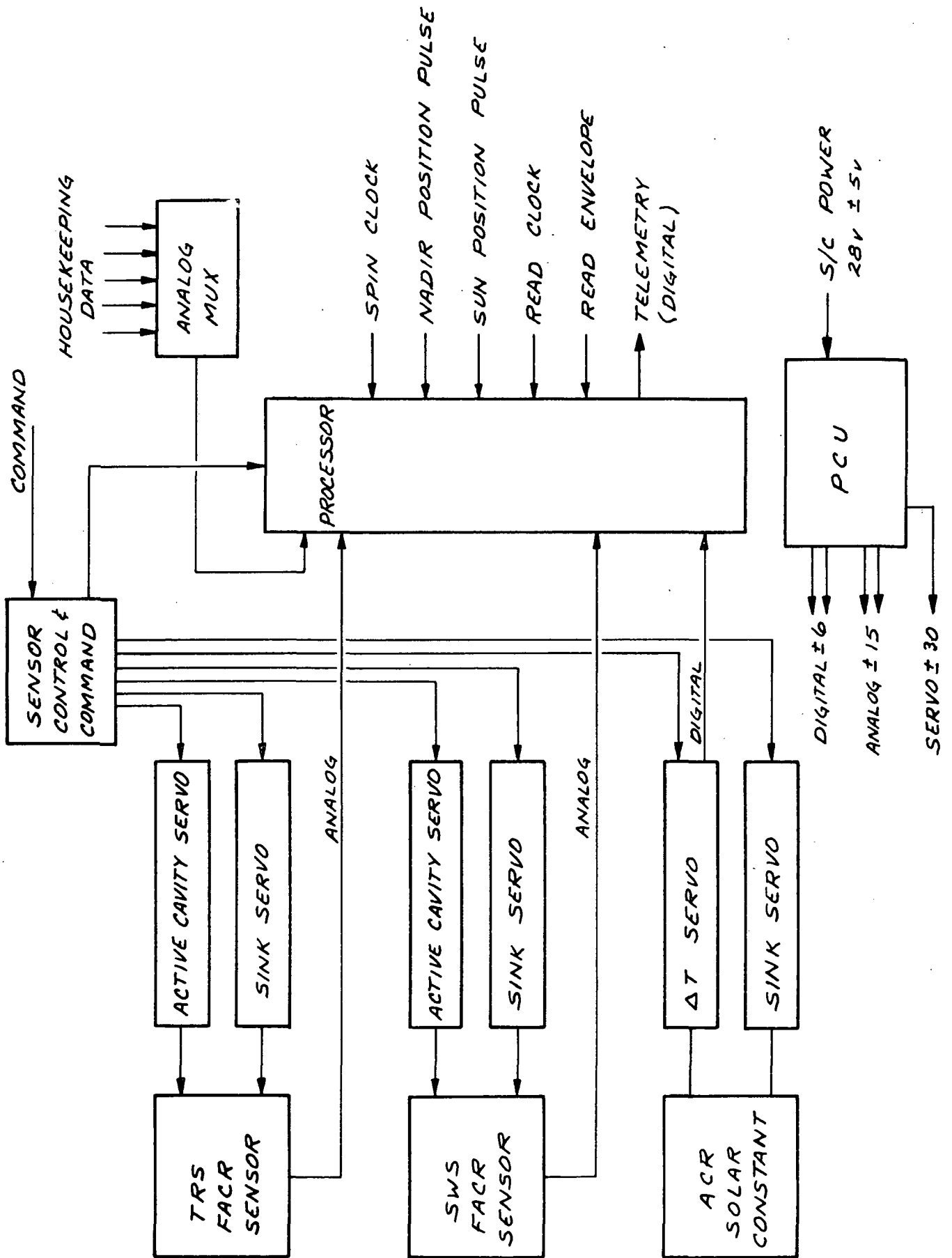
Figure XI.2. Sensor System Block Diagram

sun pointing accuracy of $\pm$ 0.5°. It is also necessary to have relatively high attitude accuracy relative to the sun for calibration of the SWS and the short wave responsivity of the TRS. The latter requirement is determined as a function of the minimum pointing angle between the sun and the sensors in Appendix L. A reasonable pointing accuracy in this case is $\pm$ 0.5° which would allow for wide FOV shortwave response determination error less than 0.2% for sensor plane sun line angles in the range $\pm$ 30°.

6. S/C Spin Requirements

Spacecraft spin axis must be parallel to the orbit plane normal within 1° and known accurately enough to meet the attitude requirements outlined in the previous subsection. The chosen spin direction results in the S/C "rolling" along the orbit. The spin rate should be approximately 6 RPM. Spin rate accuracy is not a separate requirement provided timing signals provided are sufficient to meet attitude requirements.

7. Orbital Requirements

Optimum orbit sets have not been determined. The general requirements are for 6-8 satellites in approximately circular orbits 380 n.mi. in altitude. The altitude should be as low as possible within the constraint of the desired systems lifetime. A 380 n.mi. circular orbit has a 98% probability for a 6 year lifetime. Multiple satellites with precessing orbits are necessary to obtain sufficient diurnal sampling (see Section II). Although three equally spaced satellites with precession rates of 2°/day relative to

the sun would probably provide adequate monthly averaged sampling for most longitudes, more satellites are necessary because no orbit adjust capability is employed to maintain the satellite spacings. Also, the inclusion of a polar orbit and a near equatorial orbit would improve the sampling. Sun-synchronous orbits are not desired because they severly limit diurnal sampling capabilities.

REFERENCES

AFCRL Handbook on Geophysics and Space Environments, 1965. McGraw Hill, New York City.

Bartman, F. L., 1967. The reflectance and scattering of solar radiation by the earth. Tech. Report, Department of Meteorology and Oceanography, University of Michigan, Ann Arbor.

Bignell, K. J., 1961. Heat – Balance measurements from an earth satellite – An Analysis of some possibilities. Quart. J. Roy. Met. Soc. 87, 231.

Budyko, M. I., 1969. The effect of solar radiation variations on the climate of the earth. Tellus 21, 611.

Freymuth, P., 1968. Reviews of Scientific Instruments 39, 550.

Grassoff, L. H., 1960. A method for controlling the attitude of a spin-stabilized satellite. ARS 15th Annual Meeting, Washington, D.C., December 5-8.

Hall, W. M., 1970. Effect of Low Temperature on the Thermal Emittance of Three Black Paints; Comparison of Normal and Hemispherical Emittances. JPL Space Programs Summary, No. 37-31, Vol. IV.

Hickey, J. R., and A. R. Karoli, March 1974. Radiometric Calibrations for the Earth Radiation Budget Experiment, Applied Optics, Vol. 13, No. 3.

Hoffman, R. B. and T. O. Haig, 1964. Space uses of the earth's magnetic field. Proceedings 11th Annual A F Science and Engineering Symposium, Brooks AFB, Texas.

Kendall, J. M. Sr. and C. M. Berdahl, 1970. Two Blackbody Radiometers of High Accuracy. Applied Optics 9, 1032.

Novoseltsev, Y. P. 1964. Spectral Reflectivity of Clouds. NASA TT F-328, Translation of "Spektrolnaya Otrazhatelnaya Oblakov," Trudy Glavnoz Geofizicheskoy Observatoiri Uneni A. I. Voyykova, No. 152, pp 186-191.

Remote Measurement of Pollution, 1971. SP-285, Langley Research Center, pp 227.

Report of the GARP Study Conference on the Physical Basis of Climate and Climate Modeling, 1975. GPS No. 16, to be published.

Sellers, W. D., 1969. A global climatic model based on the energy balance of the earth-atmosphere system, JAM 8, 392.

Sparrow, E. M. and V. K. Jonsson, 1963. Radiant Emission Characteristics of Diffuse Conical Cavities, J. Opt. Soc. A. 53, 816.

Study of Critical Environmental Problems (SCEP), 1970. Man's Impact on the Global Environment, The.M.I.T. Press, Cambridge, Mass.

Study of Man's Impact on Climate (SMIC), 1971. Inadvertent Climate Modification, The M.I.T. Press, Cambridge, Mass.

Suomi, V. E., 1960. Radiation Measurements of the Earth from an Artificial Satellite. Rockets and Satellites in IGY, Pergamon Press.

Sydnor, C. L., 1970. A Numerical Study of Cavity Radiometer Emissivities. JPL Technical Report 32-1463.

Vonder Haar, T. H., 1968. Variations of the earth's radiation budget. Meteorological Satellite Instrumentation and Data Processing, Department of Meteorology, University of Wisconsin, Madison.

Vonder Haar, T. H., 1969. Satellite measurements of the earth's radiation budget during a five year period. Annual Scientific Report on NASA Contract NAS5-11542, Space Science and Engineering Center, University of Wisconsin, Madison.

Vonder Haar, T. H. and Suomi, V. E., 1969. Satellite Observations of the Earth's Radiation Budget. Science 163, 667.

Wark, D. Q., G. Yamamoto, and J. Lienesch, 1962. Metorol. Satellite Lab. Rept. No. 10, U. S. Weather Bureau.

Willson, R. C., 1969. Experimental and Theoretical Comparison of the JPL Active Cavity Radiometric Scale and the International Pyrheliometric Scale. JPL Technical Report 32-1365.

Willson, R. C., 1971. Active Cavity Radiometric Scale, International Pyrheliometric Scale, and the Solar Constant. Journal of Geophysical Research 76, 4325.

Willson, R. C., 1972. New Radiometric Techniques and Solar Constant Measurements. Solar Energy 14, 203.

Willson, R. C., 1973. Active Cavity Radiometer. Applied Optics 12, 810.

APPENDIX A. CALCULATION OF NORMAL AND HEMISPHERICAL CAVITY EMITTANCES

The accuracy of the solar constant measured with an active cavity radiometer depends heavily on knowledge of the cavity absorptance. Methods of approximating and bounding cavity emittance (and therefore absorptance) are developed in this appendix. The results are sufficient to justify the uncertainty assumed for the ACR absorptance in Appendix C and Section VII.4.

1.   Apparent Emittance of the Cavity Surface

Assuming that the cavity surface is opaque and grey ($\rho = 1-\alpha = 1-\varepsilon$) that it emits and reflects diffusely, and that no radiant flux enters the cavity from the outside, the flux balance for a point x on the surface is given by the following integral equation (Sparrow et al., 1963)

$$B(x) = \varepsilon \, \sigma \, T^4(x) + \rho \int_S B(y) \, dF_{x-y} \tag{1}$$

where

ε — surface emittance

$T(x)$ — surface temperature

ρ — surface reflectance, $\rho = 1 - \alpha$, α is the absorptance.

$B(x)$ — total emitted flux.

$B(x) = \varepsilon(x) \, \sigma \, T^4(x)$, $\varepsilon(x)$ is the apparent surface emittance.

dF_{x-y} — view factor from position x to position y. It represents the fraction of the energy emitted from a small area $da(x)$ which arrives at $da(y)$.

The integral is performed over all y on the surface of the cavity. If the temperature of the cavity is uniform, Equation 1 reduces to:

$$\varepsilon(x) = \varepsilon + \rho \int_S \varepsilon(y) \, dF_{x-y}. \tag{2}$$

To determine the apparent emittance $\varepsilon(x)$ for a given cavity directly

from Equation 2 requires a numerical computer solution. However, without obtaining such a solution for each possible cavity design, we can learn a great deal about the dependence of emittance on cavity design by examining Equation 2 more closely.

First, it is clear from Equation 2 that $\varepsilon(x)$ is always greater than ε since the integral portion of the equation is positive. Therefore, the crudest possible bounds on the apparent surface emittance are:

$$\varepsilon \leqslant \varepsilon(x) \leqslant 1.$$

Substituting these bounds into the RHS of Equation 2 gives an improved set of bounds:

$$\varepsilon + \varepsilon\rho \int dF_{x-y} \leqslant \varepsilon(x) \leqslant \varepsilon + \rho \int dF_{x-y}$$

or

$$\varepsilon + \varepsilon\rho(1-F_{x-o}) \leqslant \varepsilon(x) \leqslant \varepsilon + \rho(1-F_{x-o}) \tag{3}$$

where $F_{x-o} = 1 - \int dF_{x-y}$ is the view factor from x to the cavity aperture.

Second, by writing the formal solution of Equation 2 as an infinite series in increasing powers of the reflectance, the bounds of Equation 3 can be further improved. The formal solution is as follows:

$$\varepsilon(x) = \varepsilon + \rho\varepsilon \int dF_{x-y} + \rho^2 \varepsilon \iint dF_{y-z} \, dF_{x-y} + \dots$$

$$= \varepsilon + \rho\varepsilon(1-F_{x-o}) + \rho^2 \varepsilon \int (1-F_{y-o}) \, dF_{x-y} + \dots$$

Now define F* to be the maximum of F_{x-o} for all x on the cavity. We get a lower bound to $\varepsilon(x)$ as follows:

$$\varepsilon(x) \geqslant \varepsilon + \rho\, \varepsilon\, (1-F^*) = \rho^2 \varepsilon\, (1-F^*) \int dF_{x-y} + \dots$$

$$= \varepsilon + \rho\, \varepsilon\, (1-F^*) + \rho^2 \varepsilon\, (1-F^*)\, (1-F_{x-o}) + \dots$$

$$\vdots$$

$$\geqslant \varepsilon \sum_{n=o}^{\infty} \rho^n (1-F^*)^n = \frac{\iota}{1-\rho(1-F^*)}$$

An upper bound of the same form can easily be found. Then using Equation 2 the following bounds result:

defining $\quad F_1 \geqslant F_{x-o} \geqslant F_2$

$$\varepsilon_i = \frac{\varepsilon}{1-\rho(1-F_i)} \quad i=1,2$$

$$\varepsilon + \rho\varepsilon_1 \, (1-F_{x-o}) \leqslant \varepsilon(x) \leqslant \varepsilon + \rho \, \varepsilon_2 \, (1-F_{x-o}). \tag{4}$$

Third, for a spherical cavity with a uniform surface coating, the apparent surface emittance can easily be calculated. The view factor from one area element $da(x)$ of a sphere to another $da(y)$ is:

$$dF_{x-y} = \frac{da(y)}{4\pi R^2} \tag{5}$$

for a sphere of radius R. This result is interesting because dF_{x-y} is not dependent on x. Therefore, Equation 2 shows that $\varepsilon(x)$ is a constant and is given by:

$$\varepsilon(x) = \varepsilon + \varepsilon(x)\rho \int dF_{x-y}$$

or

$$\varepsilon(x) = \frac{\varepsilon}{1-\rho \int dF_{x-y}}$$

$$= \frac{\varepsilon}{1-\rho(1-F_{x-o})} \tag{6}$$

where in terms of the area of the cavity A_c,

$$\int dF_{x-y} = 1-F_{x-o} = \frac{A_c}{4\pi R^2} . \tag{7}$$

Based on the result for the sperical cavity, we suspect that for nearly spherical cavities the apparent surface emittance will not vary a great deal over the surface. Therefore, Equation 2 can be approximated by

$$\varepsilon(x) \doteq \varepsilon + \rho\tilde{\varepsilon} \int dF_{x-y}$$

$$= \varepsilon + \rho\tilde{\varepsilon} \, (1-F_{x-o}) \tag{8}$$

where $\varepsilon(x)$ inside the integral is approximated by its area average over the surface:

$$\tilde{\varepsilon} = \frac{\int \varepsilon(x) \, da(x)}{\int da(x)} \ .$$

Now, we have developed bounds, Equation 3 and 4, and an approximation, Equation 8, from which we can proceed to obtain relations for the apparent hemispherical and normal emittance of the cavity as a whole.

2. Cavity Hemispherical Emittance

The apparent hemispherical emittance is the ratio of the emitted flux to that which would be emitted by a perfect blackbody. That is:

$$\varepsilon_a^H = \frac{\int B(x) \, F_{x-o}(x) \, da(x)}{\int \sigma \, T^4(x) \, F_{x-o}(x) \, da(x)}$$

For a uniform temperature distribution,

$$\varepsilon_a^H = \frac{\int \varepsilon(x) F_{x-o}(x) \, da(x)}{\int F_{x-o}(x) \, da(x)}$$

$$= \frac{1}{A_{ap}} \int \varepsilon(x) \, F_{x-o}(x) \, da(x)$$

(9)

where A_{ap} is the aperture area.

Substituting $\varepsilon(x)$ from Equation 4 and Equation 8 gives the following results:

$$\varepsilon + \rho \varepsilon_1 \, (1-f) \leq \varepsilon_a^H \leq \varepsilon + \rho \varepsilon_2 \, (1-f) \tag{10}$$

$$\varepsilon_a^H \doteq \varepsilon + \rho \, \tilde{\varepsilon}(1-f) \tag{11}$$

where $f = \dfrac{\int F_{x-o}^{\ 2} \, da(x)}{\int F_{x-o} \, da(x)}$.

A more useful approximation than Equation 11 can be obtained by letting $\tilde{\varepsilon} = \varepsilon_a^H$ which is a weighted average of ε over the surface. Then:

$$\varepsilon_a^H \doteq \frac{\varepsilon}{1-\rho(1-f)}. \tag{12}$$

Substituting $1-\varepsilon$ for ρ,

$$\varepsilon_a^H \doteq \frac{\varepsilon}{\varepsilon +(1-\varepsilon)f}. \tag{13}$$

For a spherical cavity of radius R, this result is exact. We can see from Equation 7 and the relation $\int F_{x-o}\ da(x) = A_{ap}$ that:

$$f = F_{x-o} = 1 - \frac{A_c}{4\pi R^2} = \frac{A_{ap}}{A_c} = \frac{1}{2}(1 - (1- \frac{r^2}{R^2})^{1/2}) \tag{14}$$

where A_{ap} is the aperture plane area, A_c is the area of the cavity and r is the aperture radius. The spherical approximation (Equation 13 with Equation 14) was compared with the emittance of three nearly spherical cavities formed from cyclinders and cones calculated numerically (Syndor,1970). The approximation was accurate to within .2% when a sphere of the same area as the nearly spherical cavity was used for the approximation.

Finally, it should be noted that the lower bound of Equation 10 is quite useful. While it may appear difficult to determine ε_1, for most cavities ε_1 is the emittance of a spherical cavity with the same aperture as the cavity of interest and with a radius such that it just fits inside.

3. Cavity Normal Emittance

The equation for apparent normal emittance is formally very similar to that for hemispherical emittance. However, instead of dealing with all of the flux emitted by the cavity, we consider only the flux emitted to an area equal to the aperture area and essentially an infinite distance away in the normal direction. The solid angle from the emitting surface to the distance area is independent of position on the cavity so the normal

emittance is given by:

$$\varepsilon_a^N = \frac{\int B(x)\ \hat{n}\ \cdot\ d\ \vec{a}_n(x)}{\int \sigma\ T^4(x)\ \hat{n}\ \cdot d\ \vec{a}_n(x)} \qquad (15)$$

where $\hat{n}$ is a unit vector in the normal direction, the area vector $d\ \vec{a}_n(x)$ is normal to the surface at x and the integration ranges over the inner cavity surface a_n bounded by the normal projection of the cavity aperture boundary. It is clear that for a spherical cavity with a constant surface temperature ($B(x)$ and $\varepsilon(x)$ are constants), the normal emittance is equal to the hemispherical emittance.

For an isothermal cavity with $\hat{n}\ \cdot\ d\ \hat{a}_n(x)$ independent of x (e.g. a cone) Equation 15 reduces to:

$$\varepsilon_a^N = \frac{\int \varepsilon(x)\ d\ a_n(x)}{\int d\ a_n(x)}\ . \qquad (16)$$

Again we can use the bounds of Equation 4 and the approximation of Equation 8 to yield:

$$\varepsilon_a^N + \rho\varepsilon_1\ (1-g) \leqslant \varepsilon_a^N \leqslant \varepsilon + \rho\varepsilon_2\ (1-g) \qquad (17)$$

and

$$\varepsilon_a^N \doteq \varepsilon + \rho\ \tilde{\varepsilon}\ (1-g) \qquad (18)$$

where $g = \int F_{x-o}(x)\ d\ a_n(x)/\int d\ a_n(x)$.

The approximation $\tilde{\varepsilon}$ used in Equation 18 has a form very similar to that for g. However, $\tilde{\varepsilon}$ is the average of $\varepsilon(x)$ over the whole cavity area, not just over a_n.

Now consider the following special cases:

CASE 1. Right Circular Cone.

Since for the cone the area a_n is the whole cavity area,

$$\int F_{x-o}\ d\ a_n(x) = A_{ap}$$

$$\int d\ a_n(x) = A_{cone}$$

and

$$\tilde{\varepsilon} \equiv \frac{\int \varepsilon(x) \, d \, a(x)}{\int d \, a(x)} = \varepsilon_a^N.$$

Therefore, $g = \sin \theta$, where θ is the half angle of the cone, and Equation 17 and 18 reduce to:

$$\varepsilon + \rho \varepsilon_1 (1-\sin\theta) \leq \varepsilon_{cone}^N \leq \varepsilon + \rho \varepsilon_2 (1-\sin \theta)$$

$$\varepsilon_{cone}^N \doteq \frac{\varepsilon}{\varepsilon + (1-\varepsilon) \sin \theta}.$$

CASE 2. Cone Plus Upper Cavity:

For simplicity we assume that the height of the upper cavity is much larger than the radius of the aperture. Then:
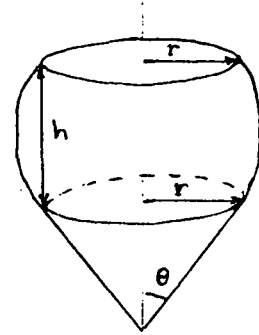
$$g = (\frac{r}{h})^2 \sin \theta,$$

and $\varepsilon_a^N \doteq \varepsilon + \rho \, \tilde{\varepsilon} \, (1 - (\frac{r}{h})^2 \sin \theta).$

Also, the normal emittance is bounded by

$$\varepsilon + \rho \varepsilon_1 (1 - (\frac{r}{h})^2 \sin \theta) \leq \varepsilon_a^N \leq \varepsilon + \rho \varepsilon_2 (1 - (\frac{r}{h})^2 \sin \theta).$$

A useful lower bound can usually be found, as mentioned in Section 2, by letting ε_1 be the emittance of a sphere which just fits into the upper cavity.

4. Application to the Solar Constant ACR

The cavity absorptance α_c of the solar constant ACR was assumed to be $.999 \pm .001$ in Appendix C . We can get a lower bound to α_c for an isothermal cavity using the result of the last section, case 2.

$$\alpha_c \geq \varepsilon + (1-\varepsilon) \, \varepsilon_{sphere} \, (1 - (\frac{r}{h})^2 \sin\theta)$$

where ε_{sphere} is the emittance of a sphere which fits into the cavity and can

be calculated using Equation 13 and 14. The appropriate dimensions are:

r = .564 cm

h = 3.4 cm

$\frac{r}{h}$ = .166

θ = 15°

R_{sphere} = 1.128 cm

The results for a few values of surface emittance are:

ϵ	ϵ_{sphere}	lower bound to α_c
.88	.9909	.9981
.90	.9926	.9986
.95	.9965	.9995

These bounds on the absorptance are significantly larger than those given in some JPL reports on the ACR. Those estimates seem to have been made using the hemispherical emittance instead of the normal emittance.

We see that an uncertainty of $\pm$ .1% for the cavity absorptance is reasonable even if significant degradation of the black coating occurs.

5.   <u>Application to the FACR</u>

The values of the apparent emittance of the FACR given in Section VI were calculated from equations (13) and (14). Since the cavity design is more nearly spherical than the cavities used for comparison with numerical results, it is felt that they are accurate to better than .1%.

APPENDIX B.   ANALYSIS OF SERVO ELECTRONICS FOR SOLAR CONSTANT RADIOMETER

This appendix briefly describes the two temperature control servos for the thermal resistance difference temperature and the heat sink temperature. It also presents the control requirements and design and error details.

1.   The Difference Temperature Servo

Referring to Figure 1, two platinum wire sensors R1 and R2 along with ultra stable resistors R3 and R4 measure the temperature difference ΔT. R1 and R2 are wound on the upper and lower (heat sink) end of the thermal resistance respectively. The bridge output is proportional to the temperature difference. This output is voltage amplified by the high gain amplifier. The amplifier output is filtered by a simple low pass R-C filter to reduce the noise (mostly contributed by the high gain amplifier) to an acceptable level. The filtered output is then fed to a zero crossing detector with small hysteresis. If ΔT is lower than the set value (set by R3, R4), output of this detector controls the up/down counter to count up and vice versa. The 16 bit counter output along with the 16 bit digital to analog converter and the unity gain power amplifier provides a DC voltage V_h that is controllable with very high resolution. Adding a count (count up) to the counter increases V_h to increase cone heater power and vice versa. At the time of every slow clock pulse a decision is made whether ΔT_L is lower or higher than the set point and a corrective action is taken by counting up or down by 1 bit - slowly tweaking V_h to regulate ΔT to its
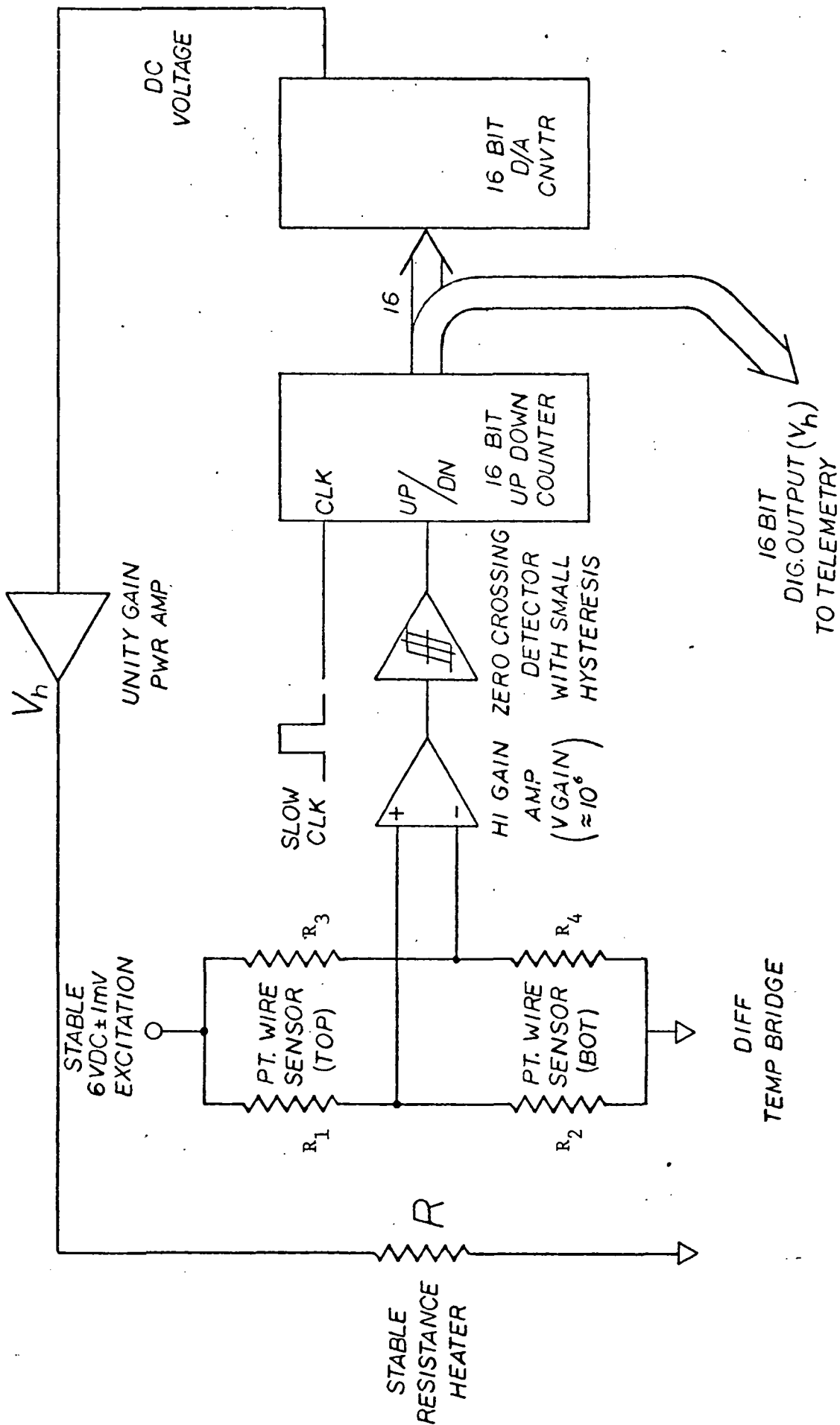
Figure 1.   ACR Difference Temperature Control Servo

proper value. The clock period is chosen to be long enough to allow temperature settling for each correction. This is done to avoid thermal oscillations in the servo which would easily set in because of very high loop gain. Note that R3, R4 and the op-amp will be placed in a temperature controlled environment to reduce their thermal drift errors. An auxiliary servo will keep these key components within $\pm$0.05°K over the measurement periods of 100 seconds regardless of ambient temperature variations.

2. Difference Temperature Control Requirements

Difference temperature setting (ΔT) $0.3°K \pm 0.1°K$

Variation in ΔT between sun and space looks $\leq 2 \times 10^{-4}°K$

Variation in ΔT over 100 second observation period $\leq 1 \times 10^{-4}°K$

3. Design and Error Details for the Difference Servo

Cone heater power P_h = 150 milliwatts

Desired accuracy in P_h = 150 microwatts

Thermal resistance of cavity support Pedestal = 500 milliwatts/°K

The difference temperature sensors are 100 turns each of 1 mil diameter platinum wire wound on the 2 cm diameter pedestal. Each sensor resistance is 1240Ω. The bridge will be excited by a stable 6 volt source - stable within $\pm$0.05%.
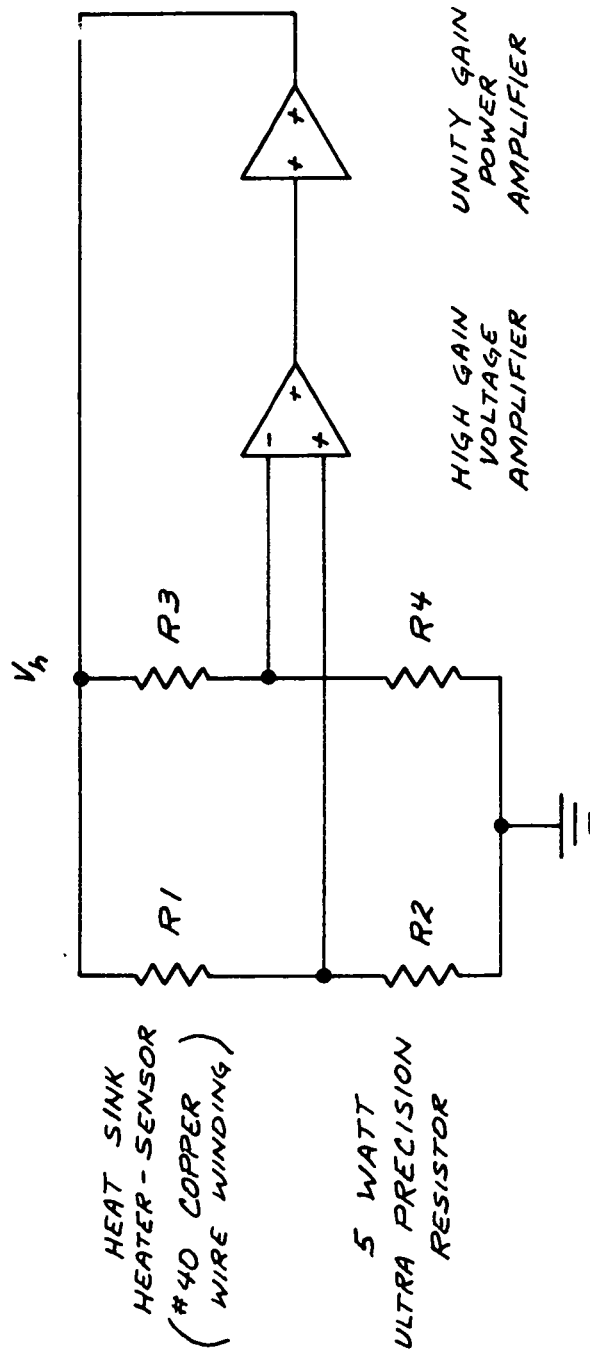
Using Vishay Technology's Ultra Precision resistors for R_3 and R_4 and a MONO OP-7 as the op-amp long term drift components can be summarized as follows:

Long term drift due to R3, R4	$1.39 \times 10^{-4}\,°K/month$
Long term drift due to op-amp	$2.22 \times 10^{-4}\,°K/month$
Long term drift – total – due to R3, R4 and op-amp	$3.61 \times 10^{-4}\,°K/month$
Note: The Platinum sensors may drift by 0.05°K over many years (3 years to 5 years)	$8 \times 10^{-4}\,°K$ to $1.3 \times 10^{-3}\,°K/month$
Total of above four terms	$1.522 \times 10^{-3}\,°K$ to $2.022 \times 10^{-3}\,°K/month$

4. The Heat Sink (Base) Servo

The heat sink servo maintains the heat sink or the base at a temperature higher than the highest expected ambient temperature during observations. Referring to Figure 2 the heat sink heater R1 is used as a sensor-heater. Along with resistors R2, R3 and R4 it forms a bridge whose output voltage imbalance is proportional to the temperature deviation from the set point value (300°K). The imbalance voltage is amplified by a high gain voltage amplifier and used to drive the bridge via a power amplifier. If the temperature falls below the set point, R1 decreases, making the + input of the voltage amplifier more positive. This increases the bridge voltage V_h; more current flows through R1 and R2; and R1 heats up. R1, having a positive temperature coefficient, increases to the point where the bridge is balanced at a new equilibrium point. Due to the high gain, the bridge is very closely maintained at null, and the heater winding is thus maintained at a precisely constant temperature.

Note that since the heater and the sensor are the same, heater-sensor time delay is extremely small; hence a large loop gain is possible without oscillations. R2, R3, R4 and the high gain voltage amplifier will be placed in temperature controlled environment to minimize their thermal drift errors. The same

HEAT SINK
HEATER-SENSOR
(#40 COPPER
WIRE WINDING)

5 WATT
ULTRA PRECISION
RESISTOR

V_h

R3

R4

R1

R2

HIGH GAIN
VOLTAGE
AMPLIFIER

UNITY GAIN
POWER
AMPLIFIER

R3, R4 ARE 1 WATT ULTRA PRECISION RESISTORS

ACR HEAT SINK TEMPERATURE CONTROL SERVO

Figure 2. Solar Constant ACR Heat Sink Temperature Control Servo

controlled environment used for the difference servo will be shared by these components. The environment is controlled to $\pm 0.05°K$ over a measurement period of 100 seconds regardless of the ambient temperature variations.

5. Heat Sink Temperature Control Requirements

Heat Sink temperature setting	$300°K \pm 0.1°K$
Heat sink temperature variation between sun and space looks	$10^{-3}°K$
Heat sink temperature instability during 100 second observation	$10^{-3}°K/100$ sec.
Heat sink temperature instability over a month	$10^{-2}°K/$month

6. Design and Error Details for the Heat Sink Servo

The heat sink heater is made up of no. 40 Copper wire having a temperature coefficient of 0.005/°C. The heater resistance is taken to be 50Ω and resistor R_2 to be 10Ω.

Bridge output sensitivity = $3.14 \text{ V}/10^{-3}°K$

R2, R3, R4 with 0.001% tolerance will allow sink temperature setting tolerance of $3 \times 0.001\% \times 300°K = 9 \times 10^{-3}°K$.

For a 6 volt $\pm 0.05\%$ excitation, power dissipated in each sensor will be constant within $\pm$ 36 microwatts. This is much smaller than the desired accuracy in P_h, i.e. 150 microwatts.

R3 and R4 will be Vishay Technology's Ultra Precision resistors having following specifications:

Resistance tolerance	0.01%
Temperature Coefficient of resistance - TCR	1 PPM/°C
Self Heating	2°C/0.1 watt
Maximum power dissipation	1 watt
Drift	5 PPM/year
Thermocouple effect error due to temperature gradient across the resistor	1 microvolt/°C
Bridge Output voltage sensitivity	4.5 microvolt/10^{-3}°K

The Op-amp will be a MONO-OP 7 having the following specifications:

Op-amp drift. Maximum (0.6 µV/°C)

Op-amp noise. 0.1 Hz to 10 Hz, (typical = 0.35 µV P-P)

Op-amp power supply drift coupling through power supply rejection ratio (PSRR = 100 DB) (power supply drift of 100 PPM/°C is assumed)

Op-amp Common mode error (CMRR) = 120 DB

Short term drift, noise error, and long term drift were calculated based on the above specifications. Results are summarized in the following table:

	BRIDGE OUTPUT ERROR VOLTAGE	EQUIVALENT ERROR IN HEAT SINK TEMPERATURE
Drift due to R3 and R4 (maintained at $\pm0.05°K$)	$0.0787\mu V$	$2.5 \times 10^{-5}°K$
Op-amp drift (max. $0.6\mu V/°C$)	$0.03\mu V$	$9.5 \times 10^{-6}°K$
Op-amp PSRR error	$0.06\mu V$	$1.9 \times 10^{-5}°K$
Op-amp CMRR error (for power change from 1 watt to 2 watts)	$0.322\mu V$	$1 \times 10^{-4}°K$
R2 thermal EMF error (Assumes gradient = 1/5 temperature rise)	$0.2\mu V$	$3.8 \times 10^{-5}°K$
R2 self heating error (for a 1 watt to 2 watt power change)		$1 \times 10^{-4}°K$
TOTAL drift during measurement cycle due to R2, R3, R4 and the op-amp		$2.915 \times 10^{-4}°K$
TOTAL noise error will be essentially that due to op-amp noise alone; allowing small increase due to noise in R1, R2, R3, R4 it will be about 0.4 V PP for a 0.1 Hz to 10 Hz bandwidth		$1.27 \times 10^{-4}°K$ P-P
Long term drift due to R2, R3, R4		$3.1 \times 10^{-4}°K/month$
Long term drift due to op-amp		$3.2 \times 10^{-4}°K/month$

NOTE: Long term drift of heater wire needs to be investigated. (Platinum wire heater would give better long term stability but will have 25% less temperature sensitivity and hence drift and noise errors will be 25% larger - which is tolerable).

APPENDIX C. ERROR ANALYSIS OF SOLAR CONSTANT RADIOMETER

The solar constant measurement uses an active cavity radiometer (See Section IV). This appendix investigates the accuracy obtainable from the specific ACR design illustrated in Figure 1. Some of the important design parameters are given in Table 1.

The ACR operating equation is derived and studied in Section 1. Using this equation, the solar constant measurement uncertainty is calculated in Section 2. The major sources of error are also summarized there.

1. ACR Operating Equation and Correction Terms

Assuming nearly steady state operation, the power balance equations for viewing the sun and space are as follows

Solar View:

Power in = Power out + Power stored.

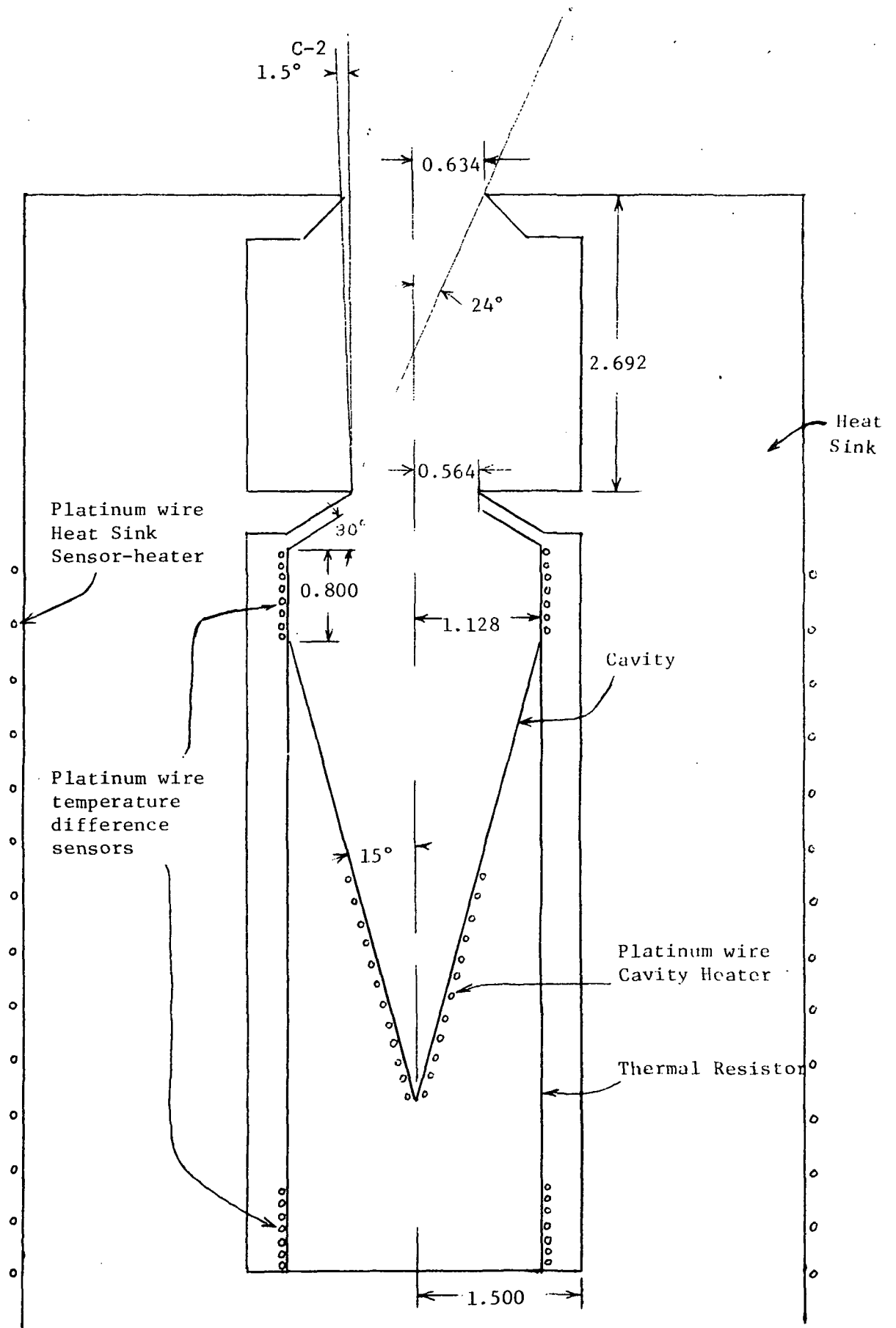$$A_c \, (\alpha_c + \rho\rho_c)H + P_e = (P_r^{out} - P_r^{in}) + P_{tr} + P_\ell + C\dot{T} \tag{1}$$

Figure 1. Specific ACR design configuration used in radiometer error analysis. Dimensions are in centimeters.

TABLE 1

Cavity aperture

    Area 1 cm^2

    Radius   .564 cm

View limiting aperture

    Area 1.265 cm^2

    Radius   .634 cm

    Limiting angle   24°

Cavity (silver)

    Area 24.6 cm^2

    Thickness   .0254 cm

    Heat capacity (neglecting resistance wires)   1.53 J/°K

Heat sink (Al)

    Volume 432 cm^3

    Mass   1.17 kg

    Heat Capacity   1044 J/°K

Thermal resistance

    Conductance   500 mW/°K

where

A_c − Cavity aperture area.

α_c − Absorptance

ρ_c − Reflectance of the cavity and cavity aperture.

ρ − Reflectance of upper heat sink cavity.

H   − Solar constant

Pe   − Electrical power input.

$P_r^{out} - P_r^{in}$ − Radiative power exchange between the cavity and the heat sink and apertures.

P_{tr} − Power conducted through the thermal resistance.

P_ℓ − Power conducted through the electrical leads.

$C\dot{T}$ − Power stored in the cavity to increase its temperature at a rate $\dot{T}$. C is the cavity heat capacity. This term represents a deviation from steady state operation.

Space View:

$$Pe' = (P_r^{out} - P_r^{in})' + P'_{tr} + P'_\ell + C\dot{T}' \qquad (2)$$

where the same notation has been used with primes indicating the space view.

The form and magnitude of the terms on the RHS of equations (1) and (2) are discussed in the next three subsections − the radiative exchange terms in 1.1, the conductive terms in 1.2 and the power stored term in 1.3.

The principle of operation of the ACR depends on using the solar view in conjunction with the space view. Subtracting equation (2) from equation (1) gives:

$$A_c (\alpha_c + \rho\rho_c)H + (Pe - Pe') = [(P_r^{out} - P_r^{in}) - (P_r^{out} - P_r^{in})'] + (P_{tr} - P'_{tr})$$
$$+ (P_\ell - P_\ell') + C(\dot{T} - \dot{T}') \qquad (3)$$

The terms on the RHS will be shown to be small in subsection 1.4. The uncertainty of solar constant measurements, the topic of Section 2, is based

on equation (3). However, the operating principle for the ACR is expressed by the equation:

$$H = \frac{Pe' - Pe}{A_c(\alpha_c + \rho\rho_c)} \tag{4}$$

The cavity absorptance α_c is assumed to be known. The error in α_c can be made small because the cavity design makes α_c almost unity, and also makes α_c insensitive to degradations of its surface coating.

1.1 Radiative Power Exchange ($(P_r^{out} - P_r^{in})$ in Equation (1))

The power exchange between the cavity aperture and the upper heat sink cavity and the exchange between the cavity exterior and the lower heat sink cavity will be considered separately.

1.1.1 Exchange with the Upper Heat Sink Cavity

If the view limiting aperture were shuttered, the power exchange ΔP_r^u would be the same as that between two infinite planes with effective emittances ε, ε_c and temperatures T, T_c, i.e.

$$\Delta P_r^u = \frac{\varepsilon \varepsilon_c}{\varepsilon + \varepsilon_c - \varepsilon\varepsilon_c} A_c \sigma (T_c^4 - T^4)$$

were A_c is the cavity aperture area. Since ε and ε_c are nearly equal,

$$\Delta P_r^u = \frac{\varepsilon}{2-\varepsilon} A_c \sigma (T_c^4 - T^4)$$

Now, since the view limiting aperture is not shuttered, the power received by the cavity is decreased by:

$$\varepsilon \frac{\Omega ap}{\pi} A_c \Omega T_c^4$$

where Ωap is approximately the solid angle of the view limiting aperture from the cavity aperture. Because the cavity emittance ε is nearly one, the power output of the cavity is essentially unchanged. Therefore, the

total power exchange can be approximated by:

$$\Delta P_r^u = \frac{\epsilon}{2-\epsilon} A_c \sigma (T_c^4 - T^4) + \epsilon \frac{\Omega ap}{\pi} A_c \sigma T_c^4 \qquad (5)$$

To estimate the size of ΔP_r^u let:

$$\epsilon = 1$$

$$A_c = 1 \text{ cm}^2$$

$$\Omega ap/\pi = (\frac{.634}{2.692})^2 = .055$$

$$T = 300°K$$

$$\Delta T = .35°K,$$

The result is: $\Delta P_r^u = .21 + 2.55$ mW.

1.1.2 Exchange with the Lower Heat Sink Cavity

Assume that the exchange ΔP_r^ℓ can be modeled by that for infinite concentric cylinders:

$$\Delta P = \frac{\epsilon_2 \epsilon_1}{\epsilon_2 + \epsilon_1 (A_1/A_2)(1-\epsilon_2)} A_1 \sigma (T_1^4 - T_2^4)$$

where subscript 1 (2) refers to the inner (outer) cyclinder, i.e.

$$\Delta P_r^\ell = \epsilon_{eff} A_{ce} \sigma (T_c^4 - T^4). \qquad (6)$$

where A_{ce} is the area of the cavity exterior and ϵ_{eff} is less than the emittance ϵ_{ce} of the cavity exterior.

Letting $\epsilon_{eff} = .3$

$$A_{ce} = 24.6$$

$$T = 300°K$$

$$\Delta T = .3°,$$

we get: $\Delta P_r^\ell = 1.36$ mW.

1.2 Conductive Power Losses ($P_{tr} + P_\ell$ in equation (1)):

Most of the power input to the cavity flows directly to the heat

sink through the thermal resistance. The power flow is given by:

$$P_{tr} = K_{tr} (T_c - T) \tag{7}$$

where K_{tr} is the conductance and $T_c - T$ is the temperature drop from the cavity to the heat sink. P_{tr} is about 150 mW ($\Delta T = .3°K$, $K_{tr} = 500$ mW/°K).

There is a small conductive loss to the platinum heating and sensing wires, which can be written as:

$$P_\ell = K_\ell (T_c - T_{cb}) \tag{8}$$

where K is the lead conductance and T_{cb} is the circuit board temperature. For

$$K_\ell = .1 \text{ mW/°K}$$
$$T_c - T_{cb} = 1°K,$$
$$P_\ell = .1 \text{ mW.}$$

1.3 Power Stored in the Detector Cavity ($C\dot{T}$ in Equation 1):

The cavity deviates from steady state operation when small changes in its temperature occur. Although the net temperature change during a measurement can be made very small, this term is significant because it is uncompensated. That is, the temperature change occurring while viewing the sun is not correlated to that occurring while viewing space.

$$P = C\dot{T} \tag{9}$$

where C is the cavity heat capacity. With heat sink control accurate to $10^{-3}°K$, the rate of change of temperature for a measurement time of 100 sec is less than $10^{-5}°K/sec$. Then

$$P = (1.53 \times 10^3) (10^{-5}) = .015 \text{ mW.}$$

1.4 Corrections to the Basic Operating Equations

Using the results of subsections 1.1-1.3, the solar view – space view difference terms of Equation (3) can be evaluated. We assume that the

TABLE II - CORRECTIONS

Radiative Exchange:

Upper heat sink cavity	+.0061 mW
Lower heat sink cavity	+.0005 mW

Conduction:

Thermal Resistance	+.13 mW
Electrical Leads (circuit board temperature variation assumed .1°K)	+.01 mW

Temperature Variations $C(\dot{T}-\dot{T}')$ +.03 mW

temperatures of the upper heat sink cavity, the lower heat sink cavity, and the detector cavity are uniform. Therefore, define:

T_u = Upper heat sink cavity temperature

T_L = Lower heat sink cavity temperature

T_c = Detector cavity temperature.

The temperature differences which will appear are:

$$\Delta T_u \equiv T_c - T_u = .35°K$$

$$\Delta T_L \equiv T_c - T_L = .3°K$$

$$\delta T_c \equiv T_c - T_c{}' = \pm 10^{-3}°K$$

$$\delta T_L \equiv T_L - T_L{}' = \pm 10^{-3}°K$$

$$\delta T_u \equiv T_u - T_u{}' = +10^{-2}°K$$

$$\delta(\Delta T_L) \equiv \Delta T_L - \Delta T_L{}' = 2.5 \times 10^{-4}°K$$

$$\delta(\Delta T_u) \equiv \Delta T_u - \Delta T_u{}' = -10^{-2}°K$$

The cavity heat sink temperature difference ΔT_L is determined by the size of the thermal resistance. The reproducibility of ΔT_L is represented by $\delta(\Delta T_L)$ and is controlled by the cavity heater-sensor servo. Likewise, the reproducibility of the heat sink temperature (δT_L) is controlled by the sink servo. The temperature differences for the upper cavity are assumed to be somewhat different from those for the lower cavity because of the different power exchanges experienced by the two.

Table II gives the corrections obtained using the above temperature differences and Equation (5)-(9). It is interesting that the errors caused by radiative exchange are essentially negligible. The only term which requires correction is that due to conduction through the thermal resistance. This term arises because the cavity servo allows a larger sink-cavity temperature difference during the solar view than during the space view (larger by $\delta(\Delta T_L)$).

2. Solar Constant Measurement Uncertainties

The expression for the solar constant from Equation (3) is:

$$H = [A_c (\alpha_c + \rho\rho_2)]^{-1} \{(Ve'^2 - Ve^2)/R + [(P_r{}^{out} - P_r{}^{in})' + (P_{tr} - P'_{tr})$$

$$+ (P_\ell - P'_\ell) + C(\dot{T} - \dot{T}')\}$$

where we have used $Pe = Ve^2/R$ with Ve = voltage across the cavity heater resistance R. The standard deviation of H is:

$$\sigma(H) = [\Sigma_i (\frac{\partial H}{\partial \xi})^2 \sigma^2 (\xi_i)]^{1/2}$$

where ξ_i are independent parameters with standard deviations $\sigma(\xi_i)$. Table III gives the parameters ξ_i and their assumed uncertainties. For those parameters making a significant contribution to $\sigma(H)$, $\left|\frac{\partial H}{\partial \xi_i}\right|$ and $\left|\frac{\partial H}{\partial \xi_i}\right| \sigma (\xi_i)$ are shown in Table IV.

The resulting value for the solar constant uncertainty is:

$\sigma(H) = .17$ mW/cm^2 which corresponds to a per cent uncertainty of .13%.

TABLE III: PARAMETER VALUES AND UNCERTAINTIES

α_c	$.999 \pm .001$
A_c	$1.000 \pm .0005 \ \text{cm}^2$
ρ_c	$.010 \pm .005$
ρ	$.02 \pm .02$
R	$1000.0 \pm .1\Omega$
V_e'	$12,500. \pm 2 \ \text{mV}$
V_e	$819. \pm 2 \ \text{mV}$
$\varepsilon_c = \varepsilon$	$.95 \pm .05$
ε_{eff}	$.2 \pm .2$
A_{ce}	$24.6 \pm .5 \ \text{cm}^2$
$\Omega ap/\pi$	$.06 \pm .01$
K_{tr}	$500 \pm 100 \ \text{mW/}^\circ\text{K}$
K_ℓ	$.10 \pm .03 \ \text{mW/}^\circ\text{K}$
C	$1.5 \pm .3 \times 10^{+3} \ \text{mW-sec/}^\circ\text{K}$
T_c	$300 \pm .1^\circ\text{K}$
$\dot{T}, \ddot{T}$ (100 sec. measurement time)	$0. \pm 10^{-5} \ ^\circ\text{K/sec}$
$\Delta T_L \equiv (T_c - T_L) = \Delta T_u \equiv (T_c - T_u)$	$.3 \pm .1^\circ\text{K}$
$\delta T_c \equiv (T_c - T_c') = \delta T_L \equiv (T_L - T_i)$	$.3 \times 10^{-3} \pm 10^{-3} {}^\circ\text{K}$
$\delta T_u \equiv (T_u - T_u') = -\delta(\Delta T_u) = -(\Delta T_u - \Delta T_u')$	$.01 \pm .01^\circ\text{K}$
$\delta(\Delta T_L) \equiv (\Delta T_L - \Delta T_L')$	$2.5 \times 10^{-4} \pm 10^{-4} {}^\circ\text{K}$
$\delta T_{cb} \equiv T_{cb} - T_{cb}'$	$0. \pm .1^\circ\text{K}$
H	$\sim 137 \ \text{mW/cm}^2$

TABLE IV

ξ_i	$\left\|\dfrac{\partial H}{\partial \xi_i}\right\|$	$\left\|\dfrac{\partial H}{\partial \xi_i}\right\| \sigma(\xi_i) \quad (mW/cm^2)$
α_c	$\dfrac{H}{(\alpha_c + \rho\rho_c)} = 137 \ mW/cm^2$	.137
A_c	$\dfrac{H}{A_c} = 137 \ mW/cm^4$	.069
ρ_c	$\left(\dfrac{\rho}{\alpha_c + \rho\rho_c}\right)H = 2.74 \ mW/cm^2$	.014
ρ	$\left(\dfrac{\rho_c}{\alpha_c + \rho\rho_c}\right)H = 1.37 \ mW/cm^2$	.027
R	$\dfrac{H}{R} = .137 \ mW/\Omega\text{-}cm^2$	.014
Ve'	$\dfrac{2\,Ve'}{A_c \alpha_c R} = .025 \ mW/mV\text{-}cm^2$	.050
Ve	$\dfrac{2\,Ve}{A_c \alpha_c R} = .0016 \ mW/mV\text{-}cm^2$	.003
K_{tr}	$\delta(\Delta T_L)/A_c(\alpha + \rho\rho_c) = 2.5 \times 10^{-4} \,°K/cm^2$	.025
$\delta(\Delta T_L)$	$K_{tr}/A_c(\alpha_c + \rho\rho_c) = 500 \ mW/°K\text{-}cm^2$	.050
$\delta(T_{cb})$	$K_\ell/A_c(\alpha_c + \rho\rho_c) = .1 \ mW/°K\text{-}cm^2$	.010
$\dot{T}$	$C/A_c(\alpha_c + \rho\rho_c) = 1.5 \times 10^3 \ mW\text{-}sec/°K\text{-}cm^2$	.015
$\dot{T}'$	$C/A_c(\alpha_c + \rho\rho_c) = 1.5 \times 10^3 \ mW\text{-}sec/°K\text{-}cm^2$	.015
$\delta(\Delta T_u)$	$\dfrac{-4\left(\dfrac{\varepsilon}{2-\varepsilon}\right)\sigma T_c^{\,3}}{(\alpha_c + \rho\rho_c)} = .61 \ mW/°K\text{-}cm^2$	.006

APPENDIX D.   EFFECT OF WINDOW ON SW SENSOR ANGULAR RESPONSE

The short wave sensor requires a window to achieve the required spectral separation. A window can affect the angular response of the sensor in two ways:

1. The reflectivity of the window varies with the angle of incidence with respect to the window surface.

2. The window has an imaging effect on the transmitted radiation which can vary with the angle of incidence.

The angular response for a flat window is not impaired by imaging effects. However, the variation of the transmission for angles of incidence from 0° to 65° can be as large as 30% and for large angles depends heavily on the polarization of the incident flux. To minimize the effect of the window reflectivity variations, a spherical window was chosen. For a spherical window with radius large compared to the detector size, radiation striking the detector is always incident nearly normal to the window surface. The imaging effects of a spherical window were studied with a ray tracing technique. It was assumed that the problem could be modelled by the two dimensional problem for which the detector is linear with a length 2ℓ as illustrated in Figure 1. The response of the detector to radiation with incident angle θ measured in a plane containing the detector is determined by the size, $w^- + w^+$, of the incident beam which strikes the detector. The normalized sensor angular response can be written in terms of w^+ and w^- as:

$$R(\theta) \equiv \cos\theta(1-E(\theta))$$

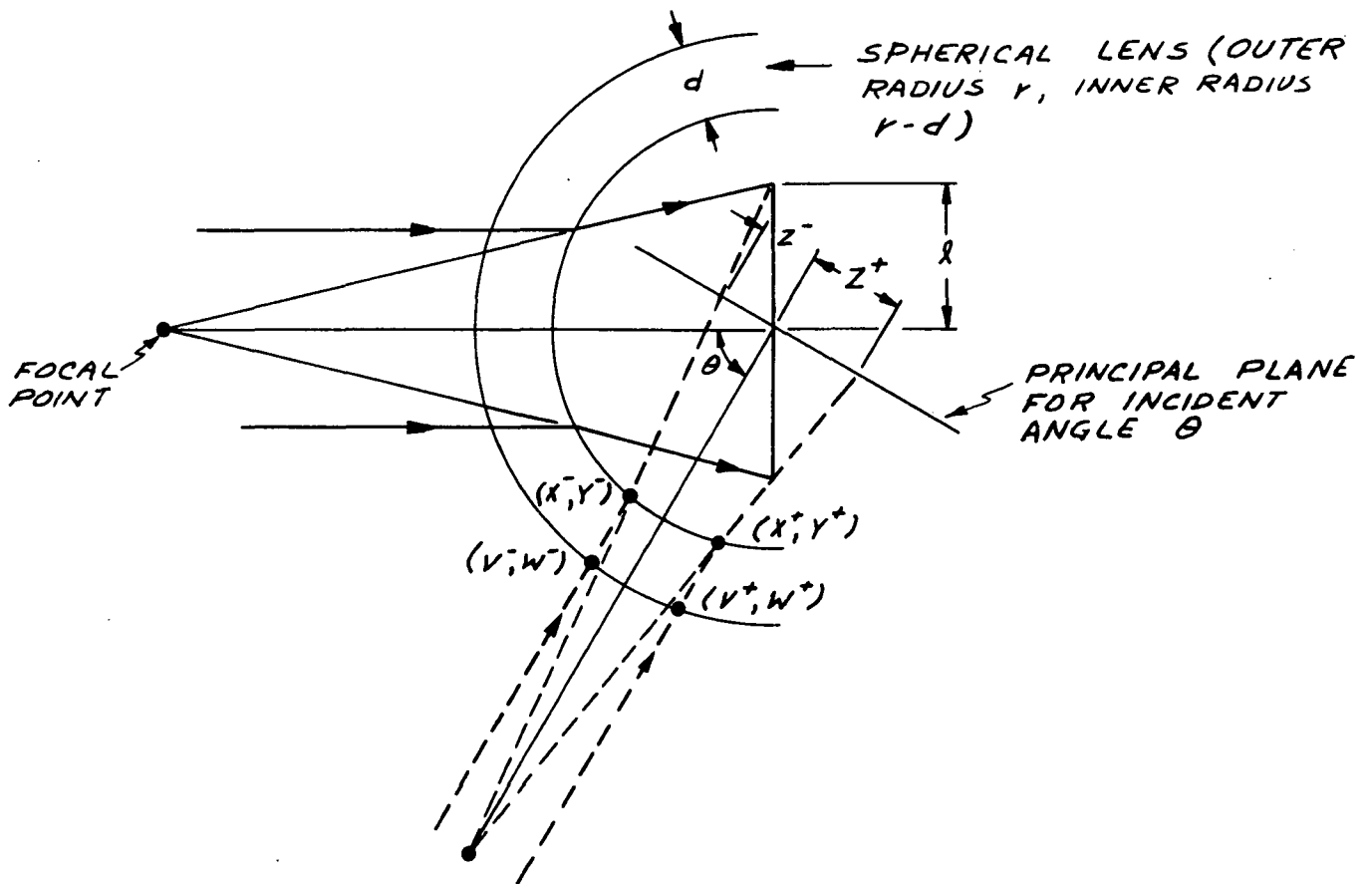$$= \frac{w^+(\theta) + w^-(\theta)}{w^+(0) + w^-(0)} \tag{1}$$

Figure 1. Geometry of the 2 dimensional model for determining the imaging effects of a spherical window on the detector angular response.

where Θ is the angle of incidence and $E(\Theta)$ is a measure of the deviation of the response from the $\cos\Theta$ dependence of an ideal flat plate detector. The procedure used to find w^+ and w^- will be described next and is followed by the result for $E(\Theta)$.

First, the portion of the inside of the window irradiated by flux which strikes the detector is calculated. The area of the irradiated portion is less than that which would be irradiated at the same location if no window were present because the window is a diverging lens. Its focal point lies in front of the window and the focal length (measured from the center of curvature) is given by the equation,

$$f = \frac{r(r-d)}{d} \frac{n}{(n-1)} \tag{2}$$

where r is the window outer radius, d is the window thickness and n is the index of refraction. Since the detector was centered at the center of curvature, for normal incidence it lies in the principle plane of the window. For other than normal incidence, a portion of the principle plane smaller than the detector is irradiated. This portion is denoted by $z^+ + z^-$ (See Figure 1) where z^+ and z^- are given by,

$$z^{\pm} = \ell\cos\Theta \left[1 \begin{array}{c} + \\ - \end{array} \frac{\ell\sin\Theta/f}{1 \begin{array}{c} - \\ + \end{array} \ell\sin\Theta/f}\right]. \tag{3}$$

By projecting the extreme rays striking the detector back to the focal point from z^+ and z^- the intersections $(x^{\pm}, y^{\pm})$ with the inner surface of the window can be determined. The results for $x^{\pm}$ and $y^{\pm}$ are,

$$x = \frac{\frac{z^2}{f} + \left[(r-d)^2 \left(1 + \left(\frac{z}{f}\right)^2\right) - z^2\right]^{1/2}}{\left[1 + \left(\frac{z}{f}\right)^2\right]} \tag{4}$$

$$y = z\,(1-x/f) \tag{5}$$

where the $\pm$ superscripts have been dropped.

Now, from the geometry illustrated in Figure 2, $w^{\pm}$ which give the angular response can be calculated using the following relationships:

$$i = \phi + \tan^{-1}(z/f) \tag{6}$$

$$\phi = \sin^{-1}\left(\frac{y}{r-d}\right) \tag{7}$$

$$\frac{\sin t}{\sin i} = \frac{1}{n} \quad (\text{Snell's Law}) \tag{8}$$

$$[(v-x)^2 + (w-y)^2] = [r^2 + (r-d)^2(1-2\sin^2 t)]$$
$$- \{[r^2 + (r-d)^2(1-2\sin^2 t)]^2 - [r^2-(r-d)^2]^2\}^{1/2} \tag{9}$$

$$w = y + [(v-x)^2 + (w-y)^2]^{1/2} \sin(\phi-t) \tag{10}$$

The result for $E(\Theta)$ defined in Equation (1) which is valid when $d/r \ll 1$ and $1/(r-d) \ll 1$ is,

$$E(\Theta) = \frac{(n^2-1)}{2n^3} \frac{d\ell^2}{r^3} \sin\Theta.$$

It is evident that, as expected, the deviation from a purely cosine angular response can be made small by making the window thin and much larger than the detector. This relationship is evaluated in Section V for values appropriate to this application.
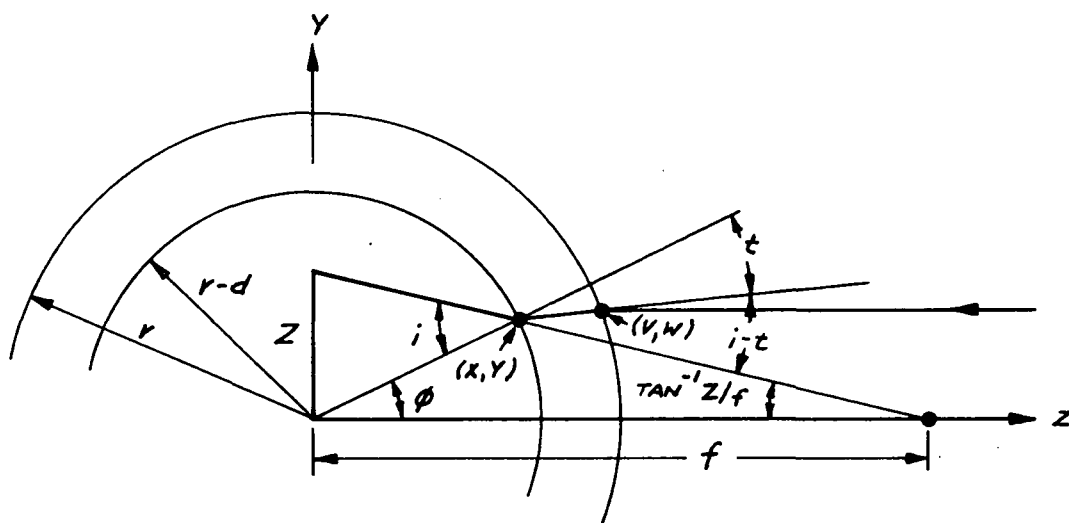
Figure 2. Geometry and definition of symbols used to find the width of the incident beam which strikes the detector.

APPENDIX E. RADIATIVE EFFECTS OF SW SENSOR WINDOWS

1. Introduction

The shortwave (SW) sensor window transmits radiation in the band from $0.2\mu m$ to $4\mu m$ and absorbs and emits radiation outside this band. Since the detector is sensitive to radiation emitted by the window, it is necessary to estimate the variability of this emission as the sensor is exposed to different long wave fluxes from the earth, sun, and space. Although hemispherical windows are used in the sensors, flat windows will be used in the thermal analysis for the sake of simplicity. Because of this simplification the results of the analysis will be approximate rather than exact. Nevertheless, they will be useful in identifying significant parameters affecting window emission variability.
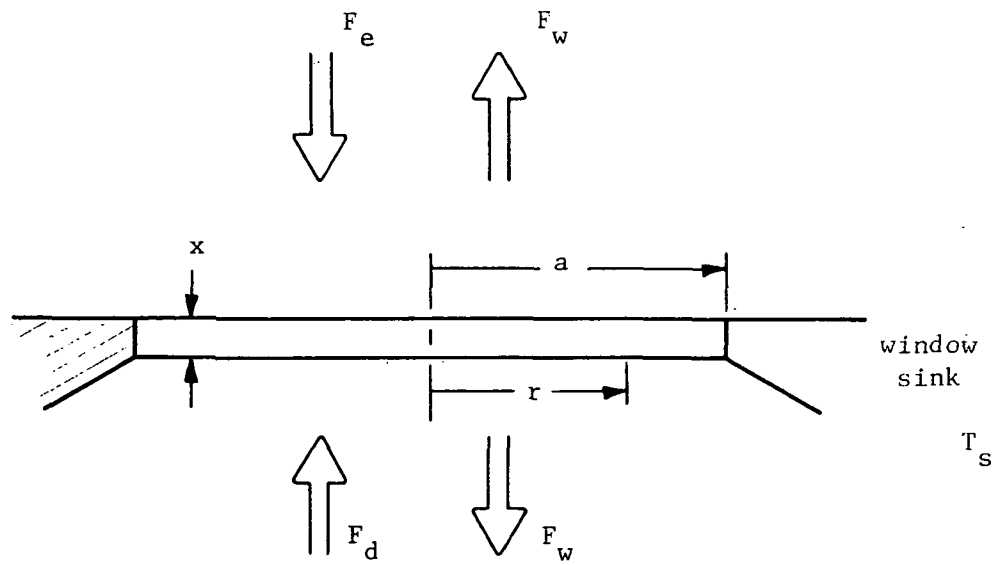
2. Thermal Model of SW Windows

Figure 1 displays the SW window configuration and the thermal model used in the following analysis. In this model we use the following notation:

x = window thickness

a = window radius

r = radial distance from the center of the window

T_s = window sink temperature

F_e = average external flux incident on the window

F_d = average flux incident on the window from the detector and detector sink

F_w = average flux emitted by the window (either outward or toward the detector)
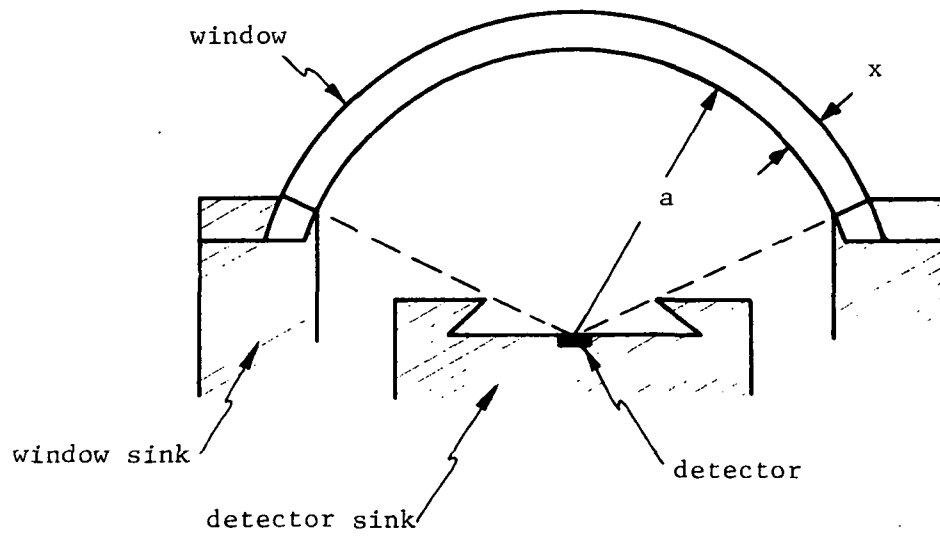
(a) ACTUAL WINDOW CONFIGURATION

(b) WINDOW THERMAL MODEL

FIGURE 1.   Short wavelength sensor window configuration (a)
and approximate thermal model (b).

It will be assumed that all fluxes are uniform over the window surface in order to calculate the radial distribution of window temperature. Given this distribution it is possible to calculate perturbed values of F_w which are accurate only if the perturbation is small compared to F_w. The validity of this approach is obvious from the results obtained.

3. Equilibrium Analysis

The heat flow equation for a disc with uniform lateral power input is given by

$$\frac{\partial^2 T}{\partial r^2} + \frac{1}{r} \frac{\partial T}{\partial r} - \frac{C\rho}{k} \frac{\partial T}{\partial t} = - \frac{F_N}{kx} \tag{1}$$

where

T = $T(r)$ = disc temperature at r

k = thermal conductivity of the disc material

C = specific heat of the disc

ρ = density of the disc

F_N = net power flux per unit area into the disc.

This equation assumes that the temperature gradient through the thickness of the disc is small compared to the radial gradients.

The solution at equilibrium ($\partial T(r)/\partial t = 0$) is given by

$$T(r) = T_s + \frac{F_N a^2}{4kx} (1 - r^2/a^2) \tag{2}$$

where F_N is given by

$$F_N = F_e + F_d - 2 F_w. \tag{3}$$

If we choose the parameter values

x = 0.1 cm

a = 1.0 cm

k = 0.0138 W/cm°C (fused quartz)

then

$$\frac{a^2}{4kx} = 0.0181°K/(W/M^2). \tag{4}$$

If we assume that the detector and window sinks are at the same temperature then $F_d \approx F_w$. If we further assume that the flux incident from the earth is approximately given by F_w ($\approx$ 300 W/M^2), for space and earth views we have the following values of F_e and F_N:

	F_e	F_N
space view	0	-300 W/M^2
earth view	300 W/M^2	0

For this example the disc is isothermal at T_s when it's at equilibrium. The steady state temperature during the space view is given by

$$T(r) = T_s - 5.43°C \ (1 - r^2/a^2). \tag{5}$$

This is illustrated in Figure 2. The worst case value T(r=0) will be used to calculate the perturbed value $\tilde{F}_w$, i.e.

$$\tilde{F}_w \approx F_w (\frac{270-5.4}{270})^4 = 0.922 \ F_w. \tag{6}$$

Thus, for the assumed conditions the flux emitted by the window drops almost 8% between earth views and space views. This is equivalent to a 20 W/M^2 change in background flux reaching the detector and would amount to a significant error if these equilibrium values were actually reached.

4. Time Dependent Analysis

The time dependence of the net flux input to the window can be approximated by a cosine function

$$F_N(t) = F_o \cos \omega t \tag{7}$$

where $2F_o$ is the net flux difference between earth and space views and ω is the angular frequency of satellite rotation. It is more convenient

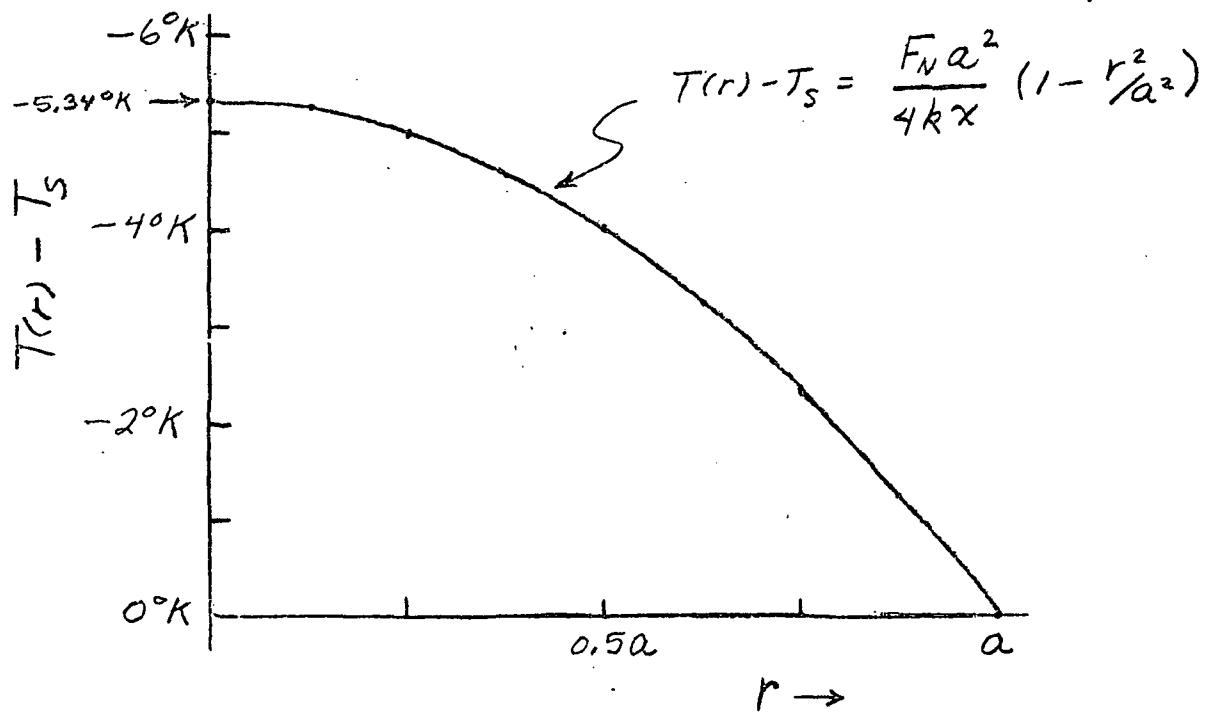$$T(r) - T_s = \frac{F_N a^2}{4 k \chi} \left(1 - r^2/a^2\right)$$

Figure 2. Equilibrium window temperature distribution during the space view.

in the solution of (1) to rewrite (7) in the form

$$F_N(t) = \frac{1}{2} F_o e^{i\omega t} + \frac{1}{2} F_o e^{-i\omega t} \tag{8}$$

and to solve (1) for each term. Substitution of the trial solution

$$T = T_o + R^{\pm}(r) e^{\pm i\omega t} \tag{9}$$

into equation (1) yields the R equation

$$\frac{\partial^2}{\partial r^2} R^{\pm} + \frac{1}{r} \frac{R}{r} \mp i\omega\alpha R^{\pm} = E \tag{10}$$

where we have used the notation

$$\alpha = C\rho/k, \quad E = \frac{F_o}{2kx} . \tag{11}$$

If we substitute

$$Z = (\mp i\omega\alpha)^{1/2} r \tag{12}$$

and multiply (10) by r^2 we obtain an inhomogenous form of Bessel's

equation

$$Z^2 \frac{\partial^2}{\partial Z^2} R^{\pm} + Z \frac{\partial}{\partial Z} R^{\pm} + Z^2 R^{\pm} = \frac{E}{\mp i\omega\alpha} Z^2 \tag{13}$$

which has the solution

$$R(r)^{\pm} = \frac{E}{\mp i\omega\alpha} + A J_o(r(\mp i\omega\alpha)^{1/2}) . \tag{14}$$

Since there can be no time dependence at $r = a$ ($T = T_s$), A must have

the value

$$A = \frac{E}{\pm i\omega\alpha J_o(a(\mp i\omega\alpha)^{1/2})} . \tag{15}$$

Thus the final pair of R solutions is

$$R(r)^{\pm} = \frac{E}{\mp i\omega\alpha} [1 - \frac{J_o(r(\mp i\omega\alpha)^{1/2})}{J_o(a(\mp i\omega\alpha)^{1/2})}] . \tag{16}$$

The values at r = o, the point of maximum temperature deviation, are given by

$$R(o)^{\pm} = \frac{E}{\mp i \omega \alpha} \, [1 - 1/J_o(a(\mp i \omega \alpha)^{1/2})].$$ (17)

In order to evaluate the Bessel function it is useful to write

$$J_o(a(-i\omega\alpha)^{1/2}) = J_o(a\sqrt{\omega\alpha} \; e^{3\pi i/4})$$ (18)

$$J_o(a(+i\omega\alpha)^{1/2}) = J_o(a\sqrt{\omega\alpha} \; \overline{e}^{3\pi i/4})$$ (19)

from which we can obtain expressions in terms of the real functions ber$_o$ and bei$_o$, i.e.

$$J_o(a\sqrt{\omega\alpha} \; e^{3\pi i/4}) = ber_o(a\sqrt{\omega\alpha}) + i \; bei_o(a\sqrt{\omega\alpha}),$$ (20)

$$J_o(a\sqrt{\omega\alpha} \; e^{3\pi i/4}) = ber_o(a\sqrt{\omega\alpha}) - i \; bei_o(a\sqrt{\omega\alpha}).$$ (21)

Defining

$$x = ber_o(a\sqrt{\omega\alpha})$$ (22)

$$y = bei_o(a\sqrt{\omega\alpha})$$ (23)

the time dependent solution r = o can be written as

$$T(o,t) = T_o + \frac{E}{\omega\alpha} \left[\frac{e^{i\omega t}}{-i} + \frac{e^{-i\omega t}}{+i}\right] - \frac{E}{\omega\alpha} \left[\frac{e^{i\omega t}}{-i(x+iy)} + \frac{e^{-i\omega t}}{+i(x-iy)}\right]$$ (24)

which can be reduced to

$$T(o,t) = T_o + \frac{2E}{\omega\alpha}\sqrt{2} \; (1 - \frac{x}{x^2 + y^2})^{1/2} \cos(\omega t + \phi)$$ (25)

where

$$\phi = \tan^{-1} \left(\frac{x-(x^2 + y^2)}{y}\right).$$ (26)

For very low frequencies, i.e. for $a\sqrt{\omega\alpha} \ll 1$ we find that

$$x \approx 1 - 64 \; (\frac{a\sqrt{\omega\alpha}}{8})^4 + \ldots$$ (27)

$$y \approx 16 \ (\frac{a\sqrt{\omega\alpha}}{8})^2 + \ .... \qquad . \tag{28}$$

Thus as $\omega \to o$

$$(1 - \frac{x}{x^2+y})^{1/2} \to \frac{\sqrt{2}}{8} \ a^2\omega\alpha \tag{29}$$

$$\frac{x - (x^2+y^2)}{y} \to o. \tag{30}$$

Inserting these limiting forms into (26) and (27) yields the low

frequency expression

$$T(o,t) = T_o + \frac{Ea^2}{4} \cos \omega t, \ \omega \to o. \tag{31}$$

Comparison of (31) with (2) shows that, as expected, for very low

frequencies the temperature variations are equal to the equilibrium

values and no phase shift is present.

However, for the expected operating conditions

$\omega = 0.628 \ \text{sec}^{-1}$ (6 RPM)

$C = .753 \ \text{W-sec/gm.°C}$

$\rho = 2.203 \ \text{gm/cm}^3$

$k = 0.0138 \ \text{W/cm.°C}$

$a = 1 \ \text{cm}$

we find that

$a\sqrt{\omega\alpha} = a\sqrt{\omega C\rho/k} = 8.689$

$x = 39.44$

$y = -50.05.$

In this case

$$(1 - \frac{x}{x^2+y^2})^{1/2} = .995 \approx 1.0 \tag{32}$$

$$\phi = .496\pi \approx \frac{\pi}{2} \tag{33}$$

and we can write (25) to good approximation as

$$T(0,t) = T_o + \frac{\sqrt{2}\ F_o}{\omega C\ \rho x} \cos\ (\omega t\ +\ \pi/2). \tag{34}$$

For F_o = 150 W/M^2 and x = 0.1 cm (3) becomes

$$T(0,t) = T_o + 0.204°K \cos\ (\omega t\ +\ \pi/2). \tag{35}$$

If we assume that (35) applies to the average window temperature, a worst case assumption, then the background flux variation induced is given by

$$F_B(t) = \frac{4\sqrt{2}\ F_o}{\omega C\rho x}\ \sigma T_s^3 \cos\ (\omega t\ +\ \pi/2) \tag{36}$$

which, for T_s = 273°K, takes on the specific form

$$F_B(t) = 0.941\ W/M^2 \cos\ (\omega t\ +\ \pi/2). \tag{37}$$

This represents a peak to peak variation of 0.2% of the solar flux and 0.6% of the average outgoing shortwave flux from the earth. However, in actual operation these errors will have very small effects because of the $\pi/2$ phase shift between window absorption and window temperature. Since data samples will be taken near points of maximum and minimum incident long wave flux inputs (i.e. at earth nadir and anti nadir), the window temperature deviation will be near minimum. This is illustrated in Figure 3 for a cosine variation of input flux.

5. Conclusions

As a result of varying long wave flux inputs to the SW window its temperature varies sufficiently to produce variations in background flux levels incident on the detector. Significant features of this variation are as follows:
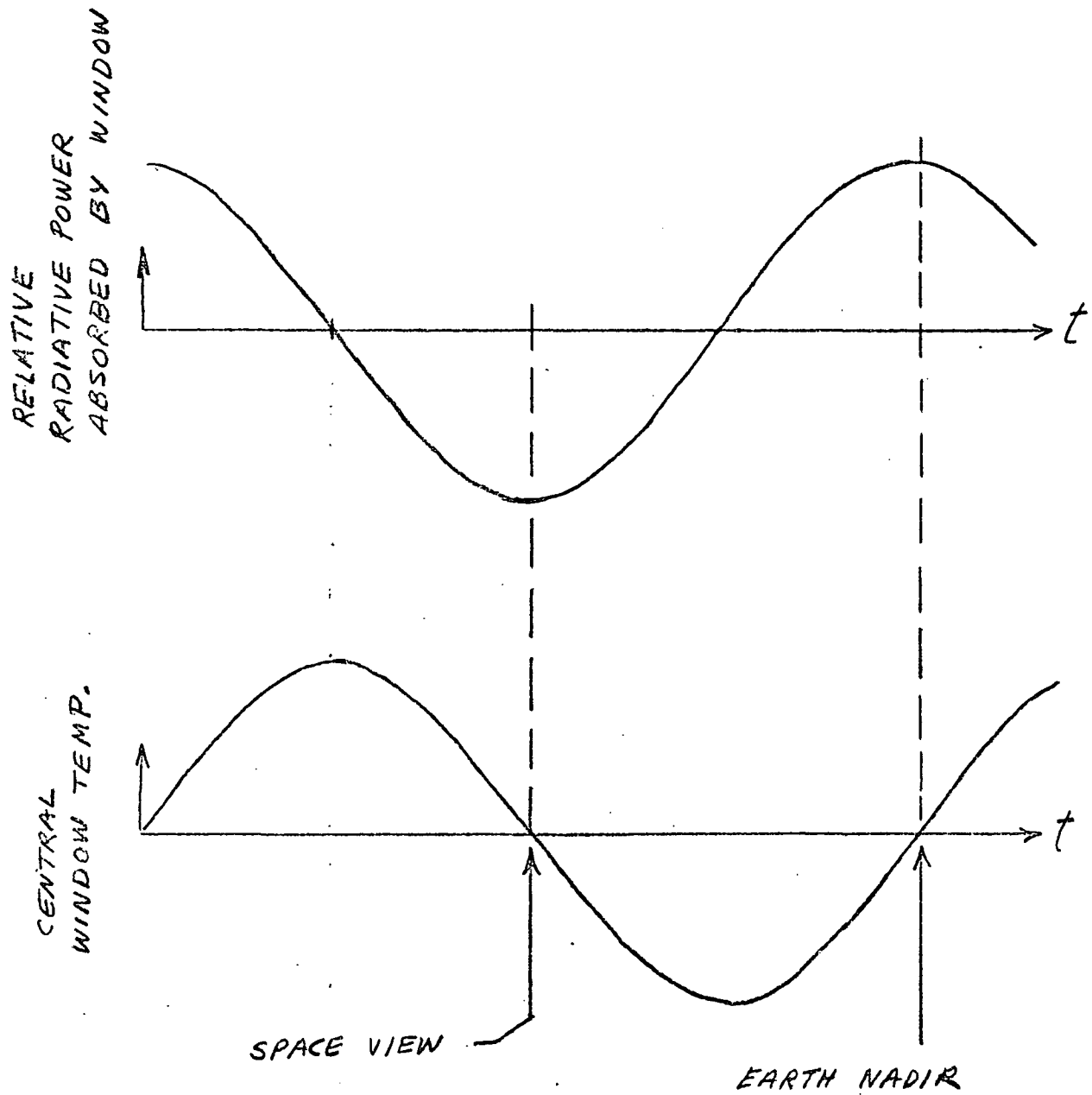
Figure 3. Relationship between window radiative heating and window
temperature variation. Note the $\pi/2$ phase shift.

(1) the magnitude is independent of the window diameter.

(2) the magnitude is inversely related to window thickness
     and rotational frequency.

(3) for probable design parameters there is a phase shift
     nearly equal to $\pi/2$ between incident long wave flux
     variations and background flux variations.

(4) for probable design parameters background flux
     deviations should be negligible.

APPENDIX F. FLUX ERRORS PRODUCED BY EMISSIVITY VARIATIONS WITH WAVELENGTH

1. Basic Equations

If a sensor with emissivity $\varepsilon(\nu)$ at wavenumber ν is calibrated at temperature T_c, then the signal output in flux equivalent terms is given by

$$F_{meas} = \frac{\int_0^\infty \varepsilon(\nu)F(\nu)d\nu}{\int_0^\infty \varepsilon(\nu)B(\nu,T_c)d\nu} \sigma T_c^4 \tag{1}$$

where

$F(\nu)$ = Spectral incident flux

$B(\nu,T_c)$ = Spectral flux produced by a blackbody at temperature T_c

σT_c^4 = Total flux produced by a blackbody at temperature T_c.

The ratio between the measured flux F_{meas} and the exact total flux

$$F = \int_0^\infty F(\nu)d\nu \tag{2}$$

is given by

$$\frac{F_{meas}}{F} = \frac{\bar{\varepsilon}_F}{\bar{\varepsilon}_c} \tag{3}$$

where

$$\bar{\varepsilon}_c = [\int_0^\infty \varepsilon(\nu)B(\nu, T_c)d\nu]/\sigma T_c^4 \tag{4}$$

$$\bar{\varepsilon}_F = [\int_0^\infty \varepsilon(\nu)F(\nu)d\nu]/[\int_0^\infty F(\nu)d\nu]. \tag{5}$$

If $F(\nu)$ has the same spectral dependence as $B(\nu,T_c)$, or if $\varepsilon(\nu)$ is independent

of wavelength then $\bar{\varepsilon}_F = \bar{\varepsilon}_c$ and the measured flux is the same as the true flux. However, since neither of these conditions are precisely net, the ratio expressed by equation (3) will differ from unity.

2. Estimation of Errors

Given a description of the surface emittance properties $\varepsilon(\nu)$ the flux error produced by this variation can be estimated by calculating $\bar{\varepsilon}_{F_k}$ for each k, of a set of n spectral flux distributions $F_k(\nu)$ which represent typical cases for the earth.

The fractional error in the kth case is

$$\delta_k = \frac{F_k - F_{meas,k}}{F_k} = 1 - \frac{\bar{\varepsilon}_{F_k}}{\bar{\varepsilon}_c} \tag{6}$$

The bias error produced by the specific surface for the n cases is just

$$\bar{\delta} = \frac{1}{n} \sum_{k=1}^{n} \delta_k = 1 - \frac{1}{\bar{\varepsilon}_c} [\frac{1}{n} \sum_{k=1}^{n} \bar{\varepsilon}_{F_k}]. \tag{7}$$

The standard deviation about the mean is given by

$$\sigma = [\frac{1}{n} \sum_{k=1}^{n} (\delta_k - \bar{\delta})^2]^{1/2} . \tag{8}$$

Substituting (6) and (7) into (8) also yields the form

$$\sigma = [\frac{1}{n\bar{\varepsilon}_c^2} \sum_{k=1}^{n} [\frac{1}{n} \sum_{j=1}^{n} \bar{\varepsilon}_j - \bar{\varepsilon}_k]^2]^{1/2} \tag{9}$$

which can also be written as

$$\sigma = \frac{1}{\bar{\varepsilon}_c} [\frac{1}{n} \sum_{k=1}^{n} \bar{\varepsilon}_k^2 - [\frac{1}{n} \sum_{k=1}^{n} \bar{\varepsilon}_k]^2]^{1/2} . \tag{10}$$

3. Test Conditions

Three surface emissivity distributions were included in this study these are listed and described below:

(a)   Parson's Black Lacquer (ε_ν at 180°C); data from Sydnor (1970)

(b)   3M Black - 101-C10, baked (ε_ν at 77°K); data from Hall (1970)

(c)   3M Black - 101-C10, baked (ε_ν at 373°K); data from Hall (1970)

Three distinct spectral distributions (Wark, 1962) were used in the study; their identifications are in terms of atmospheric conditions:

(1)   Cloudless Winter Arctic

(2)   Cloudless Summer Western US

(3)   Clouds - covered Tropics

Figure 1 displays the surface emissivities as a function of wavenumber and Figure 2 displays the spectral flux distributions for the three atmospheric conditions.

4. Results

The variation of $\overline{\varepsilon}_c$ with calibration temperature T_c is presented in Table 1.

TABLE 1.   Average Emissivities for Blackbody Spectral Fluxes as a Function of Blackbody Temperature T_c.

T_c(°K)	$\overline{\varepsilon}_c$(a)	$\overline{\varepsilon}_c$(b)	$\overline{\varepsilon}_c$(c)
200	0.915	.896	.935
210	0.915	.898	.935
220	0.915	.901	.934
230	0.916	.903	.934
240	0.916	.905	.934
250	0.916	.906	.933
260	0.917	.908	.933
270	0.917	.909	.933
280	0.917	.911	.932
290	0.918	.912	.932

The values of $\bar{\epsilon}_k$ are presented in Table 2 for each surface. Also included in this table are σ and $\bar{\delta}$ values assuming a calibration temperature of 270°K.

TABLE 2. Average Emissivities for Spectral Fluxes Typical of Earth Emissions.

SPECTRAL FLUX CLASSIFICATION	$\bar{\epsilon}_k(a)$	$\bar{\epsilon}_k(b)$	$\bar{\epsilon}_k(c)$
(1) Winter Arct.	.918	.903	.933
(2) West. US Summer	.922	.914	.926
(3) Cloudy Tropics	.919	.912	.929
$\frac{1}{3}\sum_{k=1}^{3}\bar{\epsilon}_k$ =	0.920	0.906	0.929
$\bar{\epsilon}_c$ =	0.917	9.909	0.933
σ =	1.8×10^{-3}	6.6×10^{-3}	3.1×10^{-3}
$\bar{\delta}$ =	-3.3×10^{-3}	-0.7×10^{-3}	$+3.9 \times 10^{-3}$

In all cases there is a bias error produced using a blackbody calibration procedure. The case of Parson's black demonstrates this most clearly. It's effective emissivity for absorbing earth emitted radiation is larger than its blackbody emissivity because the spectral distribution of earth fluxes always contain minima produced by water vapor and CO_2 absorption which serve to reduce the effect of the low emissivity of Parson's black at 660 cm^{-1}. The spectral emissivity of 3M black at 373°K shows an increase in this region and thus produces the opposite effect. In both cases bias errors of 0.3% - 0.4% are possible.

The random errors varied from 0.2% - 0.7%. Although these might seem quite tolerable, it should be noted that these errors are actually correlated

with latitude, season, cloud cover, etc., as a result of the spectral
flux distribution characteristics. Thus these "random" errors can result
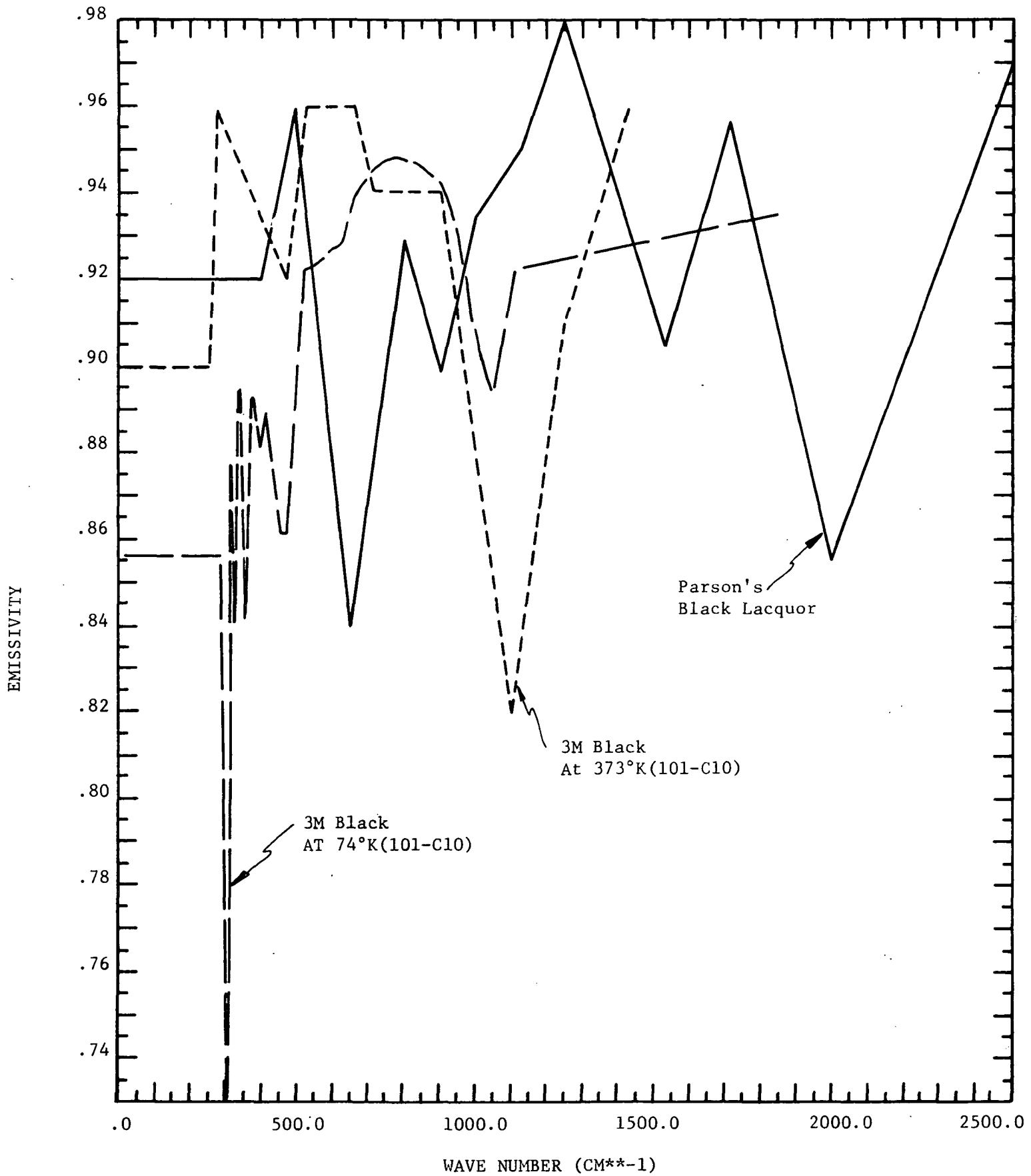in bias errors in north-south gradients and other significant parameters
as well.

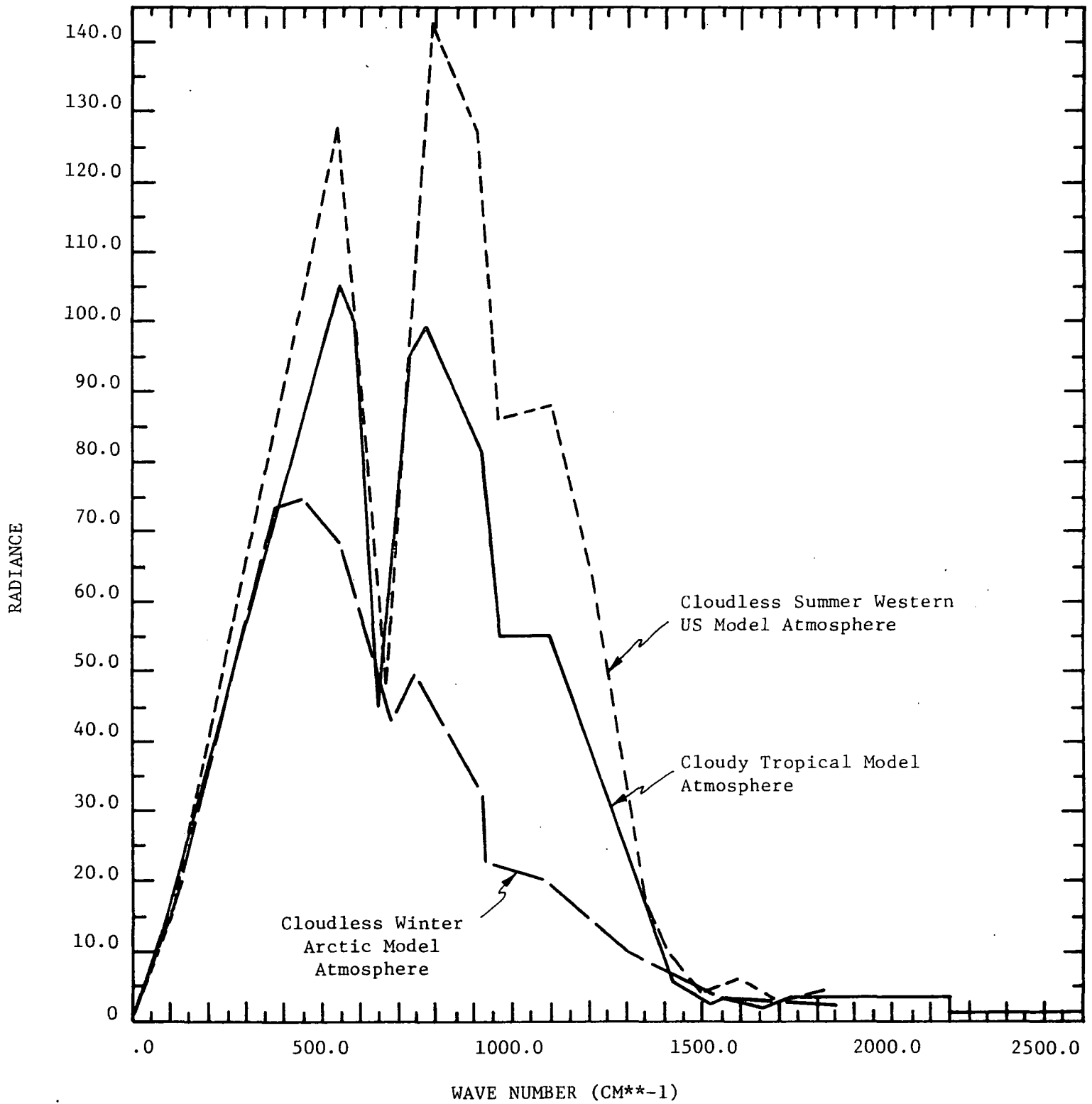FIGURE   1: Emissivity vs. Wavenumber

FIGURE 2 : Radiance vs. Wavenumber

APPENDIX G. FLUX ERRORS RESULTING FROM INCOMPLETE SPECTRAL COVERAGE AND
IMPERFECT SEPARATION OF SOLAR AND LONG WAVE COMPONENTS

Although it is possible to obtain spectral coverage adequate to measure

total radiation leaving the earth, the radiation incident from the sun,

and thus the net radiative energy exchange, all experiments which attempt

to separate reflected solar radiation from earth-emitted radiation must

face a common problem: spectral separation techniques are not rigorous.

The total radiation emitted by the earth can be rigorously separated from

the total solar radiation reflected by the earth only if they lie in entirely

separate spectral regions. On the planet earth this is not quite the case.

In the spectral region from 4μ to 5μ there is a small, but not entirely

negligible, overlap between the two components. Even a perfect long wave

cutoff filter cannot make a complete separation. A poorly designed filter

might produce significant errors. It is the purpose of this appendix to

estimate how well this separation can be made in theory and how significantly

the filter (window) cutoff wavelength affects the separation error.

1. Approximating the Missing Flux

The spectral flux from a blackbody at temperature T is given by

$$B_\nu(T) = C_1 \nu^3 [e^{c_2 \nu/T} - 1]^{-1}$$ (1)

where T is the absolute temperature ($^\circ$K) ν is the wavenumber in cm^{-1} and

the two radiation constants are

$$C_1 = 1.1906\ 1 \times 10^{-5}\ erg/cm^2 sec^{-1}$$

$$C_2 = 1.43868\ cm^\circ K.$$ (2)

The units of $B_\nu(T)$ for these constants are $erg/(cm^2\text{-}sec\text{-}(cm^{-1}))$ or $mW/m^2\text{-}cm^{-1}$.

Approximations for B_ν which apply at large distances from its peak value are

$$B_\nu \approx \pi C_1 \nu^3 e^{-C_2 \nu/T} \qquad C_2 \nu/T \gg 1 \tag{3}$$

$$B_\nu \approx T(\frac{C_1}{C_2})\nu^2 \qquad C_2 \nu/T \ll 1. \tag{4}$$

If we assume that the earth is a blackbody at temperature T_E then the total flux emitted over all wavelengths is given by

$$F(T_E) = \int_0^\infty B\nu(T_E)d\nu. \tag{5}$$

If our measured flux is wavelength limited, i.e. it only includes wave-numbers between a lower cutoff ν_1 and an upper cutoff ν_2, then the measured flux is given by

$$F_m(T_E) = \int_{\nu_1}^{\nu_2} B\nu(T_E)d\nu = \int_0^\infty B_\nu(T_E)d\nu - \int_0^{\nu_1} B_\nu(T_E)d\nu - \int_{\nu_2}^\infty B_\nu(T_E)d\nu \tag{6}$$

If $C_2 \nu_2/T \gg 1$ and $C_2 \nu_1 \ll 1$ then we can use the approximations given by equations (3) and (4) to evaluate equation (6). The integral terms are given by

$$\int_0^{\nu_1} B_\nu(T_E)d\nu \approx \frac{\pi}{3} C_1 \nu_1^4 (\frac{C_2 \nu_1}{T_E})^{-1}, \tag{7}$$

$$\int_0^{\nu_2} B_\nu(T_E)d\nu \approx \pi C_1 \nu_2^4 (\frac{C_2 \nu_2}{T_E})^{-1} e^{-C_2 \nu_2/T_E}. \tag{8}$$

We can approximate equation (6) by the expression

$$F_m(T_E) = F(T_E) - \pi C_1 \{\frac{1}{3}\nu_1^4(\frac{C_2 \nu_1}{T_E})^{-1} + \nu_2^4 e^{-C_2 \nu_2/T_E}(\frac{C_2 \nu_2}{T_E})^{-1}\}. \tag{9}$$

If we take as an example $\nu_1 = 0$ and $\nu_2 = 2500$ cm^{-1} (4μ) and $T_E = 273°K$ we find that

$$\frac{C_2\nu_1}{T_E} = 0, \quad \frac{C_2\nu_2}{T_E} = 13.17 \qquad (10)$$

and

$$F_m(T_E) - F(T_E) = 0.212 \text{ W/M}^2 \qquad (11)$$

We can calculate $F(T_E)$ using the relation

$$\int_0^\infty B_\nu(T_E)d\nu = \frac{\pi^5}{15} \frac{C_1}{C_2^4} T_E^4 = \sigma T_E^4 \qquad (12)$$

where $\sigma = 5.669 \times 10^{-5}$ mW/M^2 = 5.669×10^{-8} W/M^2. Employing equation (12), we find that

$$F(T_E) = 314.9 \text{ W/M}^2, \text{ and} \qquad (13)$$

$$\frac{F_m(T_E) - F(T_E)}{F(T_E)} = -6.73 \times 10^{-4} \qquad (14)$$

Thus a 4μ lower wavelength cutoff ($\nu_2 = 2500$ cm^{-1}) leads to a missing flux which is 0.07% of $F(T_E)$.

If we use a 4μ upper wavelength cutoff on reflected solar radiation ($T_s \simeq 5900°K$) then we find

$$\frac{C_2\nu_1}{T_E} = .6096, \quad \frac{C_2\nu_2}{T_E} = \infty. \qquad (15)$$

Although $C_2\nu_1/T_E$ does not satisfy condition (3) the errors introduced by using this approximation (Equation (3)) are relatively small and positive, i.e., the actual error will be slightly smaller than the value calculated using equation (10).

The fraction of missing flux of reflected (or incident) solar radiation is estimated to be

$$\frac{F_m(T_s) - F(T_s)}{F(T_s)} = \frac{-5 \; (\frac{C_2 \nu_1}{T_s})^3}{\pi^4} = -.0116. \tag{16}$$

Thus we find that approximately 1.2% of the solar flux is excluded using a 4μ cutoff. In order to keep the omitted flux fraction below 0.1% we must have ν_1 satisfy

$$(\frac{C_2 \nu_1}{T_s})^3 \leq .001 \times \pi^4/5 = 0.019482 \tag{17}$$

which implies that

$$\nu_1 \leq 1103 \; \text{cm}^{-1} \quad (\lambda \geq 9.06\mu). \tag{18}$$

However, this would lead to the inclusion of large percentages of long wave flux from the earth.

If we attempt to optimize the cutoff wavelength to produce equal percentages of omitted flux in both spectral regions we find that ν_1 must satisfy the condition.

$$\nu_1 = -\frac{T_E}{C_2} \ell n \; \frac{1}{3} \; (\frac{T_E}{T_s})^3. \tag{19}$$

The dependence of ν_1 on T_E and the percentage of missing flux for each case are displayed in Table 1.

2. Estimating Cross Band Contamination

No matter which cutoff wavelength is selected from Table 2, there will always be some observing conditions which result in missing fluxes of the order of 1%. In addition to the problem of not measuring part of what

should be measured, the spectral overlap also results in both SW and LW measurements containing flux contributions that they shouldn't be measuring. The SW band will accept some of the earth emitted radiation, and the LW band will accept some of the reflected solar radiation.

Two examples of cross band contamination are presented in Table 2. Both cases are for a 4.57μ cutoff wavelength. Case I approximates the radiation levels observed from a high albedo, high altitude cloud (cloud temperature 190°). Case II approximates the radiation levels present above a warm dark ocean (surface temperature $\approx$ 300°K, albedo $\approx$ 0.02). As

Table 1. Values of v_1 and the corresponding λ_1 which result in omission of the same percent of flux for both long wave and short wave measurements.*

T_E	$v(cm^{-1})$	$\lambda(\mu)$	% MISSING FLUX**
200	1564.2	6.39	0.28%
220	1677.9	5.96	0.35%
240	1785.8	5.60	0.42%
260	1891.2	5.29	0.50%
273	1958.0	5.11	0.56%
280	1993.4	5.02	0.59%
290	2043.4	4.89	0.63%
300	2092.6	4.78	0.68%
320	2189.1	4.57	0.78%

* The SW measurement is assumed to include the range $v_1 - \infty$ ($0 - \lambda_1$) and the LW measurement $0 - v_1$ ($\lambda_1 - \infty$).

** The percentages are defined as reflected outside the SW passband

$\div$ total reflected solar, or emitted radiation outside the LW passband

$\div$ the total emitted.

Table 2. Two Examples of Cross Band Contamination for a Wavelength Cutoff
         of 4.57 : Case I = bright cold cloud; Case II = dark warm ocean*
         Fluxes are in units of W/M^{-2}.

	CASE I	CASE II		CASE I	CASE II
TOTAL SOLAR	700.0	28.0	TOTAL EMITTED	73.88	459.2
SOLAR IN SW BAND	694.5	27.8	EMITTED IN LW BAND	73.88	456.9
EMITTED IN SW BAND	.003	2.26	SOLAR IN LW BAND	5.46	0.2
TOTAL FLUX IN SW BAND	694.5	30.1	TOTAL FLUX IN LW BAND	79.34	457.1
% DIFF BETW. SW IN BAND AND TOTAL SOLAR	-0.8%	+7.3%	% DIFF BETW. LW IN BAND AND TOTAL EMITTED	+7.4%	-0.5%

* The solar fluxes are based on wavelength independent reflectivity.

indicated in the table contamination levels can be considerable both in

absolute terms and as percentages. It should be noted that changing the

cutoff wavelength will change the distribution of the contamination but

will do little to reduce the contamination level.

3. The Great White Hope

     The futility of attempting to achieve accurate spectral separation

by means of filtering alone suggests a simpler method. Consider, for

example, a radiometer with a SW passband from 0.2μ (or 0.0μ) to λ_2, where

λ_2 is short enough to exclude all significant earth emission. If this

radiometer is calibrated against the sun so that it reads H_s even though

CO

CH₄

N₂O

O₃

CO₂

HDO

H₂O

SOLAR SPECTRUM

← ABSORPTION (%)

0

100

0

100

0

100

0

100

0

100

0

100

0

100

0

100

8000 5000   3000   2000   1600 1400 1200   1000 900   800   700 (cm⁻¹)

1   2   3   4   5   6   7   8   9   10   11   12   13   14   (15μ)
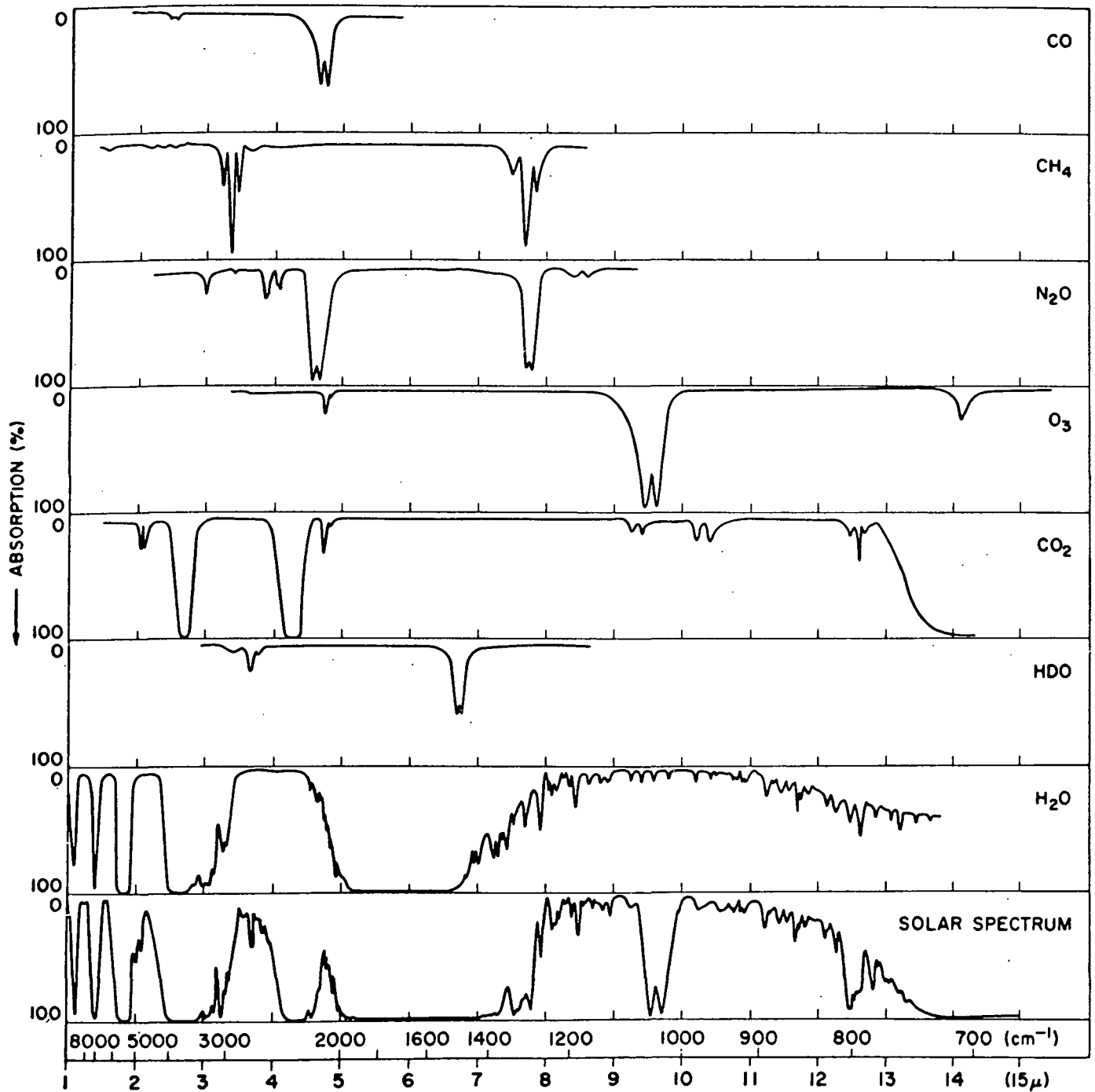
Figure 1. Comparison of the near-infrared solar spectrum with laboratory
spectra of various atmospheric gases. (AFCRL, 1965)

it misses all the solar radiation from λ_2 to ∞, and if the earth consists of a black (or dark grey) ball with perfectly white (or light grey) patches gliding over the surface (and no atmosphere), then, when the forementioned radiometer views the earth, it will produce a reading which is exactly equal to the reflected solar radiation even though it does not accept all the reflected radiation from λ_2 to ∞. In other words, the calibration process forces the radiometer to approximate the missing flux as if the average albedo from λ_2 to ∞ were the same as the average albedo from 0 to λ_2.

For the idealized earth described above (the patches were meant to represent clouds) the approximation works perfectly. For the real earth, with clouds made of water droplets and ice particles floating in an atmosphere sprinkled with water vapor and CO_2, the approximation is highly questionable. As indicated in Figure 1, there is significant atmospheric absorption in the overlap region from 4μ to about 8μ, mainly due to water vapor, CO_2 and N_2O. Thus solar radiation reflected at the bottom of the atmosphere leaves the top of the atmosphere with considerable attenuation in the 4μ to 8μ interval violating the ideal of the white (grey) hope idea. The spectral reflectivity of clouds, which account for most of the reflected solar radiation, is even more important. Estimates of cloud reflectivity (see Figure 2, for example) indicate a very sharp drop in albedo beyond 3μ due to the large IR absorbtion of liquid water drops in this region. It thus appears that reflected solar radiation in the overlap region is likely to be much smaller than would be deduced on the basis of grey (wavelength independent) reflectance.

4. Choosing a Bandpass

Based on the previous analysis the most reasonable way to separate reflected solar and emitted long wave components is to choose a cutoff

between 3μ and 4μ. This will insure that all significant emitted

radiation is accepted by the long wave passband. Since most of the

incident solar energy in the LW passband will not be reflected, the

LW band will suffer little contamination and the SW passband will

not miss any significant amount of reflected flux. This will require

a correction factor, however, for using the solar calibration since

approximately 1.5% of the solar flux will not be transmitted by the

window.

It should be noted that Figure 2, if extended to 6μ would probably

show some regions of increased albedo above 0.2. If the mean value is

below 0.2 from 3.5μ to about 6μ the missing SW and LW contamination

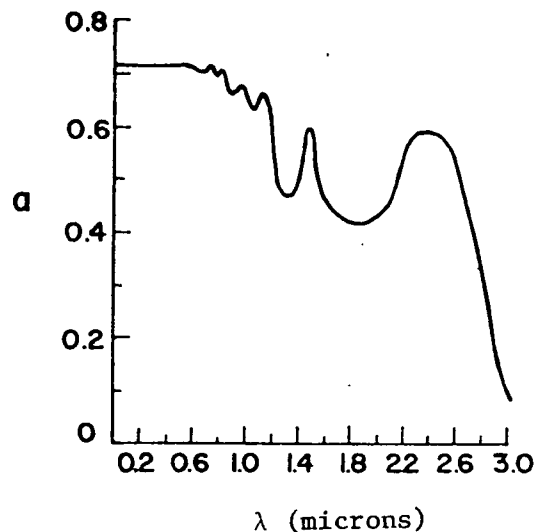errors should still be within tolerable limits.

Figure 2. The spectral albedo for middle layer clouds
(after Novoseltsev, 1964).

APPENDIX H. FLUX ERRORS RESULTING FROM NON-LAMBERTIAN
ANGULAR RESPONSE

1. Modeling Sensor Angular Response

The ideal response of a plane flux sensor is that of a perfectly absorbing flat surface; i.e., the absorbed energy from a point source at an angle Θ away from the plane normal is proportional to $\cos\Theta$, the projected area of the surface normal to the source direction.

We shall consider only one model for deviations from the ideal $\cos\Theta$ response. This model is a linear combination of $\cos\Theta$ and $\cos^2\Theta$, i.e.

$$R(\Theta) = (1 - \alpha) \cos\Theta + \alpha\cos^2\Theta, \quad 0 \leq \alpha < 1, \tag{1}$$

where $R(\Theta)$ is the sensor relative angular response and α is a deviation parameter which can be varied between zero and one.

The relative angular emissivity variation corresponding to equation (1) is just $\varepsilon(\Theta) = \varepsilon_o R(\Theta)/\cos\Theta$, i.e.

$$\varepsilon(\Theta) = \varepsilon_o [1 - \alpha (1 - \cos\Theta)]. \tag{2}$$

As illustrated in Figure 2, the emissivity thus varies between ε_o at $\Theta = 0$ and $\varepsilon_o (1 - \alpha)$ at $\Theta = 90°$.

2. Modeling Angular Distribution of Radiation from the Earth

Since our sensor will be in orbit around the earth the angular diameter of the earth will be π/γ, where $\gamma > 1$ and depends on orbital height according to the equation

$$\gamma = [1 - \frac{2}{\pi} \sin^{-1} [1 - (\frac{R_e}{R_e + h})^2]^{1/2}]^{-1}, \tag{3}$$

where R_e = 6370 km (radius of the earth) and h is the satellite altitude. For the value of h = 380 n.mi. (704 km) we find that $\gamma \approx 1.4014$.

This corresponds to an earth angular extent of $-64.22° \le \Theta \le +64.22°$.

We shall consider three different models for earth radiance angular distribution $I(\Theta)$, corresponding to uniform brightness, limb darkening, and limb brightening. These are defined as follows:

$$I_1(\Theta) = I_{1,0}, \quad -\pi/2 \le \gamma\Theta \le \pi/2 \tag{4}$$

$$I_2(\Theta) = I_{2,0}\cos^2\gamma\Theta, \quad -\pi/2 \le \gamma\Theta \le \pi/2 \tag{5}$$

$$I_3(\Theta) = I_{3,0}\sin^2\gamma\Theta, \quad -\pi/2 \le \gamma\Theta \le \pi/2. \tag{6}$$

The constants $I_{1,0}$, $I_{2,0}$, $I_{3,0}$ are chosen to satisfy the normalization condition

$$F = 2\pi \int_0^{\pi/2\gamma} I(\Theta)\cos\Theta\sin\Theta d\Theta \tag{7}$$

where F is the plane flux incident on the detector. In order for all angular distributions to yield the same plane flux F (equation (7)) we find that the coefficients must satisfy

$$I_{1,0} = \frac{F}{\pi}\left[\sin^2\frac{\pi}{2\gamma}\right]^{-1} \tag{8}$$

$$I_{2,0} = 2\frac{F}{\pi}\left[\sin^2\frac{\pi}{2\gamma} + \frac{1}{1-\gamma^2}\cos^2\frac{\pi}{2\gamma}\right]^{-1} \tag{9}$$

$$I_{3,0} = 2\frac{F}{\pi}\left[\sin^2\frac{\pi}{2\gamma} - \frac{1}{1-\gamma^2}\cos^2\frac{\pi}{2\gamma}\right]^{-1}. \tag{10}$$

3. Sensor Calibration

We shall assume that the sensor is calibrated with isotropic radiation limited to $\pm\pi/2\gamma$ in Θ. The incident flux in this configuration is given by

$$F_i = I_c \int_0^{\pi/2\gamma} 2\pi\sin\Theta\cos\Theta d\Theta = \pi I_c\sin^2\frac{\pi}{2\gamma}, \tag{11}$$

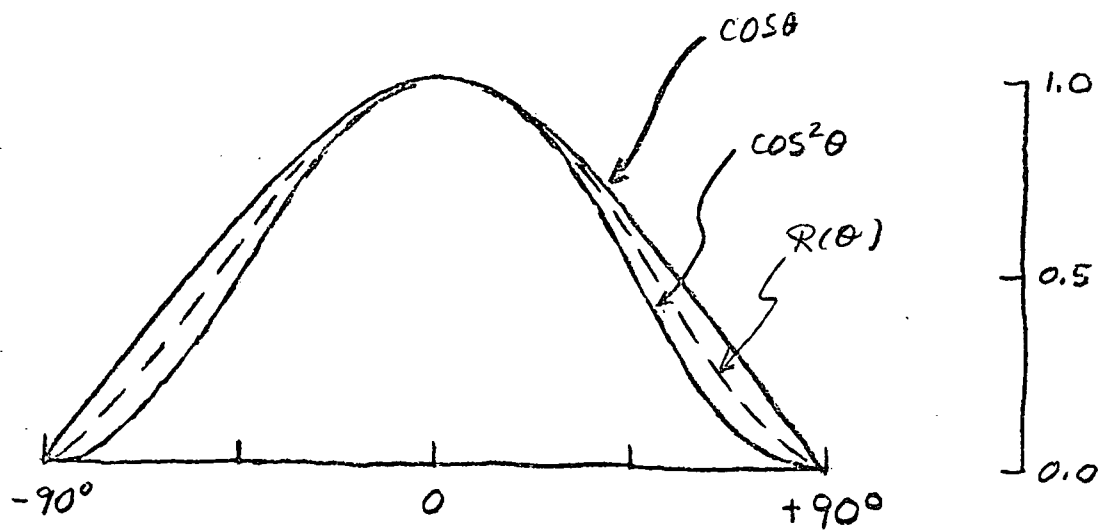where I_c is the angle independent radiance used in the calibration. The absorbed flux is given by

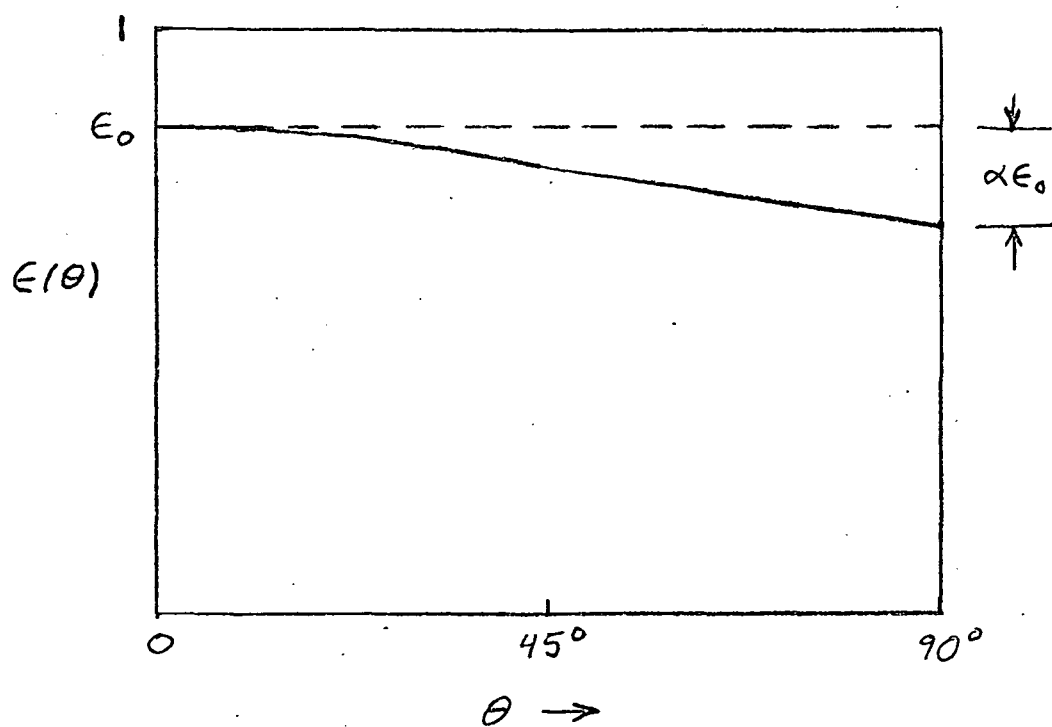FIGURE 1. Sensor Angular Response Model. $R(\theta) = (1-\alpha) \cos\theta + \cos^2\theta$.

FIGURE 2. Model for Angular Variation of Surface Emissivity.

$$F_a = I_c \int_{0}^{\pi/2\gamma} \epsilon_o [(1-\alpha) + \alpha\cos\Theta] \, 2\pi\sin\Theta\cos\Theta d\Theta \tag{12}$$

which reduces to the form

$$F_a = \pi I_c \, \epsilon_o [(1-\alpha)\sin^2 \frac{\pi}{2\gamma} + \frac{2}{3}\alpha \, (1-\cos^3 \frac{\pi}{2\gamma})] . \tag{13}$$

The calibration factor K which is subsequently used to derive incident

flux from absorbed flux is thus given by

$$K = (\frac{F_i}{F_a})_{cal} = \frac{\sin^2(\pi/2\gamma)}{\epsilon_o[(1-\alpha)\sin^2(\pi/2\gamma) + \frac{2}{3}\alpha \, (1-\cos^3 \frac{\pi}{2\gamma})]} \tag{14}$$

where the subscript "cal" on the flux ratio denotes the ratio existing

for the calibration condition. For angular intensity distributions other

than isotropic, K will not be equal to the ratio of incident and absorbed

fluxes, although, in practice, sensor output will be treated as if it were

true. In other words, we shall define the "measured" flux as

$$F_{meas} = K \, F_a \equiv K \, \epsilon_o \int_{0}^{\pi/2\gamma} I(\Theta)R(\Theta) \, 2\pi\sin\Theta d\Theta, \tag{15}$$

where in this case F_a and $I(\Theta)$ denote absorbed fluxes and correspondent

incident intensities which might be encountered in orbit.

4. Estimating Flux Errors

Measured fluxes, i.e. those calculated according to equation (15),

will be determined for $I_2(\Theta)$ and $I_3(\Theta)$. The difference between corresponding

measured fluxes F_2 and F_3 and the incident flux F are then the measurement

errors. (Since $I_1(\Theta)$ is independent of Θ, the calibration procedure assures

zero error for this case).

The equations for F_2 and F_3 are:

$$F_2 = K \, \epsilon_o \, I_{2,0} \int_0^{\pi/2\gamma} \cos^2\gamma\Theta \, [(1-\alpha)\cos\Theta + \alpha\cos^2\Theta]2\pi\sin\Theta d\Theta, \tag{16}$$

$$F_3 = K \, \epsilon_o \, I_{3,0} \int_0^{\pi/2\gamma} \sin^2\gamma\Theta \, [(1-\alpha)\cos\Theta + \alpha\cos^2\Theta]2\pi\sin\Theta d\Theta. \tag{17}$$

If we define two define integrals

$$A = \int_0^{\pi/2\gamma} \cos^2\gamma\Theta \, \cos\Theta\sin\Theta d\gamma \tag{18}$$

$$B = \int_0^{\pi/2\gamma} \cos^2\gamma\Theta \, \cos^2\Theta\sin\Theta d\Theta, \tag{19}$$

then F_2 and F_3 can be written as

$$F_2 = 2\pi K \, \epsilon_o I_{2,0}[(1-\alpha) \, A + \alpha B] \tag{20}$$

$$F_3 = 2\pi K \, \epsilon_o I_{3,0}[(1-\alpha) \, (\tfrac{1}{2} \sin^2 \tfrac{\pi}{2\gamma} - A) + \alpha B] \tag{21}$$

where

$$A = \frac{1}{4} \, (\sin^2(\tfrac{\pi}{2\gamma}) + \cos^2(\tfrac{\pi}{2\gamma})\frac{1}{1-\gamma^2}) \tag{22}$$

$$B = \frac{1}{8} \cos^2(\tfrac{\pi}{4\gamma}) \, \frac{1}{1-4^2} + \frac{1}{6} \, (1-\cos^3(\tfrac{\pi}{2\gamma})) + \frac{3}{4} \cos^2(\tfrac{3\pi}{4\gamma}) \, \frac{1}{9-4\gamma^2} \, . \tag{23}$$

Since we can write the intensity constants in the form

$$I_{2,0} = \frac{F}{2\pi} A^{-1} \tag{24}$$

$$I_{3,0} = \frac{F}{2\pi} (\tfrac{1}{2}\sin^2(\tfrac{\pi}{2\gamma}) - A)^{-1} \tag{25}$$

equations (20) and (21) can be rewritten in the form

$$F_2 = K \, \epsilon_o F \, [(1-\alpha) + \alpha \, \frac{B}{A}] \tag{26}$$

$$F_3 = K \, \epsilon_o F \, [(1-\alpha) + \alpha \, \frac{B}{\frac{1}{2}\sin^2(\tfrac{\pi}{2\gamma}) - A}]. \tag{27}$$

Evaluating A, B, and K for $\gamma = 1.4014$, we find

$$\frac{B}{A} = \frac{+.147848}{.15367} = .96212 \qquad (28)$$

$$\frac{B}{\frac{1}{2}\sin^2(\frac{\pi}{2\gamma}) - A} = \frac{+.147848}{.25177} = .58723 \qquad (29)$$

$$\varepsilon_o K = (1 - 0.3882\alpha)^{-1}. \qquad (30)$$

Thus the fluxes take on the specific values

$$F_2 = F\frac{1-.03788\alpha}{1-.24546\alpha} \qquad (31)$$

$$F_3 = F\frac{1-.41277\alpha}{1-.24546\alpha}. \qquad (32)$$

As a function of α we find the follwing percentage errors in F_2 and F_3

α	(LIMB DARKENING) $100 \times \frac{F_2 - F}{F}$	(LIMB BRIGHTENING) $100 \times \frac{F_3 - F}{F}$
.01	+ .2%	- .2%
.02	+ .4%	- .3%
.05	+ 1.1%	- .8%
.10	+ 2.1%	- 1.7%
.20	+ 4.4%	- 3.5%
.40	+ 9.2%	- 7.4%
.60	+14.6%	-11.8%
.80	+20.7%	-16.7%
1.00	+27.5%	-22.2%

Since typical limb darkening and brightening is much less than 100% the errors just tabulated should be considered as very conservative.

APPENDIX I. ESTIMATION OF FACR ANGULAR RESPONSE

ERRORS DUE TO NONUNIFORM RADIATIVE COUPLING

BETWEEN CAVITY AND SINK

For the parameterization of errors due to nonuniform radiative coupling between the cavity and its surrounding heat sink we will model the cavity as a linear plate which is divided into two regions of distinctly different coupling. As indicated in Figure 1, the plate is divided at the midpoint into Region 1 and Region 2. Significant parameters required to describe the model are:

s = the half length of the plate

χ = the thickness of the plate

k = the thermal conductivity of the plate

z = the distance along the plate

ϵ = the emissivity of the top surface of the plate

k_1, k_2 = the radiative power transfer between the plate and the sink per unit area per °K for regions 1 and 2 respectively.

$T_1(z), T_2(z)$ = temperature distributions in region 1 and 2 respectively

F_1, F_2 = incident radiative fluxes in region 1 and 2 respectively (these do not include the radiation received from the sink)

The transfer coefficients k_1 and k_2 are mathematically defined as follows:

$$k_1 = 4\epsilon_1 \sigma T^3 \tag{1}$$

$$k_2 = 4\epsilon_2 \sigma T^3 \tag{2}$$

where T is the mean temperature of the entire plate and ϵ_1, ϵ_2 are effective emissivities for radiation transfer between plate and sink. The solution for the temperature distribution along the plate is determined to be

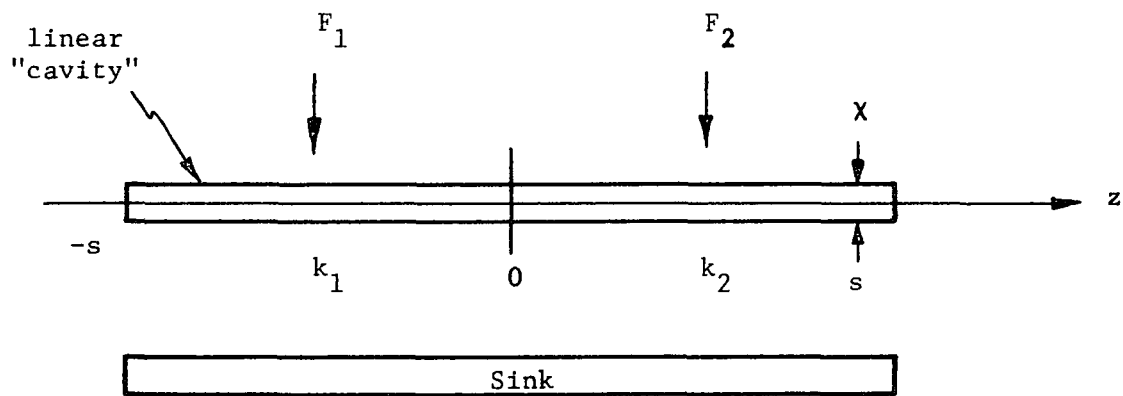$$T_1(z) = A_1[e^{a_1 z} + e^{-2a_1 s} e^{-a_1 z}] + \frac{\epsilon F_1}{k_1} , \tag{3}$$

Figure 1. Linear Model for parameterizing errors due to non-uniform radiative transfer between cavity and sink.

$$T_2(z) = A_2[e^{a_2 z} + e^{+2a_2 s}e^{-a_2 z}] + \frac{\epsilon F_2}{k_2} , \qquad (4)$$

where the constants are given by

$$A_1 = \epsilon(\frac{F_2}{k_2} - \frac{F_1}{k_1})(1 - e^{-2a_1 s})^{-1}[\coth a_1 a + \frac{a_1}{a_2}\coth a_2 s]^{-1} , (5)$$

$$A_2 = (\frac{F_2}{k_2} - \frac{F_1}{k_1})\frac{a_1}{a_2}(1 - e^{2a_2 s})^{-1}[\coth a_1 s + \frac{a_1}{a_2}\coth a_2 s]^{-1}, (6)$$

$$a_1 = (\frac{k_1}{k\chi})^{1/2} , \text{ and } \qquad a_2 = (\frac{k_2}{k\chi})^{1/2} . \qquad (7)$$

The mean cavity temperature T is found by integrating $T_1(z)$ and $T_2(z)$ over the length of the "cavity" and dividing by 2s. The result is

$$T = \frac{\epsilon}{2a_1^2 s^2} \frac{(1 - \frac{a_1^2}{a_2^2})(\frac{F_2}{k_2} - \frac{F_1}{k_1})}{[\frac{\coth a_1 s}{a_1 s} + \frac{\coth a_2 s}{a_2 s}]} \qquad (8)$$

If we define the temperature servo origin so that T is fixed at 0°, then (8) implies a fixed relationship between F_1 and F_2, i.e.

$$F_2 = -F_1(1 + \frac{1}{2}hk_2)(1 + \frac{1}{2}hk_1)^{-1} \qquad (9)$$

where the parameter h is given by

$$h = \frac{s^2}{k\chi}[f(a_1 s) + f(a_2 s)], \text{ where} \qquad (10)$$

$$f(\xi) = \frac{1}{\xi}\coth \xi - \frac{1}{\xi^2} . \qquad (11)$$

For $\xi \ll 1$ (the usual case) we can make the approximation

$$f(\xi) \doteq \frac{1}{3} , \qquad (12)$$

in which case (9) can be simplified to the form

$$F_2 = -F_1[1 + \frac{1}{3}(\frac{k_2 - k_1}{k\chi})s^2] . \qquad (13)$$

Defining the radiative flux inputs to regions 1 and 2 as $F_{1,r}$ and $F_{2,r}$, and

F_e as the electric power input per unit area (which is uniform over the

cavity surface) we find that

$$F_1 = \frac{1}{\varepsilon}F_e + F_{1,r} \text{ , and} \tag{14}$$

$$F_2 = \frac{1}{\varepsilon}F_e + F_{2,r} . \tag{15}$$

Inserting (14) and (15) into equation (13) yields the following expression

for the electrical power flux in terms of the incident radiative fluxes:

$$F_e = -[\frac{\varepsilon}{2}(F_{1,r} + F_{2,r}) + \frac{\varepsilon}{6}\frac{(k_2 - k_1)}{k\chi}s^2 F_{1,r}] \tag{16}$$

If we consider two extreme cases with different incident flux distributions,

i.e.

case (1): $F_{1,r} = F_o$; $F_{2,r} = 0$

case (2): $F_{1,r} = 0$; $F_{2,r} = F_o$

then the peak to peak fractional difference in electrical power flux for

the same total radiative input power is just

$$\frac{F_e^{(2)} - F_e^{(1)}}{F_o} = \frac{1}{6} \varepsilon \frac{(k_2 - k_1)}{k\chi} s^2 \tag{17}$$

If the mean cavity temperature has the absolute value T, then the error

expression can also be written as

$$\frac{F_e^{(2)} - F_e^{(1)}}{F_o} = \frac{2}{3} \varepsilon\sigma T^3 \frac{(\varepsilon_2 - \varepsilon_1)}{k\chi} s^2 \tag{18}$$

where $\varepsilon_2 - \varepsilon_1$ is the difference in effective emissivities for radiation

transfer between cavity and sink. These emissivities depend on the

cavity-sink geometry as well as the surface emissivities of the two components.

The s^2 factor in equation (18) applies rigorously only for the linear model used in the derivation. There is considerable uncertainty in choosing an appropriate geometry factor for a three dimensional cavity which will probably be resolved only by measurement. For order of magnitude estimates we will choose s to satisfy

$$4s^2 = A_s \tag{19}$$

where A_s is the surface area of the cavity, in which case $s \approx \sqrt{\pi}$ x the cavity radius. Inserting (19) into (18) yields the final result:

$$\frac{F_e^{(2)} - F_e^{(1)}}{F_o} = \frac{\varepsilon \sigma T^3 A_s}{6k\chi} (\varepsilon_2 - \varepsilon_1). \tag{20}$$

For typical parameter values (see Section VII) of $\varepsilon \approx 1$, $A_s \approx 19 \text{ cm}^2$, $\chi \approx 7 \times 10^{-3}$ cm, $T \approx 350°K$ and $k \approx 0.58$ W/cm°K, equation (20) has the value

$$\frac{\varepsilon \sigma T^3}{6k\chi} A_s \approx 0.19 \tag{21}$$

For a 3% difference between ε_1 and ε_2 this would imply a fraction power error of 0.5% between the two regions. Based on the results of Appendix H, this should result in angular integration errors not exceeding 0.1%.

APPENDIX J. PARAMETERIZATION OF THE FACR ANGULAR RESPONSE ERRORS RESULTING
FROM LEAD WIRE AND SUPPORT CONDUCTION

As indicated in Section VI.5, lead wire and support conduction can
produce angular response errors. In general, radiative flux incident on
the cavity near a support or lead wire contact point has a somewhat
smaller cavity heating effect than the same amount of radiation incident
on other parts of the cavity. In order to make an order of magnitude
estimate of the resulting errors, and to determine how cavity parameters
can be optimized to reduce this effect, a similar, but geometrically
simpler configuration is treated. The cavity is replaced by a disc with
a single support wire. The electrical servo power is calculated for
radiative power incident in an annulus outside this region. The power
difference for these two cases is finally related to an angular response
error.

The disc model for treating the effects of wire conduction is illustrated
in Figure 1.   Parameters used in this model are

a = Radius of the wire contacting the disk

ℓ = The wire length between cavity and the sink

b = The radius separating region I and region II on the "cavity"

c = The outer radius of the cavity

T_s = The sink temperature

$T_I(r)$ = The cavity temperature distribtion in region I

$T_{II}(r)$ = The cavity temperature distribtuion in region II

x = The cavity thickness

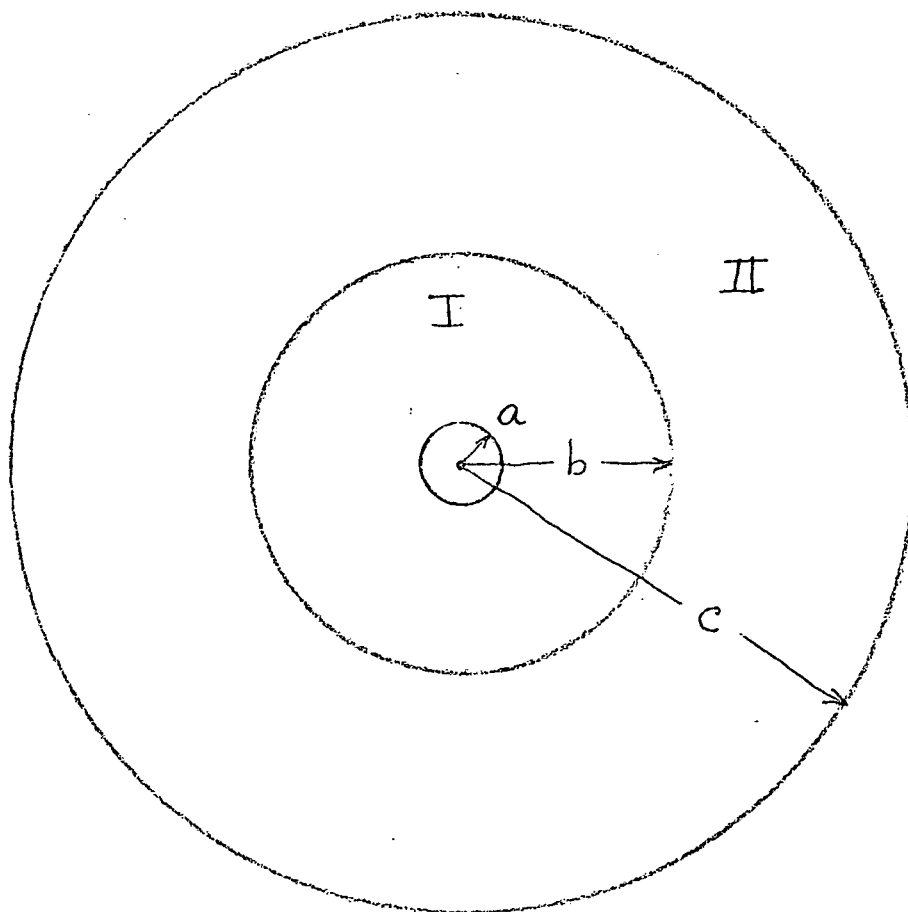k = The thermal conductivity of the cavity (and of the lead wire)

Figure 1. Cavity Disc Model for Estimating Effects of Wire
Conduction.

The differential equations for T_I and T_{II} are

$$\frac{\partial^2 T_I}{\partial r^2} + \frac{1}{r}\frac{\partial T_I}{\partial r} = -4\alpha_I, \tag{1}$$

$$\frac{\partial^2 T_{II}}{\partial r^2} + \frac{1}{r}\frac{\partial T_{II}}{\partial r} = -4\alpha_{II}, \tag{2}$$

where α_I and α_{II} are defined by

$$\alpha_I = \epsilon F_I/(4kx), \tag{3}$$

$$\alpha_{II} = \epsilon F_{II}/(4kx), \tag{4}$$

where the additional parameters are defined as

ϵ = Emissivity of the cavity surface

F_I = Net power flux in Region I

F_{II} = Net power flux in Region II

The solutions to both differential equations have the same form, i.e.

$$T(r) = A_1 + A_2 r^2 + A_3 \ln r, \tag{5}$$

Applying the boundary conditions of energy conservation, i.e.

$$2\pi akx \left. \frac{\partial T_I}{\partial r} \right|_{r=a} = \frac{k\pi a^2}{\ell} [T_I(a) - T_s], \tag{6}$$

$$\left. \frac{\partial T_I}{\partial r} \right|_{r=b} = \left. \frac{\partial T_{II}}{\partial r} \right|_{r=b}, \quad T_I(b) = T_{II}(b), \tag{7}$$

$$\left. \frac{\partial T_{II}}{\partial r} \right|_{r=c} = 0, \tag{8}$$

yields the following expression for temperature distributions

$$T_I(r) = D_1 + D_2 (r/a)^2 + D_3 \ln(r/a) \tag{9}$$

$$T_{II}(r) = D_1 + D_4 + D_5 (r/a)^2 + D_6 \ln(r/a) \tag{10}$$

$$D_1 = 4\gamma(c^2 \alpha_{II} - b^2(\alpha_{II} - \alpha_I)) - \alpha_I a^2 (4\gamma - 1) \tag{11}$$

$$D_2 = -\alpha_I a^2 \tag{12}$$

$$D_3 = 2c^2 \alpha_{II} - 2b^2 (\alpha_{II} - \alpha_I) \tag{13}$$

$$D_4 = b^2 (\alpha_{II} - \alpha_I) [1 - 2 \ln(b/a)] \tag{14}$$

$$D_5 = -\alpha_{II} a^2 \tag{15}$$

$$D_6 = 2c^2 \alpha_{II} \tag{16}$$

$$\gamma = \ell x / (a^2) \tag{17}$$

The mean "cavity" temperature, which is the quantity that is servo controlled, is determined from (9) and (10) as

$$\bar{T} = [2\pi \int_a^b T_I(r)\,rdr + 2\pi \int_b^c T_{II}(r)\,rdr]/[\pi(c^2-a^2)] \tag{18}$$

Assuming that the servo fixes the mean temperature at $\bar{T} = 0$ (the temperature origin can be chosen arbitrarily), equation (18) implies a relationship between α_I and α_{II}, namely

$$\frac{\alpha_I}{\alpha_{II}} - 1 = c^4[4\gamma - \frac{3}{2} + 2\ell n \frac{c}{a}]/[b^2 c^2 [1-4\gamma - 2\ell n \frac{b}{a}] + \frac{1}{2} b^4]. \tag{19}$$

This also implies a relationship between electrical power input and radiative power input through equations (3) and (4). Defining

F_e = Electrical power input per unit area of the disk,

F_r^I = Net radiative flux incident on region I, and

F_r^{II} = Net radiative flux incident on region II,

we find that the net power fluxes F_I and F_{II} are given by

$$F_I = F_e + F_r^I \tag{20}$$

$$F_{II} = F_e + F_r^{II} \tag{21}$$

Then the L.H.S. of equation (19) can be written as

$$\frac{\alpha_I}{\alpha_{II}} - 1 = \frac{F_e + F_r^I}{F_e + F_r^{II}} - 1 = \frac{F_r^I - F_r^{II}}{F_e + F_r^{II}} \tag{22}$$

In order to estimate the power error we shall consider two different distributions of radiative power which yield the same total radiative power incident on the cavity:

CASE 1: (Radiation incident in Region I)

$$F_r^{I} = P_r/(\pi b^2)$$

$$F_r^{II} = 0$$

$$F_e = P_{e,1}/(\pi c^2)$$

CASE 2: (Radiation incident in Region II)

$$F_r^{I} = 0$$

$$F_r^{II} = P_r/(\pi(c^2-b^2))$$

$$F_e = P_{e,2}/(\pi c^2)$$

Denoting the R.H.S. of (19) by the symbol W, we find that the electrical powers for the two cases are

$$P_{e,1} = \frac{c^2}{Wb^2} P_r \tag{23}$$

$$P_{e,2} = -P_r \frac{c^2}{W(c^2-b^2)} [1+W] \tag{24}$$

Since they should both be ideally equal to $-P_r$, the fractional error between the two cases is just

$$\frac{P_{e,1}-P_{e,2}}{P_r} = \frac{c^2}{W} [\frac{1}{b^2} + \frac{(1+W)}{c^2-b^2}]. \tag{25}$$

For $\gamma \gg 1$ (typically γ is of the order of 10^2) W can be approximated as

$$W \approx - \frac{c^2}{b^2} [1 - \frac{1}{2\gamma} (\frac{1}{4}(1 + \frac{b^2}{c^2}) - \ln \frac{c}{b})], \tag{26}$$

in which case equation (25) can be simplified to the form

$$\frac{P_{e,1}-P_{e,2}}{P_r} = -\frac{\frac{1}{4}(1+\frac{b^2}{c^2}) - \ln\frac{c}{b}}{2\gamma(1-\frac{b^2}{c^2})} \tag{27}$$

Recalling that $\gamma = \ell x a^{-2}$ and allowing for wire conductivity k_w to differ from the cavity conductivity k we can rewrite (27) in terms of two factors, i.e.

$$\frac{P_{e,1}-P_{e,2}}{P_r} = \frac{k_w a^2}{\ell k x} S \tag{28}$$

where S is a geometrical factor which, for the disc model, is given by

$$S = [-\frac{1}{4}(1+\frac{b^2}{c^2}) + \ln\frac{c}{b}] (1 - \frac{b^2}{c^2})^{-1}. \tag{29}$$

If we require b^2 and c^2 to be in the same ratio as the aperture area to the cavity area, a typical value is $c^2/b^2 \approx 16$. In which case S has the value

$$S \approx 1.2, \quad c^2/b^2 \approx 16. \tag{30}$$

For the specific cavity parameters discussed in Section VII, the error estimate for a single lead can be calculated. For

$$k_w = k = .426 \ J/°K$$

$$a = .0038 \ cm$$

$$\ell = 1 \ cm$$

$$x \approx a \frac{\pi}{2} = .006 \ cm$$

we find that

$$\frac{P_{e,1}-P_{e,2}}{P_r} = \frac{(.0038 \ cm)^2}{1 \ cm \ x \ .006 \ cm} \ x \ 1.2 = 0.29 \ x \ 10^{-2}. \tag{31}$$

Since angular response deviations of this magnitude typically resulted in integrated flux errors somewhat less than 0.1% the lead wire conduction does not present a significant problem.

APPENDIX K.   THERMAL MODEL OF THERMOPILE DETECTORS

As indicated in Figure 1 the basic components of a thermopile radiation sensor are (1) a radiation receiver which absorbs and emits radiation, (2) a thermal resistor which conducts heat between the receiver and the heat sink, (3) a heat sink, and (4) a differential temperature sensor (a thermopile) which measures the temperature difference across the thermal resistor. Analysis of this model makes use of the following notation:

A_r = area of the receiver

P_a = power absorbed by the receiver

P_r = power radiated by the receiver

P_c = power conducted by the thermal resistor

T_r = absolute temperature of the receiver

T_s = absolute temperature of the sink

ϵ_λ = receiver emissivity at wavelength λ

K = total thermal conductance of thermal resistor

V = voltage output of the differential thermopile

F_λ = incident spectral flux

$\pi B_\lambda(T)$ = spectral flux emitted by a blackbody at temperature T

Under steady-state conditions (power storage taking place only in the heat sink), conservation of energy requires

$$P_c = P_a - P_r, \tag{1}$$

where

$$\left. \begin{aligned} P_a &= A_r \int_0^\infty \epsilon_\lambda F_\lambda \, d\lambda, \\ P_r &= A_r \pi \int_0^\infty \epsilon_\lambda B_\lambda(T_r) \, d\lambda. \end{aligned} \right\} \tag{2}$$
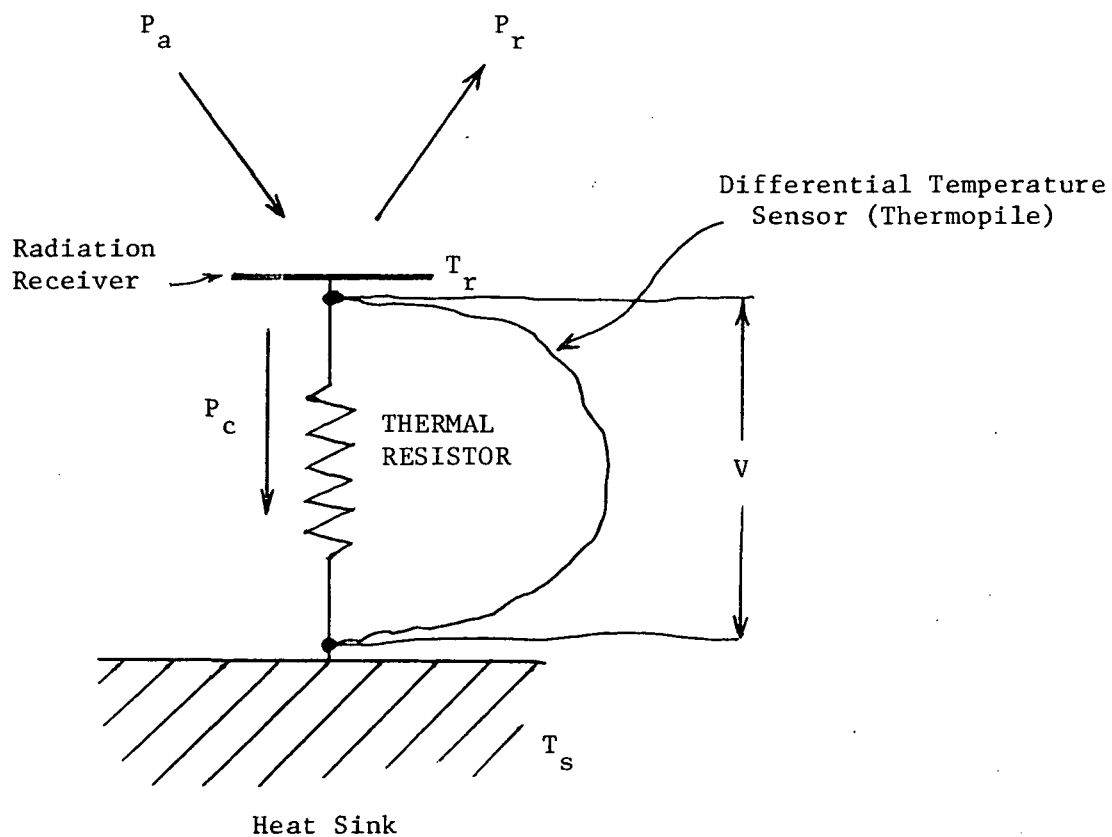
Figure 1. Thermal model of a thermopile sensor. The absorbed power is P_a, the radiated power P_r, and the conducted power P_c.

Thus (1) may be rewritten as follows:

$$P_c = A_r \int_0^\infty \varepsilon_\lambda [F_\lambda - \pi B_\lambda(T_r)] d\lambda. \qquad (3)$$

If ε_λ is a weak and slowly varying function of λ, and if F_λ and $B_\lambda(T_r)$ have approximately the same wavelength dependence, then we may approximate (3) by the following expression:

$$P_c = A_r \varepsilon (F - \sigma T_r^4), \qquad (4)$$

where

$$F = \int_0^\infty F_\lambda d\lambda, \qquad (5)$$

$$\sigma T_r^4 = \int_0^\infty \beta_\lambda(T_r) d\lambda, \text{ and} \qquad (6)$$

$$\varepsilon = \frac{\pi \int_0^\infty \varepsilon_\lambda B_\lambda(T_r) d\lambda}{\sigma T_r^4}. \qquad (7)$$

A more general expression is obtained by allowing ε_λ to vary with wavelength and F_λ to have a significantly different spectral dependence than $B_\lambda(T_r)$. In this case, if F_λ varies in amplitude but retains its basic spectral characters (e.g. reflected solar radiation), it is useful to express equation (3) in the form

$$P_c = A_r(\varepsilon_1 F - \varepsilon \sigma T_r^4) \qquad (8)$$

where we define F and ε as before and the parameter ε_1 by the following equation:

$$\varepsilon_1 = \int_0^\infty \varepsilon_\lambda F_\lambda d\lambda / \int_0^\infty F_\lambda d\lambda. \qquad (9)$$

An even more general case allows for F to contain both a component dissimilar to $B_\lambda(T_r)$, which we will refer to as the short wave component (e.g. incident and reflected solar radiation), and a component similar to $B_\lambda(T_r)$, which we

will refer to as the long wave component (e.g. infrared flux emitted by the earth). In this case we find

$$P_c = A_r \ (\varepsilon_{SW} \ F_{SW} + \varepsilon_{LW}(F_{LW} - \sigma T_r^4)) \tag{10}$$

where ε_{SW} is the average emissivity for solar radiation and ε_{LW} is the average emissivity for blackbody radiation at the receiver temperature. The temperature difference required to conduct the power P_c is just P_c/K; thus we have the steady state relation

$$K(T_r - T_s) = A_r \ (\varepsilon_{SW} F_{SW} + \varepsilon_{LW}(F_{LW} - \sigma T_r^4)) \tag{11}$$

Since, for most high speed room temperature thermopiles, $(T_r - T_s) << T_s$, we may make the approximation

$$\sigma T_r^4 = \sigma T_s^4 + 4\sigma T_s^3 \ (T_r - T_s) \tag{12}$$

in which case equation (11) may be rewritten in the form

$$(T_r - T_s) = k_1 [\varepsilon_{SW} F_{SW} + \varepsilon_{LW}(F_{LW} - \sigma T_s^4)] \tag{13}$$

where k_1 is defined by

$$k_1 \equiv A_r \ [K + 4A_r \varepsilon_{LW} \sigma T_s^3]^{-1}. \tag{14}$$

It should be noted that for thermopiles with rapid response the denominator of equation (14) will be dominated by the conductivity term, i.e. it will be found that

$$K >> 4A_r \varepsilon_{LW} \sigma T_s^3. \tag{15}$$

The voltage output of the sensor is proportional to the temperature difference across the thermal resistor, i.e.

$$V = \alpha \ (T_r - T_s), \tag{16}$$

where the proportionality factor α will depend on the thermopile materials, the number of junctions, etc., and will have a weak dependence on heat sink temperature. A similarly weak temperature dependence is usually present in

K as well. The combined effects of these temperature dependencies is typically of the order of 0.3% per °C, and will be entirely negligible as a result of temperature control of the heat sink. Substituting (16) into (14) yields

$$V = k_2 \, [\varepsilon_{SW} F_{SW} + \varepsilon_{LW}(F_{LW} - \sigma T_s^{\,4})] \qquad (17)$$

where $k_2 = \alpha k_1$.

APPENDIX L.   UNCERTAINTIES IN SOLAR INPUT RESULTING FROM ATTITUDE ERRORS

The solar input to the wide FOV sensors is proportional to the cosine of the angle γ between the vector to the sun $\hat{s}$ and the sensor pointing vector $\hat{r}$ (See Figure 1). If the actual angle is γ and the attitude uncertainty is Θ, we shall assume that the estimated pointing vector $\hat{r}$ can lie anywhere on a cone of half angle Θ centered about $\hat{z}$ the actual pointing direction. In this case the estimated solar input factor depends on ϕ according to the equation

$$\cos\Theta' = \cos\Theta\cos\gamma - \sin\Theta\sin\gamma\cos\phi, \tag{1}$$

where Θ' is the angle between the estimated vector $\hat{r}$ and the solar vector $\hat{s}$.

The square of the error is then

$$(\cos\Theta' - \cos\gamma)^2 = (\cos\gamma(1-\cos\Theta) + \sin\gamma\sin\Theta\cos\phi)^2. \tag{2}$$

The average value over all possible ϕ's is

$$<(\cos\Theta' - \cos\gamma)^2>_\phi = \cos^2\gamma(1-2\cos\Theta + \cos^2\Theta) + \frac{1}{2}\sin^2\gamma\sin^2\Theta. \tag{3}$$

Expanding $\cos\Theta$ and $\sin\Theta$ for small values of Θ yields

$$\cos\Theta = 1 - \frac{1}{2}\Theta^2 + \frac{1}{4!}\Theta^4 - \dots \tag{4}$$

$$\sin\Theta = \Theta - \frac{1}{3!}\Theta^3 + \dots \tag{5}$$

Inserting these expansions into (3) yields

$$<(\cos\Theta' - \cos\gamma)^2>_\phi \approx \cos^2\gamma\ [\frac{1}{4}\Theta^4] + \frac{1}{2}\sin^2\gamma\ [\Theta^2 - 1/3\Theta^4] \tag{6}$$

Since

$$\int_{-\infty}^{\infty} \Theta^n\ e^{-a^2\Theta^2}\ d\Theta = \frac{\Gamma(\frac{n+1}{2})}{a^{n+1}} \tag{7}$$

we find that

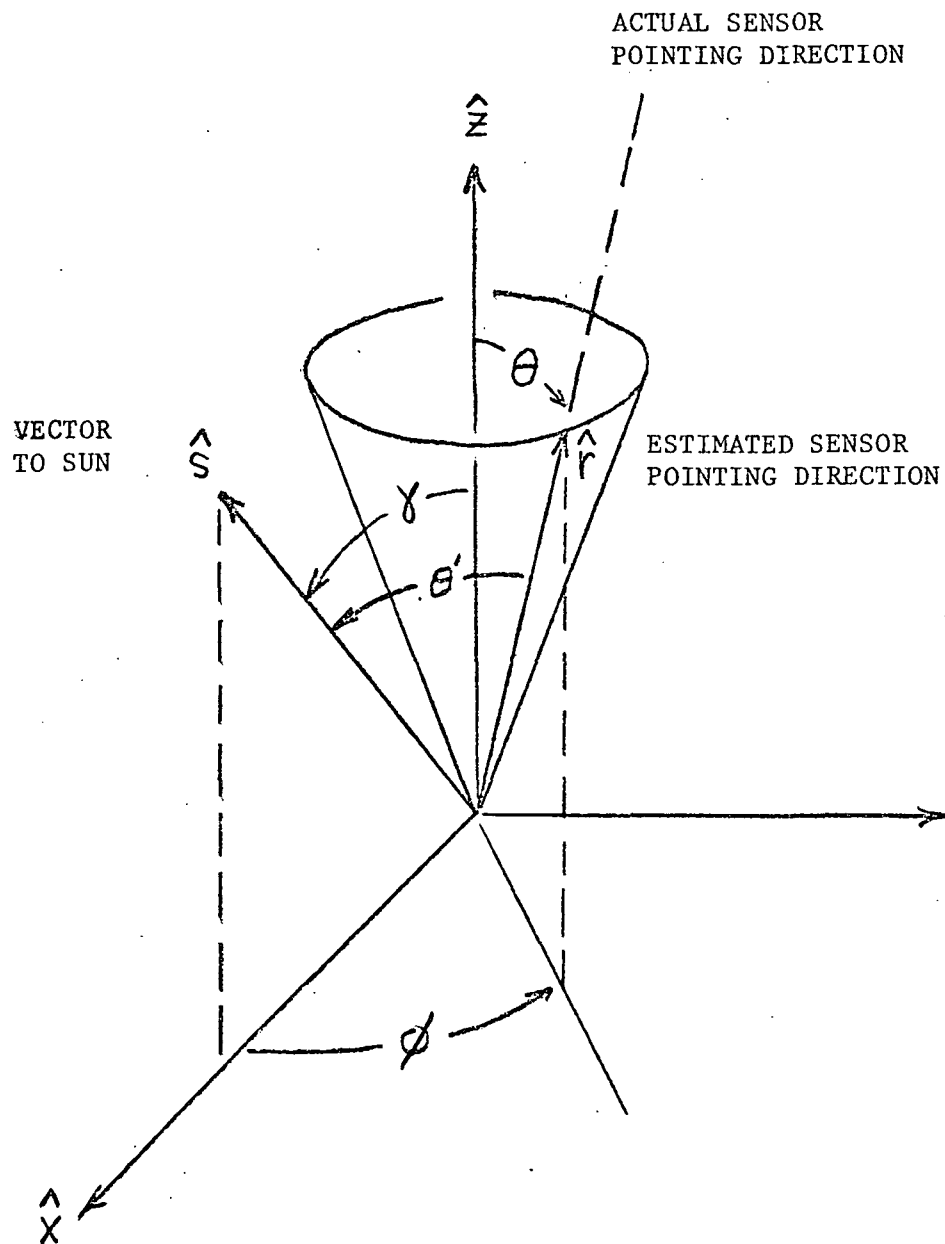$$<\Theta^4>_\Theta = \frac{\Gamma(\frac{5}{2})}{a^4\ \pi} = 3\sigma_\Theta^4 \tag{8}$$

Figure 1. Coordinate system for computing the effect of attitude
errors on estimating solar flux input to wide FOV sensors.

where

$$\sigma_\Theta = [<\Theta^2>_\Theta]^{1/2} \tag{9}$$

assuming a normal distribution of Θ values about $\Theta = 0$. Defining

$$\sigma_{cos}^2 = (cos\Theta' - cos\gamma)^2_{\phi,\Theta} \tag{10}$$

we find that

$$\sigma_{cos}^2 = 3/4\ \sigma_\Theta^4 cos^2\gamma + 1/2\ sin^2\gamma(\sigma_\Theta^2 - \sigma_\Theta^4) \tag{11}$$

The fractional standard deviation of the solar input factor cos(') is

then given by

$$(\frac{\sigma_{cos}}{cos\gamma}) = [3/4\ \sigma_\Theta^4 + 1/2(\sigma_\Theta^2 - \sigma_\Theta^4)tan^2\gamma]^{1/2} \tag{12}$$

The results of evaluating equation (12) as a function of γ are presented

in the following table for $\sigma_\Theta = 0.5°$ (.008727 radians).

γ ANGLE	$\sigma_{cos}/\cos\gamma$	% ERROR IN ESTIMATING SOLAR INPUT
0°	6.60×10^{-5}	.007
5°	8.11×10^{-5}	.008
10°	2.03×10^{-4}	.020
15°	4.48×10^{-4}	.045
20°	8.20×10^{-4}	.082
25°	1.34×10^{-3}	.134
30°	2.06×10^{-3}	.206
35°	3.03×10^{-3}	.303
40°	4.34×10^{-3}	.434
45°	6.17×10^{-3}	.62
50°	8.76×10^{-3}	.88
55°	1.26×10^{-2}	1.26
60°	1.85×10^{-2}	1.85
65°	2.84×10^{-2}	2.84

APPENDIX M. DESCRIPTION OF FACR TEST MODEL AND RESULTS

In order to verify the basic theory of the fast active cavity radio-
meter (FACR) which was presented in Section VI, and to measure the geo-
metrical coefficients applicable to the angular non-uniformity parameters,
a test model of a FACR was constructed and tested. In order to avoid
parts procurement problems and time consuming design and fabrication,
available materials and simplified design were the rule. Although this
resulted in a non-optimum design compared to that described in Section VII,
it did result in a suitable instrument for testing the performance predic-
tions of the theory. A description of the test model and the test results
are presented in the following subsections.

1. Description of FACR Test Model Construction

The physical configuration of the main components of the FACR test
model are indicated in Figures 1 and 2. The wire wound active cavity
is mounted to an adjustable mounting ring by three stainless steel
support wires. The mounting ring is attached to the heat sink (base)
by a three point spring suspension and three alignment screws. These
screws are adjusted to obtain the required spacing and parallelism
between the cavity aperture and the area defining aperture mounted
on the cover portion of the heat sink. The area defining aperture is
subsequently adjusted to be concentric with the cavity aperture. In
its final configuration, the cavity is surrounded by a heat sink of
similar shape so that radiative transfer coefficients between the
active cavity and the sink cavity will not vary significantly over the
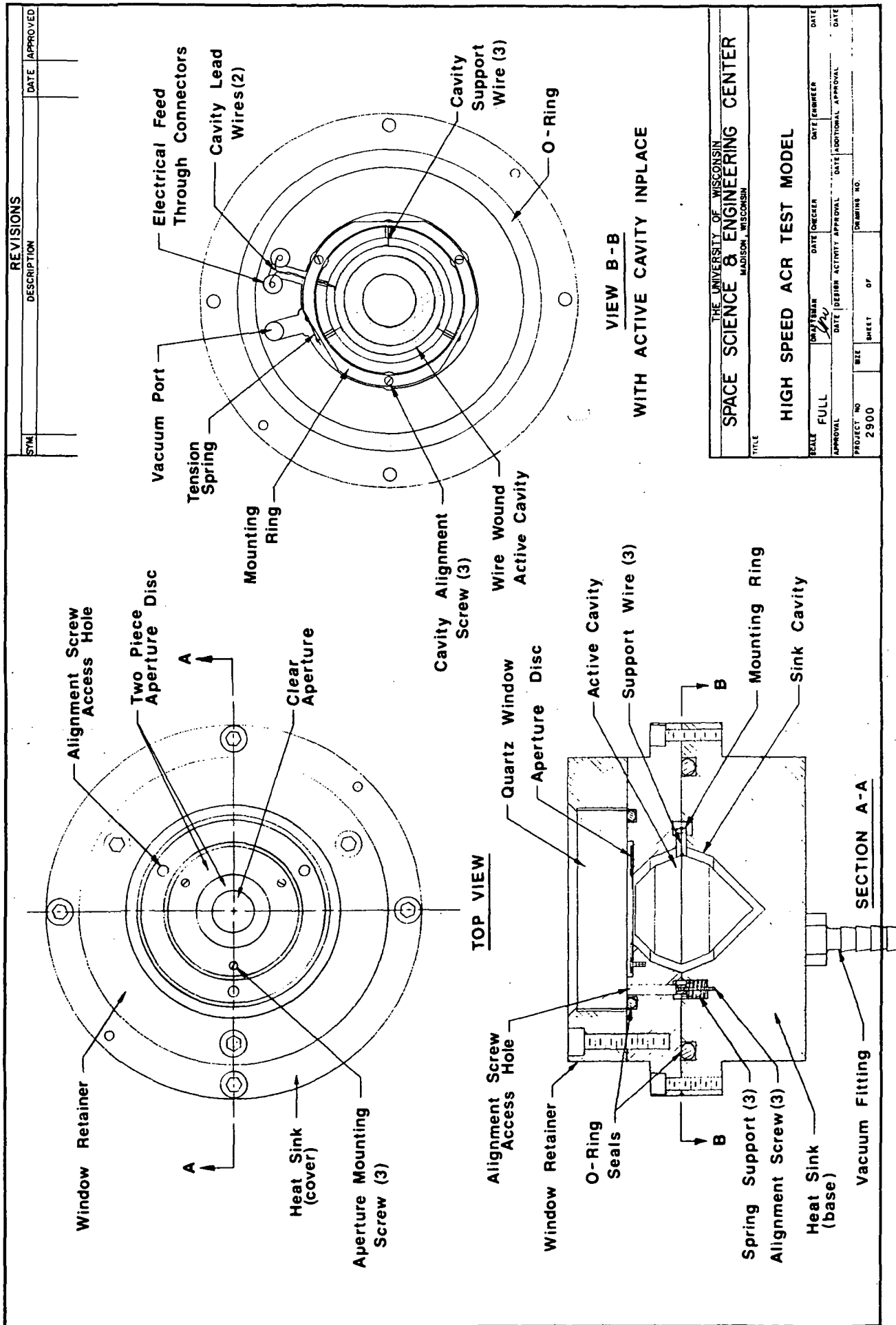surface of the active cavity.

FIGURE 1. Physical Configuration of Assembled Fast Active Cavity Test Model. Cover sink cavity, base sink cavity, and interior and exterior surfaces of the active cavity are painted with 3M Black (101-C10).
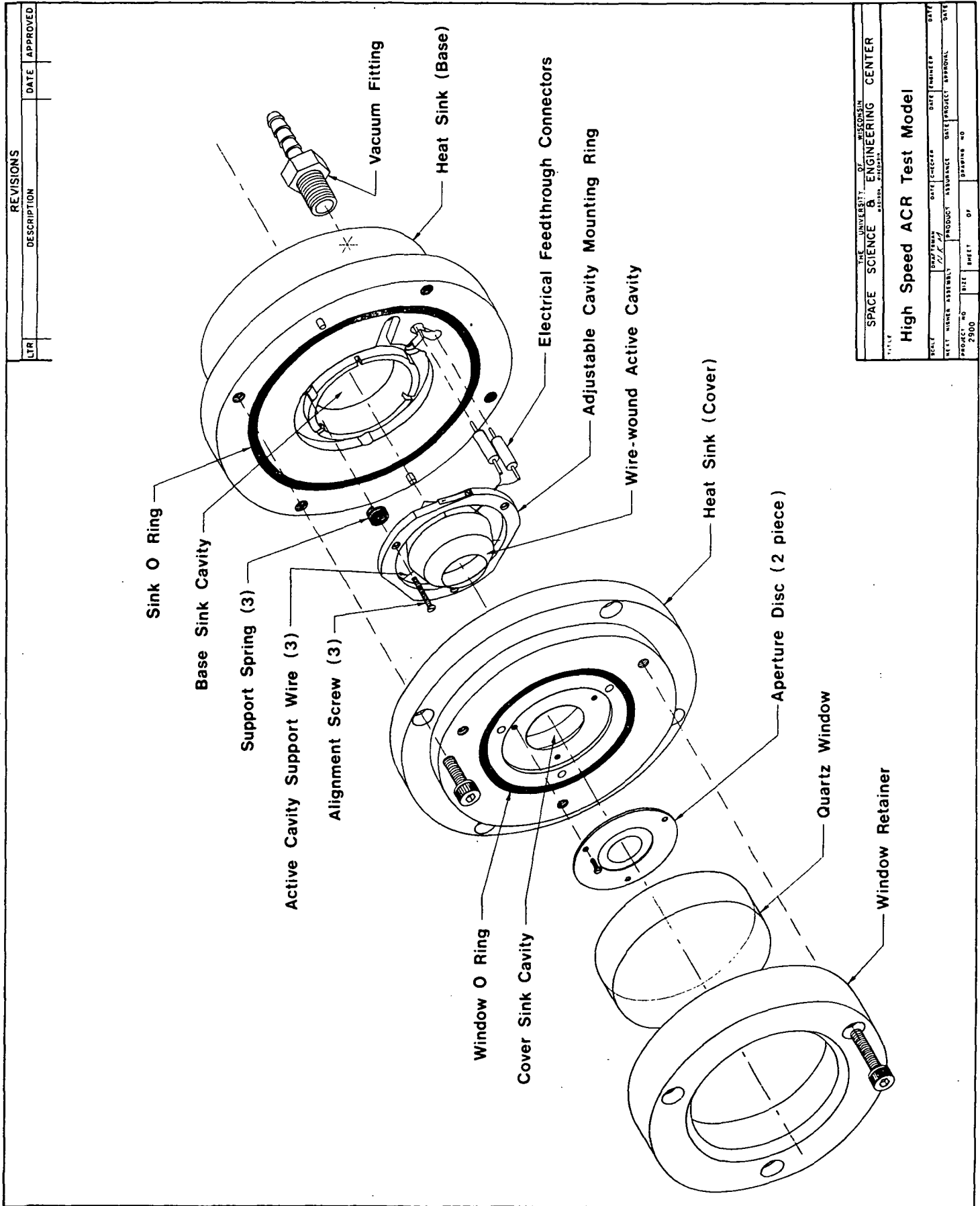
M-3

FIGURE 2. Exploded View of FACR

The active cavity is constructed in two pieces: an open-ended half which forms the cavity aperture, and closed-ended half which mates to the first section at the maximum cavity diameter. Each half is formed by winding wire non-inductively on a polyethelene mandril. The wire turns are cemented together by a very thin coating of Krylon lacquer. The two halves are subsequently coated on their interior surfaces with 3M-Black (101-C10) and cured. They are then cemented together and the exterior of the assembled cavity is painted with 3M-Black. When the exterior coating is cured, the cavity becomes quite rigid and durable.

The two piece heat sink is made of aluminum and vacuum sealed so that the volume within the heat sink cavity can be evacuated. The heat sink cavity is also painted with 3M-Black (101-C10) to maximize the radiative coupling with the active cavity. The straight cylindrical section on the base portion of the heat sink is used for winding the heater wire used in temperature control of the heat sink. It is also used for mounting the high current resistor in the cavity leg of the bridge servo used to control the active cavity temperature. The other bridge resistors and the preamp electronics are mounted on the back face of the heat sink base.

Although the preferred window is a thin hemispherical dome, the actual window available was a thick quartz disc. As a result, angular response testing must separately account for the angular response effects of the window. The reason a window was used at all was that it makes laboratory testing much more convenient.

2. <u>FACR Test Model Analysis</u>

Significant physical and geometrical parameters of the FACR test
model are presented in Table 1. From these it is possible to derive
predicted performance characteristics of the test model.

In order to calculate the electrical power required to maintain
the cavity at T_o when no incident radiation is received, we must first
estimate the effective emissivity for radiative exchange between the
cavity and the sink. This can be approximated by equation (3) Section
VII. For

$$\frac{A_1}{A_2} = \left(\frac{1.630}{1.905} \right)^2 = 0.73 \tag{1}$$

and $\varepsilon_1 = \varepsilon_2 = \varepsilon_s = 0.94$, we find that

$$\varepsilon_{eff} = \varepsilon_s \left[1 + (1-\varepsilon_s) A_1/A_2 \right]^{-1} = 0.90 . \tag{2}$$

The radiative power transferred directly from cavity to sink is thus
given by

$$P_1 = \varepsilon_{eff} \sigma A_1 \left[T_o^4 - T_s^4 \right] = 1.636 \text{ W} \tag{3}$$

where A_1 for the case of a quartz window in place, is taken to be the
sum of the cavity exterior surface area (29.11 cm^2) and the cavity
aperture area (1.81 cm^2). The portion of this power which is actually
transferred to the window can be estimated by using equation (3) with
$A_1 = 1.267 \ cm^2$. Additional power is conduced via leads and support
wires. For each term, the power conducted has the form

$$P_1 = A_i k_i (T_o - T_s)/\ell; \tag{4}$$

where k_i is the thermal conductivity of the ith wire and A_1 and ℓ_i are
the cross sectional area and length respectively. Assuming

$$k_{cu} = 3.80 \text{ w}/(cm - °c) \tag{5}$$

$$k_{ss} = 0.45 \text{ w}/(cm - °c) \tag{6}$$

Table 1. Fast Active Cavity Test Model Parameter Values

PARAMETER	MEASURED OR ESTIMATED VALUE
Cavity Mass Distribution	
Copper (#36 wire)	2.20 gm
wire insulation + Krylon	0.20 gm
3M-Black (interior)	0.24 gm
3M-Black (exterior)	0.15 gm
TOTAL	2.79 gm
Cavity Wire Diameter	
Bare Copper (#36)	0.0127 cm (.005")
with insulation	0.0152 cm (.006")
Cavity Resistance @ 20°C	26.55 Ω
@ 100°C	34.62 Ω
Cavity Major Radius	1.63 cm (0.640")
Cavity Aperture Radius	0.76 cm (0.300")
Cavity Exterior Surface Area	29.11 cm^2
Defining Aperture Radius	0.635 cm (0.250")
Area	1.267 cm^2
Distance Between Cavity Aperture and Defining Aperture	0.051 cm (.020")
Uniform Angular FOV	$\pm$ 68.2°
Active Cavity Operating Temp.(T_o)	100°C
Sink Operating Temp.(T_s)	35°C
Diffuse Hemispherical Emissivity of 3M-Black (ε_s)	0.94 (Hall, 1970)
Sink Cavity Major Radius	1.905 cm (0.750")
Cavity support wire diameter	0.025 cm (0.010")
Support wire length (ℓ_s)	0.51 cm (0.20")
Lead wire length (ℓ_e)	0.53 cm (0.21")

we thus find that each lead wire conducts 59 mW and each support
wire conducts 28 mW of power. The total electrical power P_e^o is
thus 1.838 W. These results are summarized in Table 2.

Table 2. Electrical Power Budget for Zero Radiative
Input (T_o = 100°C, T_s = 35°C)

Radiative Transfer

cavity to sink (direct)	1.569 w	
cavity to window	0.067 w	
SUBTOTAL		1.636 w

Conductive Transfer

lead wires (2)	0.118 w	
support wires (3)	0.084 w	
SUBTOTAL		0.202 w

Total Electrical Power Required (P_e^o)   1.838 w

The radiative power received by the cavity from an incident flux
equivalent to one solar constant H_s is given by

$$P_r = \varepsilon_c A_a \tau_w H_s \qquad \text{where } \tau_w \text{ is the window transmittance.} \qquad (7)$$

We can obtain an approximate value by assuming H_s = 1357 W/M^2, τ_w = 0.92,
ε_c = 0.993 (Section VII), and A_a = 1.267 cm^2 (Table 1). The result is

$$P_r \simeq 157.1 \text{ mW/solar constant} = 0.1157 \text{ mW}/(WM^{-2}) \qquad (8)$$

The voltage across the cavity is determined from the electrical power
requirement using the relationship

$$V_c = (R_1^o P_e^o)^{1/2}. \qquad (9)$$

where R_1^o = 34.62 Ω is given in Table 3. Typical voltage levels are
summarized in Table 3.

Table 3. Typical Values of Test Cavity Power and Voltage

	Space View (zero incident flux)	Solar View (1357 wm^{-2} incident flux)
Electrical Power to Cavity (P_e)	1.636 W	1.479 W
Voltage across Cavity (V_c)	7.5258 V	7.1556 V
ΔV_c per WM^{-2} change in incident flux	0.27 mV	0.28 mV

According to equation (16) Section VI, the FACR time constant is given by

$$\tau = \frac{C}{K+\Gamma} , \tag{10}$$

where C is the total heat capacity of the cavity, K is the effective conductance between the cavity and the sink, and Γ is the servo gain parameter. According to equation (8) of Section VI, K can be calculated from the power transfers listed in Table 2 as follows:

$$K = 1.636W \times 4\, T_o^{\ 3}(T_o^{\ 4} - T_s^{\ 4})^{-1} + 0.202W(T_o - T_s)^{-1} = 35.89 \text{ mW/o}_K. \tag{11}$$

The total heat capacity of the cavity is equal to the sum of the specific heat capacity - mass products of the components. Although the specific heat of copper is well known (0.393 w-sec/gm°c @ 100°C), the same is not true for the other cavity components. We will assume a value of 0.902 w.sec/gm°C for the other components since this is the value for carbon @ 100°C, the major constituent of 3M-Black. The result of this assumption is

$$C = 2.20 \times .393 + .59 \times .902 = 1.397 \text{ w-sec/°C} . \tag{12}$$

Since nearly 40% of the total heat capacity is due to the non-metallic components, the uncertainties in their specific heats makes (12) only an approximate result.

The natural time constant of the cavity (no servo action present) is given by

$$\tau = \frac{C}{K} = 38.9 \text{ sec.} \tag{13}$$

In order to achieve a τ of $\approx$ 40 ms Γ must be given by

$$\Gamma \approx 10^3 \text{ x } K \approx 36 \text{ w/o}_K \quad . \tag{14}$$

3. Servo Electronics

The circuit diagrams of the DC servo constructed for use with the test model are shown in Figures 3 thru 5. The separate portions of the circuit given in these figures are the preamplifier, the power amplifier and the analog divide and square root circuitry.

The preamplifier is an instrumentation amplifier which is appropriate here because of its good common mode rejection. The MONO OP-07 operational amplifiers used in this circuit were chosen for their low frequency noise performance. The voltage gain of the preamplifer set up for testing was measured to be 2.65 x 10^3.

The power amplifier portion shown in Figure 4 also performs an inversion and a level shift. The inversion simply gives the signal the proper sign for use with a positive supply voltage. The level shift is performed as a convenient technique to keep the voltage for the analog operation chips in their operating ranges. The shift which acts as a voltage gain w is accomplished with the transistors shown in the circuit diagram. The magnitude of w is given by the resistance ratio R_1/R_2 where R_1 and R_2 are defined in Figure 4. The value of w is related to z used in the previous description of the DC servo by $w^3 = z^2$. The reason that w does not equal
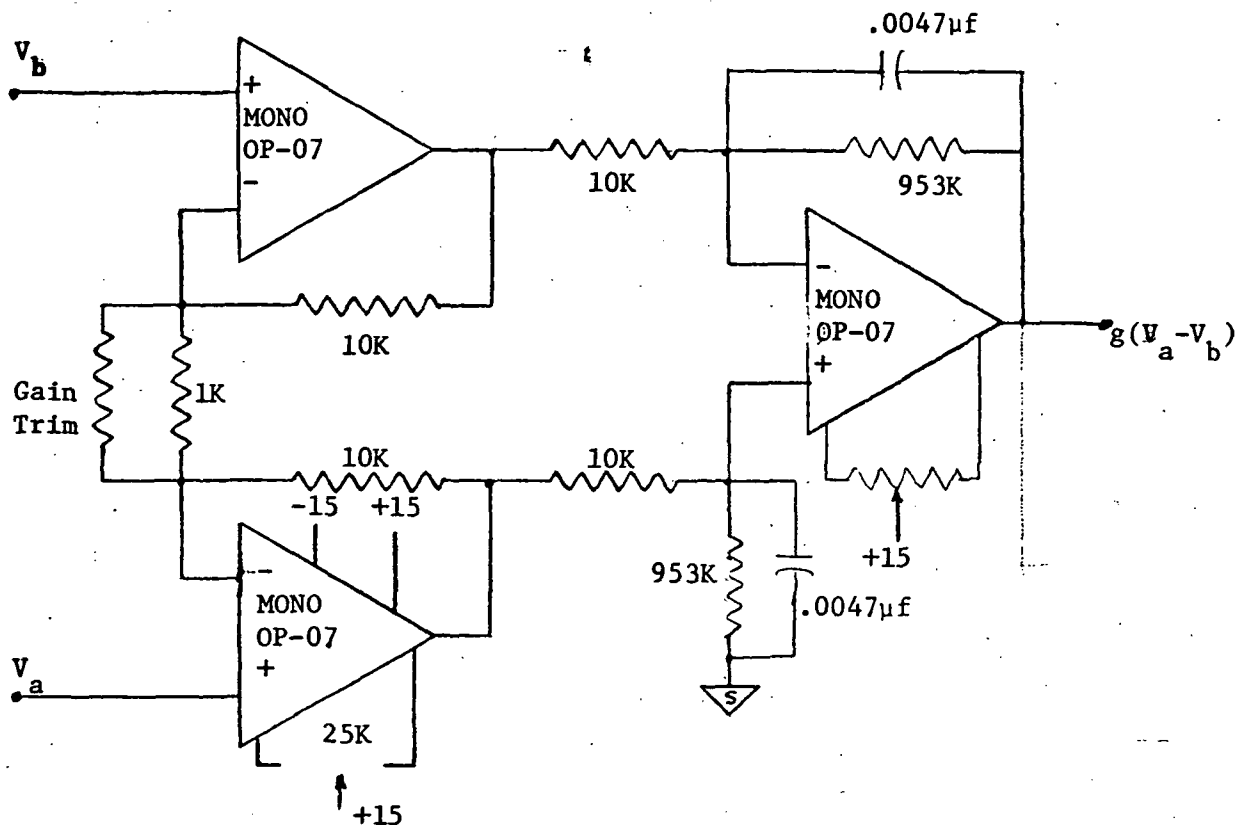
Figure 3. Preamplifier Circuit Diagram. The ground labelled s is the signal ground which is connected to the base of the bridge circuit. The voltage difference $V_a - V_b$ is the imbalance voltage of the Wheatstone bridge containing the cavity.
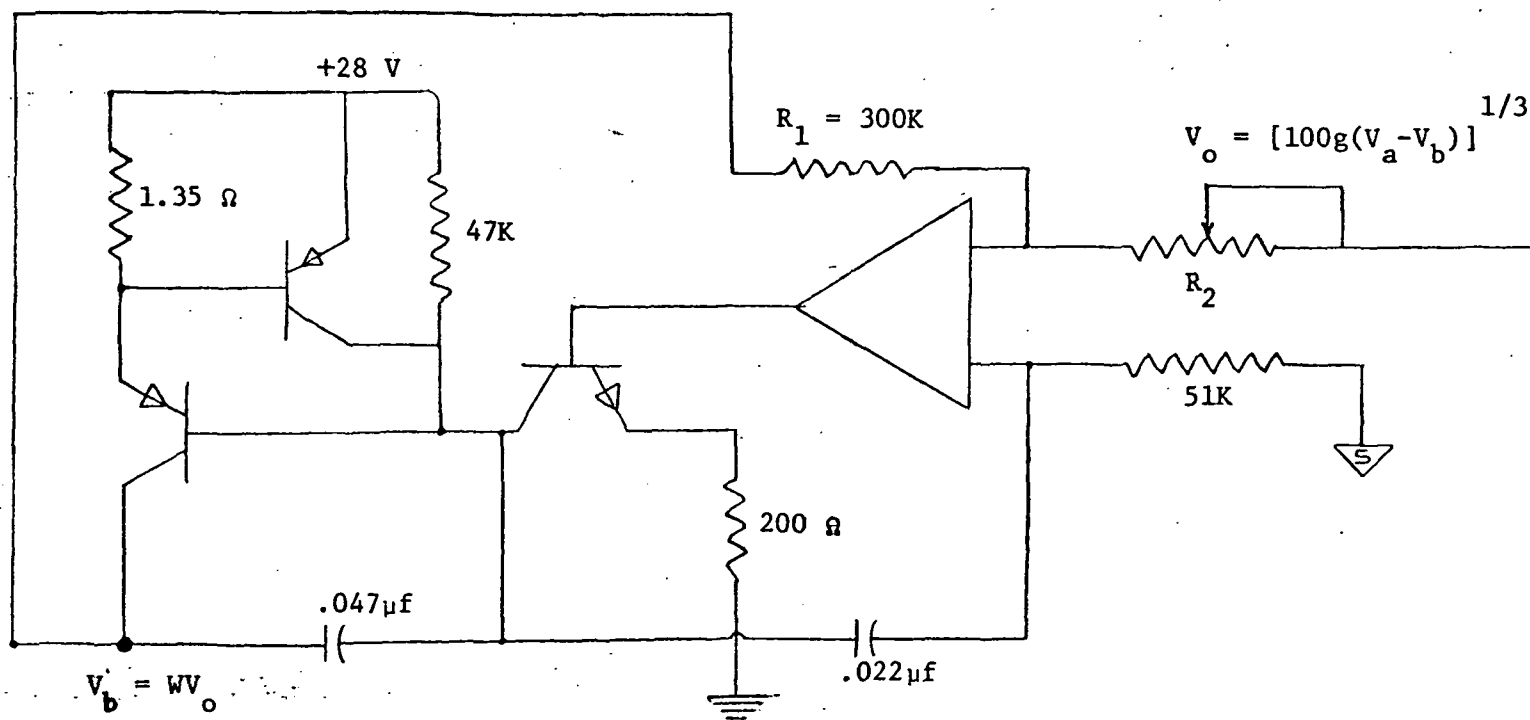

Figure 4. Power Amplifier. The hashed line ground symbol is power ground and the ground labelled s is signal ground. The voltage V_b is the voltage supplied to the bridge.
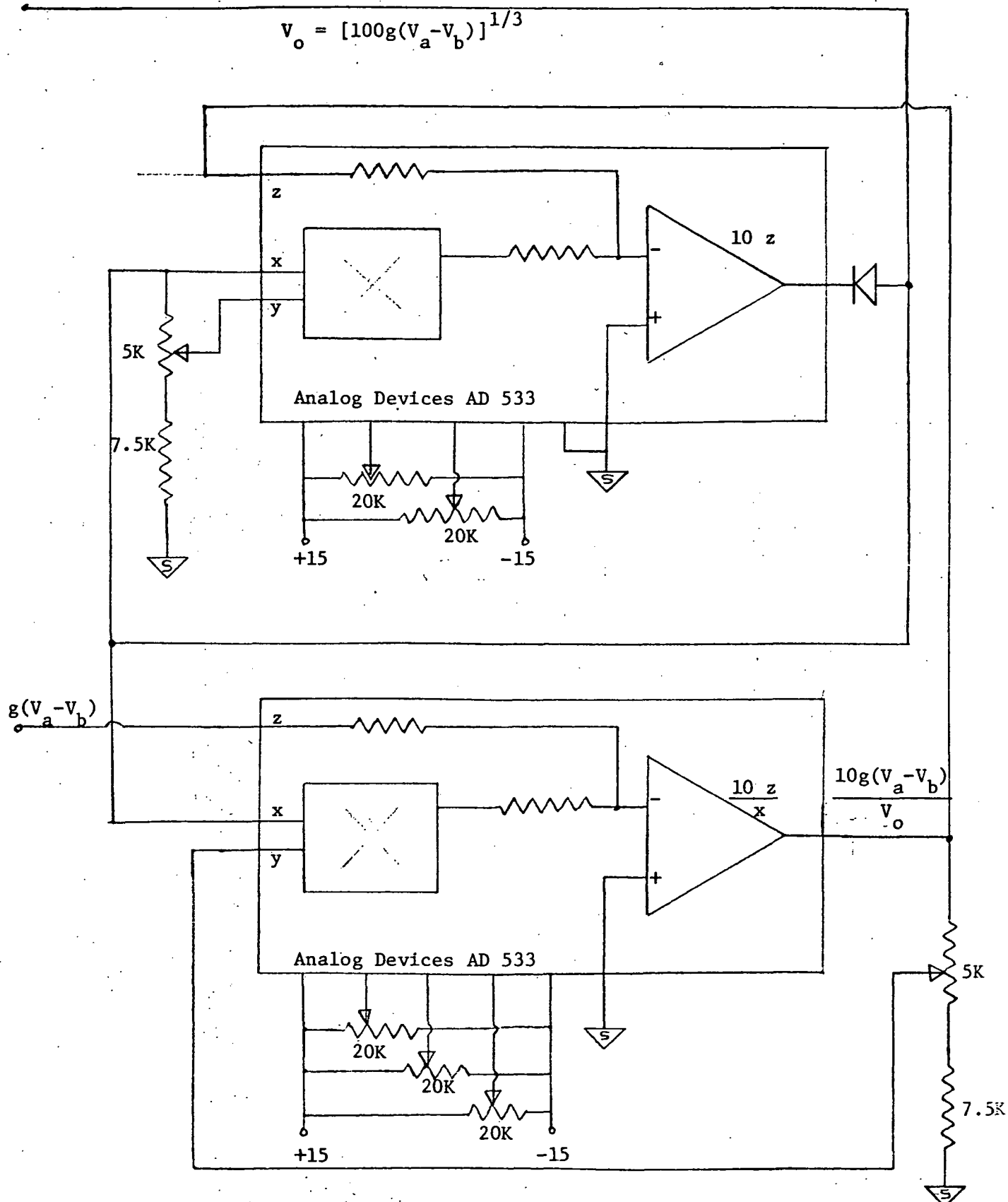
$$V_o = [100g(V_a - V_b)]^{1/3}$$

Figure 5. Analog Divide and Square Root Circuit Diagram. The transfer function of the Analog Devices AD 533 integrated circuits are given for both the divider and the square rooter. The ground labelled s is the signal ground.

z is that the preamplifier output voltage is not divided by the total

bridge voltage V_B as shown in the block diagram of Section VI, but is

divided by $V_B W^{-1}$.

The analog operations for which the circuit is shown in Figure 5

are performed using two multiplier, divider, squarer, square rooter

integrated circuits (Analog Devices A D533). The transfer functions

used for this application are shown for both chips in the figure. They

were set up using the standard instructions for their use as a divider

and a square rooter.

4. Test Results

A number of aspects of the predicted FACR performance have been

verified using the test model FACR. The following characteristics have

been examined.

   1. Time response

   2. Dependence of the time constant on servo gain

   3. Cavity power consumption.

The tests of characteristics 1 and 2 were primarily aimed at verifying

the operation of the FACR servo. The determination of cavity power

consumption tests the predictions of the radiative and conductive power

exchange between the cavity and the heat sink.

The time response of the sensor to chopped incident flux is shown

in Figure 6 for two different servo gain choices. Semi-log plots of the

response were made for several different time constants. They showed

the response to be expotential to within the uncertainty of reading

the strip chart records except for the initial 10-20 ms of the
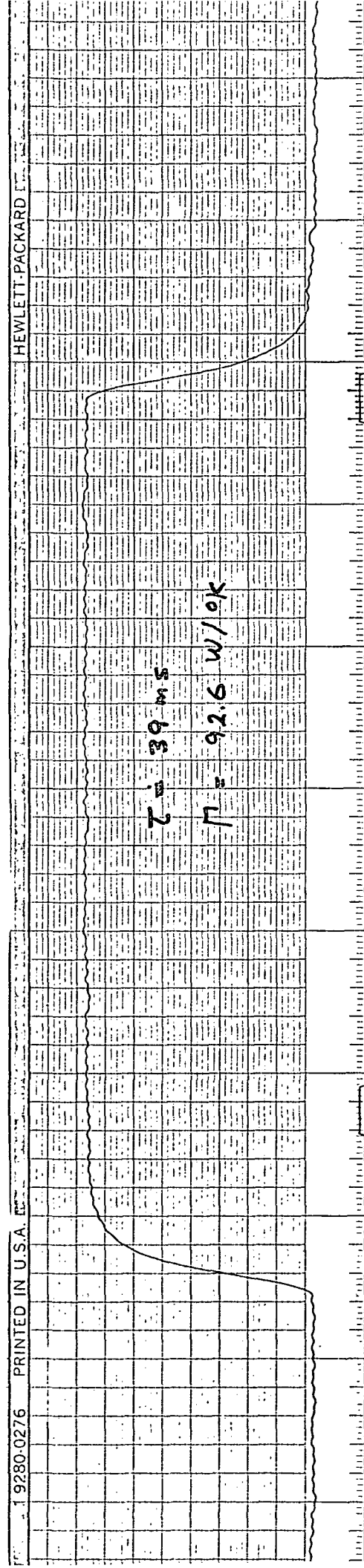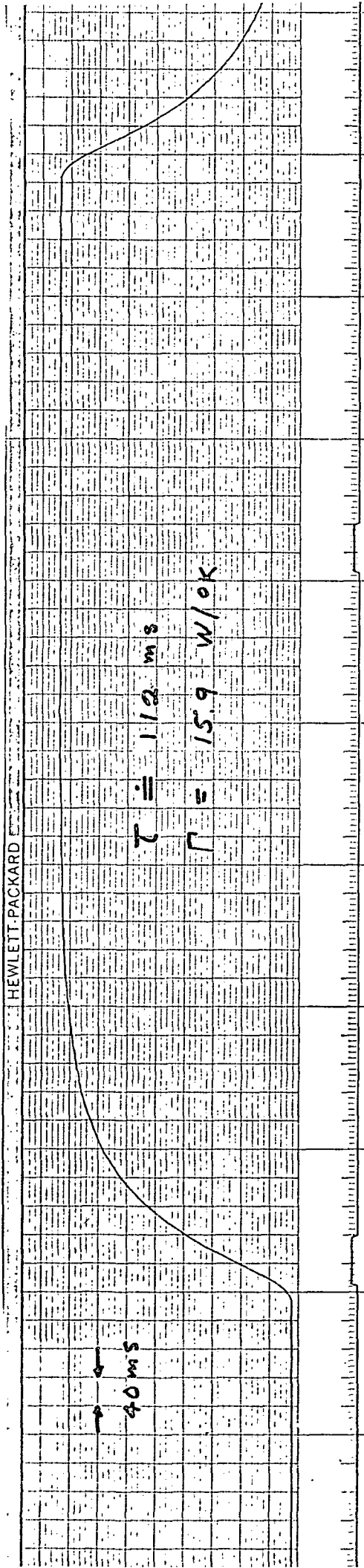
M-13

FIGURE 6. Fast ACR Test Model Response to Chopped Radiation

response. This deviation is caused by the 60 Hz filtering in the preamplifier and earlier tests performed without this filtering show that it can be eliminated. The time response tests demonstrate that the desired time constant of 48 ms is easily within reach of the FACR.

The results of measuring the FACR time constant for several different servo gains are shown in Figure 7. The time constants were measured from semilog plots of the strip chart records. The servo gain Γ was calculated from its theoretical expression which requires knowledge of the cavity resistance and temperature coefficient of resistance α along with the servo parameter gz^2y. The cavity resistance was measured precisely for three different temperatures before testing began. Therefore, α was known, and measurements of the cavity resistance performed for each test by measuring the bridge current and voltage also provided the cavity temperature. The preamplifier gain g was measured during the servo construction and z^2y was determined for each test from measurements of the bridge voltage output of the preamplifier. The results of Figure 7 indicate that, as the theory predicted, the time constant varies linearly with Γ^{-1} for time constants greater than 50 ms. Again we see that the 60 Hz filtering in the preamplifier affects the time response and causes deviations from the theoretical behavior for short time constants. The cavity heat capacity implied by these results is 1.7 W-sec/°K.

The cavity power consumption was determined from measurements of the bridge voltage and current. Table 4 shows the comparison of the test results P_{meas} and the theoretical predictions P_{calc}. The measured cavity temperature T_o and heat sink temperature T_s given in the table were used
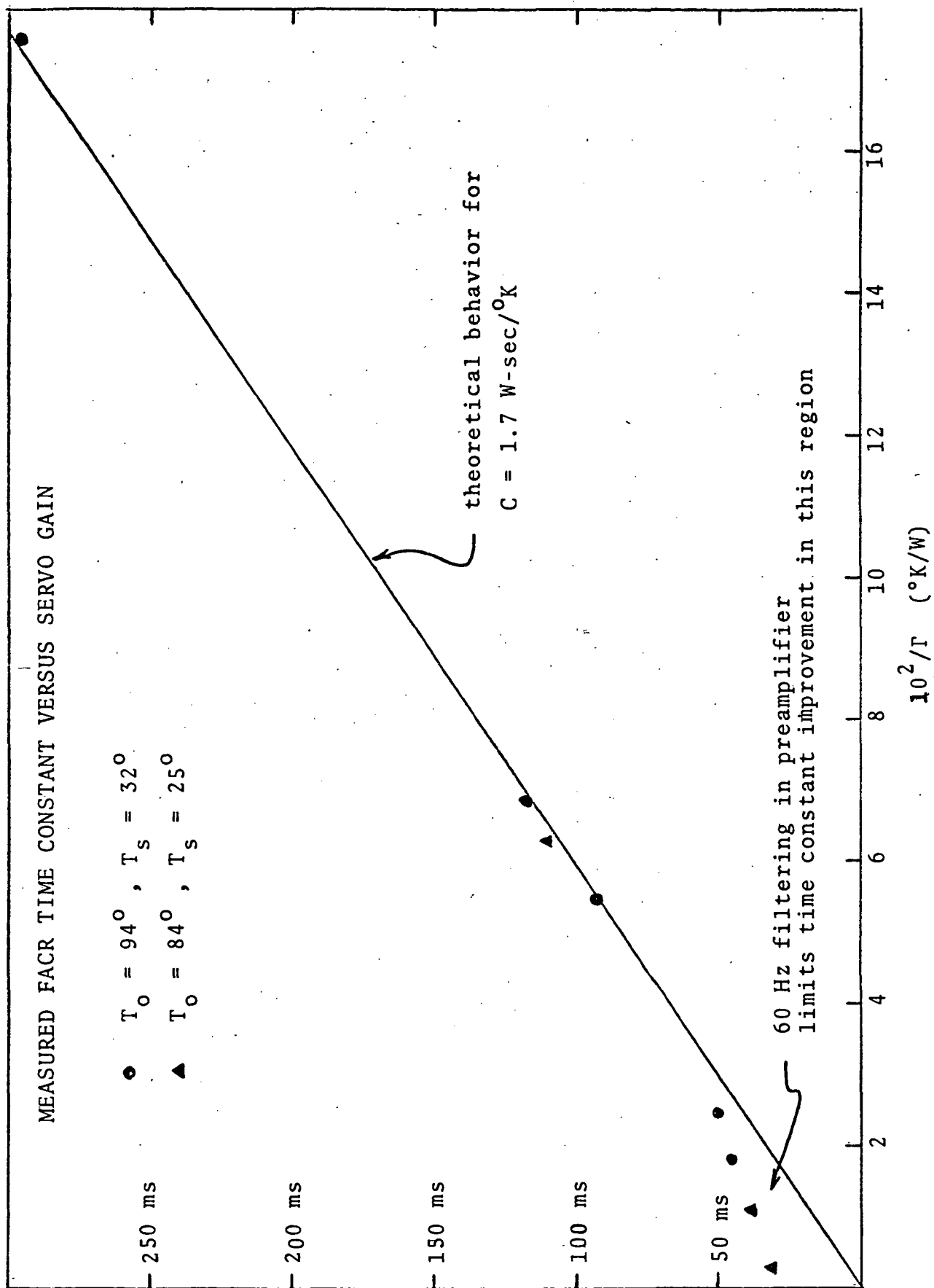
FIGURE 7. Dependence of the Fast ACR on Servo Gain Γ

TABLE 4. Comparison of Test Model Cavity Power Measurements to
the Power Predicted by the Theory.

T_o (°K)	T_s (°K)	P_{calc} (W)	P_{meas} (W)	Pressure (microns)
94.5	32.4	1.70	1.92	.013
94.5	32.4	1.70	1.90	.013
94.2	32.3	1.69	1.91	.013
94.3	32.3	1.69	1.88	.012
60.8	32.3	.680	.681	.011
60.9	32.2	.682	.681	.011
61.1	32.2	.687	.677	.010

to calculate P_{calc} (the measurement of T_o was discussed in the previous paragraph and T_s was determined using a thermistor recessed in the sink). The measured power consumption was very strongly dependent on the vacuum gauge pressure reading (see last column of Table 4), for pressures greater than 0.010 microns. Since the gauge was located at the diffusion pump, the actual pressure inside the radiometer itself was not accurately known. However, when the vacuum gauge readings reached about 0.010 microns or smaller, there was good agreement between the measured and the calculated power consumption.

Unfortunately, the initial FACR test phase was not completed, both for lack of time and money. The most obvious omission is testing of the angular response. Plans were made to verify the angular response characteristics of the FACR in a vacuum chamber to obviate the need for determining the angular response of the thick window on the test model. Other additional testing and design optimization of the FACR is necessary to completely demonstrate its capabilities. However, the success of the initial tests described in this report make us optimistic that future testing will also show agreement with the FACR theory presented here.

APPENDIX N.   AC SENSE - DC HEAT CAVITY SERVO DESIGN FOR THE FACR

The DC servo designed to control the FACR cavity temperature was
tested using a model FACR (see Appendix M) and was found to behave as
predicted by the theory presented in Section VI.   As a parallel effort
to the DC servo testing a study was performed to determine whether other
types of servo systems would offer advantages over the DC servo.   The
study was restricted to servo systems capable of producing a predictable,
single time constant response to step function changes in the irradiance
incident on the cavity.   This was the major consideration of the DC servo
design and as shown in Section VI amounts to requiring that the power
supplied to the cavity vary linearly with changes in cavity temperature.
The alternatives considered included a totally AC system, a pulsed
system and an AC sense - DC heat system.   The AC/DC combination was
found to be superior to the other alternatives and was pursued in some
detail.

1.   Basic Design and Operation of the AC Sense - DC Heat Servo

The electronics for the AC sense - DC heat servo is illustrated with two
levels of block diagrams in Figure 1.   Like the DC design a Wheatstone
bridge with the wire wound cavity as one resistance element (R_1) is used
to sense temperature changes of the cavity.   However, here the bridge is
excited with a fixed AC voltage V_{AC}.   The bridge imbalance voltage, which
is linearly related to the cavity temperature, is then amplified using a
transformer - preamplifier combination.   The amplified voltage is
synchronously demodulated and then filtered to restrict the broad band
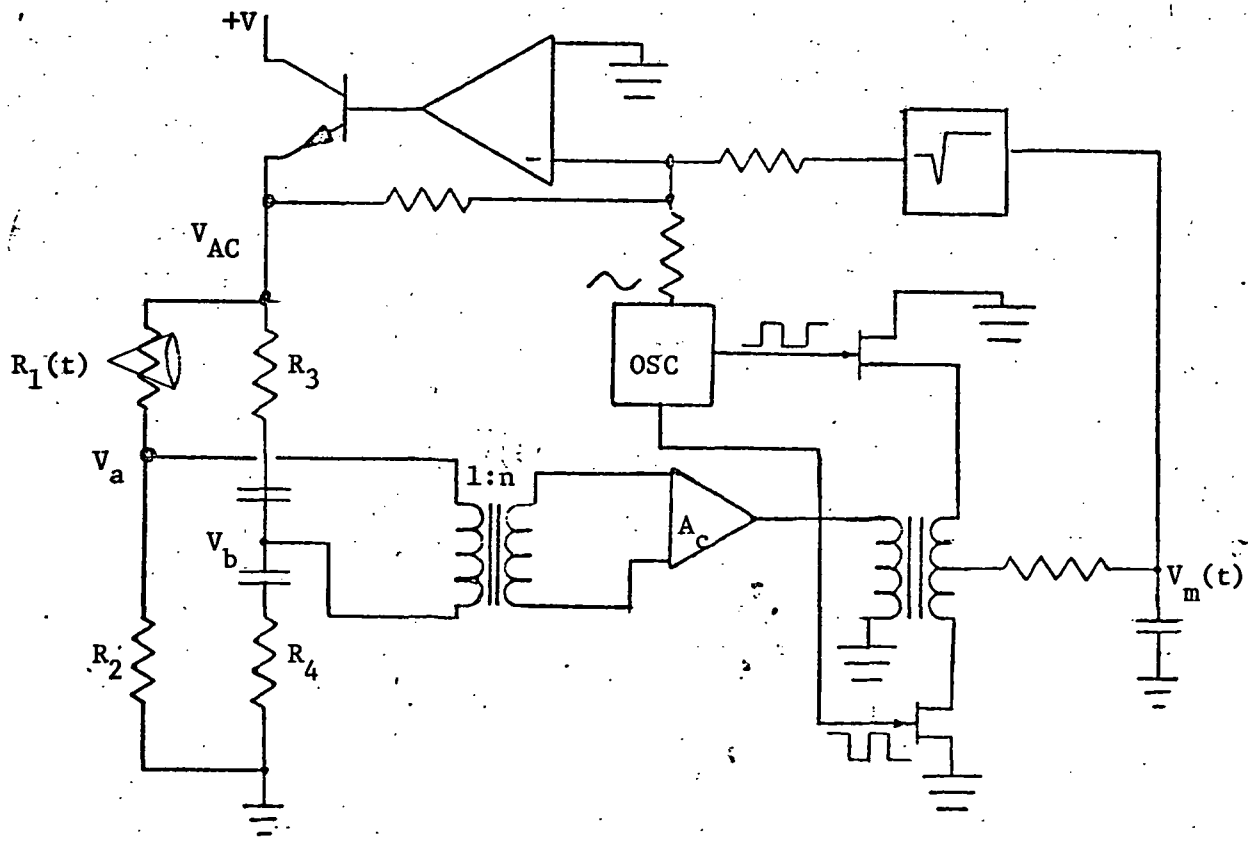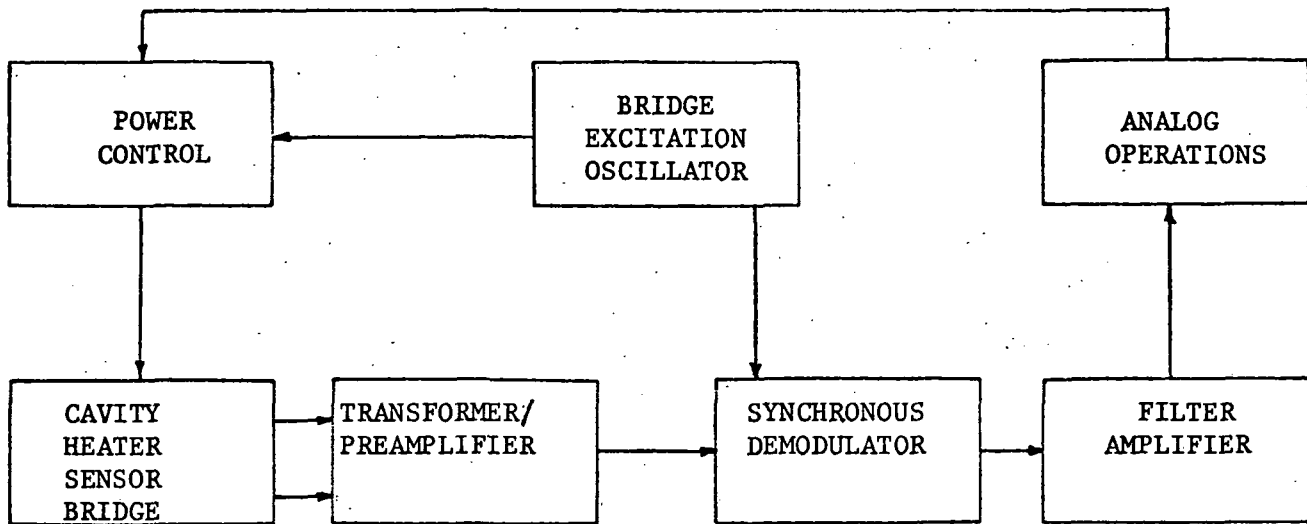noise and to attenuate undesirable signal components generated in the

Figure 1. AC Sense - DC Heat Servo Block Diagrams

rectification process. The voltage V_m emerging from the filter is of course still linearly related to the cavity temperature. Since to provide a single time constant response, the power supplied to the cavity must be linearly related to the cavity temperature, V_m is next square rooted. A power amplifier sums the output of the square rooter and the AC excitation voltage, and powers the bridge. The DC bridge power is isolated to the R_1R_2 leg of the bridge by placing capacitors in the other leg of the bridge. This allows the resistances R_3 and R_4 to be small enough that the bridge does not load the transformer appreciably and avoids dissipating large amounts of power in R_3 and R_4.

Two major advantages of the AC sense - DC heat servo are apparent at this point. First, an improvement of the signal to noise ratio over that of the DC servo can be obtained by coupling the AC signal from the bridge to the servo preamplifier via a transformer. As a result, whereas the preamplifier is the dominant source of noise in the DC servo, the preamplifier contribution to the noise of the AC/DC servo is very small. The system noise is essentially reduced to the Johnson noise of the bridge resistors. A noise analysis is given in Section 3 of this Appendix. The second advantage is the simplification of the analog operations required. By heating the cavity with a DC voltage and sensing its temperature with an AC voltage the need for the analog divide operation of the DC servo is eliminated.

2. Analysis of the Servo Operation

In this subsection the previous description of the servo operation is translated into servo operating equations similar to those given for the DC servo in Section VI. The notation of Figure 1 will be used.

The bridge imbalance voltage V_{ab} can be written in terms of the AC excitation voltage V_{AC} as follows,

$$V_{ab}(t) = V_a - V_b = V_{AC} \left[\frac{R_2}{R_1(t)+R_2} - \frac{R_4}{R_3+R_4}\right] \qquad (1)$$

$$= V_{AC} \left[\frac{(R_2 R_3 - R_1^\circ R_4)}{(R_1^\circ+R_2)(R_3+R_4)} - \frac{\alpha R_1^\circ R_2\, T(t)}{(R_1^\circ+R_2)^2}\right] \qquad (2)$$

where Equation (24) of Section VI has been used and where, as in Section VI, R_1° and α are the cavity resistance and temperature coefficient of resistance at the space view operating temperature T_o, and $T(t)$ is the deviation of the cavity temperature from T_o.

The voltage $V_m(t)$ following amplification, rectification and filtering is defined in terms of V_{ab} as follows,

$$V_m(t) = n\, A_c\, m\, V_{ab}(t) \qquad (3)$$

where

n = transformer turns ratio

A_c = preamplifier voltage gain

m = demodulator gain

It was assumed here that the transformer input impedance is sufficiently large that the transformer is not loaded by the bridge resistances.

Finally, in terms of the voltage gain of the square rooter z and the voltage gain of the power amplifier A_p, the DC voltage supplied to the bridge is given by $V_{DC}(t) = A_p\, z\, V_m(t)^{1/2}$. Substituting $V_m(t)$ from

Equation (3) and $V_{ab}(t)$ from Equation (2) yields,

$$V_{DC}^2(t) = [A_p^2 z^2 nm \, A_c V_{AC}] \, V_{ab}(t)/V_{AC} \tag{4}$$

$$V_{DC}^2(t) = [A_p^2 z^2 nm \, A_c V_{AC}] \, [\frac{(R_2 R_3 - R_1^\circ R_4)}{(R_1^\circ + R_2)(R_3 + R_4)} - \frac{\alpha R_1^\circ R_2}{(R_1^\circ + R_2)^2}] \tag{5}$$

Equation (5) can be recognized as Equation (25) of Section VI for the DC servo where the first bracketed quantity above replaces gz^2y. The DC power to the bridge is again defined by Equation (27) of Section VI, yielding

$$P_e^{DC}(t) = P_e^{\circ DC} - \Gamma \, T(t), \tag{6}$$

where

$$P_e^{\circ DC} = [z^2 A_p^2 nm \, A_c V_{AC}] \, \frac{(R_3 - \beta R_4)}{(R_3 + R_4) R_1^\circ} \, \frac{\beta^2}{(1+\beta)^3} \tag{7}$$

$$\Gamma = \frac{\beta^3}{(1+\beta)^4} \, \frac{\alpha [z^2 A_p^2 nm \, A_c V_{AC}]}{R_1^\circ} \tag{8}$$

$$\beta = R_1^\circ / R_2. \tag{9}$$

The major difference between the results for the AC/DC servo and the DC servo is the relationship of Equation (4) which gives the DC voltage in terms of the bridge imbalance voltage. The results of this analysis are summarized in Table 1 which can be compared with the DC servo analysis of Table VI.2.

3. <u>Noise Analysis</u>

The important sources of noise in the AC/DC servo system are the bridge resistances and the preamplifier. The following calculation show that the Johnson noise of the bridge dominates.

Table 1.   Summary of AC Sense - DC Heat Servo Relationships

(1) $\beta = R_1^\circ / R_2$

(2) $\Gamma = \dfrac{\beta^3}{(1+\beta)^4} \dfrac{\alpha[z^2 A_p^2 nm\, A_c V_{AC}]}{R_1^\circ}$

where,

   V_{AC} = AC sense voltage applied to the bridge (constant)

   n = Transformer turns ratio

   m = Demodulator Gain

   A_c = Preamplifier voltage gain

   A_p = Power amplifier voltage gain

   z = Gain of analog square rooter

(3) $V_{ab}(t) = \dfrac{(1+1/\beta)^2 \, R_1^\circ \, P_e^{DC}(t) \, V_{AC}}{[z^2 A_p^2 nm\, A_c V_{AC}]}$

(4) $P_e^{\circ DC} = [z^2 A_p^2 nm\, A_c V_{AC}] \, (R_3 - \beta R_4)(R_3 + R_4)^{-1} R_1^{\circ -1}(1+\beta)^{-3}\beta^2$

(5) $P_T^{DC}(t)$ = Total DC electrical power dissipated in cavity leg of the bridge

(6) $P_T^{DC}(t) = (1+1/\beta)\, P_e^{DC}(t)$

(7) $v^{DC}(t) = \left[\dfrac{[z^2 A_p^2 nm\, A_c V_{AC}] V_{ab}}{V_{AC}}\right]^{1/2} = (1+1/\beta)[R_1^\circ P_e^{DC}(t)]^{1/2}$

The expression for the mean square Johnson noise voltage of the bridge has been derived by P. Freymuth (1968).

$$\overline{v_n^2} = 4 \, k \, T_s \, R \, \Delta f \, [(1+\beta) \, (1+n/\beta) + \Delta T/T_s] \, (1+\beta)^{-2}$$

where

k = Boltzmann's constant

T_s = Sink temperature

ΔT = The difference between the cavity temperature and T_s

Δf = Equivalent noise bandwidth

$$R = \frac{R_1 R_2}{(R_1+R_2)} + \frac{R_3 R_4}{(R_3+R_4)}$$

$\beta = R_1/R_2$

$n = (R_1+R_2)/(R_3+R_4)$

Using the following parameter values from Section VII:

T_s = 320°

ΔT = 25°

$R_1 = R_3$ = 520 Ω

$R_2 = R_4$ = 460 Ω

and an equivalent noise bandwidth of 52 Hz (this corresponds to a single section filter time constant of 4.8 ms), gives an RMS noise voltage of 20 nV.

The amplifier contribution to the noise is found by dividing its RMS noise voltage by the turns ratio of the transformer. For a typical low noise amplifier with a noise bandwidth of 52 Hz, the RMS noise voltage is 315 nV. Using a turns ratio of 50 the preamplifier noise referred to the bridge is 6.3 nV.

Combining the bridge resistance noise with the amplifier noise in

RSS fashion yields a total noise voltage of 21 nV. This result was used

in Section VII to calculate the signal to noise ratio for the FACR

design.